Lehrstuhl für Thermodynamik
Technische Universität München

Performance assessment of the Aeolus Doppler wind lidar prototype

Ulrike Paffrath

Vollständiger Abdruck der von der Fakultät für Maschinenwesen
der Technischen Universität München
zur Erlangung des akademischen Grades eines
DOKTOR – INGENIEURS
genehmigten Dissertation.

Vorsitzender:	Univ.-Prof. Dr.-Ing. habil. Boris Lohmann
Prüfer der Dissertation:	1. Univ.-Prof. Dr.-Ing. Thomas Sattelmayer
	2. apl. Prof. Dr.-Ing., Dr. rer. nat. habil. Ulrich Schumann, Ludwig-Maximilians-Universität München

Die Dissertation wurde am 17.05.2006 bei der Technischen Universität München eingereicht und durch die Fakultät für Maschinenwesen am 23.06.2006 angenommen.

Table of contents

Abstract

The Atmospheric Dynamics Mission ADM-Aeolus by ESA (European Space Agency) will be the first mission worldwide to provide global observations of wind profiles by applying a Doppler wind lidar on a polar-orbiting satellite. An instrumental prototype was developed to validate this lidar system during ground and flight campaigns at DLR.

This thesis introduces a newly end-to-end simulator, representing the properties of the prototype and various atmospheric models, to study wind measurements for different atmospheric and instrumental parameters, and to analyse the performance of the prototype from ground and aircraft. The random error of simulations at 10 mJ laser energy of an airborne system, for a flight altitude of 10 km, is smaller than 0.5 m/s, whilst for a ground system, it is smaller than 1 m/s (simulations up to 10 km altitude).

The results of the simulations are used to develop and optimise the signal processing algorithms, knowing the properties of the modelled signal. The wind is determined by the Doppler shift from the molecular and aerosol backscatter signal with respect to the transmitted laser pulse. The algorithms are evaluated, optimised and compared, and those that provide results with a random error smaller than 0.15 m/s are the most suitable for this type of receiver. Simulations show the benefit of the system measuring both Rayleigh and Mie backscatter, because the wind speed measurements cover a larger atmospheric range.

Atmospheric wind is not derived but the wind speed measurement accuracy was determined by the backscatter signal of the surface of a building. The random error is larger than 0.59 m/s. Besides, cloud backscatter is demonstrated and the attenuation of backscatter signal above clouds. It is shown that the Rayleigh signal was be detected up to altitudes of 8 km in clear air.

First measurements of atmospheric backscatter with the prototype were performed at DLR (Deutsches Zentrum für Luft und Raumfahrt, or German Aerospace Centre) from ground and aircraft, and it was the first time that a direct detection Doppler wind lidar had been deployed on an aircraft. The very first measurements from these airborne studies are presented and discussed. Signals between the aircraft and ground, along with backscatter from clouds, and signals of the Earth’s surface, were detected by the instrument, showing the capability to identify the ground and cloud return at the receivers.

1 Introduction

1.1 Overview

At present, our information on the three-dimensional wind field over the oceans, the tropics, and the southern hemisphere is incomplete due to insufficient measurement data. There are still significant areas where measurements do not yield reliable data, and there is a strong demand for improvements in wind measurements throughout the atmosphere, which are crucial for both numerical weather prediction and studies related to the global climate (Baker et al. 1995).

Satellite based lidar (LIght Detection And Ranging) systems offer the potential for adequate vertical resolution and global coverage. Within the context of the Earth explorer core programme of the European Space Agency (ESA), the Atmospheric Dynamics Mission (ADM-Aeolus, named after the god of the winds in the Greek legend) comprises a lidar system to measure global wind fields from satellite, being the first European lidar in space and the first worldwide wind lidar in space. The lidar system used in the ADM is known as the Atmospheric LAser Doppler lidar INstrument (ALADIN), and was designed to provide global observations of wind profiles in clear air in the troposphere and lower stratosphere for numerical weather prediction and climate studies (ESA 1999). The most important and most challenging requirement for global meteorological analysis remains the measurement of wind profiles to high accuracy, global coverage, and good vertical resolution (Tan and Andersson 2004). Economic benefits and costs of developing and deploying a space-based wind lidar were investigated by Cordes (1995). Weissmann (2006) provided further insights into the importance of wind data, measured by an airborne Doppler lidar system. These lidar data were assimilated into a global weather forecast model of the European Centre for Medium-Range Weather Forecasts (ECMWF) and it was shown that the data have a significant impact on the analyses as well as on forecasts.

A Doppler wind lidar system generally provides range-resolved profiles of the wind velocity and can be categorized into two main types: direct detection, and heterodyne lidar. Direct detection systems determine the Doppler shift by interferometric methods, and are capable of measuring wind speed from the motion of aerosols and molecules. Heterodyne systems measure the Doppler shift by optically mixing the transmitted and backscatter signal, and due to the width of the backscatter spectra, are only able to determine wind from the motion of aerosols. The ADM lidar is a direct detection Doppler wind lidar which was designed to determine wind fields in clear air and in areas with higher aerosol loadings. The system is characterized by two receivers - one that determines the wind from molecular backscatter, and the other from aerosol backscatter. The Doppler wind lidar provides information not only on wind profiles, but also on cloud top heights, vertical distribution of clouds, and aerosol properties.

1.2 Aims of the Thesis

The main objective of this work is the validation of an instrumental prototype of ALADIN, which was developed to validate the measurement concept in realistic atmospheric conditions by providing wind measurements from the ground. The prototype is expected to be integrated into an aircraft to perform wind measurements in a downward viewing geometry, similar to how ALADIN will operate in space. The validation is performed by an end-to-end simulator, which has been developed to represent the lidar system at ground level and on aircraft (Fig. 1.1).

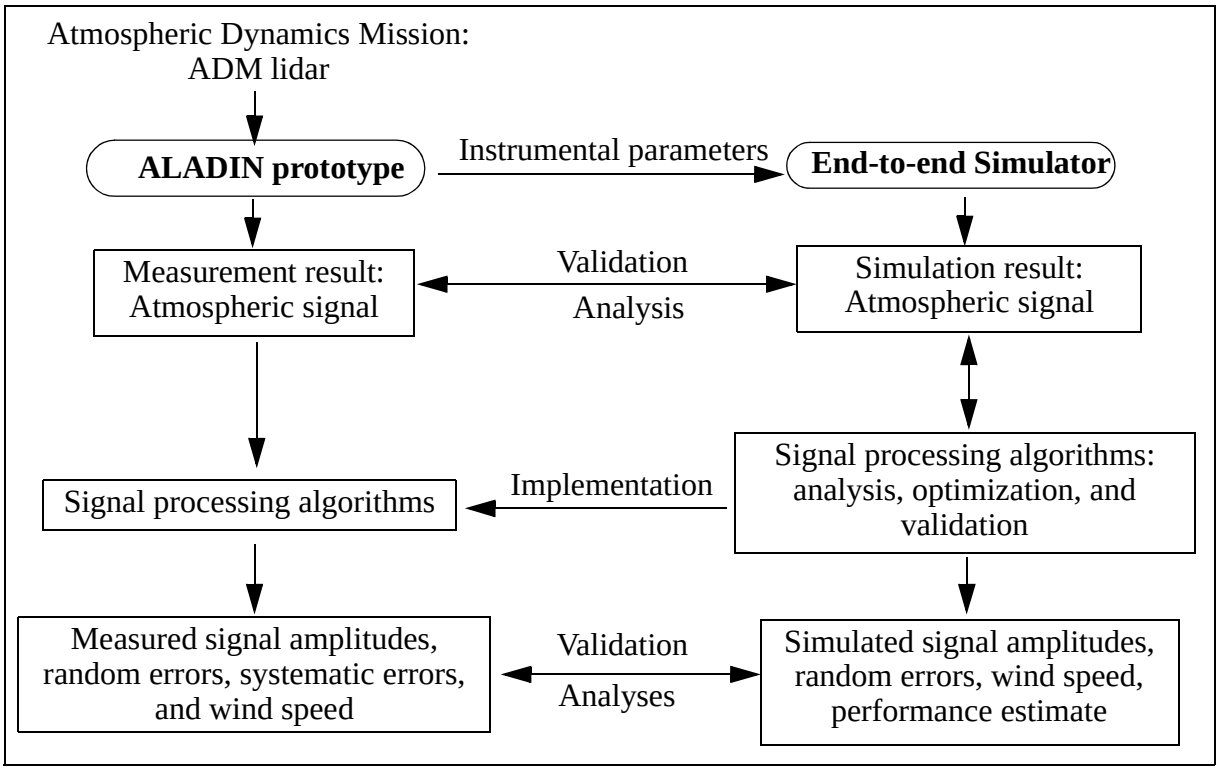

Fig. 1.1 Overview and structure of the main objectives of this thesis: the development of the end-to-end simulator, the optimization of the data processing algorithms, and the validation of the prototype.

The simulator includes the laser transmitter, the receiver, the detection unit, and the interaction of the transmitted light with the atmosphere. This enables the studies of the system under different atmospheric conditions, to analyse the radiometric performance, the wind speed, and the systematic and random error on the wind speed estimate. The results of the simulator are important for the development of the signal processing algorithms (Fig. 1.1).

The most important objective of this work is the optimisation of the signal processing algorithms and the analysis of the signals arriving at the detector. The design of both receivers provides a large field of processing options with respect to the signal information provided by the aerosol and molecular scattering processes, and several algorithms were developed, analysed, and improved.

The combination of lidar systems for detecting both aerosol and molecular backscatter has never been implemented for wind measurements before ALADIN. The possibility to make wind measurements using a Fizeau interferometer in an aerosol backscatter receiver is demonstrated

here for the first time. The molecular backscatter receiver measures the Doppler shift in the same manner as existing systems (Garnier and Chanin 1992, Gentry et al. 2000), but is characterized by a new method to separate light depending on polarization, and the advantages and results are discussed in this study. Both receivers offer the opportunity to examine, compare, and combine the measurements. The detection unit employed is a CCD (charged coupled device), capable of accumulating signals, and this is the first time an accumulation CCD is used for lidar applications.

The simulator is an important tool to validate the measurement results of the prototype. This offers the possibility of sensitivity analysis, to examine the influence of variation in instrumental and atmospheric parameters, which significantly affects the measurement results. Atmospheric and internal reference signal measurements are analysed and validated by simulations to examine consistency. How far the Rayleigh signal will be detected through clear atmosphere is another measure of the performance of the receiver. It is the first time a direct detection Doppler wind lidar is deployed on an aircraft, and the signals give an insight into the downward viewing geometry, the impact of clouds, and the possibility to detect the Earth's surface.

The results of this work leads to new insights into direct detection Doppler wind lidar systems and their capability to avoid errors by collecting information from both aerosol and molecular backscatter.

1.3 State of the art

The principle of lidar was first demonstrated in the 1930s, where the measurement of atmospheric density profiles by detection of the atmospheric scattering from a beam of light was first performed by Synge, reported by Hulburt (1937). By the early 1960s the development of the laser provided an ideal light source for light detection and ranging systems. Lidar systems have been actively researched and developed since then (Fiocco and Smullin (1963)), finding applications in range finding, vibrometry, and remote sensing of the atmosphere, land, and ocean. Lidar is used predominately for measuring atmospheric parameters, such as wind, temperature, and trace gases.

Direct detection Doppler wind velocity measurements with lidar systems were first performed and developed by Benedetti-Michelangeli et al. (1972). Doppler wind lidar systems were then studied and analysed further, leading to the development of heterodyne lidar systems (Huffaker 1970, Hall et al. 1984, Bilbro et al. 1986, Post and Cupp 1990, Hardesty 2003) and direct detection systems (Garnier and Chanin 1992, Gentry et al. 2000, Korb et al. 1992). Heterodyne Doppler wind lidar systems have been operated from ground as well as aircraft platforms (Bilbro et al. 1984, Rahm 1995, Reitebuch et al. 2001), and first spaceborne applications were started in 1994 as the Lidar-in-space Technology Experiment (LITE, Winkler 1996), followed by the Mars Orbiter Laser Altimeter 1999 (MOLA, Abshire et al. 2000, Neumann et al. 2003) and the Geoscience Laser Altimeter Satellite (GLAS), launched in January 2003 (Spinhirne et al. 2005, Palm and Spinhirne 1998, Zwally et al. 2002, Abshire et al. 2005).

Since the end of the 1980s, the prospects for space-born Doppler wind lidar systems have been evaluated by ESA (1989). In 1999, the ADM for wind profile measurement was selected as one of two core missions. Beforehand, numerous instrument options had been investigated for heterodyne and direct detection lidar systems. The heterodyne lidar systems are able to determine

the wind speed for regions where the aerosol loadings are higher, but the direct detection systems, operating at shorter wavelengths, are able to measure wind from aerosol and molecular backscatter. Thus the direct detection system was selected. The wavelength was chosen to be in the ultraviolet at 355 nm to take advantage of the λ^{-4} dependence of molecular backscatter.

Several ground campaigns have been performed in the past to validate the direct detection Doppler lidar technology, through comparisons of wind measurements from radiosondes with direct detection Doppler wind lidar, which measure wind from by the double edge method at 355 nm wavelength (Flesia et al. 2000, Gentry et al. 2000). Comparisons of wind measurements taken from direct detection Doppler lidar systems with coherent Doppler lidar and other sensors were made in Europe (Delaval et al. 2000) and USA (Hardesty et al. 2001). Whilst a direct detection Doppler lidar was never operated on board an aircraft before, heterodyne Doppler lidar systems have been developed and validated on airborne platforms in recent years (Reitebuch et al. 2001 and 2003, Rahm 2001).

During this study, the ALADIN prototype is simulated and the data processing algorithms are analysed, optimised, and validated. Chapter 2 describes the atmospheric processes relevant for lidar measurements and the lidar system generally, followed by an introduction to the lidar of the ADM prototype. Chapter 3 deals with the simulator of the ALADIN prototype and the various processing steps. In chapter 4, the signal processing is introduced, and the results are discussed in respect to the modelled signals generated by the simulator. Chapter 5 presents the results from measurements with the prototype instrument on ground and aircraft campaigns at DLR in November 2005.

2 Lidar

This chapter is divided into two sections. Section 2.1 introduces the basic processes by which light from a lidar interacts with the atmosphere, relevant to later discussions on the simulation and signal processing of lidar return signals. From Section 2.2 onwards, a general overview of the basic operating principles and theory of lidar systems is provided. Furthermore it describes the direct detection scheme of a Doppler wind lidar used for atmospheric wind speed measurements.

2.1 Atmospheric interactions

Measurements of atmospheric parameters with lidar systems are based on the interaction of the coherent light generated by a laser (Light Amplification by Stimulated Emission of Radiation) with atmospheric particles (Mie scattering) and molecules (Rayleigh scattering). When light from a laser propagates through the atmosphere, it is scattered and absorbed by the atmospheric constituents, resulting in a change in intensity and spectral characteristics of the scattered light. Some of the backscatter light is detected by the lidar system and analysed to obtain information about the atmospheric consistence (as trace gases, particles, and density) and dynamics (as wind speed and wind direction). This section describes the atmospheric processes important for Doppler wind lidars.

2.1.1 Molecular scattering

Rayleigh scattering occurs when the wavelength of the propagating light is much larger than the diameter of the particles, as in the case when light in the visible and ultraviolet region interacts with air molecules. In the case of a clear atmosphere, which for a lidar is an atmosphere which contains only air molecules, the detected signal of the Rayleigh scattered light is determined by the number of molecules, the wavelength of the laser light, the temperature, and the atmospheric pressure, in the region of atmosphere that is being investigated. The backscatter cross section depends on the number of backscattered molecules. It indicates the theoretical (effective) area where light is scattered back in a solid angle of 2π [1]. The Rayleigh backscatter cross section per molecule σ_{Mol} (m^2 sr^{-1}), for the mixture of atmospheric gases of altitudes up to 100 km, is calculated from (Collis and Russell 1976, cited in Measures 1992):

$$\sigma_{Mol} = \left[\frac{0.55 \times 10^{-6}\ m}{\lambda}\right]^{-4} 5.45 \times 10^{-32} \tag{2.1}$$

The number of molecules N_{Mol} per m^3 depending on altitude z is given by (Measures 1992 p. 42):

1. The solid angle is a 3 dimensional angle (equal to radian²) and often used to describe a cone of light. For the case the cone of light is expanded to a hemisphere, the solid angel is 2π steradian (half sphere in respect to backscatter light). Steradian (sr) is the SI unit of the solid angle.

$$N_{Mol}(\Delta z) = \left[\frac{296\ K}{T(z)}\right]\left[\frac{p(z)}{1013 \times 10^5\ Pa}\right] N_L \tag{2.2}$$

where T is the temperature and p the pressure. N_L = 2.479x10^{25} molecules per m^3, and is the Loschmidt's number referenced to a temperature of 296 K and a pressure of 1013x10^5 Pa. The backscatter coefficient per volume β_{Mol} (m^{-1} sr^{-1}) is found from:

$$\beta_{Mol} = N_{Mol} \cdot \sigma_{Mol} \tag{2.3}$$

Since the amount of backscatter energy is proportional to λ^{-4} (EQ. 2.1), shorter wavelengths are scattered far more than longer wavelengths, illustrated in Fig. 2.1. Assuming temperature and pressure profile from a reference atmosphere (U.S. standard atmosphere, Champion 1985, also see Section 3.1.1) the resulting molecular backscatter coefficients are shown in Fig. 2.1, for 10 µm, 2 µm, and 0.355 µm wavelengths, which increases by three orders of magnitude with each transition to a shorter wavelength.

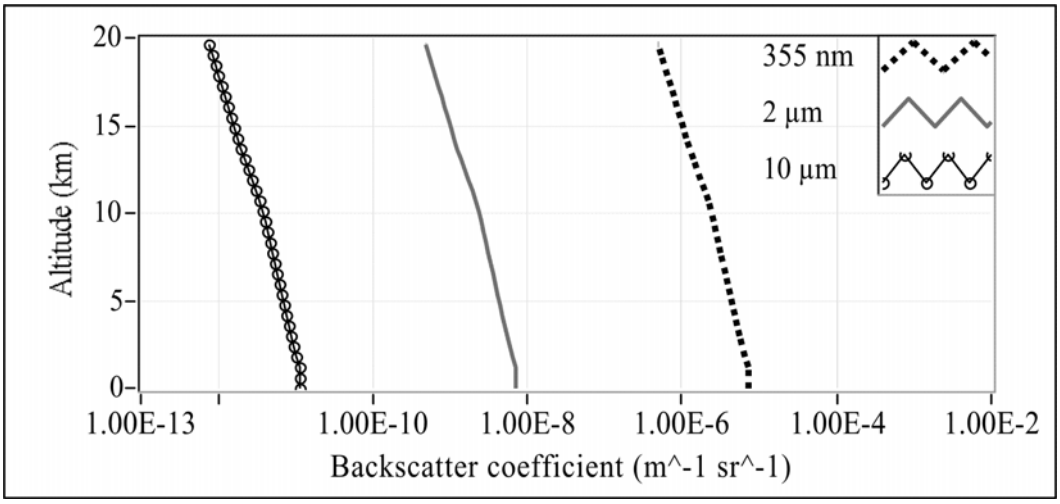

Fig. 2.1 The molecular backscatter coefficients for the U.S. standard atmosphere temperature and pressure profiles at different wavelengths (355 nm, 2 µm, and 10 µm) versus altitude.

The benefit of lidar systems operating at wavelengths of 355 nm is an increased molecular backscatter compared to lidar systems at 10 µm or 2 µm. Accordingly lidars for molecular backscatter detection operate in ultraviolet and visible wavelength range.

Wavelength distribution

The most significant factor for the Rayleigh line shape is the Doppler broadening which may be described by a Gaussian line profile function (EQ. 2.4, Measures 1992 p. 99):

$$W(\lambda) = \frac{1}{\sqrt{2\pi\sigma_R^2}} e^{-\frac{\lambda^2}{2\sigma_R^2}} \tag{2.4}$$

where σ_R (m) is the standard deviation of the Rayleigh spectrum (Fig. 2.3) and is given by:

$$\sigma_R = \frac{2\lambda_L}{c} \sqrt{\frac{k\,T\,N_A}{m_{air}}} \tag{2.5}$$

where m_{air} is the mean molecular air mass ($2.9\text{x}10^{-2}$ kg/mol), λ_L is the wavelength of the laser, k is the Boltzmann constant ($1.38\text{x}10^{-23}$ J/K), c the speed of light, and N_A the Avogadro constant ($6.023\text{x}10^{23}$ mol^{-1}).

2.1.2 Aerosol scattering

Mie scattering occurs when the wavelength of radiation being scattered is close to, or less than, the dimensions of the scattering bodies, which is the case in aerosol scattering. The intensity of the return signal from aerosol scattering depends on their concentration, which varies largely over different locations, and increases in parallel with air pollution, clouds, fog, and haze.

A convenient approach to calculating the Mie scattering parameters is to model the atmospheric backscatter coefficients, or incorporate the vertical backscatter profiles from measurements. The backscatter coefficients during this study were taken from the Reference Model Atmosphere (RMA) which was derived from a climatological database (Vaughan et al. 1995 and 1998) for Atlantic regions during the period 1988-1990. The RMA comprises data of different aerosol backscatter, cloud backscatter, extinction, background radiance and ground reflectance. The data were obtained by measurements at a wavelength 1064 nm, covering a large range of different atmospheric conditions (Section 3.1.1).

The aerosol backscatter coefficient β_0 of the model data (at $\lambda_0 = 1064$ nm) has to be scaled to the wavelength of interest (355 nm during this study). The aerosol backscatter coefficient β_A in the atmosphere at height z for a wavelength λ may be calculated by (Vaughan et al. 1998):

$$\beta_A(\lambda, z) = \beta_0(z)\left(\frac{\lambda_0}{\lambda}\right)^{\alpha(\beta_0(z))} \tag{2.6}$$

It is assumed that the scaling exponent α follows a linear law on the logarithmic scale (Vaughan et al. 1998):

$$\alpha(\beta_0(z)) = -0.104\ ln(\beta_0(z)) - 0.62 \tag{2.7}$$

The resulting aerosol backscatter coefficients are shown in Fig. 2.2, for 10 µm, 2 µm, and 0.355 µm wavelengths, which increases by more than one orders of magnitude with each transition to a shorter wavelength

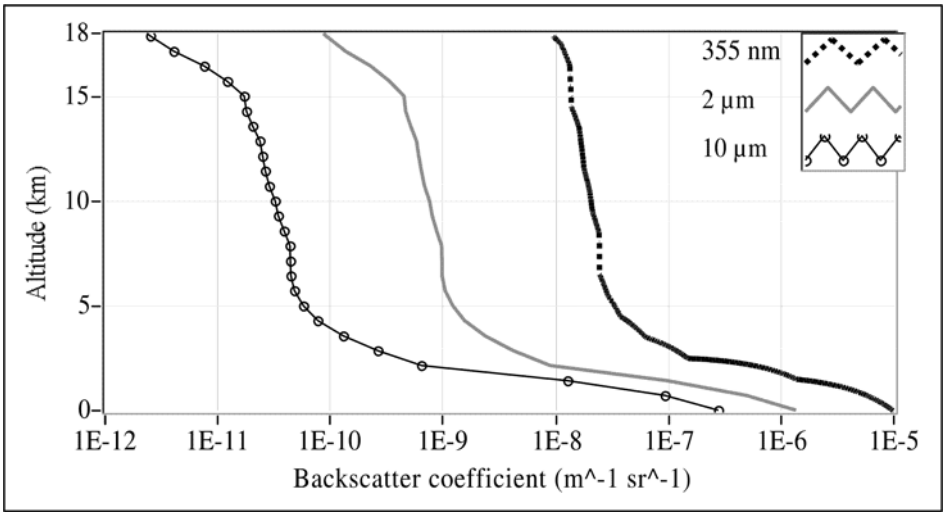

Fig. 2.2 Aerosol backscatter coefficients of an aerosol model suggested by Vaughan et al. (1998) at different wavelengths (355 nm, 2 µm, and 10 µm) versus altitude.

The benefit of lidar systems operating at wavelengths of 355 nm is an increased aerosol backscatter compared to lidar systems at 10 µm or 2 µm.

Wavelength distribution

Unlike the broad Rayleigh spectrum, the spectral width of the Mie backscatter signal is very close to the transmitted laser spectrum, due to the fact that the thermal motion of aerosols is much more smaller compared to molecules, because of their size and mass. Assuming a Gaussian wavelength distribution for the transmitted laser spectrum, the standard deviation σ_M of the Mie backscatter may be calculated by:

$$\sigma_M = \frac{\Delta\lambda_{L\_FWHM}}{\sqrt{8 \ln 2}} \tag{2.8}$$

where $\Delta\lambda_{L\_FWHM}$ is the full-width half-maximum (FWHM) of the spectral line of the laser. Typical Mie and Rayleigh scattering profiles are shown in Fig. 2.3, the narrow spectral shape from Mie scattering and the broad spectral shape from Rayleigh scattering with zero wind velocity.

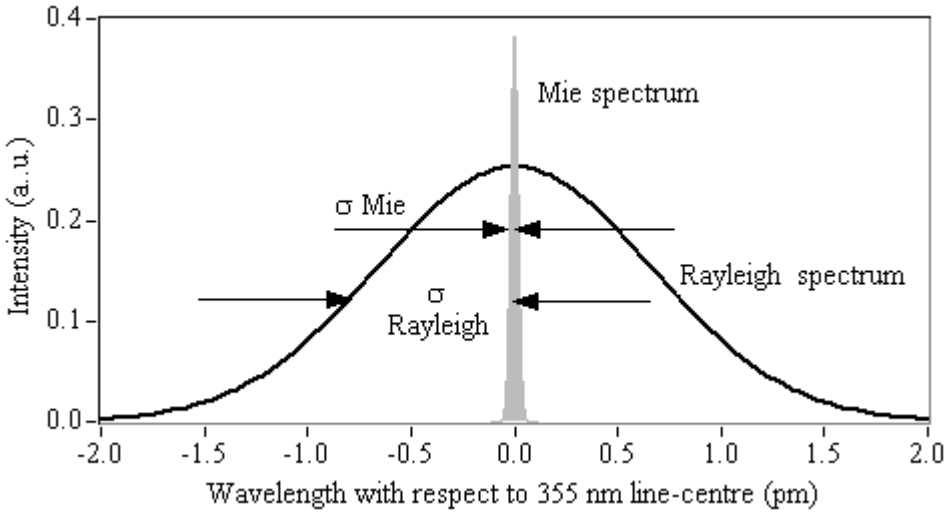

Fig. 2.3 Intensity distribution of Mie and Rayleigh (at 273 K temperature) backscatter signals with different standard deviations σ from a 355 nm source versus wavelength.

2.1.3 Extinction

Extinction is the attenuation of light due to absorption and scattering as the light passes through a medium.

Aerosols

The relationship between backscatter and extinction coefficients of aerosols has been discussed by many authors (Doherty et al. 1999, Liu et al. 2002, Evans 1988, Spinhire et al. 1997). It was shown that a linear relationship applies for monodispersed spherical particles:

$$\frac{\alpha_A}{\beta_A} = k \tag{2.9}$$

where β_A is the aerosol backscatter, α_A the aerosol extinction (attenuation) coefficient, and k the extinction-to-backscatter ratio (also called lidar ratio). Values of k vary over a large range depending on the type and concentration of the aerosols (Section 3.1.1).

Molecules

The extinction coefficient α_{Mol} is derived from the molecular backscatter coefficient by using the ratio (Measures 1992):

$$\frac{\alpha_{Mol}}{\beta_{Mol}} = \frac{8\pi}{3}\ sr \tag{2.10}$$

Since the extinction is given in units of m^{-1} and the backscatter ratio in units of $m^{-1}\ sr^{-1}$, the ratio per steradian of solid angle is $8\pi/3$.

2.1.4 Transmission

The transmission of the atmosphere is governed by the extinction of both aerosols and molecules, and the two-way transmission is described by (Measures 1992 p. 240, 298):

$$T^2(\lambda, z) = e^{-2\int_z^{z_t} \alpha(z)\, dz} \tag{2.11}$$

The total extinction is calculated by $\alpha = \alpha_A + \alpha_{Mol}$, where α_A is the extinction coefficient for aerosol and α_{Mol} for molecular scattering. Z is the altitude of the instrument and z_t is the altitude of the target. The quadratic term T^2 arises from the laser light travelling the distance from the transmitter to the target twice on the way towards the target and back to the receiver. The atmospheric transmission is demonstrated in Fig. 2.4 for a ground (left) and airborne (right) system.

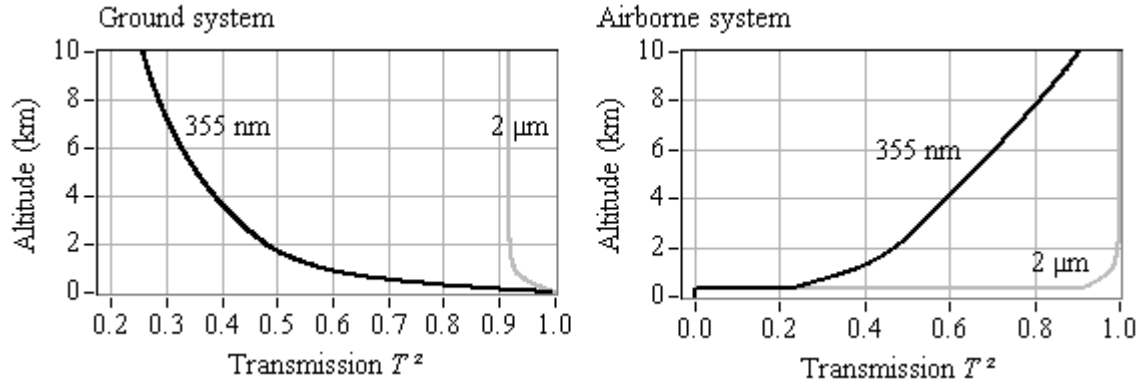

Fig. 2.4 Atmospheric transmission T^2 versus altitude of a ground (left) and an airborne system (right) for a 355 nm lidar (black line) and a 2 µm lidar (grey line).

High aerosol and molecular backscatter coefficients at 355 nm wavelength results in an overall reduction in transmission through the atmosphere. For both the ground and airborne system at 355 nm wavelength, the transmission is reduced to 25 % for a distance of 10 km to the target. The transmission of the 2 µm lidar is reduced to 90 % and hence the backscatter signal of the 2 µm system is stronger by a factor of 3.5. But this disprofit is outweighed by the fact, the backscatter intensities are up to three magnitudes stronger (Fig. 2.1 and Fig. 2.2) for the 355 nm system in respect to the 2 µm lidar.

2.1.5 Scattering ratio

The scattering ratio (also called backscatter ratio, Measures 1992 p. 297) is defined as the ratio of the sum of aerosol and molecular backscatter to molecular backscatter. The scattering ratio is be determined from aerosol and molecular backscatter coefficients and may be written as:

$$R_\beta = \frac{\beta_A + \beta_{Mol}}{\beta_{Mol}} \tag{2.12}$$

The backscatter ratio of a 355 nm system and the median aerosol model (Section 3.1.1) is illustrated in Fig. 2.5.

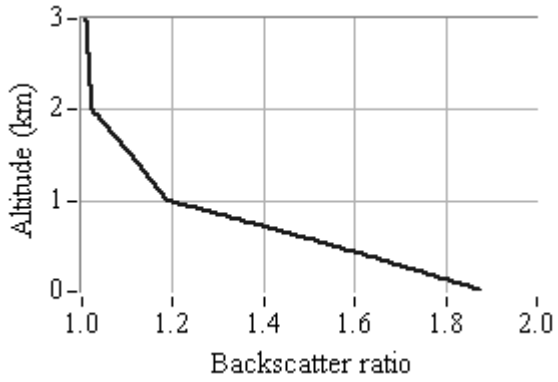

Fig. 2.5 The backscatter ratio of a 355 nm system and the median aerosol model depending on altitude.

The scattering ratio is a measure for aerosol impact referring to molecular scattering. It is used for e.g. atmospheric modelling and aerosol characterization (Section 4.2.4).

2.2 Lidar principle

A lidar consists of three main subsystems: the transmitter, the receiver, and the detection system, shown in Fig. 2.6. The transmitter is the light source which generates light pulses and directs them into the atmosphere. Lasers are an ideal light source for lidar systems because of the low divergence, narrow spectral width, and the ability to generate short pulses[1]. The optical receiver unit of a lidar collects and filters the backscatter laser signal and directs it onto the detection unit. For the case of a wind lidar the backscatter signal leads to the line-of-sight (LOS) wind speed, measuring the radial component of the wind along the laser beam, by the properties of the wavelength of the backscatter light.

1. The spectral width of laser pulses for lidar systems are in the range of MHz and the pulse length is in the range of ns.

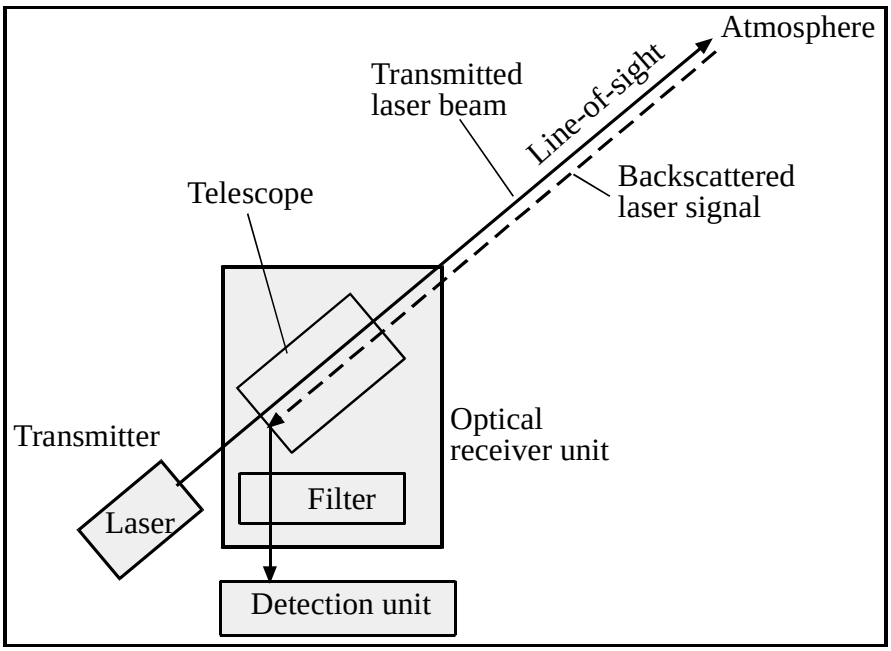

Fig. 2.6 Principle of a lidar system.

Lidar equation

The lidar equation is used to determine the energy of the backscatter signal detected by a lidar system and takes into account both the instrumental parameters and the atmospheric variables introduced in the previous section. The backscatter laser energy at a distance r from the lidar system is given by (Measures 1992 p. 243):

$$E(\lambda_L, r) = E_L \cdot \frac{\Delta R \cdot A_0}{r^2} \cdot k(\lambda_L) \cdot \beta(\lambda_L, r) \cdot T^2(\lambda_L) \tag{2.13}$$

where E_L is the energy of the transmitted pulse, λ_L the wavelength of the transmitted pulse, and $\beta(\lambda_L, r)$ the atmospheric backscatter coefficient. A_0/r^2 is the acceptance solid angle of the receiving optics with A_0 the collecting area of the telescope (optical aperture). The instrumental constant $k(\lambda)$ takes into account the response of the receiver, such as the spectral transmission factors and the overlap function of the telescope[1] (Section 3.2.2). Also contributing to the backscatter energy is the atmospheric transmission coefficient $T^2(\lambda_L)$, and the range ΔR of the atmospheric volume being irradiated. The physical length of the laser pulse τ_L limits the minimal resolution $\Delta R_{min} = \tau_L \cdot c/2$, where c is the speed of light.

1. The overlap function describes the factor of overlap between the transmitter and the receiver optical path depending on the distance to the lidar.

2.3 Doppler wind lidar

2.3.1 Concept

Doppler wind lidar (DWL) systems determine the LOS wind speed as a function of range using light-scattering particles in the air (aerosols and molecules) as tracers. The atmospheric particles that are moving with the wind velocity cause a frequency shift of the backscatter signal due to the Doppler effect. The frequency shift is related directly to the wind velocity along the laser beam (an overview recently was published by Werner 2005 p. 325, Platt 2003).

2.3.2 Doppler effect

The Doppler effect is a phenomenon that can be observed whenever there is relative motion between a source of waves, most notably sound, water or light waves, and an observer[1]. The Doppler effect is the shift of a wave's frequency caused by the relative motion of an observer and the wave source. This motion causes the frequency of the wave to increase as the source and observer move towards each other and to decrease as they move apart. The Doppler effect was first described by the Austrian physicist Christian Johann Doppler in 1842 (Doppler 1842).

Under a Doppler shift, the optical frequency of light is shifted by a factor of *v/c*, where *v* is the velocity at which the observer is approaching or receding from the source, and *c* is the speed of light. Since $v << c$, the resultant frequency *f'* of the light may be written as (Werner 2005):

$$f' = f_0 \left(1 + \frac{v}{c}\right) \tag{2.14}$$

where f_0 is the frequency of the transmitted light. The Doppler shift actually detected by a DWL system is the result of two Doppler shifts. The first shift in frequency is that seen by the scattering air particles being investigated, which constitute a moving observer. The second shift arises because the particles in the air then act as moving sources, scattering the light which has just been Doppler-shifted. Since they are sources moving with respect to the lidar system (now a stationary observer), another Doppler shift, *f''* is seen on the already Doppler-shifted light with frequency *f'*:

$$f'' = f' \left(1 + \frac{v}{c}\right) \tag{2.15}$$

The Doppler frequency shift detected back at the source is given by $\Delta f_D = f'' - f_0$. Assuming $v << c$, the shift Δf_D is given by $\Delta f_D = 2 f_0 \frac{v}{c}$, or in terms of wavelength:

$$\Delta\lambda_D = 2 \lambda_0 \frac{v}{c} \tag{2.16}$$

1. In the case of light waves, the Doppler effect is equal if either the source or the observer is in motion. For sound waves, there is a difference whether the source or the observer is moving, because sound waves require a medium for propagation.

where λ_0 is the laser wavelength. An example of a wavelength shifted Rayleigh and Mie spectrum is illustrated in Fig. 2.7. A Doppler shift of 0.5 pm corresponds to a LOS wind speed of 210 m/s.

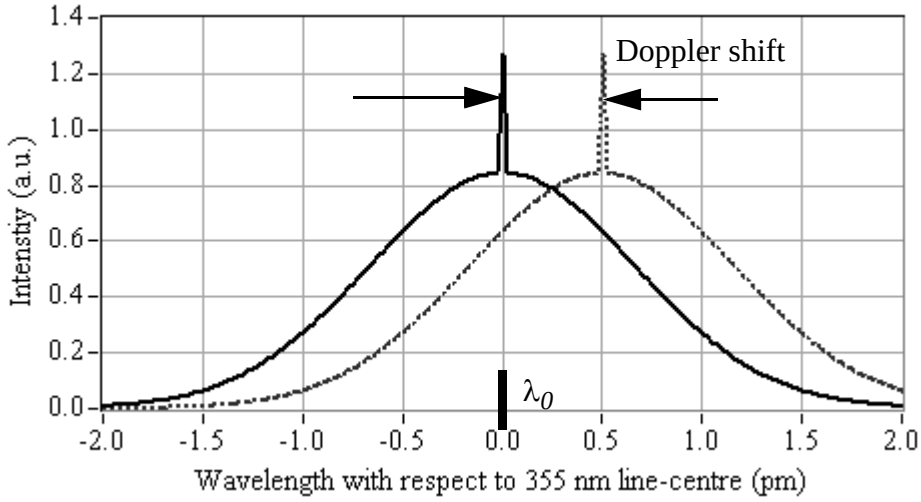

Fig. 2.7 An example of Mie and Rayleigh backscatter intensities from a 355 nm (λ_0) lidar system versus wavelength. The spectrum in respect to 0 m/s LOS wind speed (solid line) and a Doppler-shifted spectrum referring to a wind speed of 210 m/s (dashed line) is illustrated.

2.4 Methods of detection

Measurements of the Doppler shift can be achieved by two methods: direct detection and heterodyne detection[1]. Fig. 2.8 shows the general principle of both the heterodyne and the direct detection systems. Heterodyne systems employ optical frequency mixing while direct detection systems use spectral filters[2] (Section 2.5) for wavelength selection.

2.4.1 Heterodyne detection systems

Heterodyne detection is based on the optically mixing of two signal frequencies, one of which is the frequency of the local oscillator (Fig. 2.8). The local oscillator generates a signal which is slightly shifted with an intermediate frequency f_{IF} in respect to the transmitted frequency f_0. The frequency of the local oscillator (f_0+f_{IF}) is optically mixed with the backscatter signal (f_0+Δf_D). Thus the beat signal of $f_{IF} \pm \Delta f_D$ is obtained in a detectable range of MHz at the receiver (f_R). (Hardesty et al. 1981, Hardesty 2003). Such a lidar applying this technique at 2 µm wavelength (Weissmann 2005) will be used to validate the ADM prototype during a flight campaign planned in 2006.

1. Direct detection is sometimes named "incoherent" detection, whilst heterodyne detection is also referred to "coherent" or "indirect" detection.
2. Spectral filters transmit only a specific wavelength bandwidth.

2.4.2 Direct detection systems

High resolution spectral filters are used for direct detection systems to determine the spectral properties of light based on wavelength. By amplifying or attenuating light as a function of wavelength, information about the spectral wavelength distribution of the signal is obtained. The wavelength of both the transmitted (reference signal f_0) and the received light (Doppler-shifted signal f_1) is measured by means of the spectral line of the atmospheric backscatter signal. These systems then determine the Doppler shift from these two measurements. This detection technique is purpose of this thesis, and is described in detail in Section 2.6.

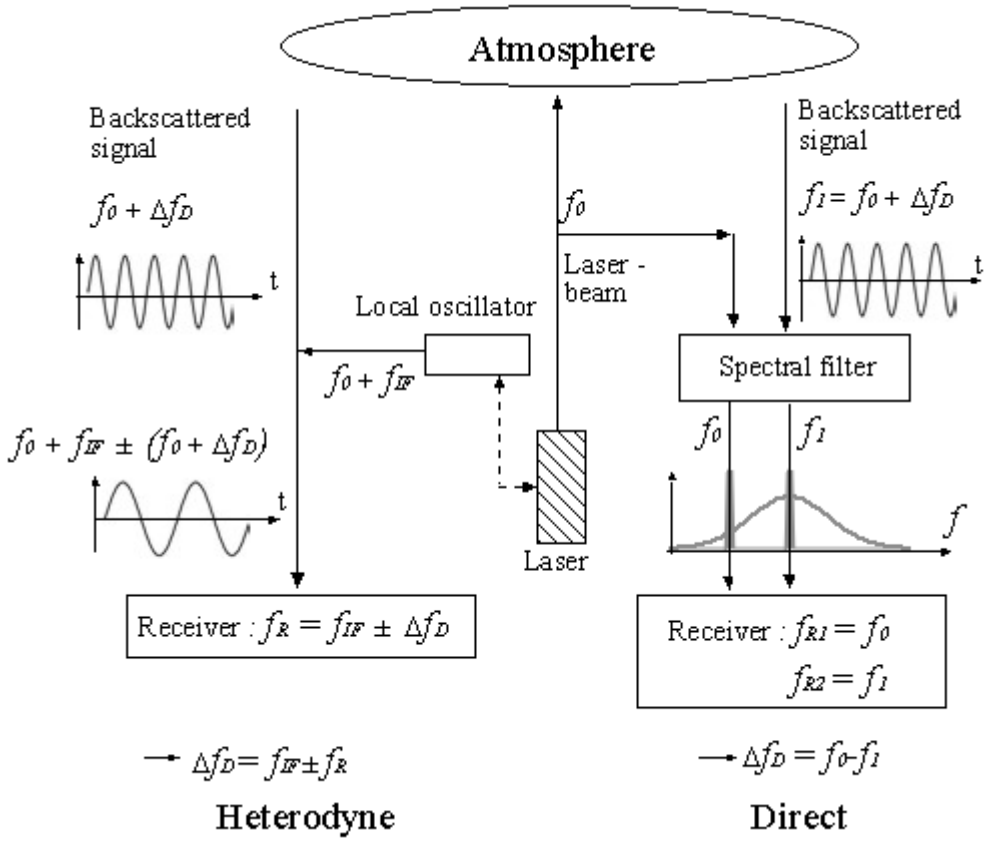

Fig. 2.8 Principle of the heterodyne (left) and the direct detection system (right).

The heterodyne method is subject to the restriction of a small-banded backscatter signal shape, and requires the narrow banded backscatter typical of Mie scattering. The broad frequency spectrum from Rayleigh scattering gives an error of the measurement that is proportional to the width of the spectrum, hence heterodyne systems are useful to make wind measurements with aerosol backscatter commonly at wavelengths of 1-10 µm. Direct detection systems, on the other hand, may be used for both the molecular and the aerosol backscatter return (McKay and Rees 2000).

2.5 Direct detection Doppler wind lidar

Direct detection DWL techniques operating with spectral filters can be distinguished by two different techniques. One technique is based on the measurement of the spatial displacement of a spectral line proportional to the Doppler shift with an imaging detector (Rees and McDermid 1990, Rallison and Sorensen 2001). An imaging detector measures the intensities as a radiometric detector and the location and shape of the filtered signal. This technique usually is called fringe imaging detection referring to the method of locating the position of the spectral line (fringe). The other technique is called the edge technique and was devised to permit interferometric Doppler shift measurements with simple non-imaging radiometric detectors. Due to this technique the shift of the spectral line is determined by a change of the intensities at the detector. Both techniques are applied for the ADM receiver of the prototype and described in the following sections.

2.5.1 Double edge detection method

The double edge technique uses two spectral filters on opposite slopes of the backscatter spectrum, symmetrically located in respect to the laser frequency (Fig. 2.9). This method was developed from the single edge method using one spectral filter (Korb and Gentry 1990) which has been improved since 1989 (Chanin et al. 1989, Korb and Gentry 1990). Because of the steep slope of the edge, small changes in frequency, produce large changes of the signal transmissions through the filter (Korb et al. 1992, Korb et al. 1997). The edge technique has been used in simple laboratory experiments to demonstrate the accuracy of measurements and for atmospheric measurements (Gentry and Korb 1994, McKay 1998a).

The filter transmission curves (filter transfer function) of the double edge method and the backscatter spectrum are shown in Fig. 2.9. A change in frequency of the incoming signal leads to a change of transmitted intensities at the detector. For the case of zero wind speed, the backscatter spectrum is centred to the laser spectrum. A Doppler shift produces a positive change in signal intensity for one edge filter, with respect to its initial position. The corresponding signal change of the other edge filter is opposite in sign. The Doppler shift is determined from the ratio of the transmissions through each filter (Korb at al. 1998, Flesia and Korb 1999). The first application of the double edge method was demonstrated by Chanin et al. (1989) with a Fabry-Perot interferometer (Section A.1).

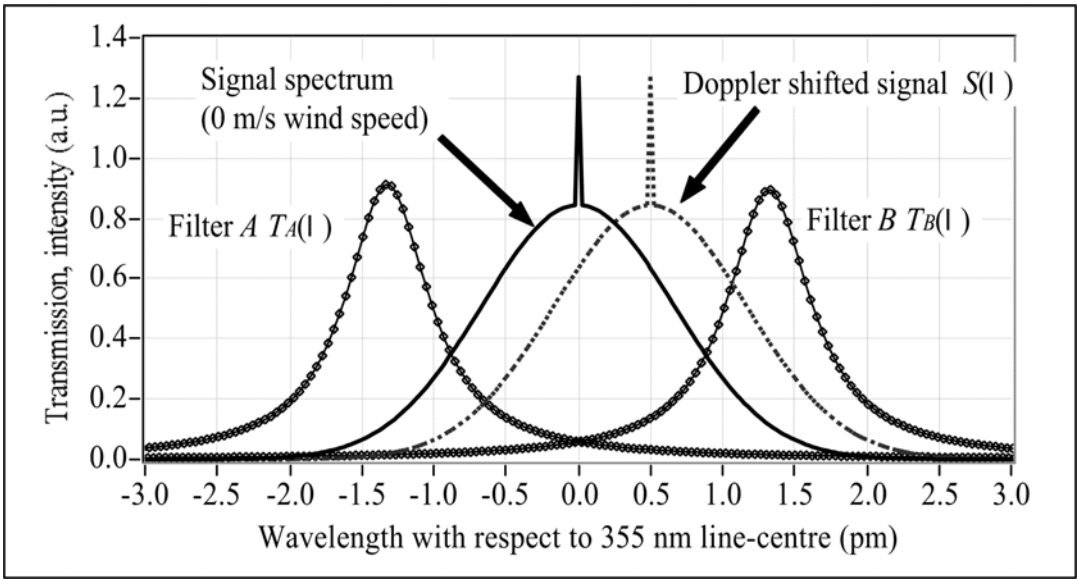

Fig. 2.9 The transmission curves of filter A and B, and the intensity distribution of the Mie and Rayleigh signal from a 355 nm source in respect to zero wind speed and to a Doppler-shifted signal versus wavelength.

The transmitted intensities I_A and I_B at the detector are calculated by a multiplication of the filter function $T(\lambda)$ and the signal $S(\lambda)$, and the integration for the wavelength interval from λ_1 to λ_2:

$$I_{A,B} = \int_{\lambda_1}^{\lambda_2} T_{A,B}(\lambda) \cdot S(\lambda) d\lambda \tag{2.17}$$

This type of wind measurement technique has been validated on the ground by several laboratories with photo-multiplier detectors and a conventional Fabry-Perot interferometer (Garnier and Chanin 1992, Rees et al. 1996, Flesia and Korb 1999). The double edge technique doubles the signal change for a Doppler shift relative to the single edge technique and improves the measurement accuracy by nearly a factor of 2 (Flesia and Korb 1999, Korb et al. 1998). Compared to the single edge technique, the double edge technique is less sensitive to intensity changes caused by factors other than wind, avoiding errors in the measurement. Thus the double edge technique was selected for the ADM receiver. A change in intensity of 0.3 % at each of both channels (0.3 % less intensity on channel *A* and 0.3 % increased intensity at channel *B*) indicates a LOS wind speed difference of 1.0 m/s.

2.5.2 Fringe imaging technique

The location of the interference fringes at the detector provided by a spectral filter is the result of the wavelength of incoming light (Section A). Thus the Doppler shift of the backscatter light is measured by a displacement of the fringe with an imaging detector (McKay 1998b, McKay and Rees 2000). The fringe imaging technique is most notably used for signals having a narrow spectral width to ensure the exact determination of the fringe location. The fringe imaging method

was first used by NASA in 1981 with a Fabry-Perot interferometer (Hays et al. 1981, Hays 1991) for measuring atmospheric temperature, wind, and density of atoms. McGill and Spinshire (1998) have shown that the measurement sensitivity of the edge technique is not different to the fringe imaging system, so measurement sensitivity is not a criterion for device selection, but only the width of the backscatter spectrum. As shown in Fig. 2.10, the narrow banded Mie signal is fully imaged at the detector and only a part of the Rayleigh spectrum.

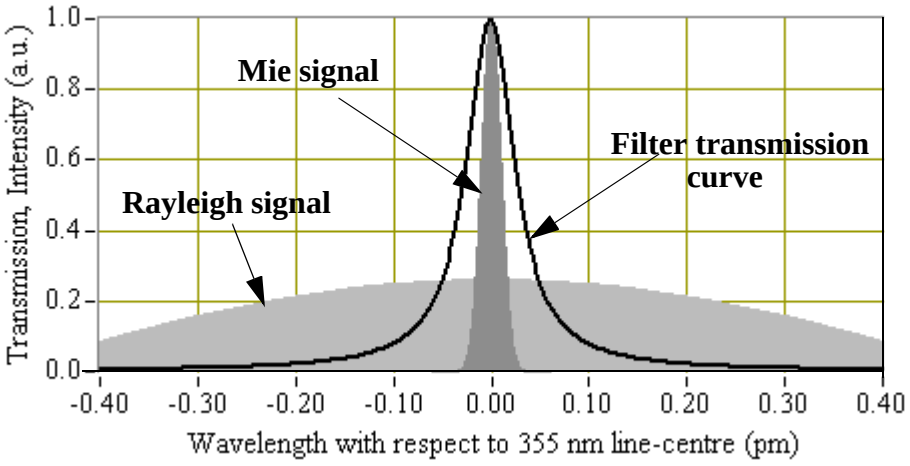

Fig. 2.10 The transmission curve of the Fizeau interferometer and the intensity distribution of the Mie and Rayleigh signal from a 355 nm source versus wavelength.

The fringe imaging technique is insensitive to the earth background and Rayleigh radiation, and is capable for laser wavelength monitoring. For the 355 nm system, a Doppler shift of 2 fm wavelength results in a change of the LOS wind speed of about 1 m/s. Details of the ALADIN receiver of the prototype and how the double edge and fringe imaging method were realized is described in the following section.

2.6 ALADIN: a direct detection ultraviolet Doppler wind lidar

ALADIN is the lidar of ADM-Aeolus, developed to measure wind over a larger atmospheric vertical range than previous lidar systems. A new technique is presented by the instrument concept of ALADIN, combining an aerosol (Mie) and a molecular (Rayleigh) receiver to benefit from their complementarities. The Mie receiver provides wind measurements for atmospheric layers with higher aerosol content or cloudy skies, whereas the Rayleigh receiver measures molecular backscatter in clear air (developed by EADS-Astrium Toulouse, France).

2.6.1 ALADIN prototype

A separate module of the pre-development program is the prototype of the ALADIN, including the transmitter, telescope, and receiver (Durand et al. 2005). The receiver and the telescope are being developed by EADS-Astrium Toulouse, France, and the transmitter was provided by EADS-Astrium Ottobrunn, Germany. At this stage of the study, the prototype was tested for the first time to make atmospheric measurements from the ground and from an aircraft at DLR, and the results are presented in Chap. 5. A further ground campaign is planned at the German Weather Service (DWD) station in Lindenberg near Berlin and a flight campaign (Reitebuch et al. 2003 and 2004).

Fig. 2.11 shows a photo of the prototype in the Falcon aeroplane at DLR during a first test flight in October 2005. The receiver is in the large box on the top of the rack, the telescope is pointing to the floor, and the laser is inside the rack just behind the telescope. The laser beam is directed down to the atmosphere below the aircraft, through a window just below the telescope.

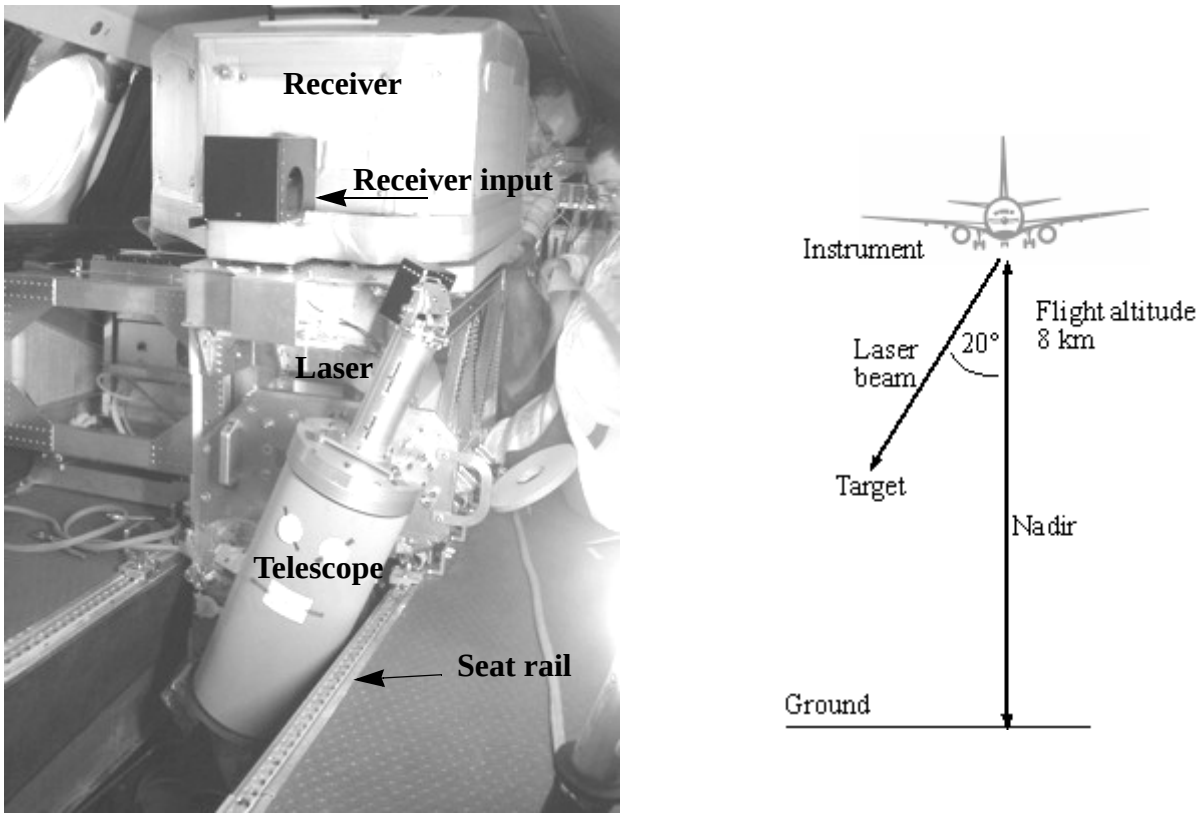

Fig. 2.11 The ALADIN prototype in the Falcon aircraft (left) and the geometry of an airborne system (right). The airborne system at a flight altitude of 8 km measures the wind at 20° off nadir.

The laser of the airborne system points into the atmosphere perpendicular to the flight direction to avoid a Doppler shift component arising from the motion of the instrument. The LOS wind speed is determined from a slant angle off nadir (Fig. 2.11) across the flight direction.

2.6.2 Transmitter

The ALDIN transmitter is a Nd:YAG laser (acronym for Neodymium-doped Yttrium Aluminium Garnet). This is a solid state laser characterized by a crystal based on a Yttrium Aluminium Garnet doped with Neodym ions. The Nd:YAG crystals can be activated (pumped) either using flash lamps or laser diodes. The latter are more efficient in respect to energy output and frequency stability. Laser diodes are also usually smaller in size and need less maintenance. They are used to produce high quality beams and have to be harmonized with the crystal material. The best amplification of light in respect to the crystal properties is at 1064 nm (Kneubühl and Sigrist 1999). The wavelength was defined by Kaminskii (1990) being 1064.15 nm at 300 K.

The wavelengths emitted by a Nd:YAG laser may be changed through harmonic generation. The term second (third, fourth) harmonic generation means the doubling (tripling, quadrupling) of the frequency. Nd:YAG lasers can be designed to provide the second, third, and fourth harmonic to generate wavelengths at 532.075 nm, 354.717 nm, and 266.037 nm[1] as given by (Koechner 1976):

$$\lambda_3 = \left(\frac{1}{\lambda_1} + \frac{1}{\lambda_2}\right)^{-1} \tag{2.18}$$

where 532.075 nm results from $\lambda_1 = \lambda_2 = 1064$ nm and 354.717 nm results from $\lambda_1 = 1064$ nm and $\lambda_2 = 532.075$ nm (Koechner 1976 p. 491, Kneubühl and Sigrist 1999 p. 194 and 338). The ALADIN laser emits narrow-band left-circularly polarized pulses at an ultraviolet wavelength (355 nm) by a tripled Nd:YAG laser. The spectrally narrow-band[2] signals are in the order of MHz and narrow enough to determine the wind speed better than the required threshold. For higher frequency stability and spectrally narrower band light emissions, a seed laser is used. Seed (master) lasers generate narrow band pulses with high frequency stability, but of very low energy. The beam of the seed laser is injected into a second (slave) laser that amplifies the power of the injected beam, thus providing narrow band pulses with increased energy. The wavelength stability is controlled by the build-up-time of the laser pulse (commonly called laser locking). This time refers to the time it takes for the laser radiation to build up before the laser pulse exits the cavity. The build-up-time of the laser is minimized, when the laser is running in single frequency mode[3]. The time is optimised by controlling the cavity length by means of a piezo at the end of the cavity. The linewidth was defined in respect to the properties of the receiver (Section 2.6.4), and consequently stable enough for the needs of the ALADIN system.

2.6.3 Telescope

The backscatter light is collected by a Cassegrain telescope, as is commonplace in DWL systems. The ALADIN telescope is characterized by two convex mirrors and the same optical axis for the transmitted and backscatter light (Naumann and Schröder 1992 p. 331). The primary mirror collects the light and the secondary mirror reflects it through a hole in the primary mirror inside

1. Named in the literature 532 nm, 355 nm and 266 nm.
2. The bandwidth of laser signals generally is in the range between Hz and GHz; the bandwidth of the ALADIN laser is 50 MHz.
3. In the single-frequency mode, a single pulse with a defined spectral distribution (bandwidth) is emitted.

the focal point. The secondary mirror obscures the beam path within the near-field, decreasing the number of photons at the detector. These shadowing effects are determined by the diameter of the telescope's mirror, the laser beam parameters, and the optical attributes (field stop, focal length). An illustration of the telescope is presented in Section 3.2.2.

2.6.4 Receiver system overview

The receiver system comprises a number of units: the front optics, the two interferometer systems, and the electronic detection units (Fig. 2.12). The front optics itself consists of the telescope, field stop, quater waveplates[1], polarizing beamsplitters[2], lens systems, and the laser output extractor. The two interferometer systems shown in the diagram are the Fizeau interferometer (Section 2.6.6) for transmitting the Mie backscatter signal and the Fabry-Perot interferometer (Section 2.6.5) for the Rayleigh backscatter signal. Both the interferometers act like spectral filters and the spectra are imaged at the detectors.

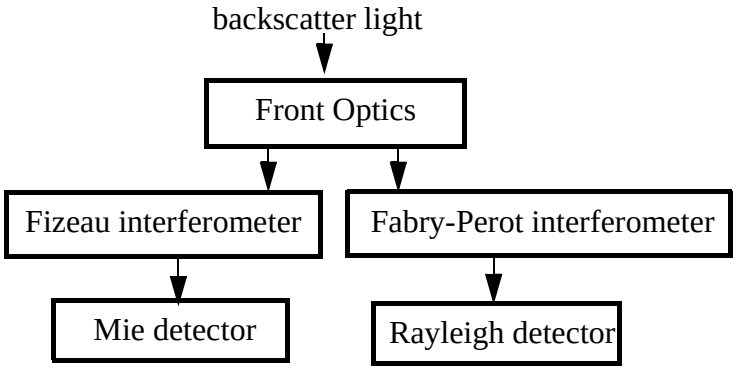

Fig. 2.12 An overview of the receiver structure

Receiver system

The main parts of the receiver system are shown in Fig. 2.13. Background light is attenuated by the front optics where the backscatter signal passes through an interference filter and is rotated into vertically polarized light. The signal is then reflected off the polarising beamsplitter into the Mie receiver. The Mie return is transmitted through the Fizeau, and provides a linear fringe whose position is directly linked to the wind speed (fringe imaging technique). The wings of the broad Rayleigh spectrum, however, are reflected from the Fizeau with opposite polarisation. The reflected light is rotated into parallel polarized light by a quarter waveplate located between the Fizeau interferometer and the mirror. The signal spectrum is then directed towards the Rayleigh receiver.

1. Quarter waveplates rotate plane polarized light into circularly polarized light and vice versa (Naumann and Schröder 1992 p. 495).
2. Polarizing beamsplitters transmit horizontally polarized light, whilst vertically polarized light is reflected (Naumann and Schröder 1992 p. 518).

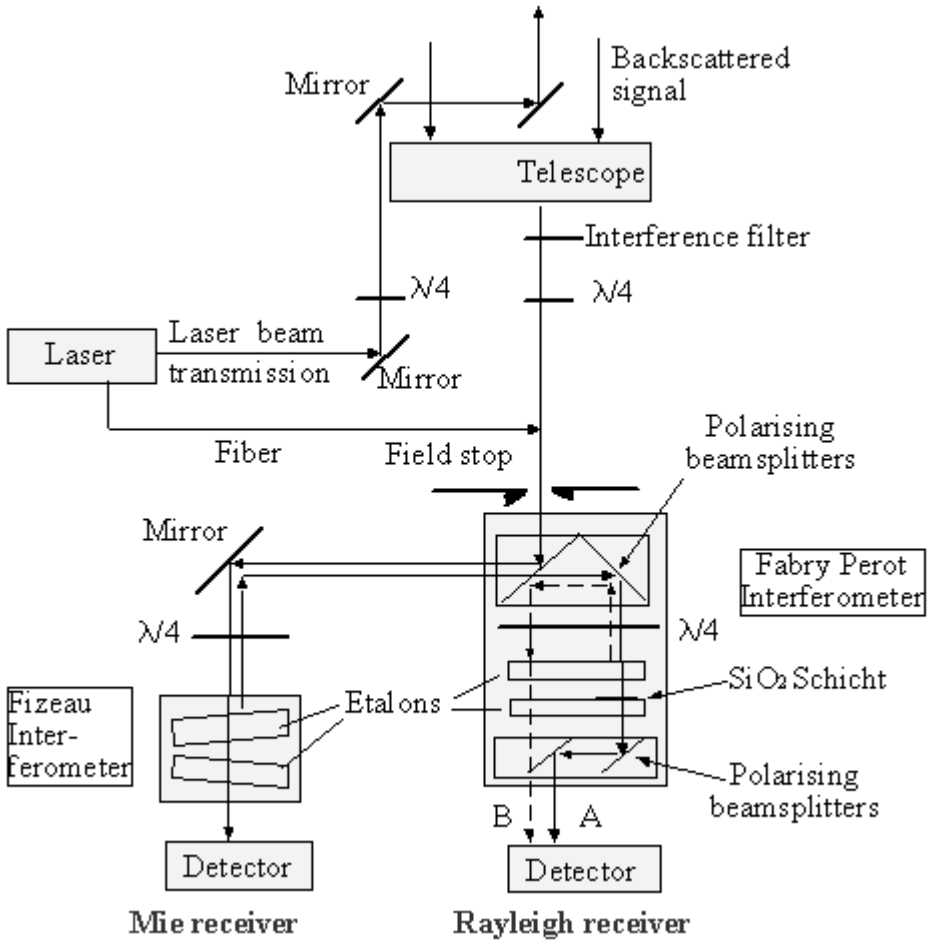

Fig. 2.13 A schematic figure of the direct detection ultraviolet DWL receiver system of the ALADIN prototype.

Because of the width of the Rayleigh spectrum, the double edge technique is applied by use of an interferometer split into two zones. This is done by sequentially routing the input beam to the Rayleigh detector unit to two sides of a sequential Fabry-Perot interferometer (Fig. 2.15). The sides of the interferometer differ in spacing due to a thin vacuum-deposited SiO_2 layer of controlled thickness (84 nm), on the inner surface of one end-plate. The different spacing between both etalons determines the different centre frequencies of both transmission curves. A polarizing beamsplitter and quater waveplate arrangement within the interferometer (patented by EADS-Astrium, Schillinger et al. 2003) allows the two sides of the Rayleigh signal to be fully transmitted without loss to the detection unit, denoted channel *A* and *B*.

2.6.5 Rayleigh receiver

A Fabry-Perot interferometer (Section A.1) consists of two etalons mounted parallel at a distance to one another. The inner faces are coated for high reflectivity (Naumann and Schröder 1997 p. 258). Transmitted light of a monochromatic source displays sharp and clear circular interference

fringes at the detector. The location of the fringes depends on the wavelength of the incident light (Vaughan 2002, Saleh and Teich 1991 p. 316).

The ratio of intensities of the incoming light I_0 and the transmitted light I_t depends on the phase difference ψ (optical delay) of the light depending on the optical separation of the plates, and is expressed as follows:

$$\frac{I_t}{I_0} = \frac{A(\psi) \cdot T^2}{(1-R)^2} \tag{2.19}$$

where T is the maximum transmission and R the reflection. $A(\psi)$ is the Airy function and can be described by (Vaughan 2002 p. 91):

$$A(\psi) = \left[F \cdot \sin^2\left(\frac{\psi}{2}\right) + 1 \right]^{-1} \tag{2.20}$$

where F is the coefficient of finesse, also known as the maximum reflectivity, which describes the quality of an interferometer (Koechner 1976 p. 205):

$$F = \frac{4R}{(1+R)^2} \tag{2.21}$$

In the case of the ALADIN receiver, the incident light is aligned to be perpendicular to the etalons surfaces, to generate the transmission maximum of zero order ($P1$ in Fig. 2.14 and Fig. A.2) at the detector to ensure maximum efficiency. Fig. 2.14 illustrates the optical path of perpendicular incident light and fringes are no longer imaged, but only the transmission maximum of zero order (circular intensity spot).

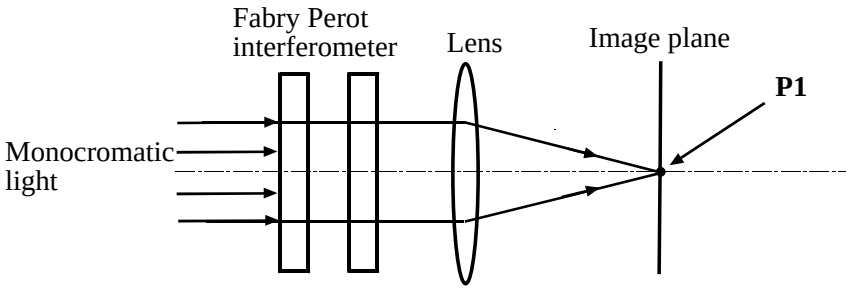

Fig. 2.14 A general schematic illustration of a Fabry-Perot interferometer and perpendicular incidence of light.

In the sequential Fabry-Perot interferometer of ALADIN (Fig. 2.15) all of the incoming photons are directed to the first channel (*A*) with a mean transmission of about 10 %. Thus 90 % of the photons are reflected off the first channel to the second channel (*B*). In both cases, 10 % of the photons are transmitted to the detection unit. Such a scheme is more efficient than conventional non-sequential (beam splitting) Fabry-Perot interferometer, where a beamsplitter halves the incoming flux to each channel, and consequently is half as efficient. The sequential routing technique results in the different peak intensities of channel *A* and *B* transmission curves shown in Fig. 2.16.

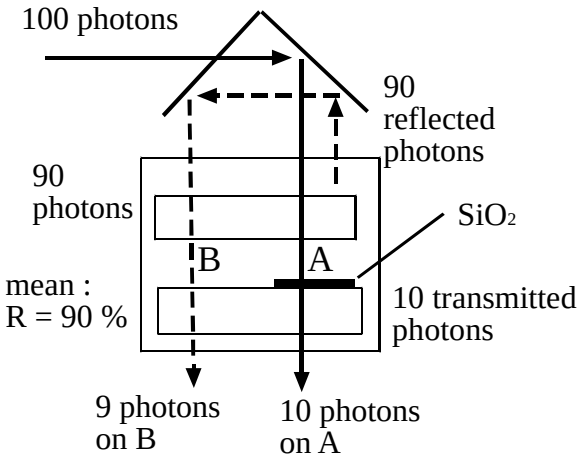

Fig. 2.15 Principle of the double sequential Fabry-Perot interferometer, and an example of the number of photons at channel *A* and *B*.

The filter curves are defined by the transmission maxima, the spectral width, and the frequency spacing between each other, as shown in Fig. 2.16. The spacing of the filter transmission curves depends on the thickness of the SiO_2 layer in the Fabry-Perot interferometer, whereas the FWHM ($\Delta\lambda_{FWHM\_A,B}$) depends on the finesse.

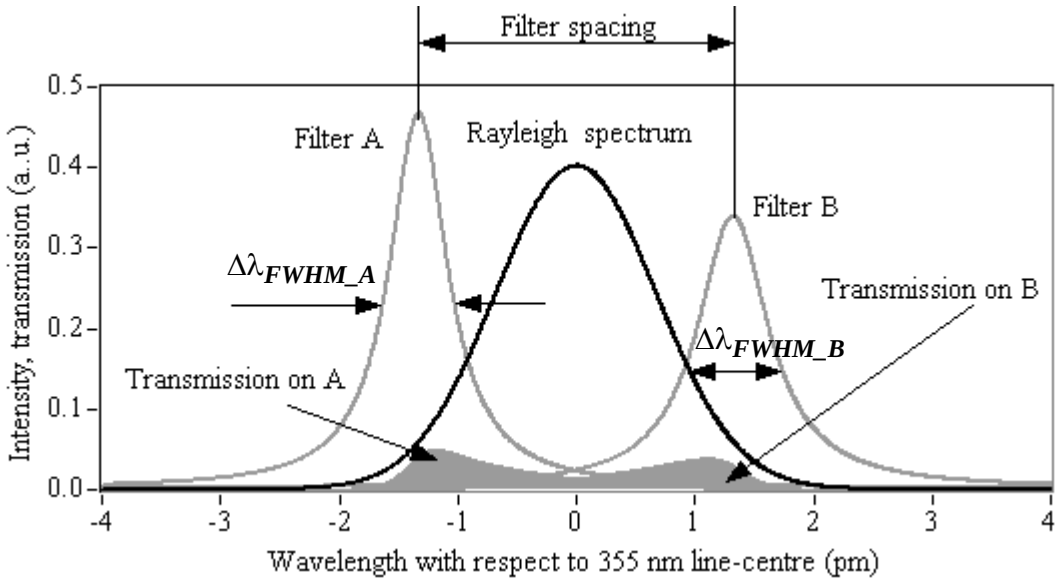

Fig. 2.16 The transmission curves of filter *A* and *B*, the intensity distribution of the Rayleigh signal from a 355 nm source, and the transmitted intensities, referring to a zero LOS wind speed versus wavelength. The filter spacing and the FWHM of filter *A* and *B* are indicated.

The transmissions of zero LOS wind speed are shown in Fig. 2.16, where the Rayleigh spectrum is centred near the crosspoint of both filter curves, so that channel *A* and *B* yield near-equal intensities. In the presence of wind speed, however, the Rayleigh spectrum is shifted towards one of the filter curves, as shown in Fig. 2.17, resulting in a difference in the transmitted intensities of the two channels.

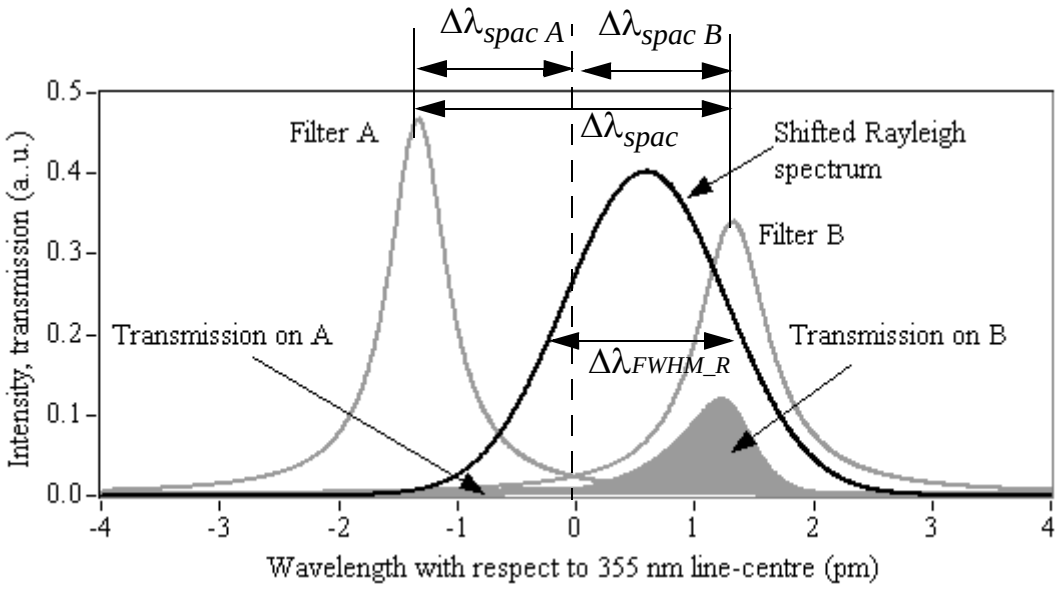

Fig. 2.17 The transmission function and the spectrum as in Fig. 2.16, but for a LOS wind speed of -250 m/s and the filter spacing of the filter *A* and *B* and the total spacing $\Delta\lambda_{spac}$.

The FWHM of filter *A* and *B*, and the filter spacing ($\Delta\lambda_{spac}$) depend on the requirements of the Rayleigh receiver. Garnier and Chanin (1992) analysed the spacing and the FWHM of the filter curves for a 532 nm system. The spacing and the filter spectral width at 355 nm was examined by Flesia and Korb (1999) for molecular backscatter and the impact of Mie backscatter, the sensitivity of the system, and the accuracy for a satellite system.

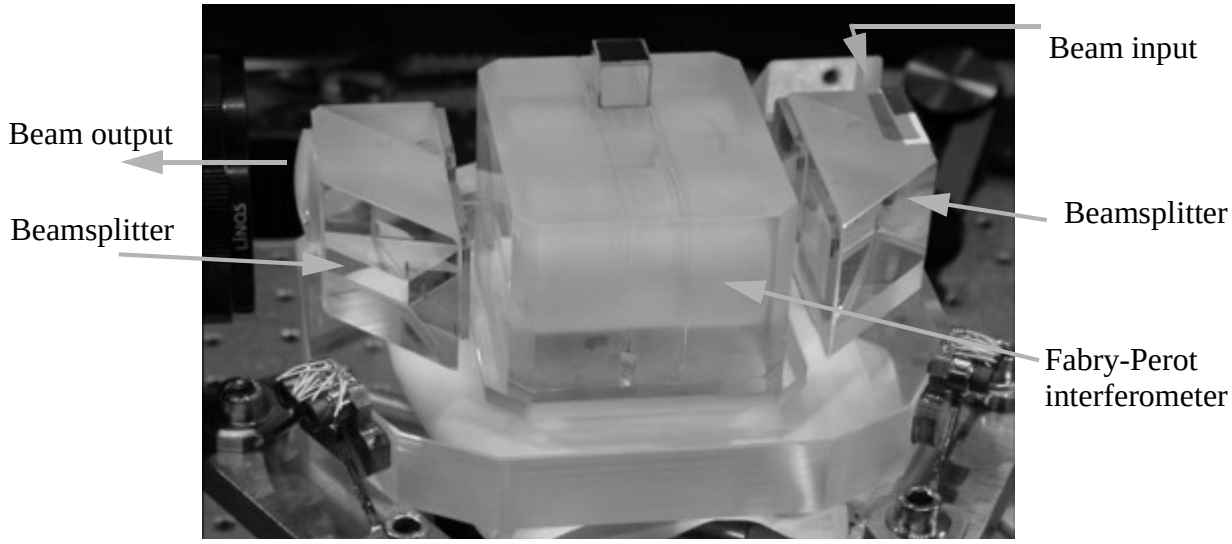

Fig. 2.18 The Fabry-Perot interferometer of the ALADIN receiver (developed and manufactured by EADS-Astrium, Toulouse. Photo: Durand et al. 2004).

The EADS-Astrium Fabry-Perot interferometer of the prototype is shown in Fig. 2.18. The system is mounted on an optical bench and the interferometer cavity is arranged in the centre with beamsplitters visible on the left and right.

2.6.6 Mie receiver

The Fizeau interferometer functions in a similar manner to a Fabry-Perot interferometer, in that both generate interference fringes due to an optical path difference between multiple reflections. The principle difference is that the optical path-difference in a Fizeau interferometer is derived from wedge-shaped etalon plates (Pérez 1996 p. 403). Unlike the circular fringes provided by the Fabry-Perot interferometer, the Fizeau interferometer produces localised fringes of equal thickness, which in the case of monochromatic light at normal incidence, results in sharp, well-defined and equally-spaced straight lines of constant width, parallel to the edge of the wedge. As with Fabry-Perot interferometers, the location of the fringes indicates the wavelength of the incident light. Depending on the angle between the plates, the image of the fringes from the Fizeau interferometer at the detector is either asymmetric, or nearly symmetric, like the Airy function shown in Section A.2. For the ALADIN interferometer the parameters of the Fizeau are choosen to generate nearly symmetric fringes close to the ideal Airy ideal function at the detector as demonstrated by Dolfi-Bouteyre and Garnier (2002). It is possible to apply the fringe imaging technique, because the Fizeau interferometer provides a fringe at the detector narrow-banded as the Mie backscatter spectrum. The spectral width of the filter transmission function is broader than the width of the Mie spectrum (Fig. 2.10), which leads to a broadening of the signal spectral shape up to the width of the filter after passing the Fizeau interferometer. Best results for signal processing in respect to the design of the EADS-Astrium detection unit are achieved for a width of the imaged fringe larger than one pixel by spreading the spectrum across the detector (ESA 1999).

Up to now the imaging technique for DWLs was normally used in combination with a Fabry-Perot interferometer. The detector used in the fringe imaging technique is either a custom made device with a circular geometry designed to match the Fabry-Perot interferometer interference rings or a conventional detector with a special optical component to convert the circular fringes of a Fabry-Perot interferometer into a linear pattern (Skinner et al. 1994, Irgang et al. 2002). Both techniques require either a complex imaging detector or a more complex converter to produce a linear pattern. A Fizeau has the advantage of generating linear and sharp interference fringes, which allows the use of a conventional detection unit (Kajava et al. 1994).

The resolving power of the Fizeau is only modestly less compared to a Fabry-Perot interferometer of the same dimensions and parameters (McKay 2002). The required performance has been tested successfully in the ESA Technology Research Programme (ESA 1999).

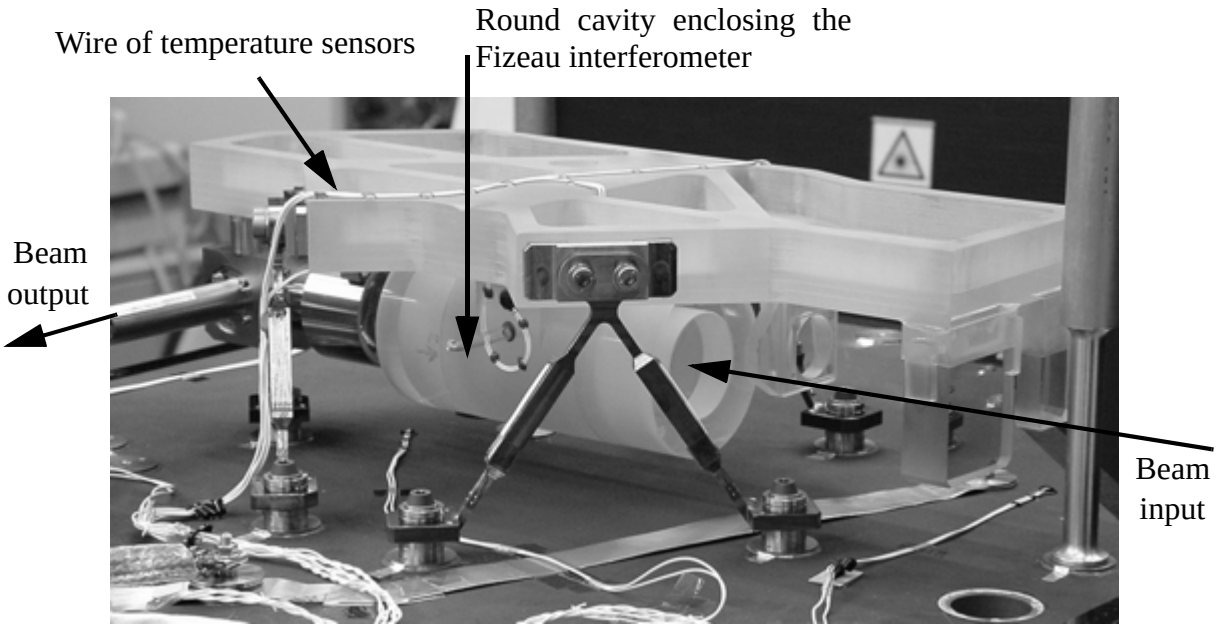

Fig. 2.19 The Fizeau hardware of the ALADIN prototype (developed and manufactured by EADS-Astrium, Toulouse. Photo: DLR).

The ALADIN hardware of the Fizeau is shown in Fig. 2.19. The round cavity includes the two etalons. The incoming beam arrives from the right, passes the round cavity, and is directed through the metal tube (left side of the photo) towards the detection unit.

2.6.7 Detection unit

Detection systems of DWLs have a light sensitive area, consisting usually of photodetectors, as charge coupled devices (CCD), photomultipliers, and photodiodes. The advantages of a CCD in respect to photomultipliers are the small size and the capability to accumulate signals, and they have a higher sensitivity as photodiodes for plane imaging. The smallest sensitive area of a CCD is called a pixel (abbreviation for picture element). Previous indirect detection DWLs used photodetectors where the quantum efficiency was about 0.1 at 1064 nm (Menzies 1986). The quantum efficiency is defined as the ratio of the generated electrons at the detector and the incoming photons. Skinner and Hays (1994) showed that the use of a CCD instead of formerly common photodetectors increases the efficiency of the system by a factor of 10. A non accumulation CCD for a direct detection DWL was demonstrated by Irgang et al. (2002). The ALADIN detector is the first accumulation CCD (ACCD) for lidar systems and the dimensions of the ACCD is about 0.6 mm square. The same type of detector (Fig. 2.20) is used for both the Mie and Rayleigh receiver.

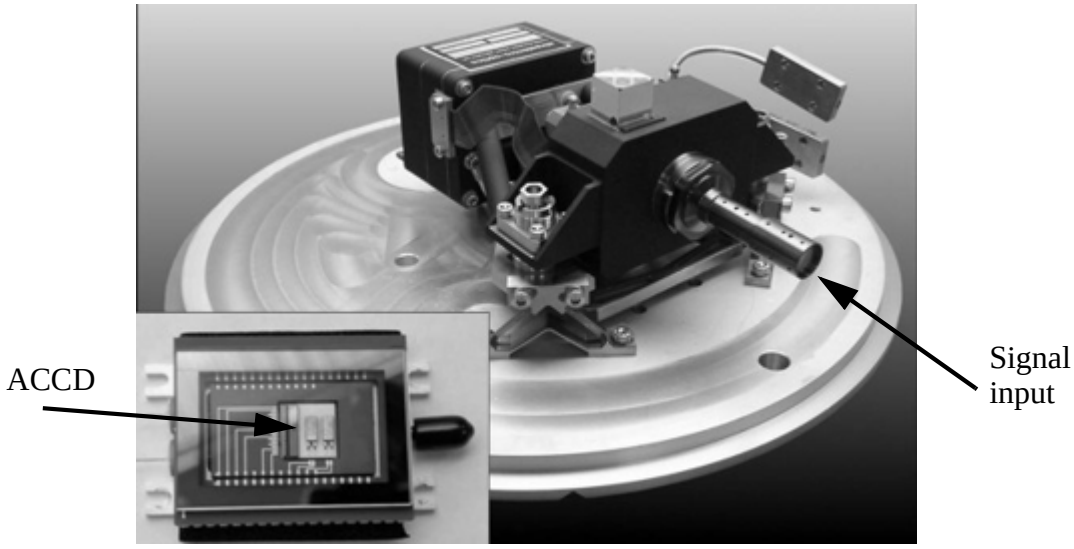

Fig. 2.20 The hardware of the ALADIN detection system. The ACCD itself is shown in the small figure (developed and manufactured by EADS-Astrium, Toulouse. Photo: Durand et al. 2004).

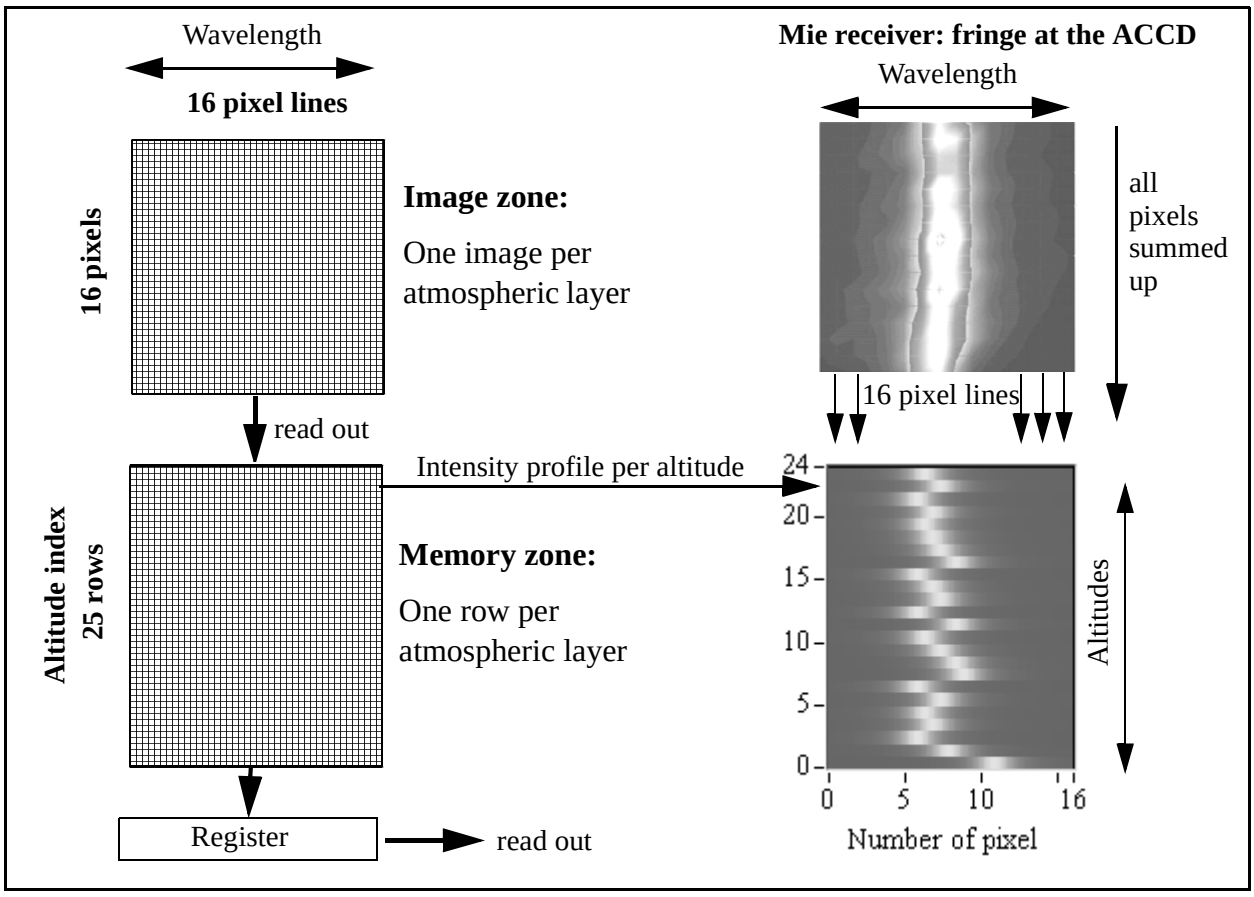

Fig. 2.21 A diagram of the ALADIN ACCD with the image and the memory zone (left) and an example of the Mie receiver (right) where a fringe is imaged at the image zone and the intensities of each image for a defined altitude are stored in the memory zone.

The ACCD of ALADIN is used to digitize a laser return as a function of altitude and wavelength. The ACCD operates in an accumulation mode, patented by EADS-Astrium, to reduce noise effects. The light sensitive area is a 16x16 matrix of pixels (image zone, Fig. 2.21). One image corresponds to a defined atmospheric layer in respect to one laser pulse. The integration time (the time it takes to collect the backscatter light) for each image depends on the desired horizontal range resolution of the atmospheric measurements. Each line of the image zone is stored in one pixel of the memory zone, where 25 rows of 16 pixels are available, and each row in the memory zone corresponds to an atmospheric layer. The memory zone accumulates the images per pulse until the desired number of accumulated laser pulses is achieved. For each laser pulse the new image, depending on atmospheric range, is added to the memory zone until the required number of pulses is accumulated. At the end of an accumulation cycle the memory zone is read out via a serial register to be stored at the data unit.

The lower limit of the dynamic range[1] of the ACCD is set by the detection chain offset and the noise. The main sources of the offset are the dark current and the ACCD output noise (also called read noise). The dark current is the thermally induced current that exists normally in electrical image sensing device in the absence of incident light. The output noise arises from the process of converting the charge of the pixels into a voltage signal for the output of the ACCD. The number of 16 pixels was chosen to satisfy the demand for low noise arising from a low signal at the satellite, whilst giving the desired resolution and accuracy in wind speed measurements. The detection chain offset is determined from measurements in darkness, and is a constant for each measurement, regardless of time.

For each atmospheric layer the backscatter signal is stored in one row of the memory zone. The read out process takes 25 * 2.1 µs for 25 atmospheric layers, leading to 50 µs to store and read out the signal of one laser pulse (Fig. 2.22). The range resolution of 2.1 µs leads to an atmospheric layer range of 315 m.

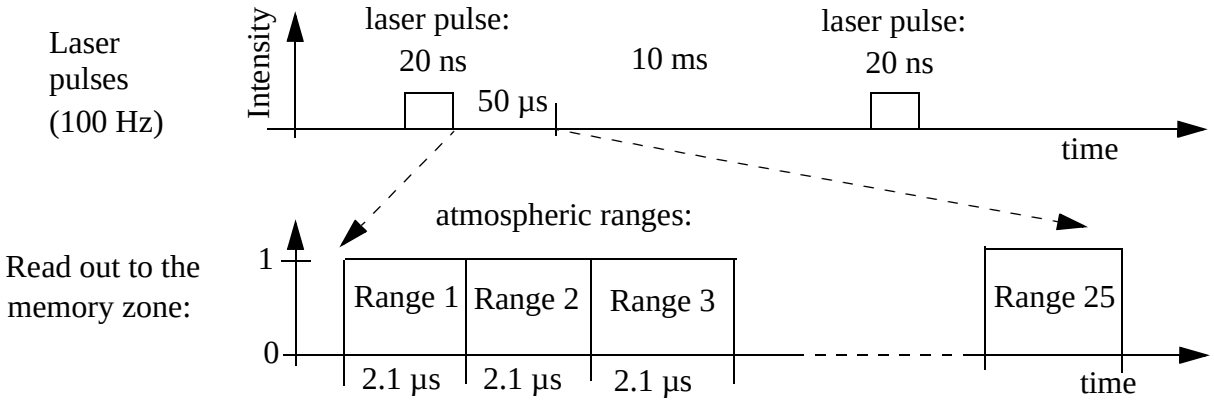

Fig. 2.22 The times of the laser pulse transmission compared to the integration times of the ACCD.

1. The dynamic range is the maximum charge with signal information that can be stored in a pixel

a) Rayleigh ACCD

The purpose of the ACCD is to record the light levels from the dual channel Rayleigh interferometer, since the ratio of the intensity is a measure of the wind speed. Fig. 2.23 shows the measured intensities corresponding to channels *A* and *B* on the ACCD image zone. As demonstrated in Fig. 2.13, the transmitted intensities are imaged as a circular spot.

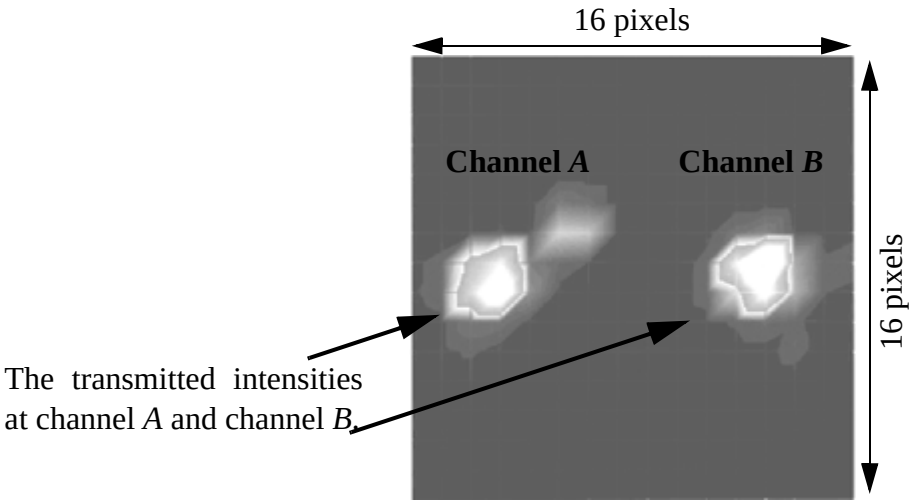

Fig. 2.23 The measured intensities of the Rayleigh spots arising from the transmission curves of the Fabry-Perot interferometer (Photo: Durand et al. 2004).

b) Mie ACCD

For the Mie backscatter, however, it is the location of the fringe, rather than intensity, which provides a measure of the LOS wind speed. A modelled signal in the image zone is demonstrated in Fig. 2.24 where the white vertical line corresponds to the Fizeau fringe maximum.

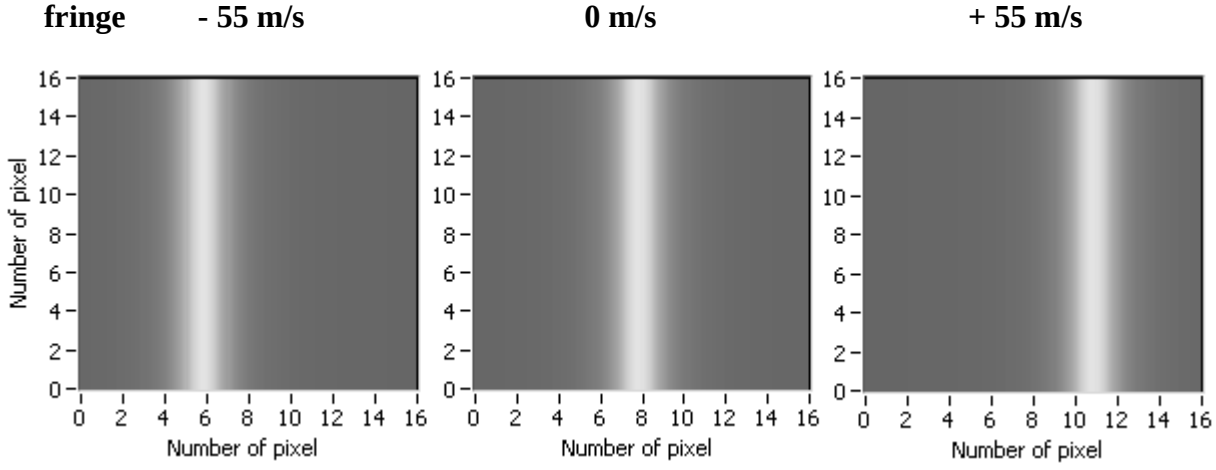

Fig. 2.24 A modelled fringe at three different locations at the detector in the image zone referring to different LOS wind speeds of -55 m/s, 0 m/s, and 55 m/s.

In the Mie ACCD, 1 pixel corresponds to a LOS wind speed of 18.35 m/s. An actual Mie fringe measured by the ACCD is shown in Fig. 2.25.

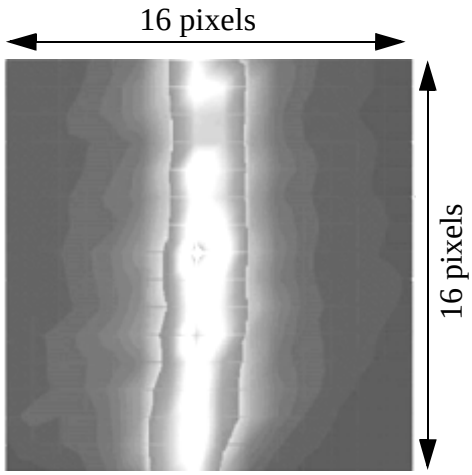

Fig. 2.25 The imaged fringe, measured at the ACCD (Photo: Durand et al. 2004).

3 Simulator of a direct detection Doppler wind lidar

Simulation software provides a powerful tool for the investigation of the performance of a lidar system under various conditions. An end-to-end simulator was developed to evaluate the ALADIN prototype, which consists of a forward and a retrieval module (Fig. 3.1). The forward module includes the input parameters, the simulation process, and the output (spectral information of the backscatter signals) of the system. The results are processed and analysed in the retrieval module.

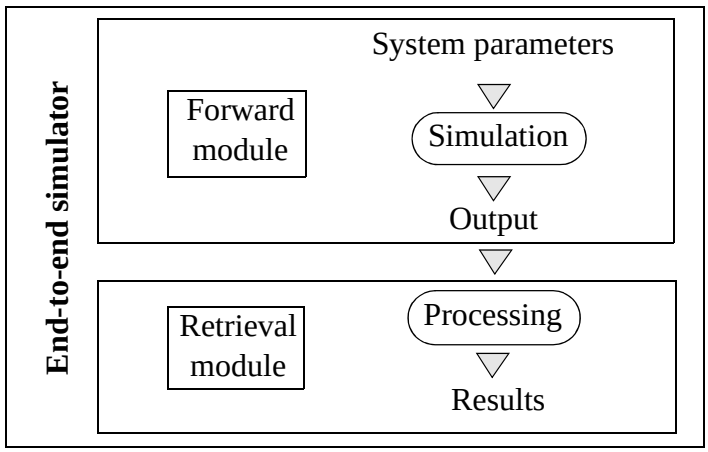

Fig. 3.1 A general diagram of an end-to-end simulator.

The forward module of the simulator generates the signals at the detector by modelling the atmosphere and the instrument. The retrieval module includes the data processing routines to obtain the LOS wind speed and is discussed at greater length in Chap. 4.

Different Doppler lidar end-to-end simulation software has been developed and improved in the last three decades (Abreu 1979, Streicher et al. 1998, McGill et al. 1999, Veldemann 1999, Leike 2000, Marseille and Stoffelen 2003).

Abreu (1979) introduced the possibility of direct detection DWL measurements from satellite. He analysed the expected range resolution and measurement accuracy of wind measurements by the use of a Fabry-Perot interferometer with a multiple-ring anode detector[1]. The simulations were done for an orbital platform at 530 nm and 550 nm wavelengths.

McGill et al. (1999) analysed the performance of direct detection DWL systems at 355 nm wavelength for different atmospheric models. The receiver included two Fabry-Perot interferometers for the double edge method and a multiple-ring anode. A new technique was developed to model more realistic atmospheric profiles based on airborne lidar observations. The model included solar variance, cloud, and aerosol variability. The results of the study reveal the particular importance for the validation of simulation tools with regard to atmospheric conditions as measured by e.g. radiosondes.

1. Such systems require a circular anode at the detector to match the circular fringe pattern of the Fabry-Perot interferometer.

The Lidar Performance Analysis Simulator (LIPAS) was introduced by Veldman (1999) to analyse the performance of the ADM phase-A system (ESA 1999). It was further developed by Marseille and Stoffelen (2003), and focused on the atmospheric modules. The atmospheric parameters for the phase-A study were taken from the RMA (Section 3.1.1), provided by ESA. Cloud data were taken from the ECMWF database (Becker et al. 1996), and the possibility of large biases in the Rayleigh receiver was pointed out, in respect to clouds and background light. To analyse the ADM performance under different atmospheric conditions, the LIPAS database was upgraded by taking molecular, aerosol, and cloud backscatter data from the Lidar In-space Technology Experiment[1] (LITE). Other atmospheric data (wind field, humidity, temperature, pressure) have been obtained from ECMWF analyses (Stoffelen et al. 2002). For the LITE data, winds are retrieved from the simulated Mie receiver, even in the higher altitudes (up to 20 km), which can be attributed to the fact that the retrieved backscatter shows up to an order of magnitude more aerosols than the RMA data (median aerosol model). Estimating the performance of the satellite version of ALADIN, it was shown that an improved quality control is required to avoid errors of the Mie receiver results caused by the low vertical resolution (1-1.5 km) in clouds.

A computer program to simulate the direct detection lidar for the ADM phase-A system was developed by Leike et al. (2001). The atmospheric parameters of this module were taken from the DWD for a period of 10 days in January 1998 around the globe. The system results in effective measurements of layers with aerosols and molecules, but experiences stronger attenuation especially with light propagation in clouds. The simulation was compared to a direct detection Doppler lidar at the Observatoire de Haute Provence, which employed the double edge detection method, and the results of both the measurements and the simulations are in good agreement (Hertzog and Garnier. 2002). Leike (2000) has also adapted the Direct Detection DWL (3DWL) model to incorporate the ALADIN satellite instrumental features, requirements, and parameters.

The ALADIN prototype simulator (AProS) developed in this study, is based on modules of the 3DWL (Leike 2000) and was adapted to the special features of the prototype (Section B). AProS was designed to enable wind measurement studies and the analysis of the ALADIN prototype from aircraft and ground under various atmospheric conditions, and instrumental parameters. AProS was adapted to incorporate all the differences between the satellite system and the ground and aircraft platforms. The simulation tool differs from others in its high vertical resolution of the atmospheric layers (15 m) and cloud variability. AProS is based on Monte Carlo[2] simulations (Ermakov 1975 p 65, Marchuk et al. 1980) to ensure more realistic signals at the detector.

In 2003 AProS was based on a single photon simulation, and each photon was generated and processed through the instrument. This technique was then supplanted by the simulation of the spectra per single laser pulse with a random number of scattered photons (Section 3.1.2). The results match the output data of the single photon technique, but the simulation time was significantly reduced. The atmospheric database of AProS was taken from the RMA. AProS is fast in processing, includes the random properties of emitted photons, and can be adapted to any

1. A lidar operating at 1064 nm, 532 nm, and 355 nm was flown on a space shuttle which provides atmospheric data during the period from 09.09 to 18.09.94.
2. The goal of the Monte Carlo method is to simulate a physical system by random sampling to describe the system evolution. This method is used in many diverse applications e.g. the radiation transport in the Earth's atmosphere.

change of instrumental parameters. The instrumental parameters were varied to validate and analyse the system.

An overview of AProS is shown in Fig. 3.2. The input parameters are used to calculate the qualities of the backscatter signal photons. The signals are then processed though the receiver components and the intensities at the detector are modelled. The atmosphere is divided into small layers with variable depth (typically 15 m), where the atmospheric conditions are assumed to be constant (wind speed, temperature and pressure). The aerosol backscatter coefficients and the transmission for clear and cloudy air are taken from model atmospheres (Section 3.1.1). The backscatter spectrum is calculated through all the optical components of the system and the signals at the detector are simulated.

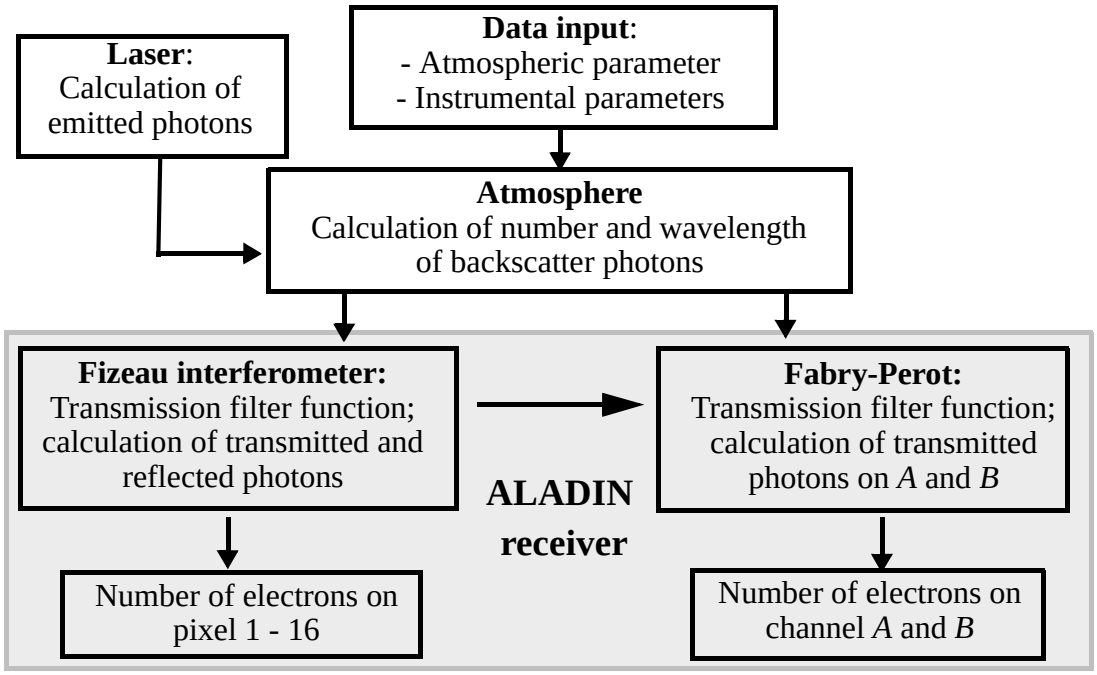

Fig. 3.2 The structure of the simulation software.

3.1 Atmosphere

3.1.1 Standard and reference model atmosphere

The RMA data (Section 2.1.2) have been frequently used for lidar in space simulations (Stoffelen et al. 2002, Di Girolamo et al. 2004). The temperature and pressure profiles (U.S. standard atmosphere) are defined by the Air Force Geophysics Laboratory (AFG Lab), and represent an idealized state of the Earth's atmosphere, referring to a period with moderate solar activity for various climatic conditions (Champion 1985). Additionally, temperature, pressure, cloud cover, and wind data can be taken from the local model (Doms et al. 1999) of the German Weather Service (DWD). Table 3.1 presents the different data sources.

Table 3.1 Atmospheric input parameter

Parameter	Literature	Model data
Temperature	AFG Lab	DWD data
Pressure	AFG Lab	DWD data
Aerosol	RMA	DWD data
Extinction-to- backscatter ratio	RMA, constant	Constant
Wind	Constant	DWD data
Cloud model	RMA	DWD data

The different temperature and pressure profiles are named U.S. tropical, U.S. mid latitude summer, U.S. mid latitude winter, U.S. sub arctic summer, U.S. standard atmosphere illustrated in Fig. 3.3.

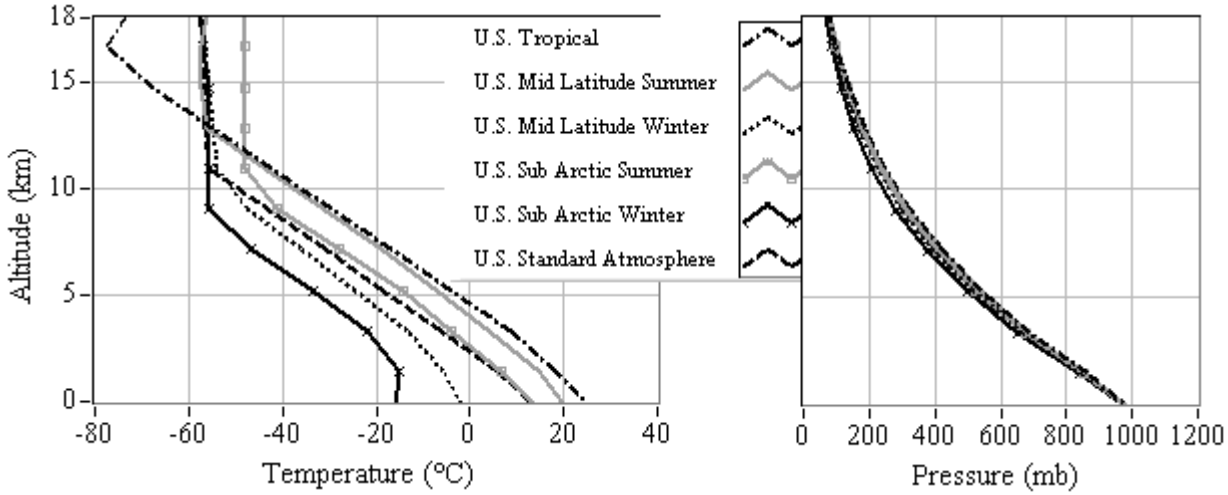

Fig. 3.3 Altitude profiles of temperature (left) and pressure (right) of different climatologies of the Air Force Geophysics Laboratory.

Aerosol models (RMA):

The RMA includes data of atmospheric backscatter measured at 10.6 µm wavelength. Five backscatter profiles from the ground up to 16 km altitude are illustrated in Fig. 3.4. The aerosol backscatter decreases with altitude for all models. The aerosols diminish above the boundary layer while near-ground aerosols may be found in great quantities. The profile of the higher decile model also illustrates the effects of thin and transparent clouds for altitudes at 4 km and 10 km. The backscatter profiles are scaled to 355 nm wavelength using EQ. 2.6 and EQ. 2.7.

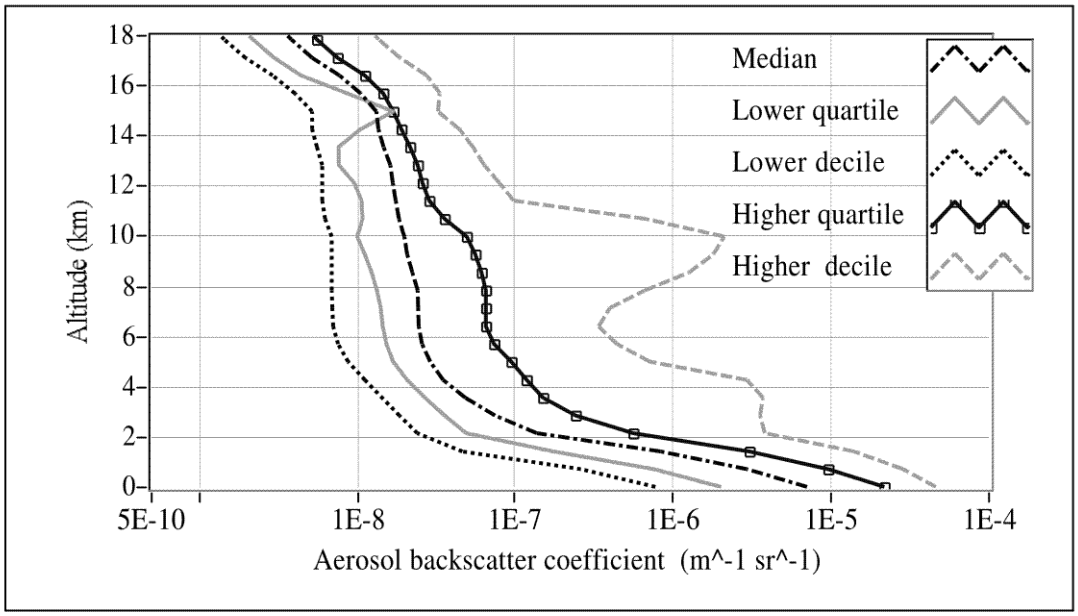

Fig. 3.4 Different aerosol backscatter profiles referring to a wavelength of 355 nm versus altitude.

The percentiles are those values of backscatter at which a given percentage of the data is greater or less than this value. Thus the upper/lower quartiles have 25 % of data greater/less than, whilst the upper lower deciles have 10 % of data greater/less than.

The RMA profiles were derived from field campaigns before the eruption of volcano Pinatubo in June 1991, which leads to an increased aerosol concentration even in the stratosphere. During the LITE campaign in 1994 the effects of Pinatubo could be still observed. The atmospheric database taken from the RMA for higher aerosol loadings is quite well in line with the atmospheric parameters of LITE, and the RMA median model agrees within an order of magnitude with the EARLINET database (The European Aerosol Research LIdar NETwork, set up to Establish an Aerosol Climatology, Bösenberg and Matthias, 2003). EARLINET consists of a network of 21 stations distributed over most of Europe which measure the vertical distribution of aerosols, and provide a database of aerosol distribution on a continental scale. The results are shown in Fig. 3.5, where three profiles of the RMA are illustrated (median, lower and higher decile). The average aerosol backscatter of the LITE measurements was derived from cloud-free profiles and adapted from Stoffelen et al. (2002). The EARLINET profiles (summer and winter) were adapted from measurements in Munich presented by Wandinger (2003).

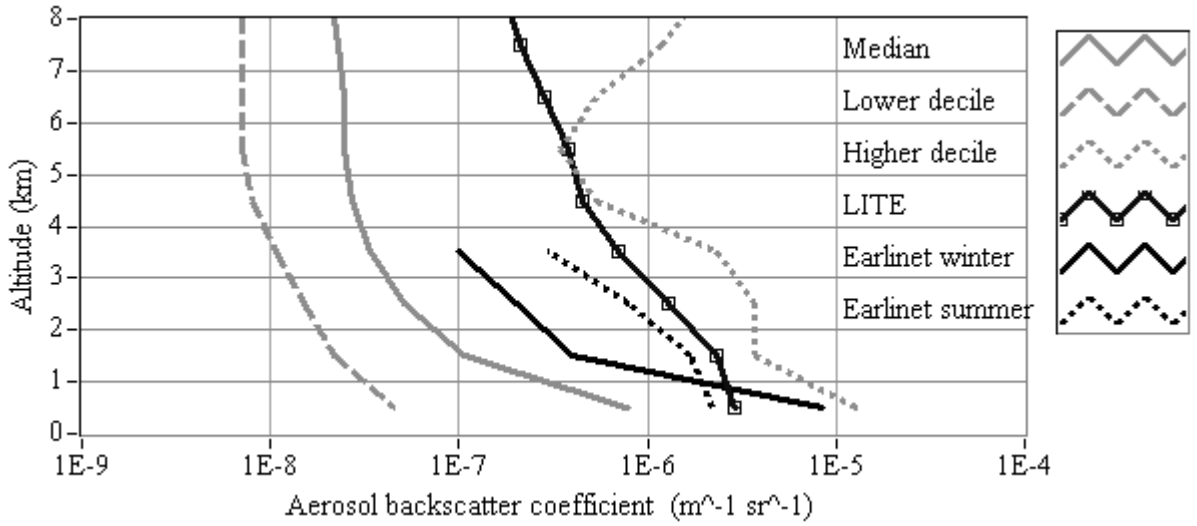

Fig. 3.5 Different aerosol backscatter profiles from the RMA (median, lower and higher decile), EARLINET (winter and summer in Munich), and LITE data (The LITE data were provided by G. J. Marseille) versus altitude.

The RMA backscatter scenario is close to the EARLINET and LITE data. The RMA was chosen during this study because of the large range in respect to the aerosol backscatter coefficients. This offers the possibility to analyse the Mie and Rayleigh receiver for different aerosol variability (Section 4.2.4).

Extinction

The extinction is calculated from the extinction-to-backscatter ratio (Section 2.1) for air molecules and aerosols, where the ratio of molecules is constant ($8\pi/3$ sr, EQ. 2.10). The ratio of aerosols corresponds to a change in particle size, not in density, as demonstrated by Li et al. (2000) at 532 nm wavelength. A large field of studies in the extinction-to-backscatter ratio of aerosols (lidar ratio) was performed in the past because of the correlation to high particle size sensitivity (Evans 1988, Li et al. 2000, Chen et al. 2002, Liu et. al. 2002). Evans (1988) suggested a model to compute the lidar ratio and compared the results to the literature. The agreement was found to be good. The lidar ratio of the model depends on the refractive index and the particle size, and was analysed for different regions and wavelengths at 1064 nm and 690 nm. The variation of the lidar ratio for cirrus clouds was determined by Chen et al. (2002) at 523 nm. An average ratio of 29 sr +/-12 sr was measured for all clouds in the period 1999 and 2000. Below 12 km the lidar ratio varies randomly, and within 12 - 15 km the lidar ratio is between 20 and 40 sr. High clouds at about 15 km lead to lidar ratios between 10 sr and 30 sr. The values depend on the temperature, which causes an increased uncertainty. Liu et al. (2002) analysed the lidar ratio at 532 nm during the Asian dust period in spring 1998 and 1999. The measured values range from 42 sr to 55 sr. In respect to the studies made for backscatter ratios there is a large scale of variation noticeable from 10 sr to 55 sr. The ratio at 355 nm is smaller than at 532 nm. In this study the lidar ratio is assumed to be 50 sr, following the most recent works and the results suggested by Vaughan (1998 p. 51). He proposed values with a dependency on altitude in the range of 13 sr (cirrus clouds) to 60 (volcanic) for a 355 nm lidar system. A lidar ratio of 50 sr was suggested by Tan and Andersson (2004), and this value has been used in previous studies as well.

Cloud models

About two-thirds of the globe is covered by cloud. As a consequence, it is necessary to assess the performance of ALADIN for wind measurements in regions with significant cloudiness. Dense clouds attenuate the signals strongly, so that wind speed cannot be measured. At the cloud border or in semi-transparent clouds, there is a strong Mie backscatter, so the Mie receiver is used for wind estimation. Inside clouds, the signals are strongly attenuated. Areas with broken clouds may allow profiling the full atmosphere. Various investigations can be found in the literature to determine the cloud cover factor. Tan and Andersson (2004) analysed different cloud model data. The ECMWF atmospheric model was compared to the cloud cover data from LIPAS using LITE data as input parameters. The LIPAS model based on constant cloud profiles for horizontal ranges of 1 km and no distinction was made between backscatter from liquid clouds and ice clouds, but the droplet size is assumed to vary linearly with pressure. The ECMWF model cloud cover underestimates cloud cover of LITE by 20 % on average and has a systematic lack of low-level cloud. Current investigations are done to analyse the GLAS data (Geoscience Laser Altimeter System[1]) on cloud variability (Palm et al. 2005, Palm and Spinhire 1998) and in the near future data can also be expected from the satellite mission Calipso (Cloud-Aerosol Lidar and Infrared Pathfinder Satellite Observation). Palm et al. (2005) showed that for low and middle clouds the ECMWF provides good results but often misses the location and amount of high cirrus clouds. There is an overestimation of high cloud fraction too, and this error increase with forecast length.

Astin and Kiemle (2003) analysed the effects of broken clouds on lidar measurements from airborne lidar data, obtained from UV lidar measurements during the CLARE'98 (Cloud Lidar And Radar Experiment) campaign. The advantages of increased horizontal resolution by analysing each ACCD image of 50 accumulated pulses (3.5 km) instead of accumulating 700 pulses (50 km) were discussed. The effects of data loss through accumulation over 50 km were shown in the study. An analytic approach was demonstrated by Astin and Latter (1998). The cloud distribution and the breaks in cloud cover were assumed to follow exponential distributions, and the probability was chosen randomly for individual sections. This gives a good approximation of typical cloud distribution.

During this study, the cloud cover coefficients of the DWD local model are taken for simulations with AProS. The local model is a non-hydrostatic model with a vertical resolution of 31 levels (10 levels within the first 1500 m) and an operational horizontal resolution of 7 km, which is suitable to simulate atmospheric variability in respect to the resolution of the simulations. Each atmospheric cell during simulation is labelled by a mean cloud cover value. This is a good estimate for simulations with a larger vertical (> 1 km) and horizontal mesh size and enables short simulation times.

Besides the cloud cover coefficients, which can vary with each laser pulse over each 15 m vertical range, the corresponding backscatter and extinction values (Table 3.2) are selected for use in the case of clouds during this study. The backscatter and extinction coefficients for clouds were taken from the RMA, and are calculated for water clouds, treating water droplets as spherical particles (Dermendjian 1964). The cloud backscatter β_{cloud} depends on altitude z, and the aerosol backscatter $\beta_{A,cloud}$ is determined by:

1. Mission launched in 2003; GLAS is a laser altimeter designed to measure topography, clouds and aerosol height structure.

$$\beta_{A,\,cloud}\,(z) \;=\; \beta_A\,(z) + \beta_{cloud}(z) \tag{3.1}$$

where β_A is calculated by EQ. 2.6 and β_{cloud} is taken from Table 3.2. When the DWD data are used in a simulation, the cloud cover coefficient (*clc)* has additionally taken into account. The aerosol backscatter is then considered as follows:

$$\beta_{A,\,cloud}\,(z) \;=\; \beta_A\,(z) + \beta_{cloud}(z) \cdot clc \tag{3.2}$$

The cloud cover coefficient from the DWD data is scaled in a range of zero to one. Total sky coverage by clouds is represented by the value one.

Whilst the molecular backscatter coefficient is not affected by cloud cover, clouds do have effects on the molecular return signal by attenuation of transmission, calculated from molecular extinction (Section 2.1.3). The resulting extinction of aerosols and molecules is calculated by:

$$\alpha_{A+Mol,\;cloud}\,(z) \;=\; \beta_{A,\,cloud}\,(z) \cdot k + \alpha_{Mol} \tag{3.3}$$

where k is the lidar ratio (EQ. 2.9), α_{Mol} the molecular extinction (EQ. 2.10), and α_{cloud} is taken from Table 3.2. For cloudy skies the Mie backscatter signal is very strong and the Rayleigh backscatter is attenuated. This is considered in the calculation of the two-way transmission T^2:

$$T_{cloud}^{\;2}(z) \;=\; e^{\,-2\int_{z1}^{z2}\alpha_{A+Mol,\,cloud}\,(z)\,dz} \tag{3.4}$$

Table 3.2 RMA backscatter and extinction coefficients of cloud models

Types of cloud	Backscatter coefficient β_{cloud} [$m^{-1}\,sr^{-1}$]	Extinction coefficient α_{cloud} [m^{-1}]	Altitude [m]
Stratus	$5x10^{-3}$	$9x10^{-2}$	200 - 700
Cumulus	$6x10^{-4}$	$1.2x10^{-2}$	750 - 1000
Cumulonimbus	$1x10^{-2}$	$1.8x10^{-1}$	2000 - 4000
Altostratus	$1x10^{-3}$	$1.8x10^{-2}$	4000 - 4500
Cirrus	$1.4x10^{-5}$	$2x10^{-4}$	8500 - 9500

The shape and size of droplets and ice crystals leads to multiple scattering and depolarisation, so that changes in the aerosol backscatter signal can be observed. Depolarisation and multiple scattering, however, are not considered in AProS, since there is negligible influence on the Doppler shift for multiple scattering in direct detection Doppler lidar systems (Leike et al. 2000), because the field of view of the instrument is very small (Werner et al. 2005 p. 174). Multiple scattering increases if a cloud is present. Benayahu et al. (1995) demonstrated that for the presence of clouds single scattering still accounts for 95 % of the return signal when the field of view divergence is smaller than 0.5 mrad. The field of view of the ALADIN prototype is 0.1 mrad, and it is reasonable to neglect multiple scattering effects.

Depolarisation is defined as the ratio of linearly polarized light (orthogonal to the propagation vector) to the light with parallel polarisation. Depolarisation is weak in clear air (1.4 %, Vaughan et al. 1998) but increases significantly for ice crystals (cirrus clouds, Vaughan et al. 1998). Therefore an increase in depolarisation indicates the presence of non-spherical particles such as ice crystals. Measurements at 532 nm by Chen et al. (2002) shows depolarisation values from 0.3 to 1.0 for cirrus clouds. The backscatter from cirrus clouds is high compared to depolarisation and therefore not considered in AProS.

3.1.2 Photon backscatter statistic

The mean number of backscatter photons N_{ph} is calculated by the lidar equation (EQ. 2.13), and varies according to a Poisson distribution with a standard deviation of $\sigma_N = \sqrt{N_{ph}}$.

The wavelength distribution of the backscatter Mie and Rayleigh photons is represented by a Gaussian approximation (Section 2.1.1 and Section 2.1.2). The standardised Gaussian distribution is calculated separately for the Mie and Rayleigh photons:

$$N_j(\lambda) = N_{ph} \cdot \frac{1}{\sqrt{2\pi} \cdot \sigma_{R,M}} e^{-\frac{\Delta\lambda_j^2}{2\sigma_{R,M}^2}} \tag{3.5}$$

where N_j is the number of photons of wavelength interval j, $\sigma_{R,M}$ is the standard deviation of the Gaussian spectrum for the Rayleigh or Mie spectrum (EQ. 2.5, EQ. 2.8), $\Delta\lambda_j$ the mean wavelength of wavelength interval j, and N_{ph} is the mean number of backscatter photons. The Rayleigh and the Mie spectrum of the backscatter photons are shifted with respect to the Doppler effect $\Delta\lambda_D$. Fig. 3.6 illustrates the Rayleigh backscatter spectrum with a Gaussian shape calculated with a Poisson distribution of the intensities per wavelength interval.

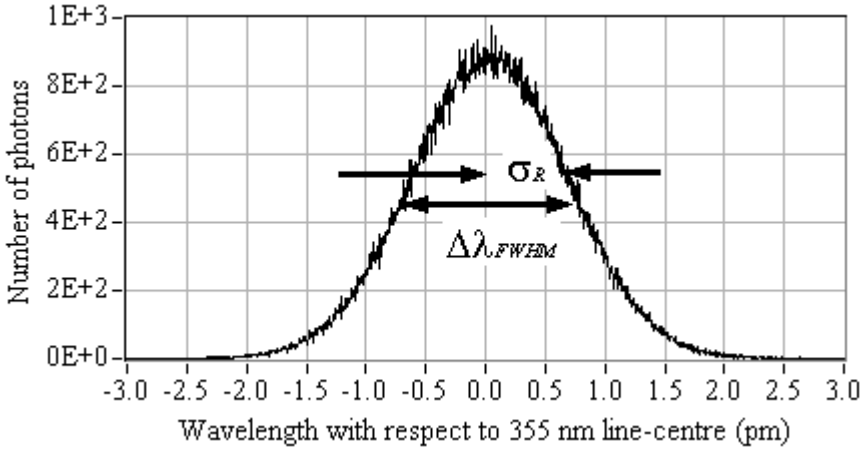

Fig. 3.6 The Rayleigh backscatter photons versus wavelength from a 355 nm source including noise. The differences between the FWHM $\Delta\lambda_{FWHM}$ and the standard deviation σ_R are indicated.

The Rayleigh spectrum is modelled for a wavelength interval from +4 pm to -4 pm in steps of 5 fm. The Mie spectrum is modelled for a wavelength interval of +/-0.08 pm in steps of 0.05 fm, which provides best simulation results in respect to the wavelength interval and resolution.

3.2 Instrument

3.2.1 Laser

The number of the emitted photons is calculated by the energy per photon $h * c / \lambda$ (for a frequency *f*) and the laser pulse energy E_L:

$$N_e = \frac{\lambda_L}{h\ c} E_L \tag{3.6}$$

where *h* is the Planck's constant (6.625×10^{-34} J s). The number of backscatter photons $N_{ph(M,\,R)}$ of the Mie and Rayleigh spectrum collected by the telescope depends on the backscatter energy $E(\lambda_L, r)$ (received by lidar EQ. 2.13) and can be described by:

$$N_{ph(M,\,R)}(\lambda, r) = \frac{\lambda_L}{h\ c} E(\lambda_L, r) \tag{3.7}$$

3.2.2 Receiver optics

The backscatter photons collected by the telescope are attenuated by the transmission of the transmitter τ_T and receiver optics τ_R of the front optic modules. These parameters include the telescope, mirrors, quarter waveplates, beamsplitters, and spectral filters in front of the interferometers.

Telescope overlap function:

The laser is transmitted coaxial (Fig. B.2) to the optical axis of the telescope (Fig. 3.7). In front of the telescope the backscatter light toward the primary mirror *M*1 is obscured by the secondary mirror *M*2. Farther than 330 m, the backscatter light from the laser is attenuated by partial obscuration of the secondary mirror and the overlap of both the laser beam and the telescopes receiver volume (also denoted as geometric form factor or crossover function in the literature). Full overlap occur at 3382 m distance.

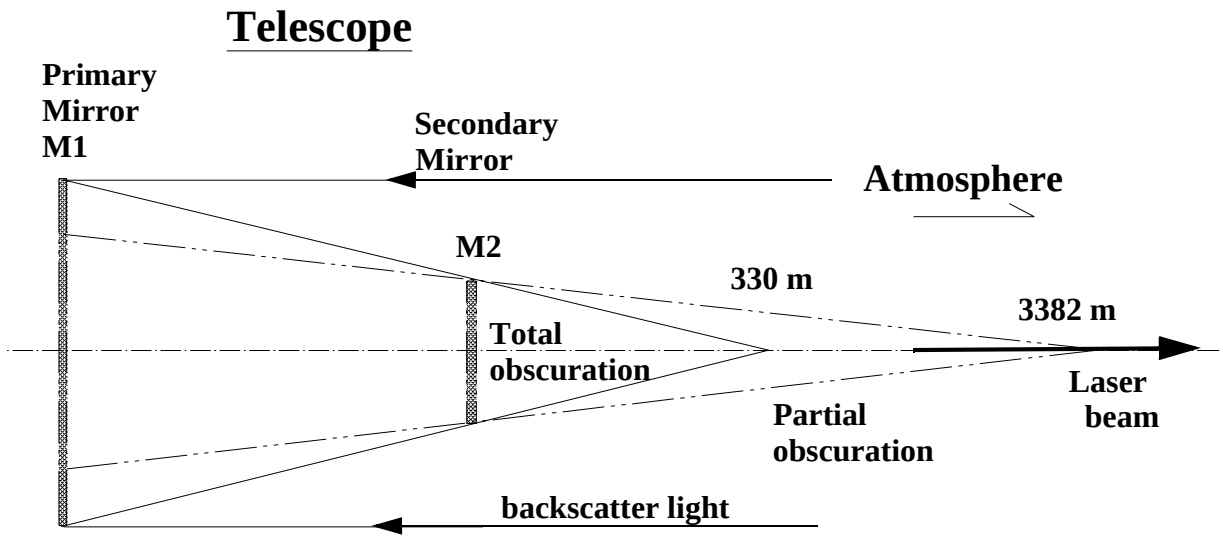

Fig. 3.7 A schematic design and the optical path of the ALADIN prototype Cassegrain telescope with the primary mirror *M*1 and the secondary mirror *M*2.

Several attempts were made to estimate the profile of the overlap factor theoretically for non-coaxial and coaxial systems (Halldorsson and Langerholc 1978), and experimentally by Dho et al. (1997). The overlap of a direct detection system was determined by Wandinger and Ansmann (2002) experimentally and theoretically with an iterative approach. The overlap function was implemented within the simulator (Fig. 3.8) using the algorithms performed by Meister (2005), and is important for near-field measurements on the ground. The overlap damping in respect to R^{-2} demonstrates the backscatter intensities depending on the distance.

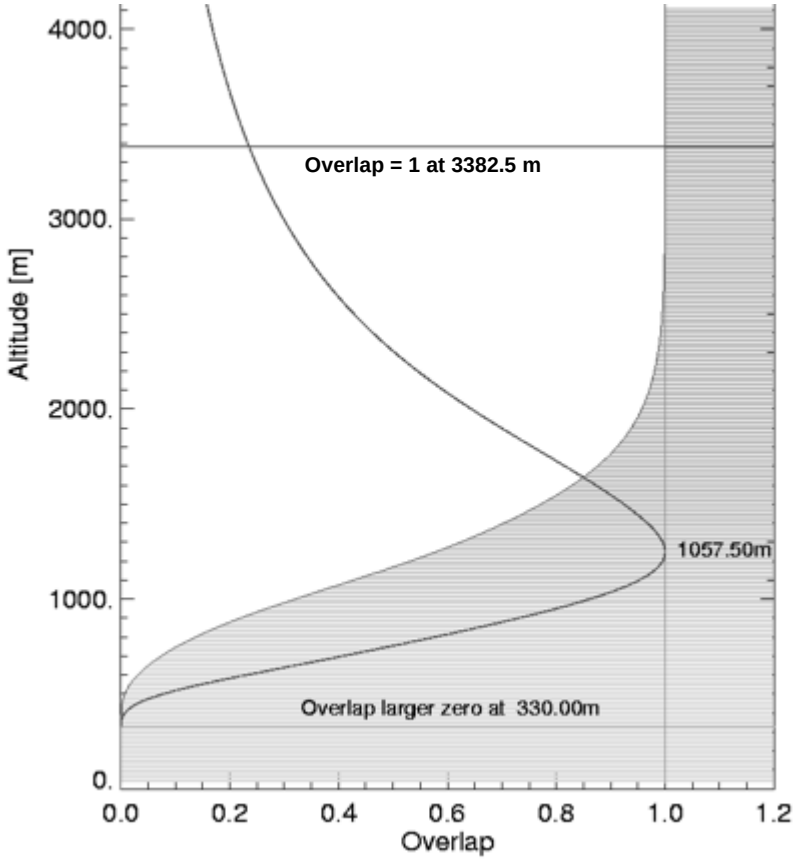

Fig. 3.8 The overlap function (grey field) and overlap damping in respect to $1/R^2$ (black line). A Gaussian beam profile was assumed (adapted from Meister 2005). There is no overlap near the receiver up to 330 m distance, then the overlap increases to 1 at 3382.5 m. The maximum intensities are received from a distance of 1057.5 m.

The parameters of the overlap function are calculated by 100 µrad field of view, 70 µrad laser beam divergence, 20 mm laser beam diameter, 200 mm diameter of primary mirror, 85 mm obscuration by mirror 2, a focal length of 1513 mm, and a mirror spacing of 487 mm.

3.2.3 Filter transmission function

Denker and Tritschler (2005), and Gittins et al. (1998) demonstrated an ideal accordance of measured Fabry-Perot interferometer transmission functions and the Airy function (EQ. 2.20). For both the Fabry-Perot interferometer and the Fizeau interferometer, the Lorentzian function was used to model the filter function, which is an adequate approximation of the filter Airy function (Sahlech and Teich 1994, Winzer et al. 2001, Flesia and Korb 1999). The Lorentzian function may be written as (Vaughan 2002 p. 102):

$$T(k, \varphi) = \left(4\left[\frac{(\varphi - 2\pi k)}{FWHM}\right]^2 + 1\right)^{-1} \tag{3.8}$$

where φ is the phase difference, k is an integer, and maxima occur for $\varphi = 2\,\pi\,k$. The shape of the filter transmission function is presented in Fig. 3.9 for $\varphi = 150$ (start value), FWHM = 50, and $k \in [0, 50]$.

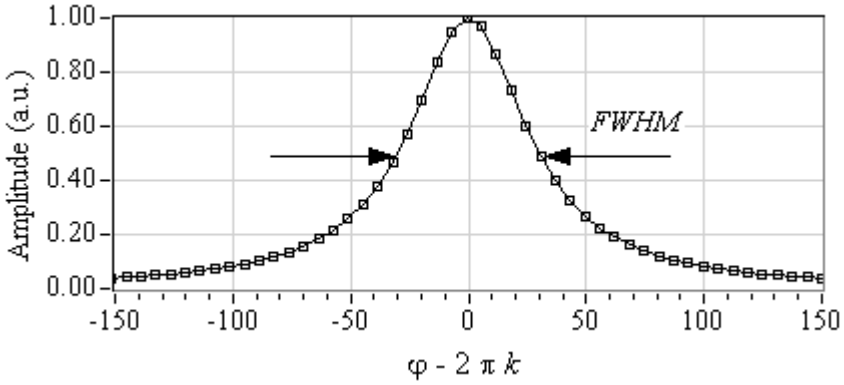

Fig. 3.9 The amplitude of a computed Lorentzian shape versus φ - $2\,\pi\,k$ (EQ. 3.8).

3.2.4 Fizeau interferometer

The instrumental parameters of the Fizeau interferometer, used in AProS, are the filter peak transmission T_{p_F}, the pupil truncation ratio (Fig. 3.10), the filter FWHM ($\Delta\lambda_{FWHM}$), the filter useful spectral range (USR, $\Delta\lambda_{USR}$), and the free spectral range (FSR, $\Delta\lambda_{FSR}$, values in Table 3.3). The Mie filter peak transmission is the maximal transmission of the Fizeau interferometer including absorption. The pupil truncation ratio defines the ratio of the photons imaged at the square field of the ACCD and the incoming photons limited by the round pupil of the field of view.

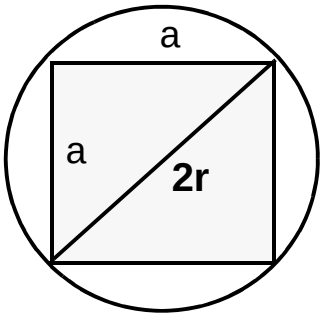

Fig. 3.10 The parameters to calculate the pupil truncation ratio.

The illuminated square field of the detector is calculated by $A_{sq} = a^2 = 2\,r^2$. The round illuminated spot is calculated by $A_c = r^2\,\pi$. The ratio of the photons on the square field to all the incoming photons can be written as $A_{sq} / A_c = 2 / \pi$, hence the number of incoming photons are reduced by the factor of $2 / \pi$.

The filter transmission curve (transfer function), filter FWHM, USR, FSR, and a typical Rayleigh spectrum are demonstrated in Fig. 3.11. The range of the measurements is limited by the USR (0.695 pm) which defines the maximum wind speed measurement range. The transmitted photons are calculated depending on wavelength within the USR. The FSR reiteration was taken into account for the reflected Rayleigh photons and the corresponding larger wavelength interval.

Dolphi-Bouteyre and Garnier (2002) examined the parameters of the Fizeau interferometer of ALADIN (surface defects and misalignment) and the asymmetric fringes (Section A.2). It was demonstrated that the fringes may assumed to be symmetric for the ALADIN configuration.

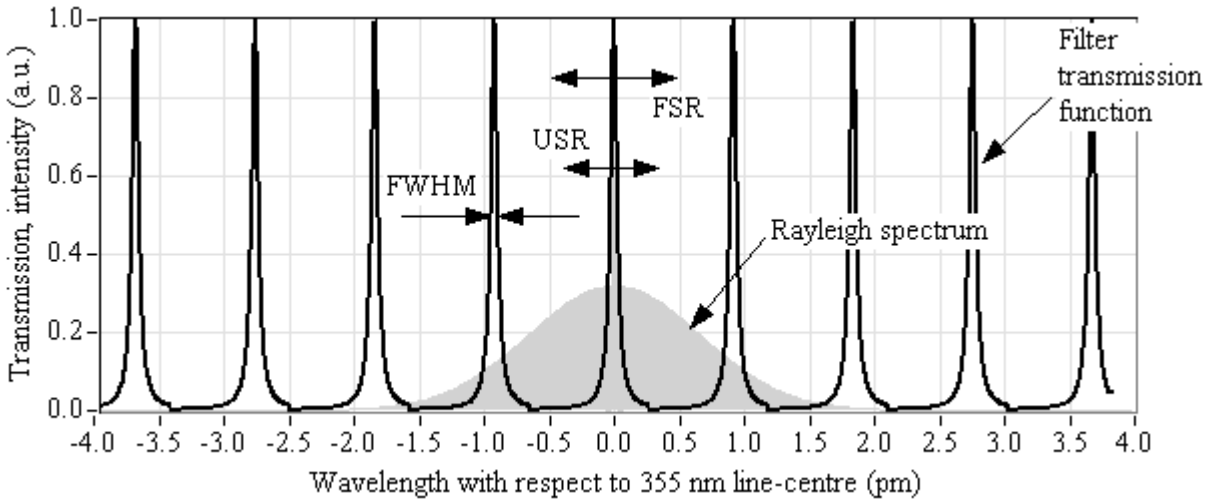

Fig. 3.11 Transmission curves of the Fizeau interferometer (black) and the Rayleigh spectrum (grey) in respect to the Rayleigh wavelength interval. The FSR, USR, and FWHM of the transmission curves are indicated.

Transmission at the Fizeau interferometer

The photons at the Mie receiver for each atmospheric layer are stored in lines of 16 pixels in the ACCD memory zone and each pixel is linked to a part of the transmission curves during simulation. The Fizeau interferometer can be considered as a sequence of Fabry-Perot interferometers in the plane parallel to the wedge (Dolfi-Bouteyre and Garnier 2002).

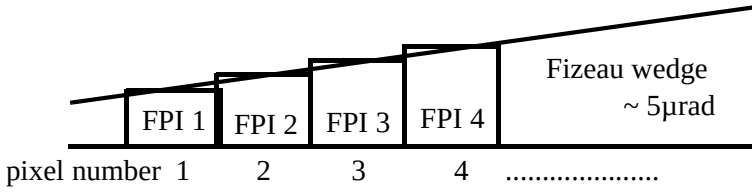

Fig. 3.12 The Fizeau interferometer is simulated by a series of Fabry-Perot interferometers (FPI) with increasing mirror separation referring to the wedge angle.

The Fizeau is simulated by Fabry-Perot interferometers with different physical separations of the etalon plates as shown in Fig. 3.12. Fig. 3.13 shows the transmission curve for the incoming Mie spectrum for zero wind speed (left figure) and a Doppler-shifted signal (right figure). The change in colour (grey and black) of the transmission curve symbolise the calculated transmission of each pixel. The Mie spectrum is always fully transmitted and broadened by the filter transfer function.

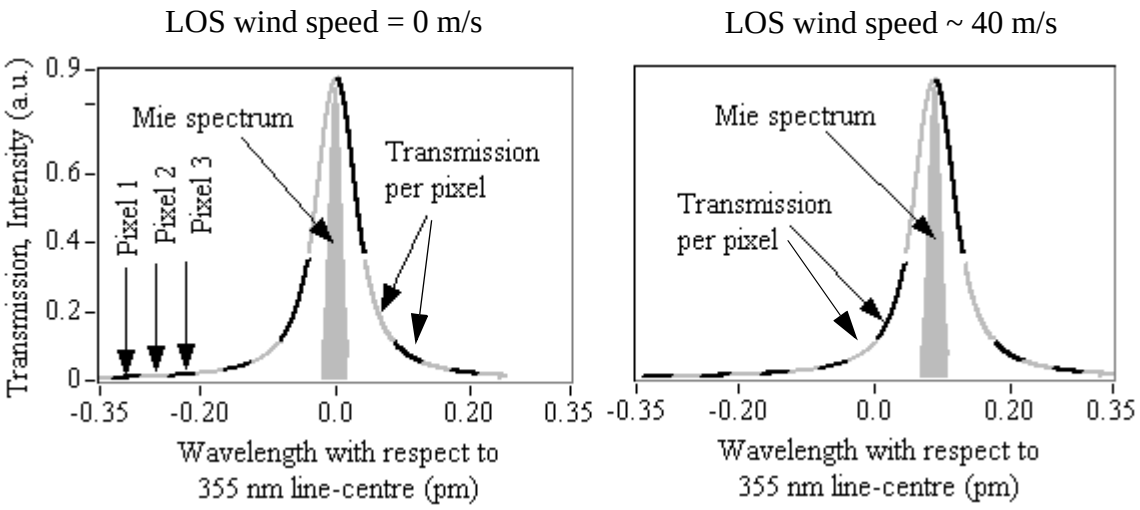

Fig. 3.13 A schematic view of the Fizeau transmission curves and the Mie spectrum from a 355 nm source depending on the wavelength of the incoming light. Left figure shows a Mie spectrum equal to the laser wavelength and in the right figure the backscatter light is Doppler-shifted (~40 m/s LOS wind speed). The change in black and grey of the transmission curve indicates the transmissions in respect to the pixels.

One pixel represents 4 Fabry-Perot interferometers to increase the resolution and to improve the accuracy, and results in a mean transmission curve per pixel. A number of performance tests provided good results and short simulation times for this configuration. The $T_{Fiz}(\lambda_i)$ of EQ. 3.8 at a wavelength index i for $\varphi - 2\pi k = \lambda - \Delta\lambda$ and scaled to the peak transmission T_{p_F} is described by:

$$T_{Fiz}(\lambda_i) = \frac{2}{\pi} \frac{T_{p\_F}}{16 \cdot 4} \sum_{j=1}^{j_{max}=4} \left(\frac{4(\lambda_i - \Delta\lambda_j)^2}{\Delta\lambda^2_{FWHM}} + 1 \right)^{-1} \tag{3.9}$$

where $\Delta\lambda_j$ (j = 1...4) are the wavelength steps of each pixel, λ_i is the mean wavelength interval of the corresponding pixel, and $2/\pi$ is the pupil truncation ratio. The transmission is scaled to the 16 pixels by taking the factor 1/16 in EQ. 3.9 into account. The transmitted photons per pixel of EQ. 2.13 arise from a multiplication of the incoming spectrum (EQ. 3.7) with the transmission curves and are derived from:

$$N_{Fiz}(r, \lambda) = T_{Fiz}(\lambda) \cdot N_{ph(M,R)}(r, \lambda) \cdot \tau_T \cdot \tau_R \tag{3.10}$$

To obtain the intensities per pixel, the photons are summed up over a wavelength interval corresponding to pixel i. The transmitted photons $N_{Fiz}(r, i)$ of the atmospheric range r at the Mie receiver are written as:

$$N_{Fiz}(r, i) = \sum_{\lambda} N_{Fiz}(r, \lambda) \tag{3.11}$$

To make an estimate for the photons at the Mie receiver and to determine the efficiency of the interferometers and front optics, the different optical parts of the system are defined by constant

values as demonstrated in the following figure. The spectral efficiency is defined by 2.04*1/16 and the optical peak transmission is defined by the transmitter and receiver optics, the filter peak transmission, and the pupil truncation (0.112*0.449*2/π).

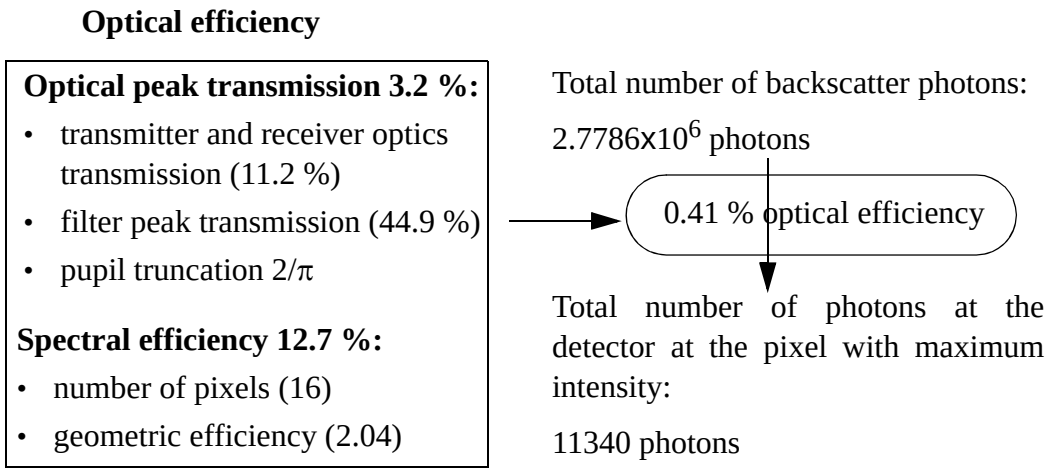

Fig. 3.14 An overview of the transmission parameters of the Mie receiver

The geometric efficiency arises from the sum of the transmission values of each pixel. The resulting optical efficiency of the Mie receiver is nearly half a percent and is the product of the spectral efficiency and the optical peak transmission. That is enough to image clear signals and not too much to saturate the ACCD. There are 2.7786×10^6 backscatter photons in front of the instrument at 1.5 km altitude for an airborne system (700 shots accumulated, 70 mJ laser energy, and 15 m range). The optical efficiency of 0.41 % leads to 11340 photons at the pixel with maximal intensity.

Reflection at the Fizeau interferometer

The reflection for a broad-banded signal was calculated for the Rayleigh wavelength range of +/-4pm. The filter transfer functions are shown in the following figure.

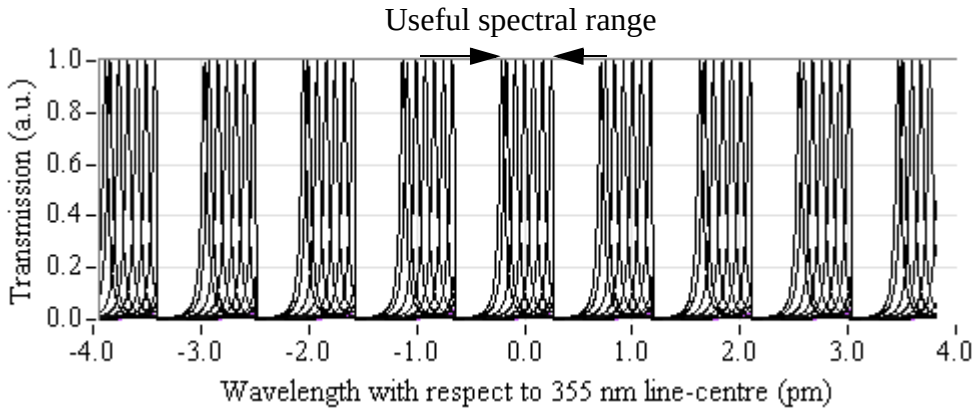

Fig. 3.15 The periodic transmission function of the Fizeau interferometer for the Rayleigh wavelength interval and the useful spectral range.

Because the transmission is limited by the USR, the 16 filter transmission curves are only provided across the USR. Now the transmission may be calculated by a multiplication of the spectrum with each transmission curve and then integrated with respect to the wavelength range. On the other hand, the transmission can be integrated first, and then multiplied with the transfer function of the filter. The latter leads to shorter simulation times and the results of the transmission curve arising from integration are shown in Fig. 3.16. The transmission varies between 0 % and 10 %.

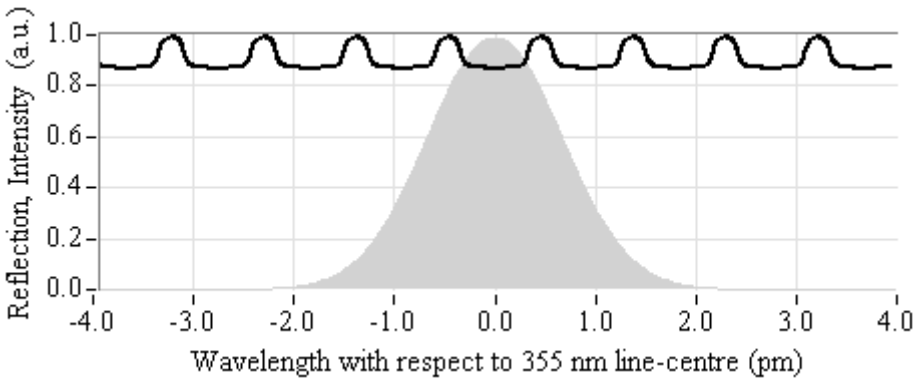

Fig. 3.16 The resulting filter transfer function (black line) and the Rayleigh spectrum (grey area) from a 355 nm source versus wavelength.

The reflected photons are calculated by:

$$N_{Fiz,\ refl}(r, \lambda) = (1 - T_{Fiz}(\lambda)) \cdot N_{ph(M,\,R)}(r, \lambda) \cdot \tau_T \cdot \tau_R \tag{3.12}$$

which are now directed towards the Fabry-Perot interferometer.

3.2.5 Fabry-Perot interferometer

The instrumental parameters of the Fabry-Perot interferometer, used in AProS, are the filter peak transmission on channel *A* (T_{p_A}), the filter peak transmission on channel *B* (T_{p_B}), the filter $\Delta\lambda_{FWHM\_A}$, the filter $\Delta\lambda_{FWHM\_B}$, and the filter spacing $\Delta\lambda_{spac}$. The filter peak transmission is the maximum value $T_{p\_A,\,B}$ of the transmission curve of channel *A* and *B* (including absorption). The incoming Rayleigh spectrum (grey) is shown in Fig. 3.17. The intensity is reduced by the Fizeau filter reflection at the centre and slightly at the wings. Because the effect is symmetric, the wind speed determination is not affected.

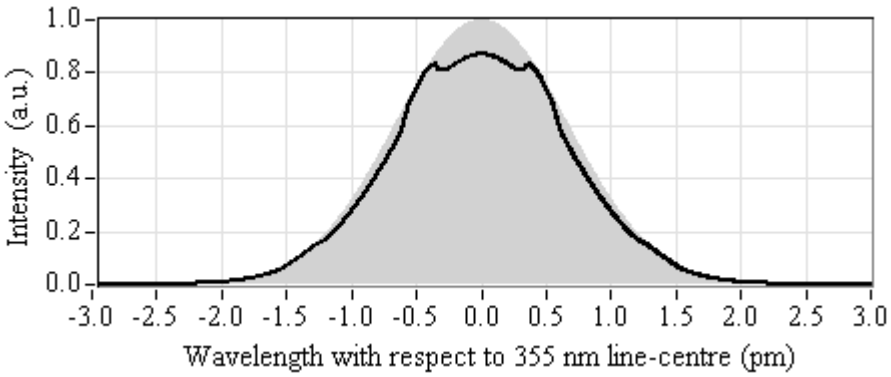

Fig. 3.17 The Rayleigh spectrum before (grey) and after reflection (black line) at the Fizeau interferometer from a 355 nm source versus wavelength.

The filter transmission of the Fabry-Perot interferometer derived from EQ. 3.8 leads to:

$$T_{A,B}(\lambda) = T_{p\_A,B}\left(\left[\frac{\lambda - \left(\pm\frac{1}{2}\Delta\lambda_{spac\_A,B}\right)}{\Delta\lambda_{FWHM\_A,B}}\right]^2 + 1\right)^{-1} \tag{3.13}$$

where $+1/2\Delta\lambda_{spacA,B}$ is used for calculation of the filter curve *A* and $-1/2\Delta\lambda_{spacA,B}$ for calculation of filter transmission curve *B*. In respect to EQ. 2.13, the number of photons for channel *A* may be written as:

$$N_A(r,\lambda) = T_A(\lambda) \cdot N_{Fiz,\ refl}(r,\lambda) \cdot \tau_T \cdot \tau_R \tag{3.14}$$

The photons $N_{Fiz,\ refl}$ reflected at *A* are reduced by $(1 - T_A(\lambda))$. The photons on channel *B* are calculated as follows:

$$N_B(r,\lambda) = T_B(\lambda) \cdot (1 - T_A(\lambda)) \cdot N_{Fiz,\ refl}(r,\lambda) \cdot \tau_T \cdot \tau_R \tag{3.15}$$

To make an estimate for the Rayleigh intensities, the different optical parts of the system are defined by constant values as demonstrated in Fig. 3.18. The spectral efficiency is defined by the ratio of photons transmitted towards the detector and the photons in front of the interferometer. The optical efficiency is defined by the filter peak transmissions and the transmitter and receiver optics.

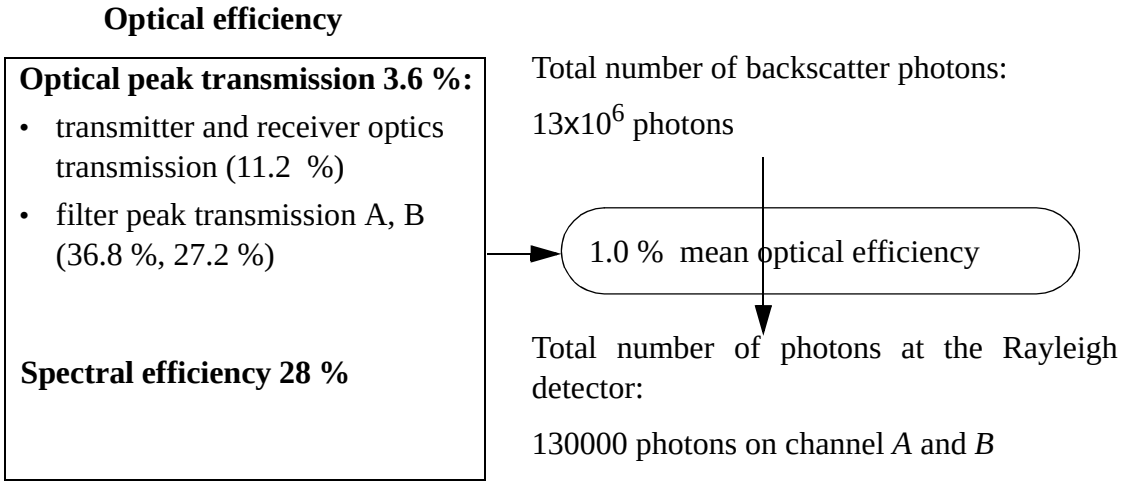

Fig. 3.18 An overview of the transmission parameters of the Rayleigh receiver

There are 13×10^6 backscatter photons in front of the instrument at 6 km altitude for an airborne system (700 shots accumulated, 70 mJ laser energy and 15 m range) and 130000 photons are on the ACCD due to the optical efficiency of 1 %.

3.2.6 Detection unit

The simulation results are affected by the standard deviation of the readout noise N_{noise} (Section 2.6.7) and the detector quantum efficiency μ_{eff}. The readout noise was measured in laboratory conditions for 50 accumulated laser pulses for each measurement and is considered in AProS with Poisson distributed numbers of electrons per pixel. Each photon detected by the ACCD generates an electron at the respective pixel with respect to the quantum efficiency.

The Mie receiver:

At the Mie detector the number of signal electrons per pixel *i* are calculated by:

$$N_{Fiz}(r, i) = N'_{Fiz}(r, i) \cdot \mu_{eff} \tag{3.16}$$

The Rayleigh receiver:

The number of electrons at the Rayleigh receiver channel *A*, per laser pulse, is written as:

$$N_{FP\_A}(\lambda_L, r) = N_A(\lambda_L, r) \cdot \mu_{eff} \tag{3.17}$$

respectively at channel *B*:

$$N_{FP\_B}(\lambda_L, r) = N_B(\lambda_L, r) \cdot \mu_{eff} \tag{3.18}$$

The simulation process generates the signals imaged at the detector of the receiving unit. The signal processing algorithms to calculate the LOS wind speed are described in the following chapter. An overview of the instrumental parameters (used during simulation) is shown in Table 3.3 (EADS-Astrium 2004, 2005b).

Table 3.3 Instrument parameters

Module	Parameter	Notation	Value
Laser	Pulse energy	E_L	70 mJ
	Pulse repetition frequency		50 Hz
	Wavelength	λ_L	355 nm
	Linewidth	$\Delta\lambda_{L\_FWHM}$	0.021 pm (50 MHz)
	Beam divergence		70 µrad
	Pulse length		20 ns
	Beam diameter		20 mm
Receiver optics	Transmit optics transmission	τ_T	0.4
	Receive optics transmission	τ_R	0.28
Fizeau interferometer	Filter peak transmission	T_{p_F}	0.449
	Pupil truncation ratio		$2/\pi$
	Filter FWHM	$\Delta\lambda_{FWHM}$	0.059 pm
	Filter USR	$\Delta\lambda_{USR}$	0.67 pm
	Filter FSR	$\Delta\lambda_{FSR}$	0.919 pm
Fabry-Perot interferometer	Filter peak transmission T_{p_A}	T_{p_A}	0.368
	Filter peak transmission T_{p_B}	T_{p_B}	0.272
	Filter $\Delta\lambda_{FWHM\_A}$	$\Delta\lambda_{FWHM\_A}$	0.74 pm
	Filter $\Delta\lambda_{FWHM\_B}$	$\Delta\lambda_{FWHM\_B}$	0.70 pm
	Filter spacing: $\Delta\lambda_{spac}$	$\Delta\lambda_{spac}$	2.65 pm
ACCD	Noise on Mie	N_{noise}	6e-/pix/50p
	Noise on Rayleigh	N_{noise}	6 e-/pix/50p
	Quantum efficiency	μ_{eff}	0.8

4 Signal processing and wind retrieval algorithms

This chapter introduces the signal processing algorithms which were developed and analysed, and which have been applied to determine the LOS wind speed from the Mie and Rayleigh signals. Various algorithms in respect to the Mie receiver signals are analysed and evaluated particularly concerning the resolution of the Mie ACCD. It is demonstrated that appropriate algorithms reduce the systematic LOS wind speed error of the Mie receiver to 0.05 m/s, using signals without any noise. The random error for a simulated airborne system due to photon noise and electronic noise of the ACCD is demonstrated to be larger than the systematic error.

An overview of the data processing structure is shown in Fig. 4.1. The signals provided by measurements are processed with the support of calibration data to obtain the LOS wind speed estimate. Signals also obtained from the simulator are used to validate the processing algorithms and to analyse and validate the signals of the measurements.

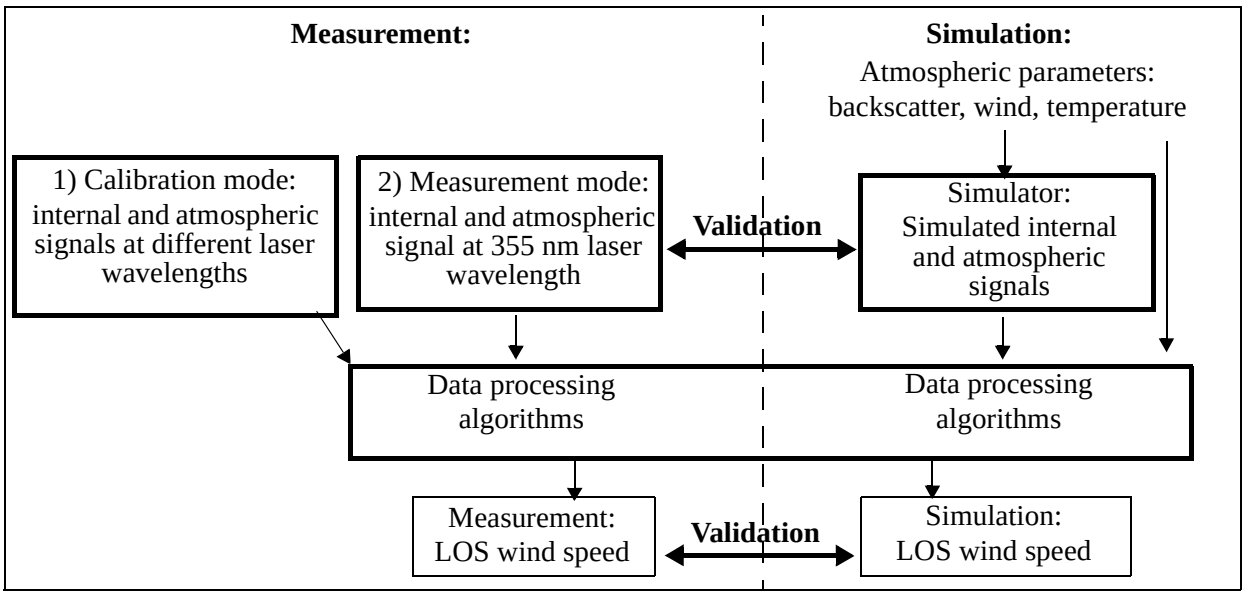

Fig. 4.1 The structure of the signal processing and the input parameters to retrieve the LOS wind speed from measurements and simulations.

The data processing to provide wind speed from measurements is divided into two parts (Fig. 4.1, left):

- The calibration mode is used to determine the receiver filter transmission curve (transfer function) and the instrument response functions (calibration curve) by measuring the internal reference signal[1] and the atmospheric signal for different frequencies. The atmospheric measurements are provided at zenith to minimize a potential Doppler shift component.
- The measurement mode provides data of an atmospheric measurement to determine the LOS wind speed and additionally the corresponding internal signal as a reference.

1. The internal reference is determined from a measurement, where the laser signal is directly sent towards both the receivers through a fibre (Fig. 2.13).

Each atmospheric measurement consists of a number of accumulated laser pulses *P* at the ACCD. The number of accumulated pulses is chosen to avoid saturation of the ACCD and to achieve the maximum possible intensity that will enable optimum signal-to-noise ratio. For wind speed calculations the number of *M* measurements are summed up to obtain one observation (*M***P*), including 700 laser pulses. Each measurement provides 25 range bins. The first atmospheric layers close to the instrument are affected by obscuration of the telescope, consequently one of these range bins is used to detect the internal laser reference signal, whilst the remaining range bins are used for atmospheric measurements. The width of the atmospheric range is defined by the integration time (exposure time) of the ACCD. The atmospheric background is determined before the transmission of the next laser pulse.

4.1 Mie receiver processing

4.1.1 Mie receiver response function

The line shape of the Fizeau interferometer is analysed and (if a useful signal maximum is detected) the energetic centroid of the signal (mean wavelength) is a measure of the wind velocity. Mean wavelength estimators were examined in detail for Doppler Radar[1] (Frehlich and Yadlowsky 1994), Doppler Sodar[2] (Reitebuch 1999 p. 50), and heterodyne Doppler lidar systems (Frehlich and Yadlowsky 1994). The receiver response function describes the correlation of the location of the energetic centroid of the signal line shape and the wavelength. Because the Fizeau interferometer has never been implemented for wind speed measurements prior to ALADIN, extensive investigations are necessary. Fig. 4.2 illustrates the modelled backscatter Mie signal, which is broadened by the filter transmission function. The filter transmission function corresponds to the shape of the signal imaged at the detector. The constant value of 10^6 electrons (at the edge of the spectrum, pixel number 0 and 15) arises from the photons of the Rayleigh backscatter spectrum.

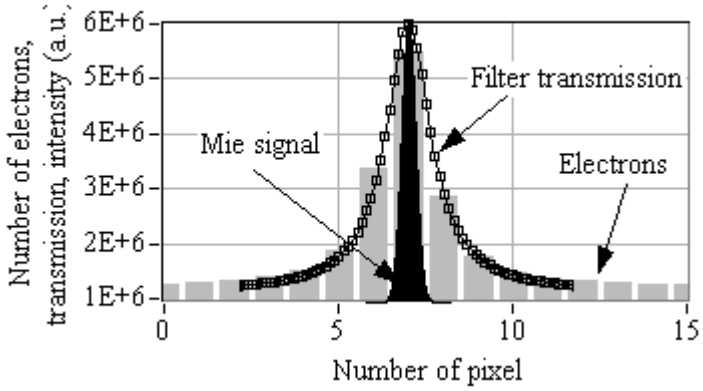

Fig. 4.2 Number of electrons detected by the ACCD (grey bars), the filter transmission (black dotted line), and the Mie signal intensity (black) versus pixel index.

1. Radar is an acronym for Radio Detection and Ranging.
2. Sodar is an acronym for Sound Detection and Ranging.

The measurement accuracy is expected to be better than 1 m/s corresponding to a Doppler shift of 0.0024 pm (ESA 1999 p. 93). To meet this, the incoming Mie spectrum (FWHM = 0.002 pm, corresponding to the laser FWHM) is broadened by the Fizeau interferometer to 0.06 pm (30 m/s). One pixel of the ACCD integrates the signal from a wavelength interval of 0.04 pm, corresponding to a LOS wind speed of 18.35 m/s. Various algorithms are examined to investigate the effect of the resolution of the ACCD on the systematic and random error.

4.1.2 Calibration mode

During calibration, the laser frequency changes in steps (31 MHz) over the wavelength interval of the wind speed measurement range (USR = 0.695 pm or 1.64 GHz) and results in the receiver response function which is essential for the LOS wind speed estimation from atmospheric measurements. At each wavelength step the ACCD accumulates 700 laser pulses.

The receiver response function $R_{M,C}(\lambda)$ for the internal laser signal is shown in Fig. 4.3. The mean sensitivity of the Mie receiver $\alpha_{M,C}$, from calibration, is the slope of the best straight line fit to the Mie response function. The generation of the Mie response function requires a mean wavelength estimator to be applied (Section 4.1.4). Accordingly the same algorithm has to be used during the atmospheric measurements to be consistent with the calibration data. The offset $\Delta\lambda_{off}$ to the zero wavelength is determined, and represents the intercept of the curve (see Fig. 4.3).

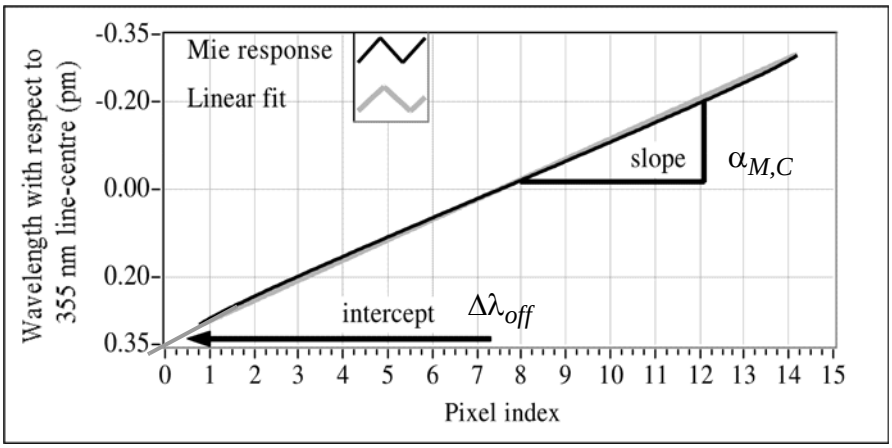

Fig. 4.3 The wavelength difference to a 355 nm source versus pixel index. The Mie response function (black line), the slope of the linear fit (grey), and the intercept are labelled, determining the sensitivity of the system in respect to the range of the USR.

The Mie receiver response function can be derived from:

$$R_{M,C}(\lambda) = \alpha_{M,C} * \lambda + \Delta\lambda_{off} + \Delta\lambda_{err\_M} \tag{4.1}$$

The linearity error $\Delta\lambda_{err\_M}$ is the difference between the measured response curve and the best straight line fit and depends on the type of mean wavelength estimator algorithm (Section 4.1.4). An example of the linearity error is illustrated in Fig. 4.4.

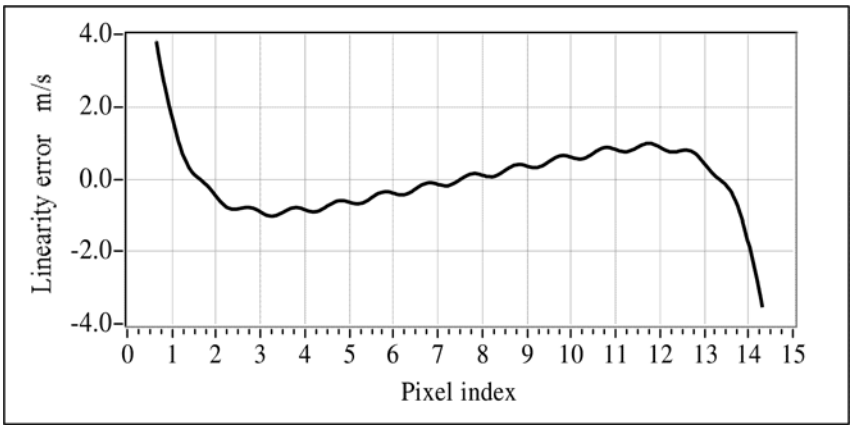

Fig. 4.4 An example of the wind speed linearity error versus pixel index.

4.1.3 Measurement mode

The intensities of the internal laser signal of the Mie receiver $I_{M,I}$ are detected within one range bin per measurement, are reduced by the detection chain offset *dco* described earlier. The atmospheric measurements $I_{M,A}$ are reduced by the *dco* and the background light. The background light I'_{bkg} is scaled to the exposure time t' of the background range bin and the integration time t of the atmospheric range bin after subtraction of the *dco*:

$$I_{bkg}(i) = \frac{t}{t'} \cdot (I'_{bkg}(i) - dco) \tag{4.2}$$

The measurements are summed up for one observation (700 laser pulses). A mean wavelength estimator (Section 4.1.4) is applied and results in one response value of the internal reference $r'_{M,I}$ (zero wind speed) and one response value of the measurement $r'_{M,A}$ per atmospheric layer. An overview of the processing procedure is shown in Fig. 4.5.

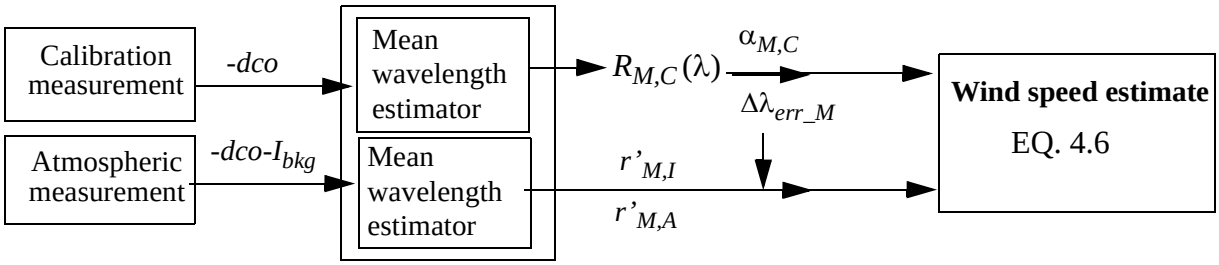

Fig. 4.5 An overview of the Mie signal processing procedure and the acronyms.

From EQ. 4.1, the internal wavelength value λ_I depending on the corresponding response value $r'_{M,I}$ can be determined by:

$$\lambda_I = \frac{r'_{M,I} - \Delta\lambda_{err\_M} - \Delta\lambda_{off}}{\alpha_{M,C}} \tag{4.3}$$

The atmospheric wavelength value λ_A depending on the corresponding response value $r'_{M,A}$ can be derived from:

$$\lambda_A = \frac{r'_{M,A} - \Delta\lambda_{err\_M} - \Delta\lambda_{off}}{\alpha_{M,A}} \tag{4.4}$$

where $\alpha_{M,A}$ is the slope of the atmospheric calibration. The Doppler shift is determined from the difference between the internal and the atmospheric wavelength value. The corresponding wavelength shift $\Delta\lambda_D$ is derived from:

$$\Delta\lambda_D = \frac{r'_{M,A} - \Delta\lambda_{err\_M} - \Delta\lambda_{off}}{\alpha_{M,A}} - \frac{r'_{M,I} - \Delta\lambda_{err\_M} - \Delta\lambda_{off}}{\alpha_{M,C}} \tag{4.5}$$

The slope of the atmospheric signal corresponds to the slope of the internal reference ($\alpha_{M,A} = \alpha_{M,C}$) because the line shape of the internal signal is comparable to the atmospheric Mie signal. Considering the factor $c/2\lambda_L$, the wind speed is estimated by:

$$v_{LOS} = \frac{c}{2\,\lambda_L} \cdot \frac{r'_{M,A} - r'_{M,I}}{\alpha_{M,C}} \tag{4.6}$$

Various mean wavelength estimators were analysed and evaluated for the modelled signals of AProS with the advantage, the true wind speed is known and the signals can be analysed with and without noise.

Most algorithms require the reduction of photons which do not arise from the Mie backscatter (Rayleigh backscatter, background light, *dco*). The previous processing step eliminates the background and *dco*, but not the Rayleigh backscatter at the Mie receiver. The pure Mie signal intensities from measurements are obtained by subtracting the minimum intensity value of all 16 pixels.

The algorithms of Section 4.1.4 are analysed with signals generated by AProS without any noise.

4.1.4 Mean wavelengths estimators

Centroid method:

The centroid method is a common algorithm, used to determine the centre of gravity (Bronstein and Semendjajew 1987 p. 218). The equation was proposed by Gagné et al. (1974) for spectral lines:

$$\lambda = \frac{\sum_{i=k}^{i=k+m} \lambda_i \cdot I_i}{\sum_{i=k}^{i=k+m} I_i} \tag{4.7}$$

where λ is the resulting wavelength of the centre of the centroid, *m* are the number of pixels around maximum intensity (typically 5 or 7), *k* is first pixel number to start centroid calculation, I_i is the intensity, and λ_i is the wavelength at the centre of pixel number *i*.

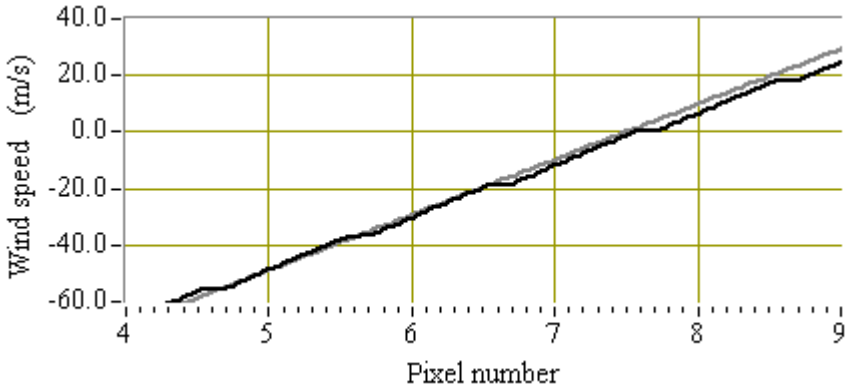

Fig. 4.6 The wind speed values versus pixel index: the response function (black line) compared to the true response function (grey), demonstrating the steps of the curve (an enlargement of Fig. 4.3, but indicated with wind speed values).

The resulting response function (Fig. 4.6) shows steps, which are caused by discretisation due to the 16 pixels of the ACCD (steplike signal shape). For the following, the wind speed is indicated instead of wavelength values, to point out the effect on the wind speed estimate. The true wind speed is the value expected from simulations. The wind speed systematic error (bias) between the response function of the true wind speed and the response function received from simulated signals are illustrated in Fig. 4.7.

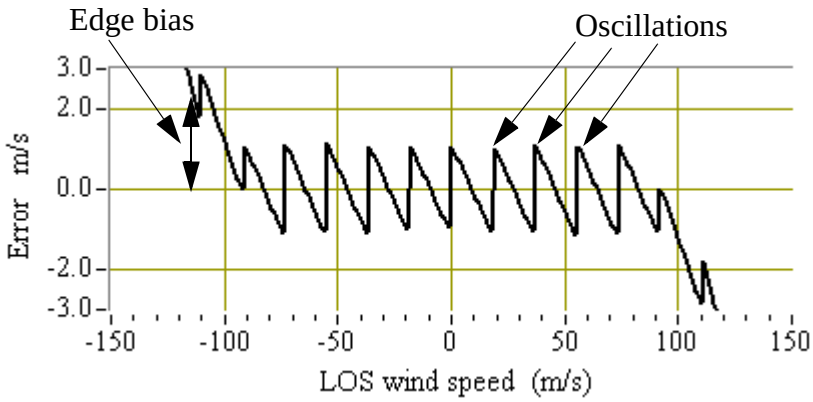

Fig. 4.7 The wind speed error versus the LOS wind speed. The algorithm implicates an error which is characterized by an edge bias and by oscillations.

For the estimation of higher wind speed values larger than 100 m/s, the systematic error increases rapidly caused by the limited range of the USR where the line shape of the signal is no longer fully imaged. This discrepancy depends on the wind speed and is called the edge bias. The other errors which are caused by discretisation are called oscillations. To illustrate the cause of the oscillations, three different signals are shown in Fig. 4.8. The symmetric signals, where the maximum is on both pixels (Fig. 4.8(a)) or only on one pixel (Fig. 4.8(c)), provides LOS wind

speed estimates with nearly no error. For asymmetric signals (Fig. 4.8(b)) however, the error is largest.

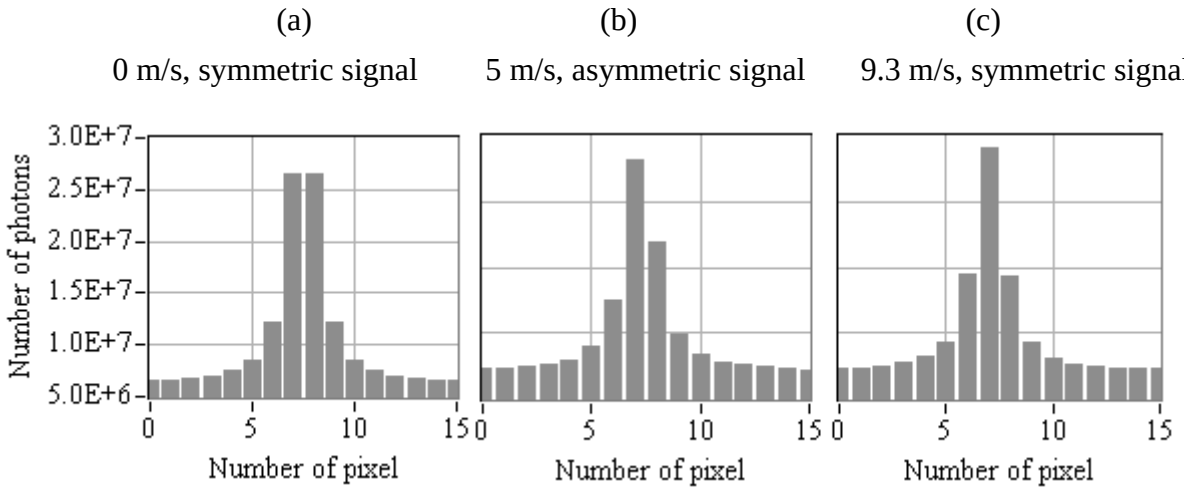

Fig. 4.8 Electrons on Mie receiver ACCD for wind speed values 0 m/s (a), 5 m/s (b), and 9.3 m/s (c) versus the pixel index.

The centroid method was analysed by using $m = 5$ and $m = 7$ pixels, and the results are shown in Fig. 4.9. The error resulting by the use of 7 pixels is slightly smaller than the error by the use of 5 pixels.

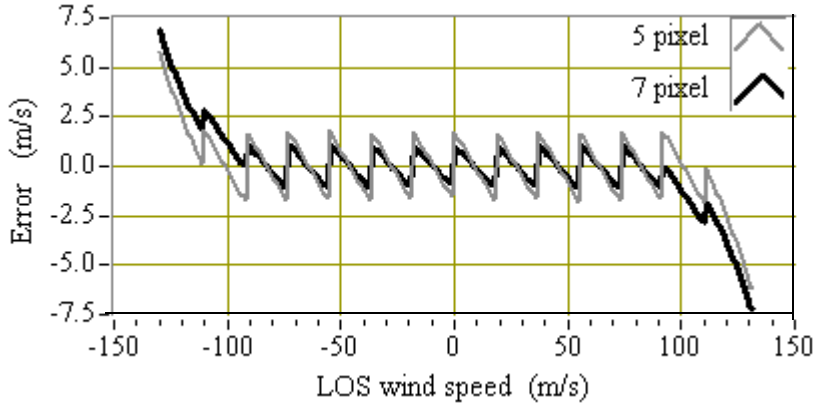

Fig. 4.9 The wind speed error versus the LOS wind speed of the measurement range of the centroid method in respect to 5 and 7 pixels.

The algorithm results in correct wind speed outputs where the signal at the detector is symmetric. The error of the oscillations is quite large (< 2 m/s). Both the errors are systematic errors and depend on the wind speed value.

Gaussian correlation algorithm

A correlation algorithm as proposed by EADS-Astrium (2005a p. 53), was applied to determine the location of the centroid. The signal at the detector is assumed to have a Gaussian line shape. The cross correlation algorithm determines the pixel index, where the correlation function has its maximum by setting the first derivative of the correlation algorithm to zero.

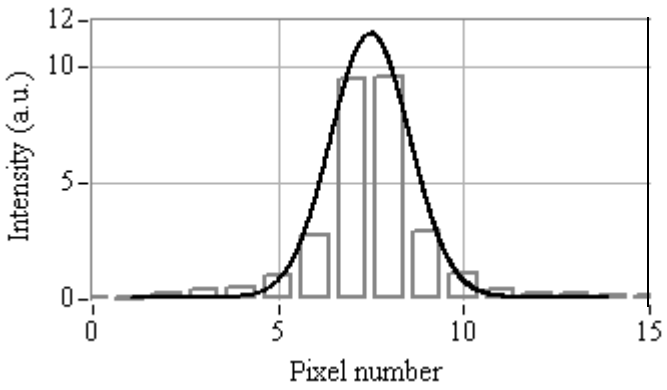

Fig. 4.10 The intensities of the signal at the ACCD (grey bars) versus pixel index compared to a modelled Gaussian line shape (black line).

The Gaussian function (EQ. 2.4) depends on the wavelength (λ) and the FWHM ($\Delta\lambda_{FWHM}$, EQ. 2.8) may be written as:

$$W(\lambda) = \frac{\sqrt{8ln2}}{\sqrt{2\pi} \cdot \Delta\lambda_{FWHM}} e^{-\frac{4ln2 \cdot \lambda^2}{\Delta\lambda^2_{FWHM}}} \tag{4.8}$$

The correlation function of the signals with intensity I_i and the Gaussian function $W(\lambda_i)$ at wavelength λ_i and index i, is given by:

$$C(\lambda_0) = \sum_{i=1}^{i_{max}} I_i \cdot W(\lambda_i - \lambda_0) \tag{4.9}$$

where i_{max} is the maximum index used for calculation and λ_0 is the centre wavelength. To determine the maximum, the first derivative of the correlation function is assumed to be zero:

$$C'(\lambda_0) = \sum_{i=1}^{i_{max}} I_i \cdot W'(\lambda_i - \lambda_0) = 0 \tag{4.10}$$

An equation depending on the parameter λ_0 is obtained by calculating the derivative and resolving the equation to λ_0. This leads to an iterative algorithm to determine the centre wavelength by setting the value of λ_0 in the equation to λ_n and an increase for each iteration step leads to the wavelength value λ_{n+1}. The iterative algorithm is written as:

$$\lambda_{n+1} = \frac{\sum_{i=1}^{i_{max}} I_i \cdot \lambda_i \cdot W(\lambda_i - \lambda_n)}{\sum_{i=1}^{i_{max}} I_i \cdot W(\lambda_i - \lambda_n)} \tag{4.11}$$

An assumption is needed for the unknown parameter $\Delta\lambda_{FWHM}$ of the Gaussian function, which is approximately determined by FWHM of the Mie signal at the detector. The width of the signal depends on the Fizeau interferometer filter width. The results of two different FWHM input parameters lead to different systematic errors as illustrated in Fig. 4.11. The error due to a FWHM input value of 0.059 pm (which is the actual width of the Fizeau filter) is characterized by relevant oscillations. The edge bias increases for higher values of the FWHM but leads to a decreased error in respect to the oscillations.

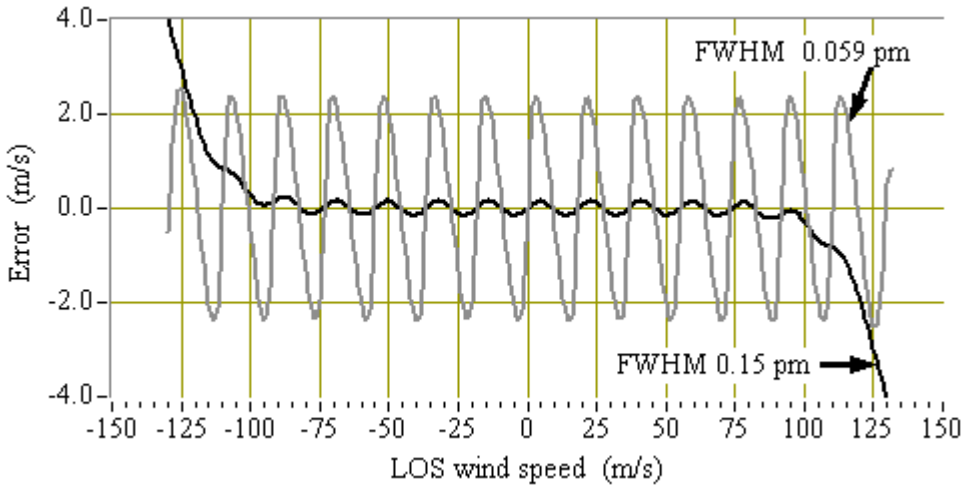

Fig. 4.11 The wind speed error depending on the LOS wind speed. The difference of the true and estimated wind speed for a FWHM input value of 0.059 pm (grey line) and 0.2 pm (black line).

The error of the amplitude of the oscillations depends on the choice of the FWHM input value and is shown in Fig. 4.12 (left) in respect to a wind speed of 4 m/s. The error shows a minimum for a FWHM of 0.3 pm. The figure on the right illustrates a decrease in oscillations for larger values of the FWHM input value, but an increase of the edge bias.

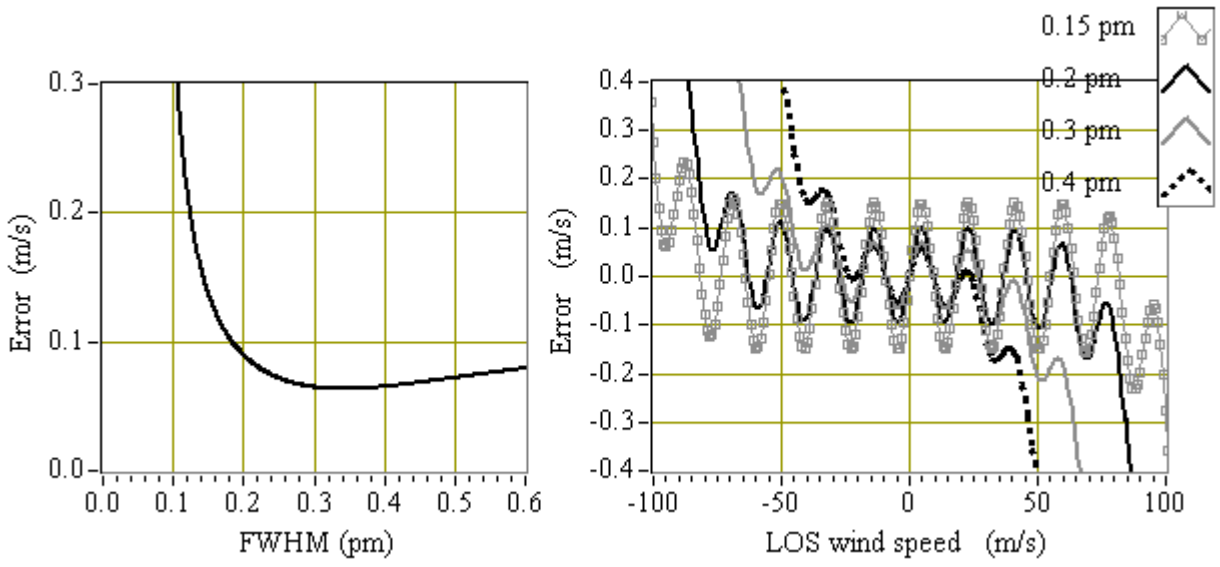

Fig. 4.12 The error of the maximum oscillation depends on a change in the FWHM input value at a LOS wind speed of 4 m/s (left). The error of the LOS wind speed depends on the value of the FWHM (right).

A modelled signal of Lorentzian lineshape discretised to 160 pixels is illustrated in Fig. 4.13, to demonstrate the discretisation error. Using a filter FWHM input value of 0.059 pm to calculate the Gaussian curve (black line), signal information is lost at the wings of the Lorentzian shaped signal

and the discretisation error increase. By spreading the Gaussian curves across the USR (black and grey dotted line), only less or no signal information is lost because the Gaussian curve covers the signal shape.

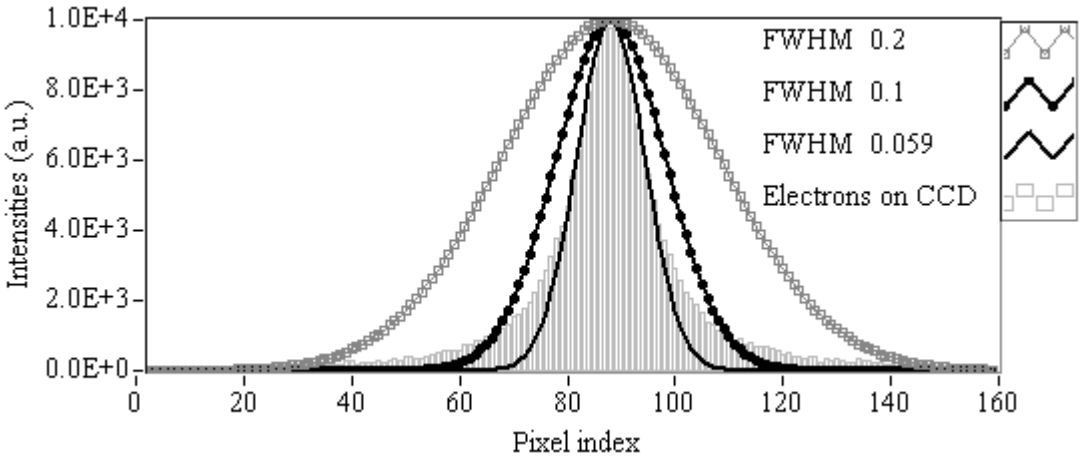

Fig. 4.13 The intensities of signals versus pixel index. Three Gaussian line shapes are illustrated, depending on different FWHM input values to be compared to the signal electrons at the ACCD.

Further investigations were done to reduce the oscillations by increasing the number of points of the Gaussian curve. The Gaussian curve may be calculated for 16 points (16 pixel) of for a larger number of points (e.g. 160). Taking an increased number of points into account, the intensity value per pixel can be calculated by: i) the mean intensity value of the Gaussian curve and ii) the integration of the Gaussian curve over one pixel, which results in another output as the calculation of the mean value. For the following, each pixel is supposed to have 10 data points and the results are illustrated in Fig. 4.14. It is shown that the error of the oscillations is reduced in respect to a FWHM input value of 0.059 pm, but for increased FWHM input values (0.1, 0.2 pm), the differences are negligible (not shown).

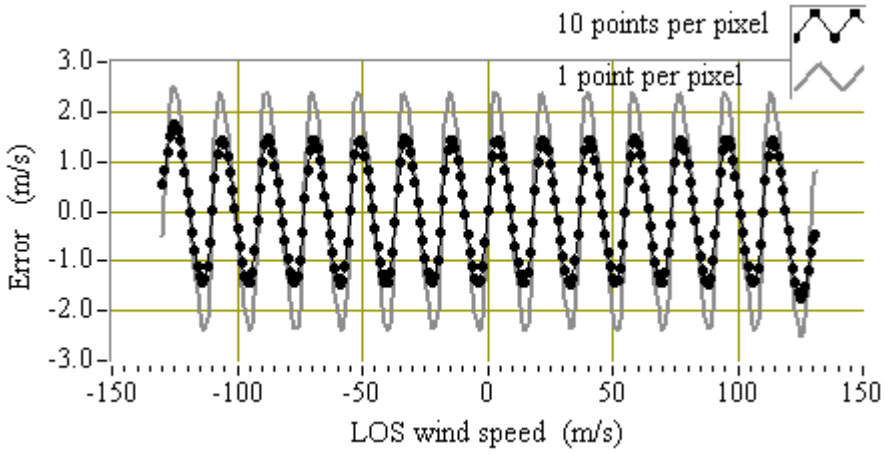

Fig. 4.14 The systematic error depending on the LOS wind speed for a Gaussian curve referring to 1 or 10 points per pixel and an algorithm FWHM input value of 0.059 pm.

Concluding, the type of the oscillations is comparable to the centroid method but smaller in amplitude (Table 4.1). For a larger FWHM input value the oscillations decrease, but the edge bias and a slope error increase and the sensitivity decreases. The oscillations are smaller than 0.1 m/s for a careful selection of the FWHM input value. The edge bias increases (FWHM 0.2 pm) for wind speed values which are larger than +/-50 m/s.

Maximum likelihood function

If $N_{Fiz}(i)$ are the detected electrons at the receiver at pixel index i and $N_i(\lambda)$ is a supposed intensity distribution for wavelengths in respect to the pixel index, a probability density function for $N_i(\lambda)$ gives the likelihood Λ of detecting $N_{Fiz}(i)$. The method of maximum likelihood finds the maximum of Λ as a function of $N_i(\lambda)$. The algorithm was described by Helstrom (1968 p. 262) and Van Trees (1968 p. 65). Applications for heterodyne lidar systems were implemented by Frehlich and Yadlowsky (1994 and 1999), and Smalikho (2003).

The intensity distribution is supposed to be Lorentzian. The density distribution is supposed to be Lorentzian and is described by a probability density function (likelihood function). The Lorentzian function is described by (adapted from Measures 1992 p. 96):

$$L(\Delta\lambda_D) = \frac{1}{\pi}\frac{2}{\Delta\lambda_{FWHM}}\left(4\frac{\Delta\lambda_D{}^2}{\Delta\lambda^2{}_{FWHM}}+1\right)^{-1} \tag{4.12}$$

$\Delta\lambda_{FWHM}$ is the scale parameter specifying the FWHM of the signal. The number of electrons at the detector arises from $N_e(\lambda) = n_s * L(\Delta\lambda_D)$, where n_s is the number of all electrons at the ACCD for a Lorentzian function. Taking the total number of electrons of the background N_{bkg} into account, the distribution of the electrons may be expressed as:

$$N_e(\Delta\lambda_D) = n_s\frac{2}{\pi}\frac{1}{\Delta\lambda_{FWHM}}\left(4\frac{\Delta\lambda_D{}^2}{\Delta\lambda^2{}_{FWHM}}+1\right)^{-1} + \frac{N_{bkg}}{\Delta\lambda_{USR}} \tag{4.13}$$

where $\Delta\lambda_D$ is the Doppler shift.

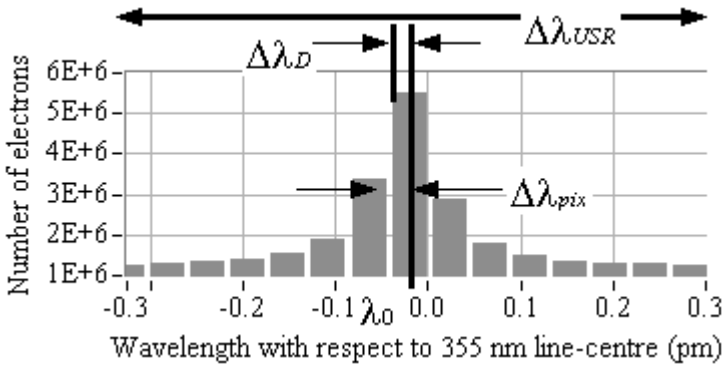

Fig. 4.15 A figure with the notations used during the calculations. The number of electrons versus pixel index $\Delta\lambda_{USR}$, the centre of the wavelength range λ_0, the Doppler shift $\Delta\lambda_D$, and the width of one pixel $\Delta\lambda_{pix}$ are illustrated.

The mean number of electrons of pixel i ($i = 0, 1, 2, \ldots, 15$) is calculated by:

$$N_i = \int_a^b N_e(\Delta\lambda_D) d\Delta\lambda_D \tag{4.14}$$

where $\Delta\lambda_{pix}$ is the width of one pixel calculated by $\Delta\lambda_{USR} / 16$.

The lower limit is defined by $a = i \cdot \Delta\lambda_{pix} - \Delta\lambda_D - \Delta\lambda_{USR}/2$ and the upper limit may be written as: $b = (i + 1) \cdot \Delta\lambda_{pix} - \Delta\lambda_D - \Delta\lambda_{USR}/2$.

Solving the integral analytically one obtains the number of photons per pixel index i (to keep the equations more compact, $N_i(\lambda)$ is indicated as N_i and $N_{Fiz}(i)$ is indicated as N_{Fiz}):

$$N_i = \frac{n_s}{\pi} \left[arctan\left(\frac{2}{\Delta\lambda_{FWHM}} b \right) - arctan\left(\frac{2}{\Delta\lambda_{FWHM}} a \right) \right] + \frac{N_{bkg}}{16} \tag{4.15}$$

Rearranging the term, the equation results in:

$$N_i = \frac{n_s}{\pi} arctan\left(\frac{(2\Delta\lambda_{pix})/\Delta\lambda_{FWHM}}{1 + \frac{4}{\Delta\lambda^2_{FWHM}} \cdot a \cdot b} \right) + \frac{N_{bkg}}{16} \tag{4.16}$$

n_s and $\Delta\lambda_D$ are the unknown parameters in this equation. This intensity distribution will be used for the maximum likelihood function.

The maximum likelihood function Λ is described by the probability density function p (Bronstein and Semendjajew 1987 p. 663) for the intensity distribution N_i from EQ. 4.16:

$$\Lambda(\Delta\lambda_D, n_s) = \prod_i p(N_i) \tag{4.17}$$

The probability p to measure N_{Fiz} electrons in pixel number i is Poisson distributed and depends on the theoretically mean number of signal electrons N_i and number of measured signal electrons at the Mie ACCD N_{Fiz}:

$$p(N_i) = \frac{N_i^{N_{Fiz}}}{N_{Fiz}!} e^{-N_i} \tag{4.18}$$

To simplify the following calculations, a logarithmic calculus is applied:

$$\Lambda_{ln}(\Delta\lambda_D, n_s) = ln\left(\prod_i p(N_i) \right) = \sum_{i=0}^{15} ln(p(N_i)) \tag{4.19}$$

The value of $\Delta\lambda_D$ may be determined where the function takes its maximum. Using EQ. 4.18, one obtains:

$$\Lambda_{ln}(\Delta\lambda_D, n_s) = \sum_{i=0}^{15} ln\left[\frac{N_i^{N_{Fiz}}}{N_{Fiz}!} e^{-N_i} \right] \tag{4.20}$$

and:

$$\Lambda_{ln}(\Delta\lambda_D, n_s) = \sum_{i=0}^{15} N_{Fiz} \cdot lnN_i - \sum_{i=0}^{15} ln(N_{Fiz}!) - \sum_{i=0}^{15} (N_i) \tag{4.21}$$

The second term includes the measured intensities at the detector and is a constant value represented by *C*. The third term is the signal intensity n_S.

$$\Lambda_{ln}(\Delta\lambda_D, n_s) = \sum_{i=0}^{15} N_{Fiz} \cdot lnN_i - C - n_S \tag{4.22}$$

Combined with EQ. 4.16, the function is written as:

$$\Lambda_{ln}(\Delta\lambda_D, n_s) = \sum_{i=0}^{15} N_{Fiz} \cdot ln\left[\frac{n_S}{\pi} arctan\left(\frac{(2\Delta\lambda_{pix})/\Delta\lambda_{FWHM}}{1 + \frac{4}{\Delta\lambda^2_{FWHM}} \cdot b \cdot a}\right) + \frac{N_{bkg}}{16}\right] - C - n_S \tag{4.23}$$

No analytical solution exists for this equation and an iterative approximate maximisation process is required. The unknown parameter $\Delta\lambda_D$ is replaced by $\Delta\lambda_{pix}$ ($\xi - 0.5\ \Delta\lambda_{USR}$), where ξ is the step width of the algorithm (typically 0.0024 pm, respectively 1 m/s). Now the maximum likelihood function is calculated for each point of the USR and the maximum of the function gives the resulting wind speed estimate (Fig. 4.16).

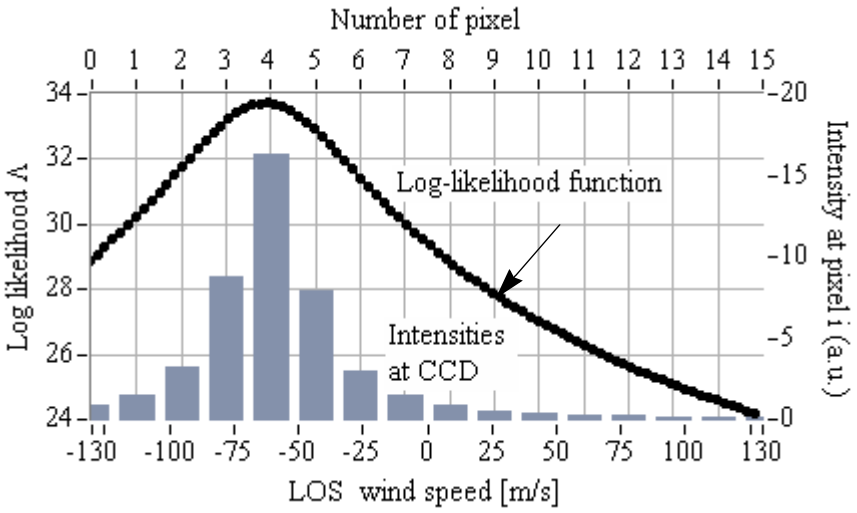

Fig. 4.16 The maximum likelihood (black dotted line) and the intensities at the pixels of the ACCD (grey bars) depending on the LOS wind speed and the pixel index.

The results of the algorithm (Fig. 4.17) show an edge bias increasing for wind speed values larger than 50 m/s. The oscillations are smaller than 0.15 m/s and in comparison to the Gauss correlation algorithm, the slope error is slightly increased (right plot in Fig. 4.17).

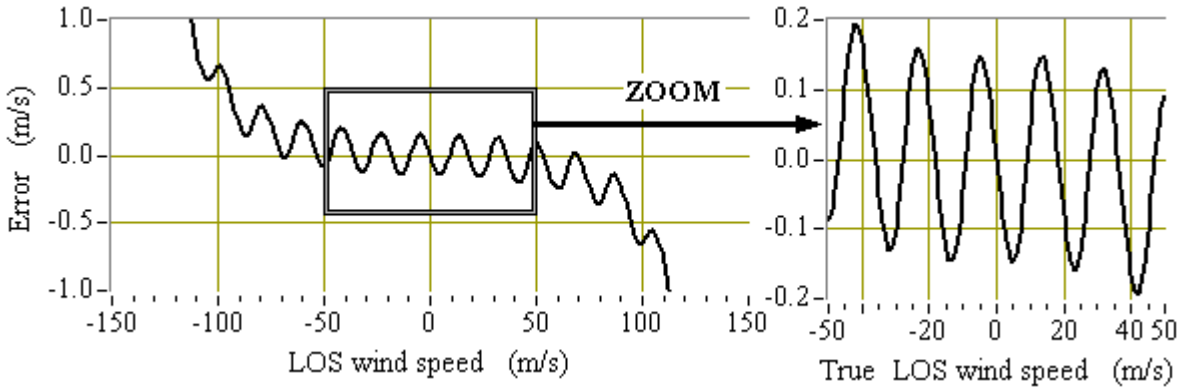

Fig. 4.17 The LOS wind speed error in respect to the LOS wind speed. The difference between the true and the estimated wind speed (left) and an enlargement of the left figure demonstrates a slight slope (right).

Downhill simplex method

The downhill simplex method was presented by Nelder and Mead (1965). The algorithm consists of determining the minimum (respectively maximum) of a function of more than one independent variable with the help of simple geometrical bodies (simplex). The simplex size is multidimensional and the method attempts to enclose the minimum inside the simplex. The simplest body with $n + 1$ corners within an n-dimensional geometry is a triangle ($n = 2$). For each calculation step, the corners are analysed and the worst one is replaced by another. The difference to other algorithms is, that it does not use derivatives, asserting safer convergence. The downhill simplex method was implemented as described in detail in Press et al. (1988 p. 304).

For the signals at the Mie receiver, the lineshape function is assumed to be Lorentzian (EQ. 4.12). The parameters which vary during the calculation are the FWHM (a_1) and the position of the maximum (a_2), which indicates the Doppler shift. The algorithm starts with user defined values for a_1 and a_2, and after each iteration step of the algorithm, the previous start parameters are varied (Δa) and combined with the others. There are three combination possibilities (a_1, a_2; $a_1 + \Delta a$, a_2; a_1, $a_2 + \Delta a$). The three Lorentzian functions are generated for each set of values. An iteration algorithm was developed and the Lorentzian curve is determined by (EQ. 4.12):

$$L(\Delta\lambda) = A\left(4\,\frac{(\Delta\lambda - a_2)^2}{a_1^2} + 1\right)^{-1} \tag{4.24}$$

where A is the amplitude determined by the maximal intensity at the Mie ACCD. Each pixel is represented by ten points and the Lorentzian function is generated for 160 wavelength steps ($\Delta\lambda$). A number of performance tests demonstrated this step width to be the optimum. The squares of the differences between the generated Lorentzian curve and the signal at the ACCD are determined and summed up. The three resulting values represent the corners of the simplex ($n = 2$). The corners of the algorithm are compared for different values of Δa and the worst ones are replaced. If a threshold for the difference is reached, the best parameter for the Lorentzian

curve is reached. This algorithm is used to determine the position of the signal maximum at the Mie receiver and the FWHM of the signal. The error between the true and the estimated wind speed is shown in Fig. 4.18 referring to a start value of the FWHM of 0.1 pm.

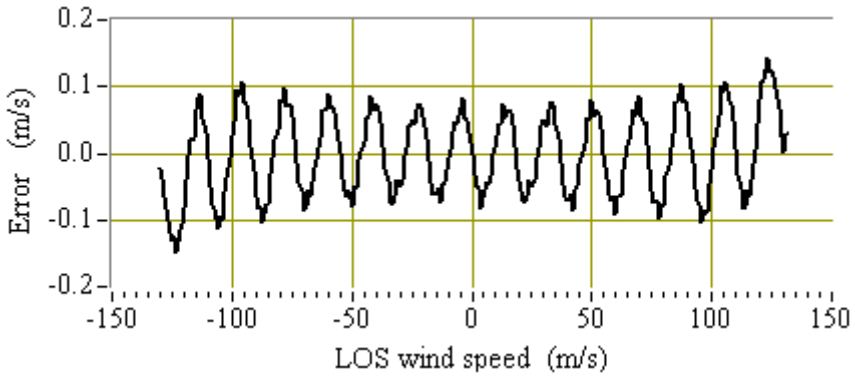

Fig. 4.18 The error between the true and the estimated LOS wind speed for a FWHM start value of 0.1 pm.

The downhill simplex algorithm seems to be sensitive to the FWHM start parameters. The different wind speed errors for the FWHM of 0.059 pm and 0.1 pm are shown in the following figure.

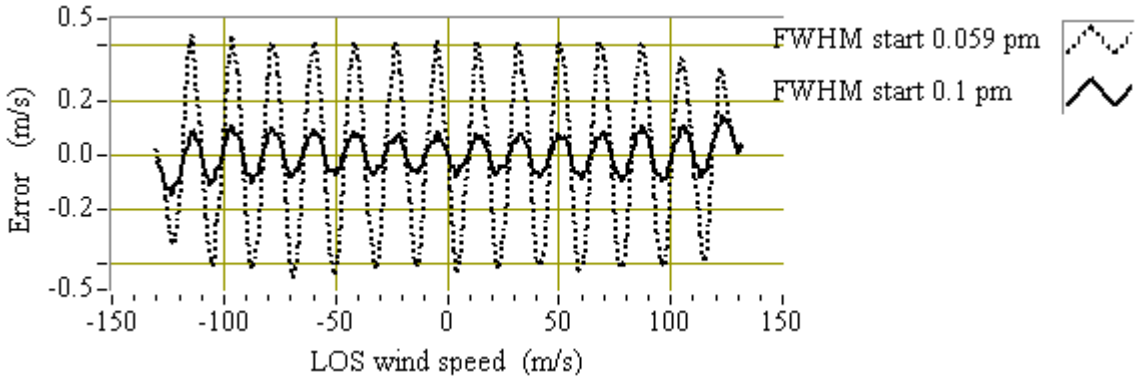

Fig. 4.19 The error between the true and the estimated wind speed for the measurement LOS wind speed range due to different FWHM start parameters (0.059 pm and 0.1 pm).

The oscillations (Fig. 4.18) are smaller than 0.1 m/s for a regardful selection of the FWHM. Compared to the other algorithms, the downhill simplex method induces no edge bias and no slope error.

Comparison of Mie receiver algorithms

Four algorithms were analysed and a comparison of the difference between the true and the estimated wind speed in respect to the different algorithms is illustrated in Fig. 4.20.

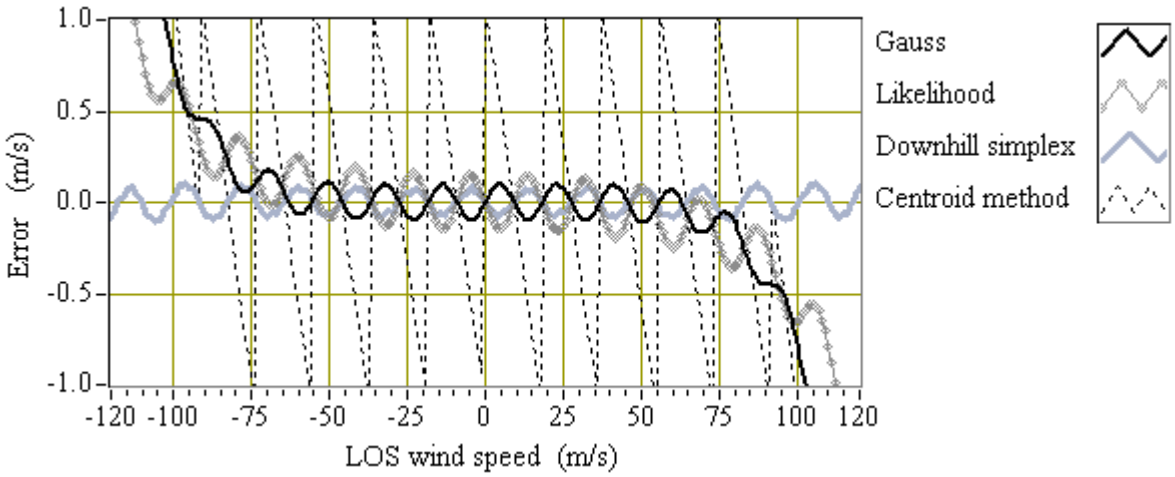

Fig. 4.20 The difference between the true wind speed and the wind speed estimate versus the LOS wind speed, received from the Gauss correlation (FWHM input value 0.2 pm), the maximum likelihood (FWHM start value 0.1 pm), the downhill simplex (FWHM start value 0.1 pm), and the centroid algorithm.

The slope error decreases the sensitivity of the system. The oscillations point out a decreased and increased sensitivity depending on the slope of the steps of the response function. The errors of the oscillations are shown in Table 4.1. The smallest error of the oscillations is provided by the downhill simplex algorithm (start FWHM 0.1 pm) and the Gauss correlation method (FWHM input value 0.2 pm) where the error is smaller than 0.1 m/s. The smallest the edge bias is provided by the downhill simplex algorithm. The systematic error of the centroid method is larger by a factor of 5 in respect to the other algorithms and is not be taken into account for further investigations.

4.1.5 Mie receiver performance results

During calibration measurements, the slope $\alpha_{M,C}$, the intercept $\Delta\lambda_{off}$, and the linearity error $\Delta\lambda_{err\_M}$ (EQ. 4.1) are obtained. The measurements are corrected by the linearity error (EQ. 4.1) and the systematic error (oscillations, slope, and edge bias) should be eliminated. Investigations are performed to analyse the linearity error and the residual error, which is the error remaining after correction of the measurements by the linearity error. Both are demonstrated in Fig. 4.21. The calculation was performed for a wind speed range of +/-130 m/s and the Gauss correlation algorithm in respect to different FWHM input values.

For a FWHM input value of 0.059 pm the linearity error is 2.5 m/s and the residual error is reduced after calibration to 0.4 m/s. For FWHM input values of 0.1 pm and 0.2 pm, the residual error is below 0.05 pm. For the larger FWHM input values another effect arises. There is a weak modulation of the linearity error curve (a shape like a sinus across the complete range). This

results from an effect of the response function having a steeper slope in the centre, then the slope decrease and nearly become zero to the border of the USR. For a larger FWHM, the modulation increase, because the Gaussian modelled shape loose information due to the fact, the wings of the modelled curve are out of the USR.

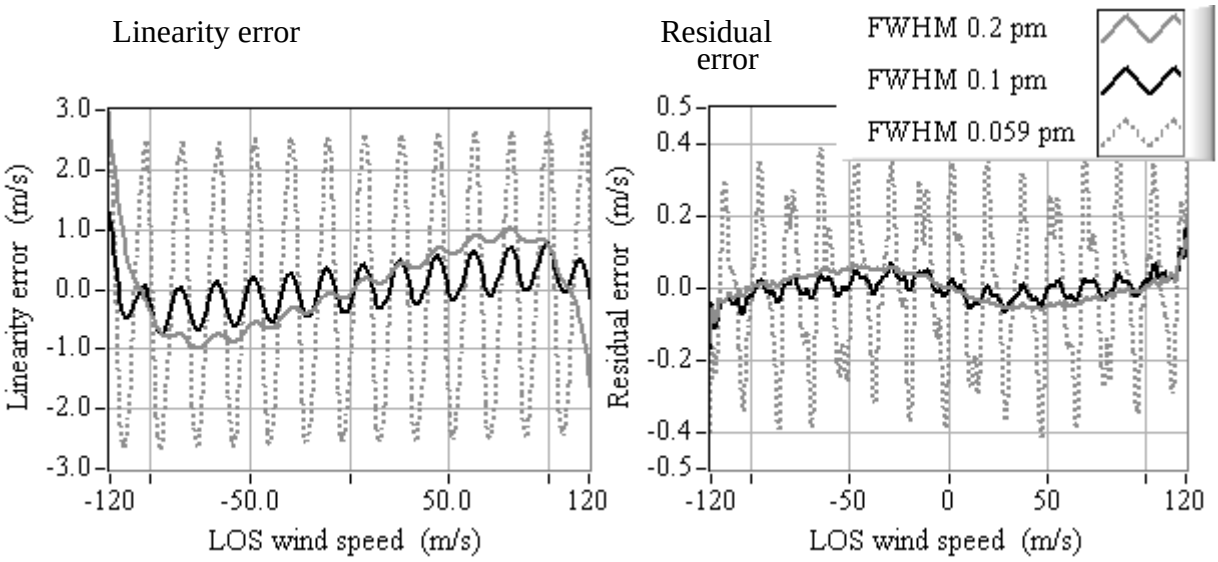

Fig. 4.21 The output of the calibration is the linearity error (left) and the residual error after correction by the linearity error (right) in respect to the LOS wind speed. The differences of the curves arise from the different FWHM input values of the Gauss correlation algorithm (0.2 pm, 0.1 pm, and 0.059 pm)

The right illustration in Fig. 4.21 shows small fluctuations in the curves (smaller than the oscillations). This effect arises after correction by the linearity error and is reproducible (a systematic error). The linearity and residual error of the Gaussian algorithm are demonstrated in the following figure Fig. 4.22.

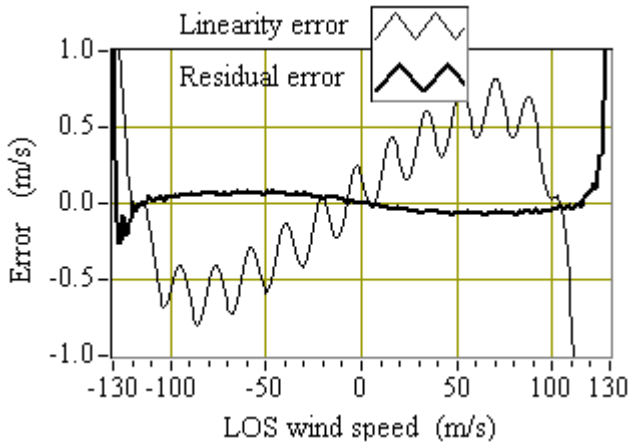

Fig. 4.22 The linearity and residual error depending on the LOS wind speed for the Gauss correlation algorithm (FWHM input value 0.2 pm).

The results of the linearity and residual error of the maximum likelihood and the downhill simplex algorithm are shown in Fig. 4.23.

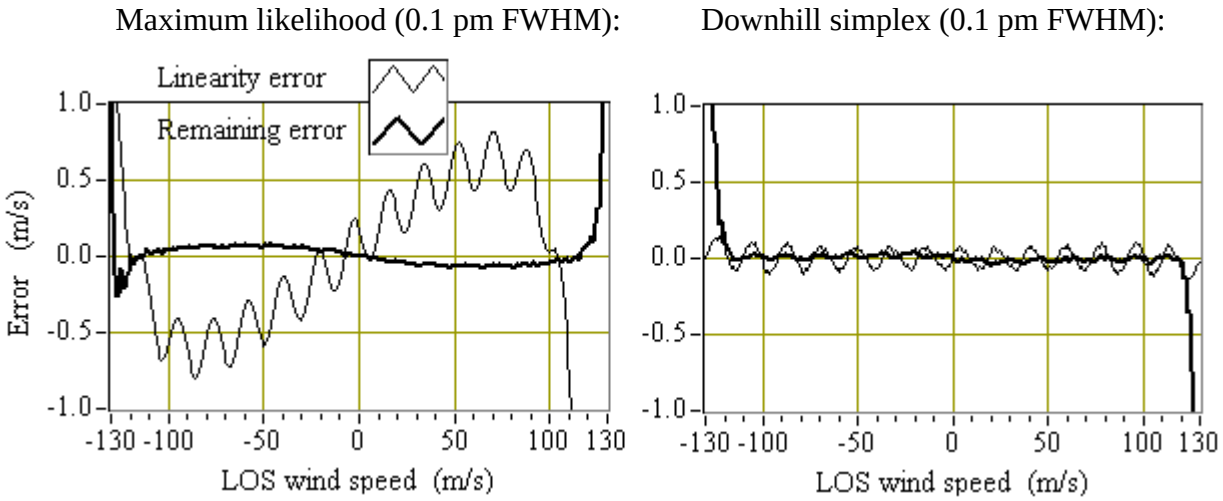

Fig. 4.23 The errors of the maximum likelihood algorithm (left) and the downhill simplex systematic errors (right) in respect to the LOS wind speed (FWHM input parameter 0.1 pm). The thin curve shows the linearity error and the fat curve represents the residual error.

The oscillations, the edge bias, and the slope error after corrections by the linearity error are reduced after applying the maximum likelihood method, but a modulation smaller than 0.1 m/s is induced. The oscillations of the downhill simplex are also reduced and only a very weak modulation is induced (<0.05 m/s).

The residual errors are illustrated in Fig. 4.24 for the Gauss correlation algorithm, the maximum likelihood, and the downhill simplex method. The residual oscillations and modulations are comparable in magnitude and shape of all algorithms. The fluctuations within the oscillations are systematic and they are reproducible.

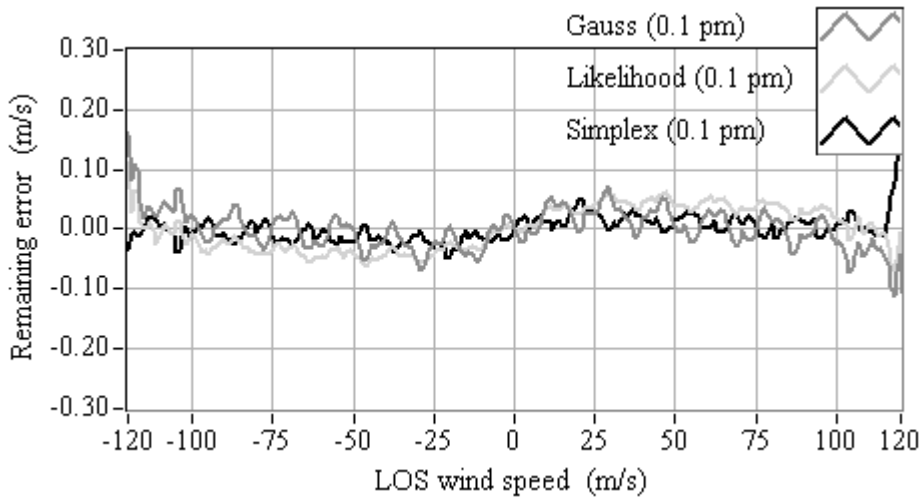

Fig. 4.24 The residual error depending on the LOS wind speed of different algorithms. The Gauss correlation algorithm, the maximum likelihood, and the downhill simplex are applied for a FWHM of 0.1 pm.

Random error:

The investigations to the systematic error were performed without photon and electronic noise of the ACCD. To study the random error of the algorithms, noise is included. Fig. 4.25 shows the results for the Gauss correlation algorithm with a FWHM input value of 0.2 pm. The modelled signals during this analysis are comparable to signals of the boundary layer in respect to 70 mJ laser energy for a ground system where 700 pulses are accumulated. Compared to Fig. 4.21, the error shows random fluctuations, but the systematic oscillations are still visible.

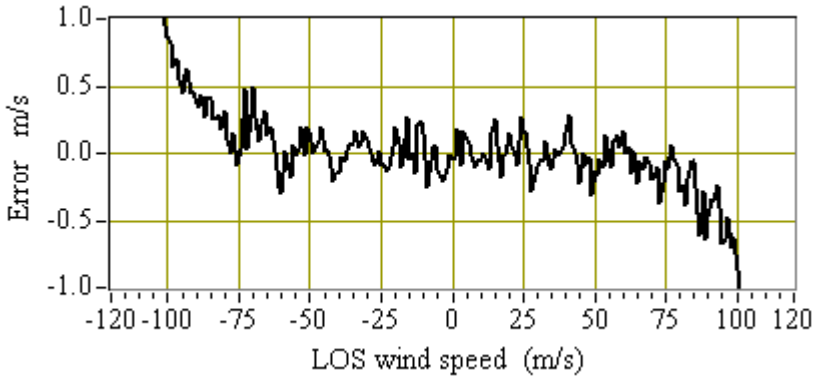

Fig. 4.25 The error between the true and the estimated wind speed including noise for the Gauss correlation algorithm (0.2 pm FWHM input value) versus the LOS wind speed.

To demonstrate how much the results are affected by the noise, a simulation was provided for an airborne system at 12 km flight altitude, the signal was taken from a range at 0.5 altitude, and 70 mJ laser energy and instrument parameters in Table 3.3. The results of the residual error are demonstrated in Fig. 4.26 for the three different algorithms.

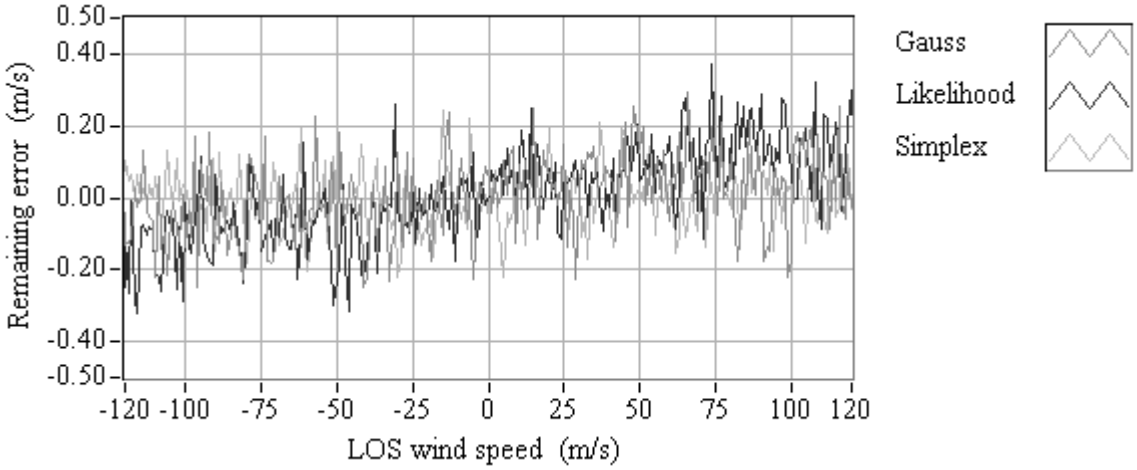

Fig. 4.26 The residual error with noise effects depending on the LOS wind speed for the Gauss correlation algorithm (FWHM input value 0.2 pm), the maximum likelihood (FWHM input value 0.1 pm) and the downhill simplex method (FWHM input value 0.1 pm).

Because of the small residual error, the effects of noise cover the remaining oscillations. However, the random error (> 0.1 m/s) overlaps the systematic error (< 0.1 m/s).

In the following, the random error of the wind speed estimate depending on altitude (affecting the signal-to-noise ratio) was analysed. The result is demonstrated in Fig. 4.27 (left) in respect to the corresponding backscatter ratio (right, Section 2.1.5) of the median aerosol model. A good signal-to-noise ratio is obtained in the boundary layer up to 2 km where the signal intensity is about 2 times stronger than the noise. The standard deviation of the centroid method is larger than 1 m/s and not illustrated in Fig. 4.27.

The Gauss correlation algorithm for a FWHM input value of 0.059 provides the largest random error, which is definitely reduced by a calculation with 10 points per pixel. The Gauss correlation algorithm due to a FWHM input value of 0.2 pm is as good as the maximum likelihood (FWHM start value 0.1 pm). For the case, the signal quality decrease (with altitude), the maximum likelihood is a little bit better. The downhill simplex method results in the smallest random error values and the error increases more slowly with decreased signal-to-noise ratio. An overview of the results of the algorithms is shown in Table 4.1.

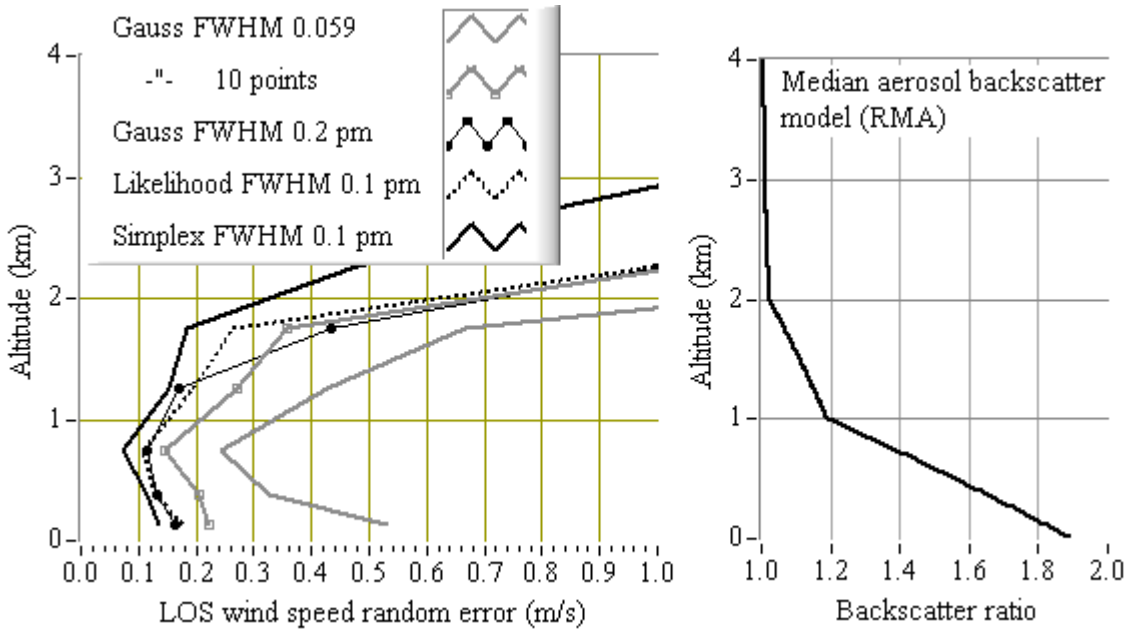

Fig. 4.27 The different LOS wind speed random errors (standard deviation) depending on altitude (left) in respect to the Gauss correlation algorithm with 0.059 pm and 0.2 pm FWHM input values (due to 1 point and 10 points per pixel calculation), the maximum likelihood algorithm with 0.1 pm FWHM input value, and the downhill simplex method with 0.1 pm FWHM input value (the last two ones calculated with 1 point per pixel). The corresponding backscatter ratio depending on altitude is illustrated in respect to the median aerosol model (right).

Table 4.1 Systematic and random errors of the Mie algorithms

Algorithm	Systematic error of oscillations (m/s)	Residual error (m/s)	Random error at 1km altitude (m/s)
Centroid method (7 pixels)	< ± 1.0	not calculated	> 1.0
Gauss correlation (FWHM 0.059 pm)	< ± 2.5	< 0.4	0.34
Gauss correlation (FWHM 0.059 pm, 10 points per pixel)	< ± 1.5	< 0.3	0.20
Gauss correlation (FWHM 0.2 pm)	< ± 0.1	< 0.1	0.14
Maximum likelihood	< ± 0.15	< 0.1	0.15
Downhill simplex	< ± 0.1	< 0.05	0.11

Number of pixels

The dependency of the oscillations with respect to the number of pixels was studied. For an increased number of pixels the error is significantly reduced as illustrated in Fig. 4.28.

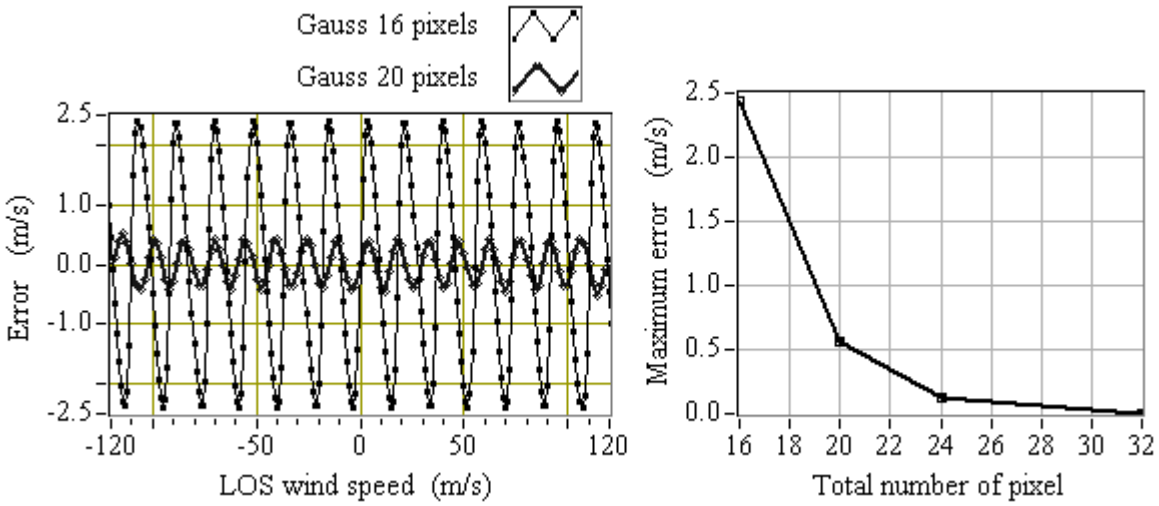

Fig. 4.28 The systematic error of the Gauss correlation algorithm for a FWHM input value of 0.059 pm for 16 and 20 pixels in respect to the LOS wind speed (left) and the maximum error of the oscillation depending on the number of pixels at the ACCD (right) due to the Gauss correlation algorithm and a FWHM input value of 0.059 pm.

The results of Fig. 4.28 arise from the Gauss correlation algorithm and 0.059 pm FWHM input value at 4 m/s wind speed. This wind speed value was chosen because it shows a maximum in the oscillations. An increased number of pixels at the ACCD will reduce the error between the true wind speed and the wind speed estimate significantly. Taking 20 pixels into account, the

systematic error of the Gauss correlation algorithm is reduced from 2.5 m/s to 0.5 m/s and the algorithm applied for an ACCD with 24 pixels results in a systematic error smaller than 0.1 m/s. Besides it should not be ignored that an increased number of pixels leads to lower signal per pixel and an increased noise effect. This may only slightly affect the signals of the measurements on ground but the satellite measurements with a low number of backscatter photons.

Summary

It was shown that the systematic error of the oscillations can be reduced to values smaller than 0.1 m/s and that the residual error after calibration is smaller than 0.05 m/s. All values of Table 4.1 are only achieved from signals without any noise. The differences of the Gauss correlation algorithm in respect to the different FWHM values arise from the filter Lorentzian function which does not exactly correspond to the modelled Gaussian function. Additionally it was demonstrated that an increase of pixel numbers at the ACCD to 20 pixels reduces the error of the oscillations by a factor of 5. The random error from the Gauss correlation (FWHM 0.2 pm), the downhill simplex, and the likelihood algorithm is smaller than 0.15 m/s, which arises from intensities at the detector, where the signal is at least 2 times stronger than the noise or background. However, the random error overlaps the systematic error.

4.2 Rayleigh processing

It was shown in Section 2.6.7 that the transmitted signal through filter *A* is detected by the first 8 pixels by the CCD, whilst the remaining 8 pixels detect the transmitted signal through filter *B*. The background intensity I'_{bkg} is determined for each measurement and is scaled to the exposure time *t*' of the background range bin and integration time *t* of the atmospheric range bin, and reduced by the detection chain offset *dco*[1]:

$$I_{bkg}(i) = \frac{t}{t'} \cdot (I'_{bkg}(i) - dco) \tag{4.25}$$

4.2.1 Rayleigh receiver response function

The intensities of both the channels *A* and *B* at the Rayleigh receiver yield the Rayleigh response value *R*. The Doppler shift can be measured from either a differential measurement of the intensities (*A* - *B*) or from a relative measurement:

$$R = \frac{A - B}{A + B} \tag{4.26}$$

Chanin et al. (1989) demonstrates the advantages of relative calculations, as less sensitivity to background light and noise effects. This function is commonly used for the double edge method (Gentry et al. 2000, Souprayen et al. 1999a). The use of a differential technique to measure the Doppler shift renders the measurement insensitive to laser frequency jitter and drift. Korb et al. (1992) demonstrated that the edge technique is nearly insensitive to the spectral width and shape of the laser.

4.2.2 Calibration mode

During calibration, the laser frequency changes in steps over a defined wavelength interval[2] and results in the receiver response function (calibration curve). At each wavelength step the ACCD accumulates 700 laser pulses. The wavelength intervals and the results of the Rayleigh calibration mode are shown in Fig. 4.29. To obtain the transmission curves of the Rayleigh filters *A* and *B*, a calibration measurement across a wavelength range of 3.8 pm (9 GHz) is performed with frequency steps of 0.1 pm (250 MHz). Within the wind speed measurement range (limited by the USR of the Mie receiver) of 0.695 pm (1.64 GHz) around the crosspoint of the filter curves, the frequency step resolution is increased to 0.01 pm (25 MHz).

1. The constant value of the detection chain offset differs to the *dco* of the Mie ACCD and depends on electronic setting.
2. The maximal wavelength range in respect to the settings of the laser is 3.78 pm (9 GHz).

Rayleigh calibration:

wavelength range 9 GHz ⟶ Filter transmission curves

wavelenth range 1.64 GHz ⟶ Rayleigh response function for wind speed determination

Fig. 4.29 The wavelength ranges and the results of the Rayleigh calibration.

The parameters of the measured filter transmission curves (FWHM, spacing, transmission maxima) are the input parameter of the simulator. The receiver response function describes the correlation of the response values and the wavelength, and is calculated for the smaller wavelength range.

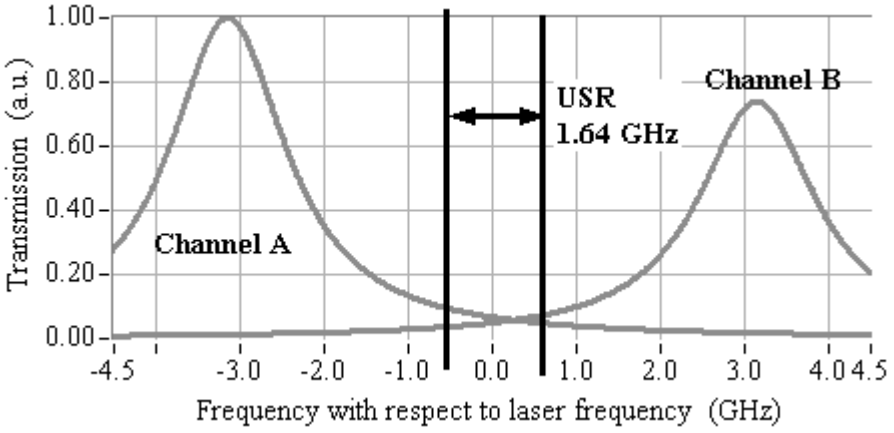

Fig. 4.30 The transmission of the Rayleigh filter *A* and *B* versus frequency to illustrate the frequency intervals of the calibration mode (9 GHz and a USR of 1.64 GHz).

The intensities for each channel are reduced by the *dco* and the results are corrected to a laser energy drift:

$$A_{R,I}(\lambda) = A'_{R,I}(\lambda) \cdot \frac{E_n}{E_0} \tag{4.27}$$

where $A'_{R,I}(\lambda)$ is the intensity measured in channel *A*, E_0 is the energy measured at λ_0 (first wavelength step), and E_n is the energy at wavelength step *n*. After energy correction of channel *B* according to EQ. 4.27, EQ. 4.26 is applied, and the receiver response function $R_{R,C}$ for the internal signal is generated. The internal $R_{R,C}(\lambda)$ and the atmospheric response function $R_{R,AC}(\lambda)$ received from simulations are illustrated in Fig. 4.31. The atmospheric response function is calculated by modelling a Gaussian shaped spectrum in respect to the atmospheric temperature (EQ. 2.4 and EQ. 2.5) and simulating the transmitted intensities on channel *A* and *B* (EQ. 3.14 and EQ. 3.15). The different slopes of the function arise from the different FWHM values of the Rayleigh spectrum (1.6 pm at 270 K temperature) und the laser signal (0.02 pm).

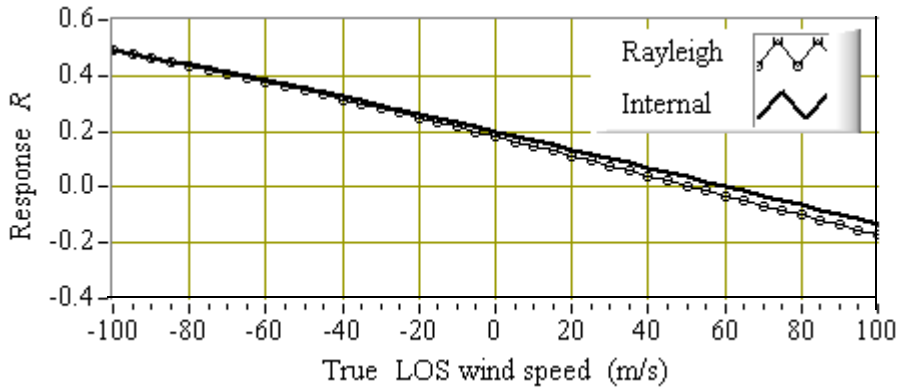

Fig. 4.31 The receiver response function depending on the LOS wind speed of the internal laser spectrum (black line, FWHM 0.02 pm) and a Rayleigh spectrum at 270 K (dotted line, FWHM 1.6 pm).

The mean sensitivity of the receiver in respect to the internal reference $\beta_{R,C}$ and to the Rayleigh atmospheric response function from calibration $\beta_{R,AC}$ is the slope of the best straight line of the response function. The offset to the zero frequency (intercept of the curve) for the internal $\Delta\lambda_{off,C}$ and atmospheric response function $\Delta\lambda_{off,AC}$ is determined. The difference between the best straight line and the response function is the linearity error ($\Delta\lambda_{err\_R,AC}$ for the atmospheric signal and $\Delta\lambda_{err\_R,C}$ for the internal signal). The response function from the atmospheric $R_{R,AC}(\lambda)$ and internal $R_{R,C}(\lambda)$ calibration can be calculated from:

$$R_{R,AC}(\lambda) = \beta_{R,AC} * \lambda + \Delta\lambda_{off,AC} + \Delta\lambda_{err\_R,AC} \tag{4.28}$$

$$R_{R,C}(\lambda) = \beta_{R,C} * \lambda + \Delta\lambda_{off,C} + \Delta\lambda_{err\_R,C} \tag{4.29}$$

The response functions from the atmospheric calibration depend on atmospheric temperature T (Section 4.2.4).

4.2.3 Measurement mode

The response values for the atmospheric measurement in each range bin are calculated from EQ. 4.26 and result in one response value of the internal reference $r'_{R,I}$ and the response values of the atmospheric measurement $r'_{R,A}$ for the different atmospheric layers. An overview of the Rayleigh processing procedure is shown in Fig. 4.32.

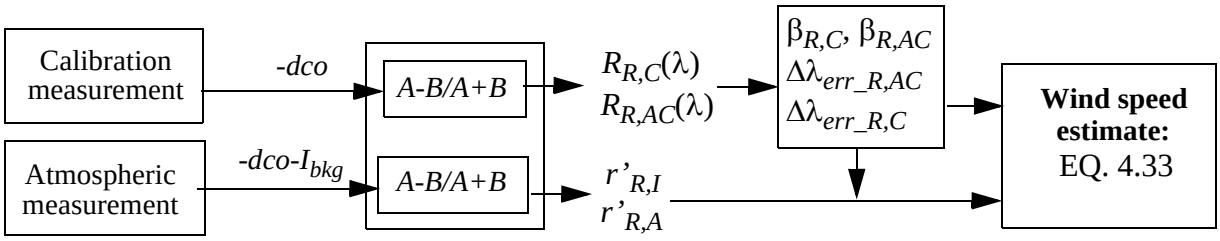

Fig. 4.32 An overview of the Rayleigh signal processing procedure.

From EQ. 4.29, the internal wavelength value λ_I depending on the corresponding response value $r'_{R,I}$ can be determined by:

$$\lambda_I = \frac{r'_{R,I} - \Delta\lambda_{err\_R,C} - \Delta\lambda_{off,C}}{\beta_{R,C}} \tag{4.30}$$

From EQ. 4.28, the atmospheric wavelength value λ_A depending on the corresponding response value $r'_{R,A}$ can be determined by:

$$\lambda_A = \frac{r'_{R,A} - \Delta\lambda_{err\_R,AC} - \Delta\lambda_{off,AC}}{\beta_{R,AC}} \tag{4.31}$$

The Doppler shift is determined from the difference between the internal and the atmospheric wavelength value. The corresponding wavelength shift $\Delta\lambda_D = \lambda_A - \lambda_I$ is derived from:

$$\Delta\lambda_D = \frac{r'_{R,A} - \Delta\lambda_{err\_R,AC} - \Delta\lambda_{off,AC}}{\beta_{R,AC}} - \frac{r'_{R,I} - \Delta\lambda_{err\_R,C} - \Delta\lambda_{off,C}}{\beta_{R,C}} \tag{4.32}$$

Considering the factor $c/2\lambda_L$, the wind speed is estimated by:

$$v_{LOS} = \frac{c}{2 \cdot \lambda_L} \cdot \Delta\lambda_D \tag{4.33}$$

4.2.4 Rayleigh processing performance results

The simulated linearity errors $\Delta\lambda_{err\_R,AC}$ and $\Delta\lambda_{err\_R,C}$ are shown in the following figure received from the atmospheric and internal response function.

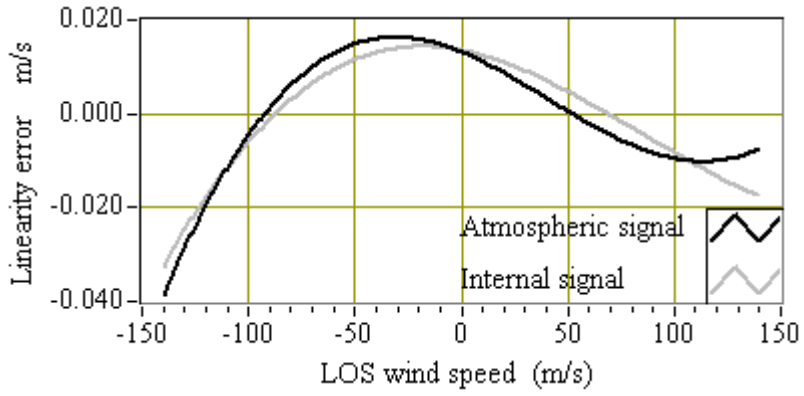

Fig. 4.33 The linearity error of the Rayleigh response function of the atmospheric (270 K temperature) and internal laser signal in respect to the LOS wind speed.

The shape of the linearity error strongly depends on the filter parameters (FWHM, spacing, transmission) and of the width of the signal spectrum.

Errors on Rayleigh wind speed estimation

Background light and increased Mie backscatter results in an intensity change on channel *A* and *B*, consequently an error is induced on the Rayleigh wind speed estimate. The temperature determines the width of the Rayleigh spectrum and this affects the simulated response function as well. The Rayleigh response function is determined by simulations for comparisons to measurements and for the case, it is not available from measurements.

a) Temperature effects

The effects of a change in temperature on the Rayleigh response function are shown in Fig. 4.34.

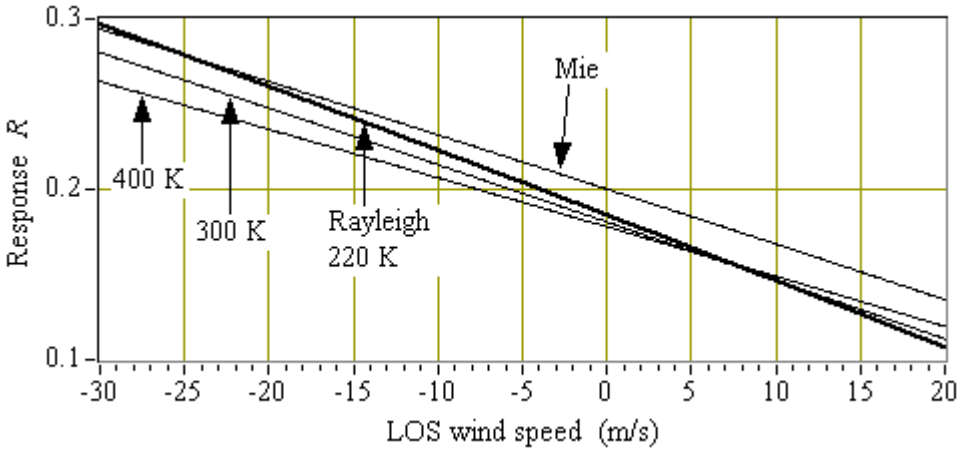

Fig. 4.34 Rayleigh receiver response *R* for different atmospheric temperatures (220 K, 300 K, 400 K) and the response of the laser signal (Mie signal) versus the LOS wind speed.

The intercept and the slope of the curves depend on the width of the spectrum. The slope decrease for increased temperature values of the Rayleigh spectrum and lowest slope results from the Mie response function. This leads to a non-linear temperature dependence as illustrated in Fig. 5.11.

In Fig. 4.35 a change in intensity change on both channels (*A* + *B*) and the LOS wind speed offset is shown in respect to temperature variation for a LOS wind speed of 0 m/s. A change in temperature of 10 K leads to a change in 2 % of intensity and a wind speed error of 0.1 m/s. Thus the atmospheric temperature profile has to be known more accurate than 10 K to determine the Rayleigh LOS wind speed profile with an accuracy better than 0.12 m/s.

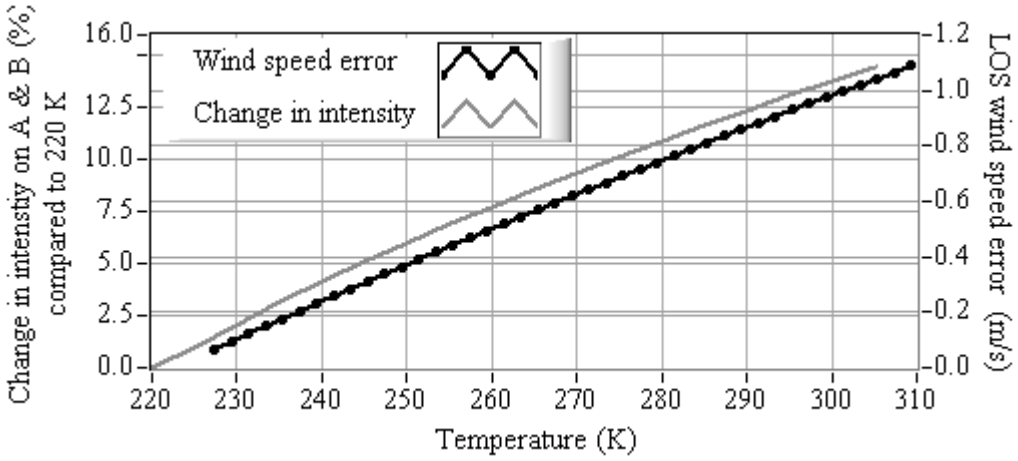

Fig. 4.35 Intensity change on the sum of channel *A* and *B* and the wind speed error depending on a change in atmospheric temperature in respect to 0 m/s wind speed.

b) Mie contribution

For the case of a mixed Rayleigh-Mie backscatter spectrum difficulties arise to determine the LOS wind speed from the measurements at the Rayleigh receiver. Mie contribution on the Rayleigh double edge receiver was examined by Garnier and Chanin (1992) for a system at 532 nm laser wavelength. This study demonstrated for an increased filter spacing from 3.2 to 5.3 pm and FWHM from 1.2 to 2.3 pm an increased insensitivity of the response function in the case of Mie contribution, but results in a lower sensitivity of the system. Souprayen et al. (1999b) analysed the effect of Mie contribution for a direct detection Doppler lidar with the double edge method. The errors are estimated by the knowledge of the scattering ratio. The remaining bias after correction was less than 1 m/s for a backscatter ratio of 10 and the bias was less than 0.6 m/s for a backscatter ratio of 5.

The method described in this chapter uses the information of the signal at the Mie receiver to determine and correct the bias at the Rayleigh receiver.

Correction of Mie contribution

The strength of the Mie and Rayleigh signal at the Mie receiver are used to generate the Rayleigh atmospheric response function and to calculate the wind speed estimate from this new response function. Fig. 4.36 demonstrates the signal at the Mie receiver. The minimum value of all 16 pixels determines the Rayleigh signal intensity and the difference between the minimum and the maximum is a measure of the pure intensity of the Mie signal.

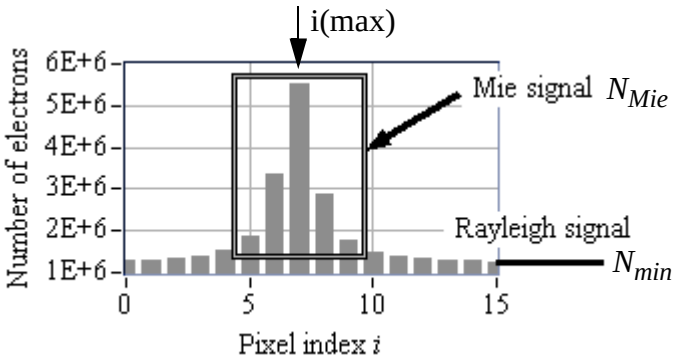

Fig. 4.36 The Mie and Rayleigh electrons at the pixels of the Mie receiver, and the notations used during calculation in this section.

The Mie and Rayleigh spectra are generated by simulations in respect to the ratio of the measured Mie and the Rayleigh intensities at the Mie receiver. The Mie-to-Rayleigh-ratio (*MRR*) at the Mie ACCD signal is used to determine the strength of the Mie signal N_{Mie} at the Rayleigh receiver and may be written as:

$$MRR = \frac{N_{Mie}}{N_{Ray}} = \frac{\sum_{i(max)-2}^{i(max)+2} (N_i - N_{min})}{16 \cdot N_{min}} \tag{4.34}$$

where the Rayleigh signal is determined by the minimum intensity N_{min} (Fig. 4.36) and the Mie signal is determined from five pixels around the pixel with maximal intensity *i(max)* without the Rayleigh signal N_{Ray}. It is assumed that the ratio *MRR* corresponds to the signals ratio after reflection at the Fizeau interferometer and the transmission through the Rayleigh Fabry Perot interferometer. The Rayleigh atmospheric response function is calculated for a signal, which includes a Mie and a Rayleigh spectrum and the Mie spectrum (number of Mie photons) is scaled to:

$$N_{Mie} = N_{Ray} * MRR \tag{4.35}$$

The notations used for calculation are illustrated in Fig. 4.36. The response functions (Fig. 4.37) are calculated for a pure Rayleigh signal and a Rayleigh signal with Mie contribution.

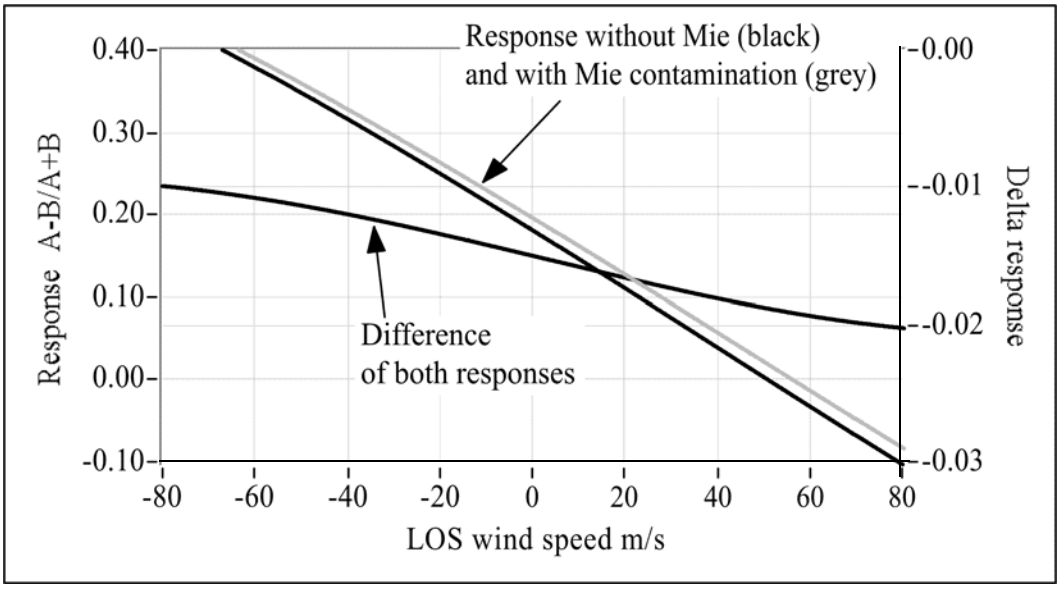

Fig. 4.37 The response functions without and with Mie contribution for a typical MMR of 0.7 (corresponding to the intensities in Fig. 4.36) and the difference plot of both are illustrated versus the LOS wind speed.

Simulations were performed for a ground system where the backscatter intensities results from an altitude of 300 m, the median aerosol model, 70 mJ laser energy, and 700 accumulated pulses (instrumental parameters Table 3.3). The results are demonstrated in Fig. 4.38. The bias is reduced for different wind speed values and the algorithm seems to be very stable. The bias at 0.5 km altitude arises from aerosol backscatter for a backscatter coefficient of 4.3×10^{-6} m^{-1} sr^{-1} respectively a backscatter ratio of 1.56. The left figure shows the bias of the wind speed estimate calculated by response functions of a pure Rayleigh spectrum (black line) and the bias of the wind speed estimate calculated by response functions which include Rayleigh and Mie spectra (black dotted line). The bias is reduced to values smaller than 0.3 m/s after correction of the response function. Both wind speed estimates depending on altitude are illustrated also in the right figure and the grey line represents the true wind speed of 0 m/s.

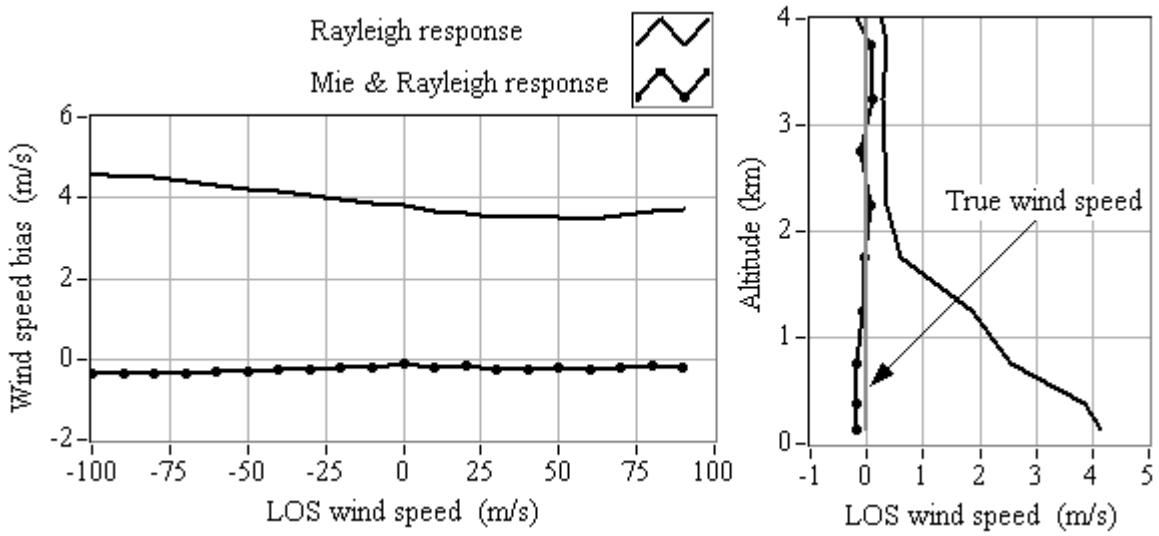

Fig. 4.38 The LOS wind speed bias of the Rayleigh wind speed estimate due to Mie contribution (black line) and after correction (dotted black line) of the response function (left) depending on the LOS wind speed in respect to a backscatter ratio of 1.56. The LOS wind speed estimate, the LOS wind speed after correction of the response function, and the true LOS wind speed of 0 m/s (right).

The bias is reduced by a factor of 10 in respect to new response functions considering the Rayleigh and Mie spectrum, which intensities depend on the detected *MMR* at the Mie receiver.

Summary

It was shown, that atmospheric temperature effects are low and for the case the temperature is known better than 10 K, the difference LOS wind speed between measurements and simulations is smaller than 0.1 m/s. A new algorithm was presented to reduce the LOS wind speed error arising at the Rayleigh receiver from increased Mie backscatter. The resulting wind speed error is reduced by a factor of 10.

4.3 Wind speed results of simulations

4.3.1 Random error

The random error of the wind speed estimate σ_v can be obtained by a statistic from n wind speed measurements with index i, and may be written as (Bronstein and Semandjajew 1987):

$$\sigma_v = \sqrt{\frac{\sum_0^n (v_i - v_m)^2}{n-1}} \tag{4.36}$$

where v_m is the mean wind speed value.

Fig. 4.39 illustrates the random error of an airborne system at 12 km flight altitude for different laser energy parameters, 700 accumulated laser pulses, instrumental parameters according to Table 3.3, and the median aerosol model. Below 2 km the random error of the Mie receiver is shown, which is smaller than the error of the Rayleigh receiver. In regions above 2 km, the Rayleigh random error wind speed is mapped, because the Mie receiver error is larger.

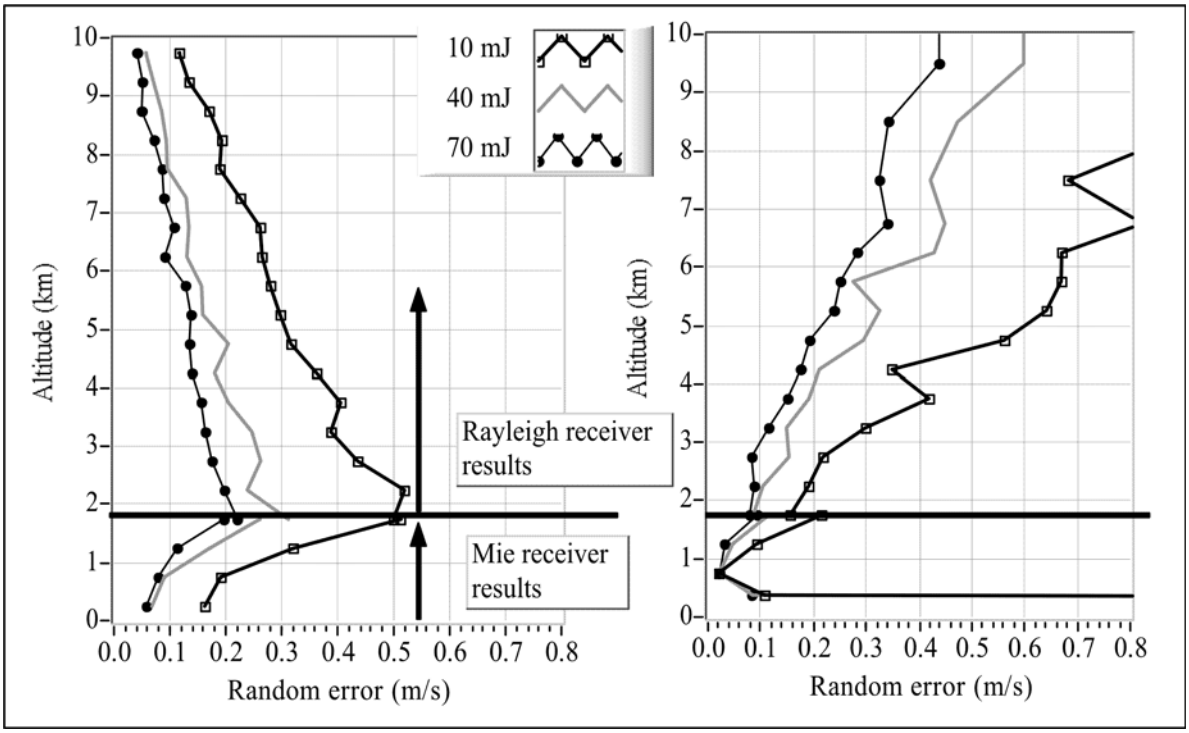

Fig. 4.39 Random error of the wind speed for different laser energy parameters (10 mJ, 40 mJ, and 70 mJ) for an airborne system at 12 km flight altitude (left) and a ground system (right) versus altitude. The random error of the Mie receiver is illustrated for altitudes below 2 km, and the random error of the Rayleigh receiver is illustrated above 2 km altitude.

There is a decrease of the random error for increased laser energy for both the airborne and ground system. The differences between the different laser energies increase for larger distances R to the target because of the $1/R^2$ dependence of the signal. The random errors of the airborne system in

respect to the Mie signal increase with larger distances in the boundary layer, because the impact of increasing aerosol backscatter is stronger than the signal attenuation by $1/R^2$. Caused by the overlap and the reduction of photons in respect to the ground system, there is no signal below 500 m and reduced signal below 1 km altitude. The resulting random error values are shown in Table 4.2.

Table 4.2 Random error for the airborne and the ground system

Laser energy	Rayleigh random error above 2 km (m/s)		Mie random error up to 2 km (m/s)	
	Airborne	Ground	Airborne	Ground
10 mJ	< 0.5	< 1.0	< 0.5	< 0.2
40 mJ	< 0.3	< 0.6	< 0.3	< 0.1
70 mJ	< 0.3	< 0.5	< 0.3	< 0.1

4.3.2 Wind speed selection

The combination of the Mie and Rayleigh receiver provides the opportunity to select the Mie receiver results in case of higher aerosol loadings and the Rayleigh receiver results for pure molecular backscatter areas. To decide whether the Mie or the Rayleigh signal is chosen for the LOS wind speed results, the intensities of the Mie receiver are analysed. For the case, the ratio of maximal to minimal intensities (of the 16 pixels) of the Mie signal is larger than a threshold, the Mie receiver results are chosen. Otherwise the results of the Rayleigh receiver are selected and an example is illustrated in Fig. 4.42.

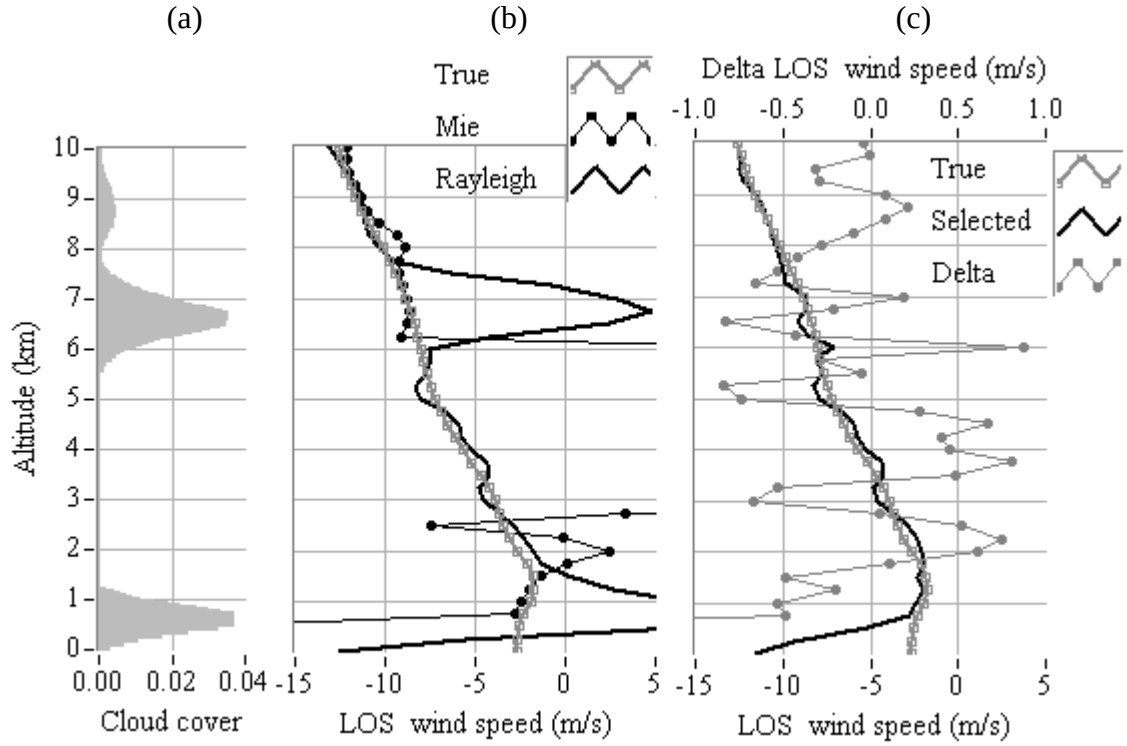

Fig. 4.40 The cloud cover coefficient profile (a), the LOS wind speed results of the Rayleigh and Mie receiver (b), and the results of the selected wind speed compared to the true wind speed (c) versus altitude. "Delta" wind speed is the difference between the selected and the true wind speed.

Simulations were performed for an airborne system at 12 km flight altitude, 70 mJ laser energy, 700 accumulated laser pulses (instrumental parameters in Table 3.3), and the median aerosol model. The atmospheric wind speed and the clouds were taken from the local model (DWD). The cloud cover demonstrated in Fig. 4.40(a) and indicates a low cloud cover at about 1 km, 7 km, and 9 km altitude.

Fig. 4.40(b) illustrates the true wind speed and the wind speed estimate of the Mie and Rayleigh receiver. The Rayleigh receiver wind speed estimate corresponds to the true wind speed for clear air, but in the case of clouds or increased aerosol loadings in the boundary layer, a bias increases which can be larger than 5 m/s. The Mie receiver wind speed estimate corresponds to the true wind speed in case of clouds or higher aerosol loadings, whilst in clear air the error is quite large (> 5 m/s). For both the Rayleigh and Mie receiver the signals are attenuated in such an extent below 0.5 km altitude, that a wind speed estimation is not possible.

Fig. 4.40(c) illustrates the true wind speed, the selected wind speed, and the differences between both. For the case, the ratio of the maximal and minimal intensity at the Mie receiver is above a threshold, the Mie wind estimate is selected. Otherwise, the Rayleigh wind speed estimate is used. The residual error after selection is below 1 m/s.

The performance of an airborne system at 12 km flight altitude and along a flight track of 680 km in the case of cloudy sky and in occurrence of a jet was simulated. Cloud cover, temperature, and wind were taken from the DWD local model at October 12th 1999. The backscatter signals during the flight were simulated with 70 mJ laser energy, 700 accumulated pulses per measurement, and the median backscatter model. The instrument filter parameters were taken from Table 3.3. The model LOS wind speed and the cloud cover coefficients of the model are presented in Fig. 4.41.

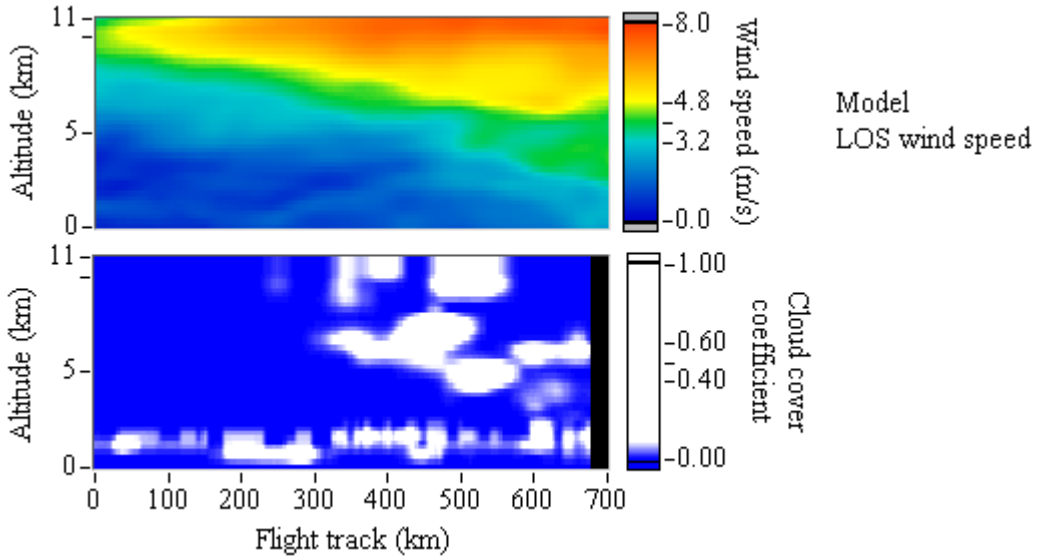

Fig. 4.41 The model wind speed and cloud coverage of the local model along the flight track depending on altitude.

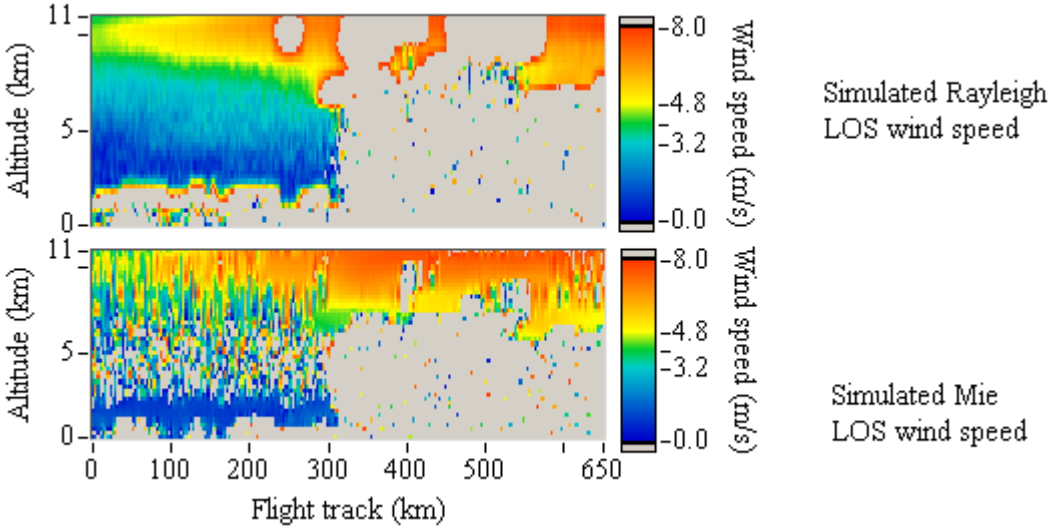

Fig. 4.42 The simulated LOS wind speed results of the Rayleigh and the Mie receiver along the flight track depending on altitude.

Fig. 4.42 shows the Rayleigh and Mie receiver wind speed estimate. The Rayleigh winds are obtained from simulations for the first 300 km of the flight track, except from the boundary layer. Because of high and middle clouds after 300 km, the Rayleigh signal is strongly attenuated and the wind speed estimate is biased. The Mie receiver wind speed estimate accords to the model

wind speed partly in the boundary layer and from clouds where the cloud cover coefficient is low. There are areas (grey fields) in Fig. 4.42 where the with speed estimate is out of the indicated wind speed range of the model. The signal there is either attenuated by clouds or the increased Mie backscatter induces a bias on the Rayleigh wind speed estimate of the Rayleigh receiver. The results of the Mie and Rayleigh receiver are combined and the selected wind speed is shown in Fig. 4.43:

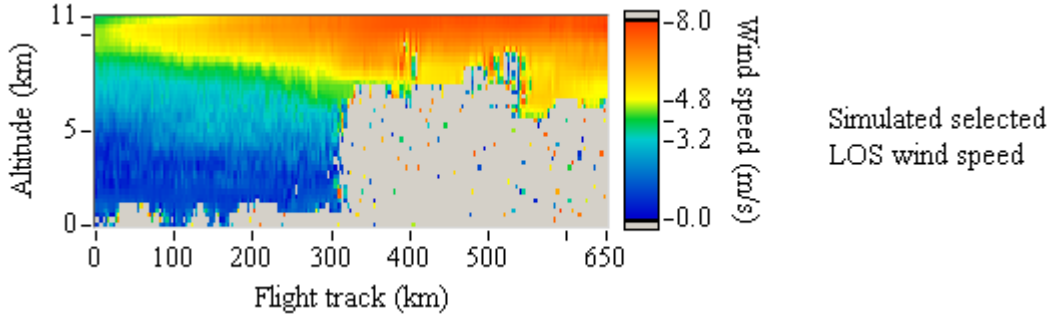

Fig. 4.43 The simulated selected wind speed results along the flight track versus altitude.

The selected wind speed results (Fig. 4.43) are superior to results from either the Mie or the Rayleigh receiver because they cover a larger altitude range.

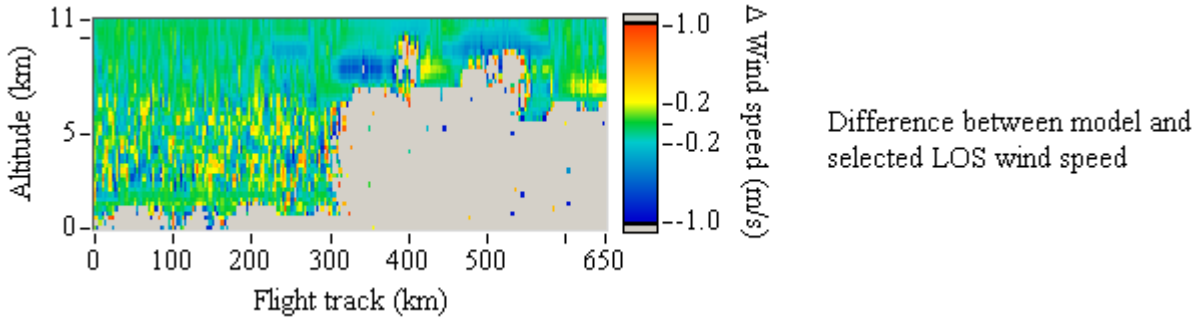

Fig. 4.44 The difference of the model and the simulated selected LOS wind speed along the flight track versus altitude.

Fig. 4.44 shows the differences between the selected and the model LOS wind speed and the error of the wind speed estimate is smaller than +/- 1 m/s for those areas of the atmosphere where the attenuation of clouds is low.

Summary

From simulations it was demonstrated that the random error of an airborne system at 70 mJ (requirement of the prototype) is below 0.3 m/s for both the Mie and Rayleigh receiver.

In respect to different atmospheric conditions, the LOS wind speed results were selected from either the Mie receiver (aerosol backscatter) or the Rayleigh receiver (for clear air), and the selection routine is determined by a threshold. This leads to LOS wind speed errors below 1 m/s and a larger coverage of atmospheric ranges, than measurements from either the Mie or the Rayleigh receiver.

5 Measurement results and evaluation

As described in the previous chapter, the data processing algorithms were analysed and optimised by means of simulation signals, to enable performance tests of the receiver with measured signals. This chapter shows the first measurement results from the ground (Section 5.1) and from an aircraft (Section 5.2) of the prototype performed at DLR. Atmospheric and internal measurements from the ground are analysed and discussed in respect to simulation results.

5.1 Measurements results on ground

The results are provided from measurements during November 2005. The receiver system, the telescope, and the laser are mounted to a rack and set up in the container at DLR.

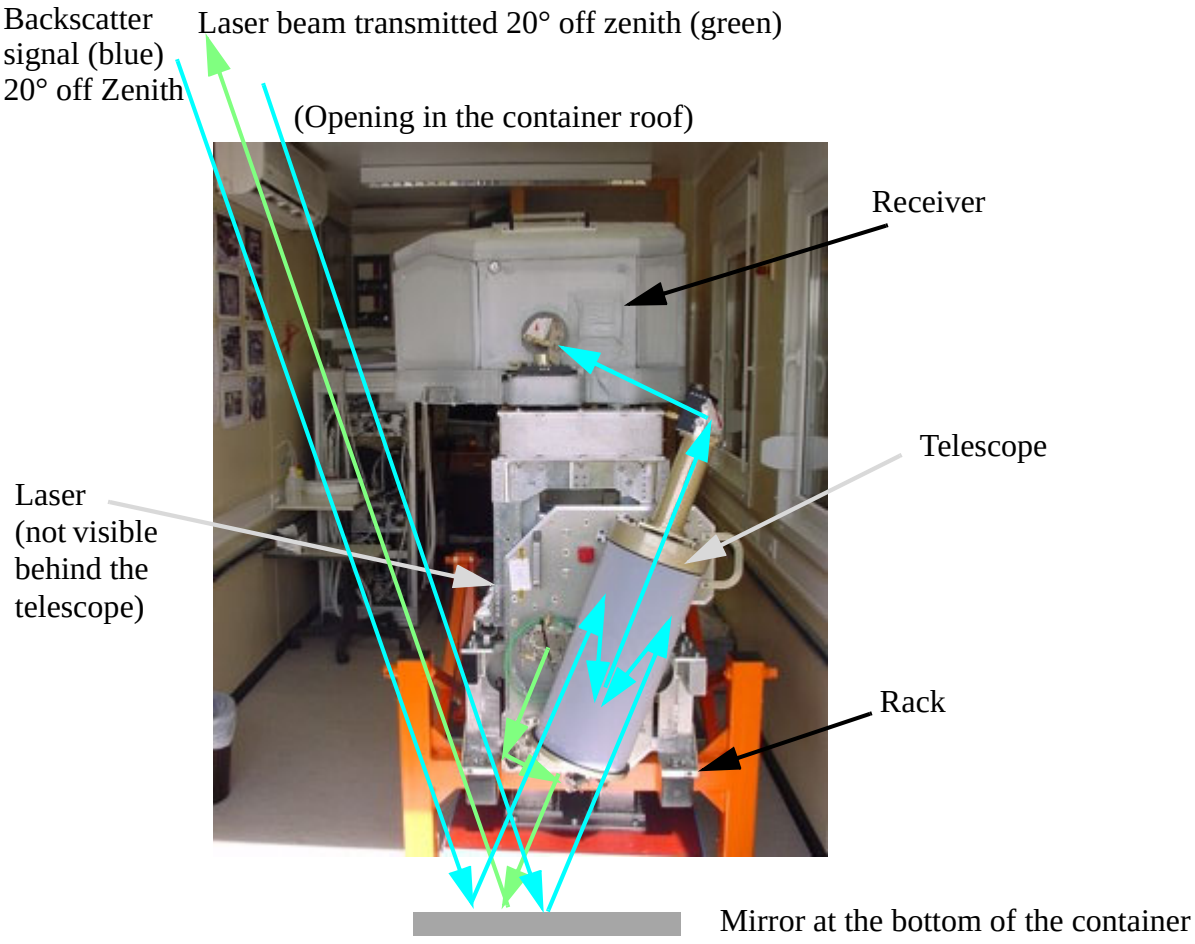

Fig. 5.1 The ALADIN prototype in the container at DLR in November 2005 and the optical paths of the transmitted and backscattered light.

The extracted laser beam (Fig. 5.1, green lines) is transmitted coaxial to the optical axis of the telescope (Fig. B.2) and then reflected off the mirror at the bottom of the container into the atmosphere through a wide opening in the container roof. The backscatter signal (blue lines) is reflected off the mirror at the bottom into the telescope and the collimated beam after passing the telescope, is reflected straight into the receiver.

An internal calibration measurement (Chap. 4) was performed to determine the response function of the Mie and Rayleigh receiver, to generate the transmission curves of the Rayleigh receiver, to determine the linearity error, and to test the sensitivity (slope of the response function, Korb et al. 1998, Gentry et al. 2000) of the receiver systems. The measured results are compared to simulations by AProS.

5.1.1 Rayleigh receiver calibration measurement

The results presented in the following, arise from 700 accumulated laser pulses per frequency step of 231 MHz. The Rayleigh spectrometer temperature was at 26.8°C (+/-0.02°C) and the temperature of the optical bench assembly was at 25.3°C, as not denoted otherwise. During the Rayleigh receiver calibration, the parameters of the transmission curves are determined to upgrade the simulator and the response function (calibration curve) of the Rayleigh receiver is determined.

Internal calibration

A calibration measurement (Section 4.2.2) was performed to determine the parameters of the filter transfer function of channel *A* and the results are shown in Fig. 5.2. Because the laser energy was not determined, the factor E_n/E_0 (EQ. 4.27) cannot be taken into account.

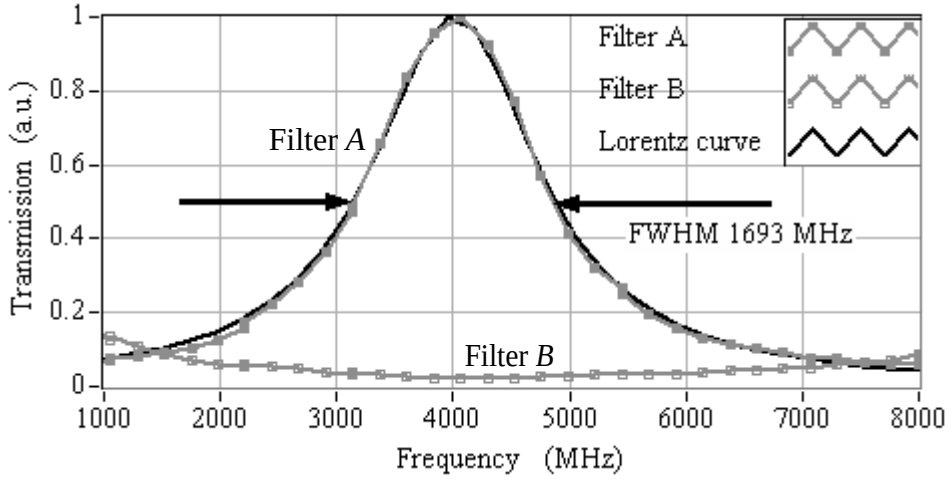

Fig. 5.2 The measured transmission of the Rayleigh receiver filter *A* (grey line with filled dots) and filter *B* (grey line with square dots), and the modelled Lorentzian function corresponding to filter *A* (black line) versus frequency (24.11.2005).

The measured filter curve of channel *A* and a Lorentzian filter curve (EQ. 3.8) modelled by AProS to the corresponding measured FWHM of 1693 MHz and normalized to the maximum transmission, are shown in Fig. 5.2. A calibration measurement for a larger frequency range was performed and Fig. 5.3 shows the coincidence between simulated and measured transmission curves.

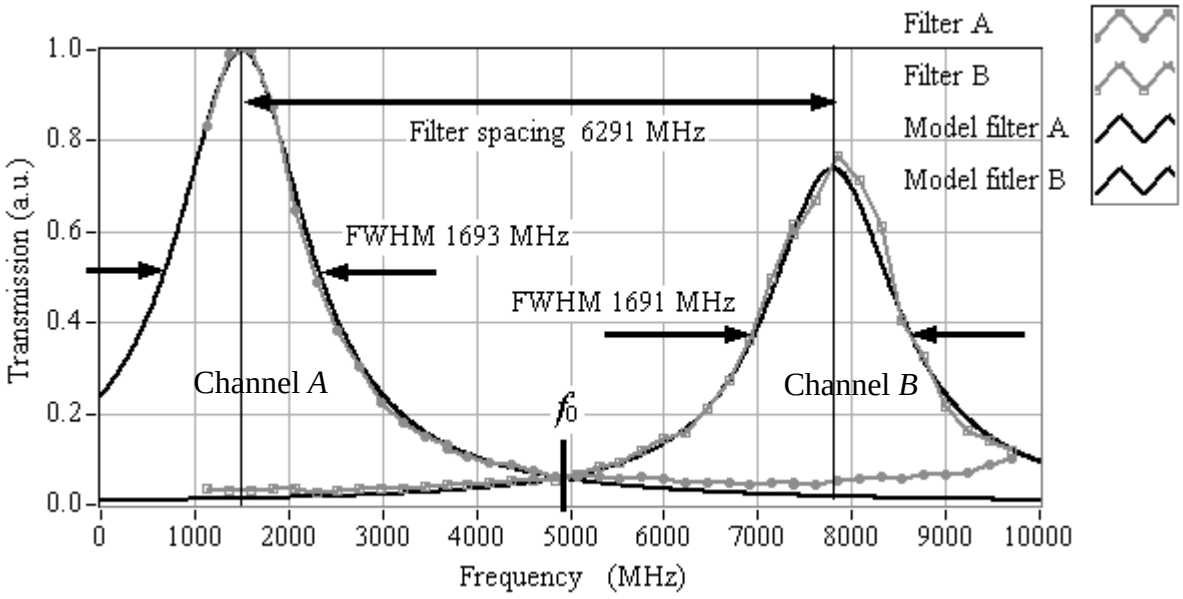

Fig. 5.3 The measured transmission of the Rayleigh receiver filter *A* (grey line with filled dots) and filter *B* (grey line with square dots), and the corresponding modelled Lorentzian functions (black line) versus frequency. f_0 is the frequency at the crosspoint of the filter curves (18.11.2005).

f_0 is the frequency at the cross point of the filter curves and determines the centre of the wind measurement interval. The measured FWHM of filter *B* is 1691 MHz and the filter spacing is 6291 MHz. The transmission of *B* is at 75 % of transmission on *A* corresponding very good to previous values[1] (EADS-Astrium 2004). There are two main discrepancies of the modelled and measured curves. First the discrepancy rightmost in the figure in a frequency range between 7000 and 10000 MHz shows an increase in transmission of filter curve *A* from the measurement by contrast to the simulated curve, where the transmission values decrease to nearly zero. This discrepancy is caused by AProS, simulating only a single transmission curve and not taking the increase towards the next transmission maximum into account. The measured filter curves increase again to the next transmission maxima (periodic function in Fig. 3.15). This discrepancy does not affect simulations in respect to the wind speed determination. The other discrepancy is the shape of filter *B* around its maximum at 8000 MHz. It is assumed that either the laser energy or the frequency monitoring did not work correct during the measurements. The response function according to EQ. 4.26 and calculated from the filter transfer functions is presented in Fig. 5.4.

1. EADS-Astrium 2004: $T_A = 0.368$ and $T_B = 0.272 = 0.368 * 0.75$.

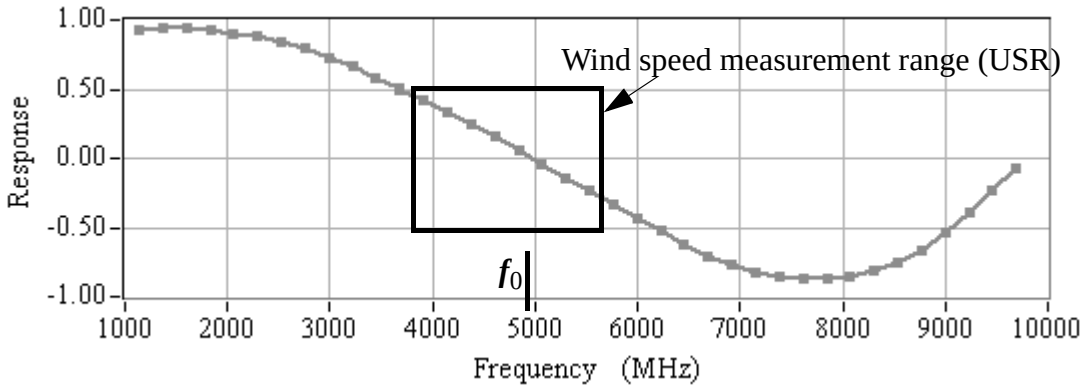

Fig. 5.4 The response values of the transmission transfer functions of Fig. 5.3 versus frequency. The USR of the Mie receiver is the wind measurement range of the instrument.

Fig. 5.5 represents the curve for the wind speed measurement range (USR) of 1.64 GHz, with steps of 31 MHz. The Rayleigh receiver sensitivity of is 0.039 %/MHz (Table 5.1) is obtained from a linear fit to the response curve in Fig. 5.5.

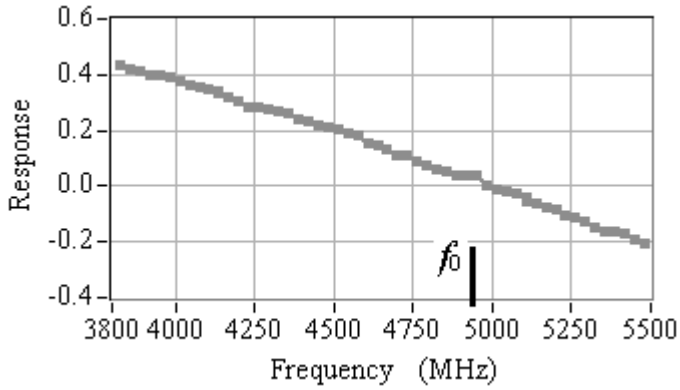

Fig. 5.5 The response values of the Rayleigh receiver for the wind measurement range as denoted in Fig. 5.4 versus frequency.

The results of AProS (adapted to the measured filter parameters) lead to a Rayleigh receiver sensitivity of 0.0571 %/MHz and of 0.0569 %/MHz in the case of photon noise (Section 3.1.2). For a slightly broadened signal (i.e. due to laser frequency fluctuations) the sensitivity value is 0.0572 %/MHz. Hence a decrease in sensitivity arises from noise and an increase in sensitivity is caused by a broadened signal.

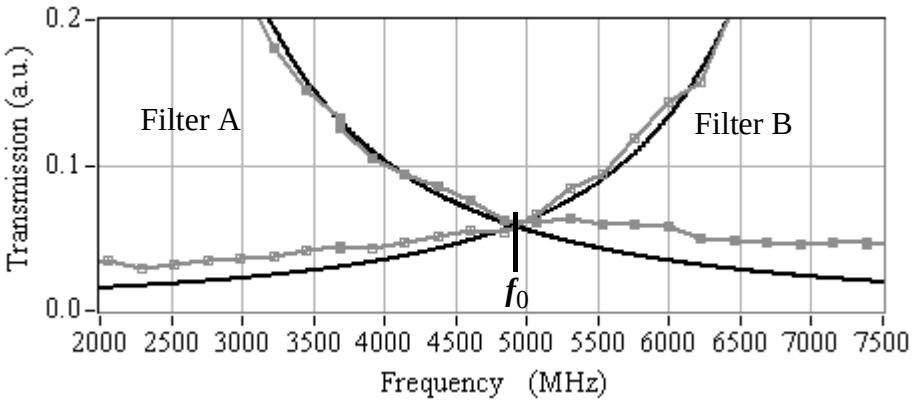

Fig. 5.6 An enlargement of Fig. 5.3: the Rayleigh transmission values near the frequency at the filters cross point at f_0 for the measured (grey) and modelled (black) curves versus frequency.

The differences between measurements and simulations may indicate that assuming a Lorentzian profile of the filter curves is not adequate enough to calculate the sensitivity. The filter curves of the simulations seem to have a steeper slope at the crosspoint than the slope of the measured transmission curves (Fig. 5.6). That is the reason, why the simulated sensitivity is larger than measured.

The linearity error results of the difference between the response function and a linear curve fit. A mean linearity error (EQ. 4.29) corresponding to an USR of 1.3 GHz[1] was calculated from three calibration measurements, to reduce the effect of laser energy fluctuations. The measured and simulated linearity errors are illustrated in Fig. 5.7. The simulation was performed in respect to the measurement interval and the cross point f_0 of the filter curves.

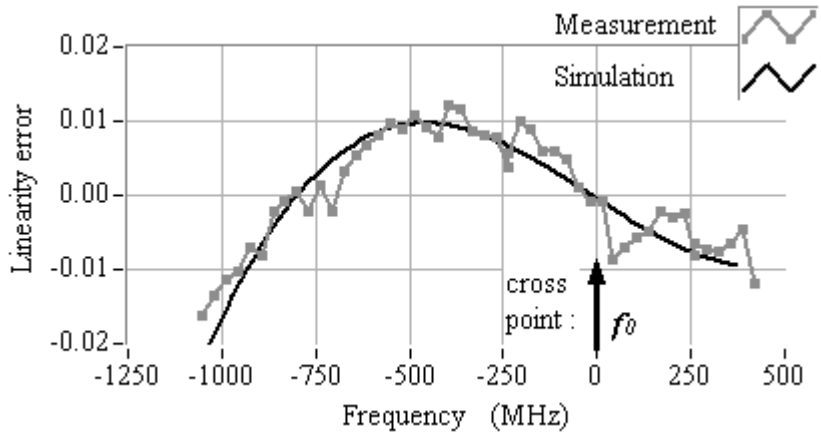

Fig. 5.7 The linearity error (response value[2]) resulting from measurements (grey) and simulation (black) in respect to the filter cross point at f_0 versus frequency (22.11.2005).

1. The USR (defined to be 1.64 GHz) is sometimes reduced due to the laser parameters (e.g. laser lock status and energy fluctuations).
2. For a Rayleigh receiver sensitivity of 0.04 %/MHz, the response value of 0.0004 corresponds to 1MHz.

Both the amplitude and the shape of the simulated linearity error agree with the measurements for the corresponding frequency range. The maximum of 0.01 (response value) is at about -500 MHz (related to f_0) and the modulation of both curves is nearly identical. The fluctuations of the linearity error (standard deviation, 1 m/s) may arise from the laser properties and photon noise. An overview of the internal calibration results of the Rayleigh receiver is illustrated in Table 5.1.

Table 5.1 Rayleigh receiver: calibration measurement values

	EADS-Astrium 2004 (at 25°C Rayleigh spectrometer)	**Measured at DLR** (at 25.8°C Rayleigh spectrometer)	**Simulator**
Sensitivity (%/MHz)	0.0486	0.0398 Random error: 9.96×10^{-4} %/MHz	0.0571 0.0569 (photon noise) 0.0572 (broadened signal)
FWHM *A* / *B* (MHz) (pm)	1737.7 / 1727.7 (0.73 / 0.726)	1693 / 1691 (0.711/ 7.10)	from measurement
Spacing (MHz) (pm)	6320 (2.655)	6380 (2.643)	from measurement
Peak transmission *A* / *B*	0.368 / 0.272 0.367 / 0.75*0.368	T_A / 0.75 T_A	0.368 / 0.272
Linearity error	values in respect to f_0 not determined	Maximum: 0.01 at -500 MHz Random error ~ 1 m/s	Maximum: 0.01 at -500 MHz Random error < 0.1 m/s

The mean sensitivity of the measurements is 0.0398 %/MHz (over 8 observations) with a standard deviation (EQ. 4.36) of 9.96×10^{-4} %/MHz. The measured sensitivity is lower than measured in 2004 (EADS-Astrium 2004) and depends on the increased spacing of 6380 MHz. The sensitivity of simulations is higher than the measured sensitivities. This points out that a simulated Lorentzian profile of the transmission function is not adequate enough. The ratio of the maximum transmission values of both channels corresponds to the transmission values measured by EADS-Astrium (2004). The linearity error which results from simulations agrees quite closely to shape and amplitude. Concluding, the values are close to the measured values by Astrium and correspond to the simulation results. The fluctuations of the linearity error are large (>1 m/s) and may arise from laser frequency fluctuations.

Atmospheric calibration:

Besides the internal calibration an atmospheric calibration was performed to determine the atmospheric signal for different frequencies and to calculate the sensitivity of the receiver for the Rayleigh signal (Section 4.2.3). These very first atmospheric measurements results with this system are presented in the following. The response function of the atmospheric calibration for an altitude at 2 km (where low Mie backscatter is expected) is shown in Fig. 5.8 compared to the linear fit function.

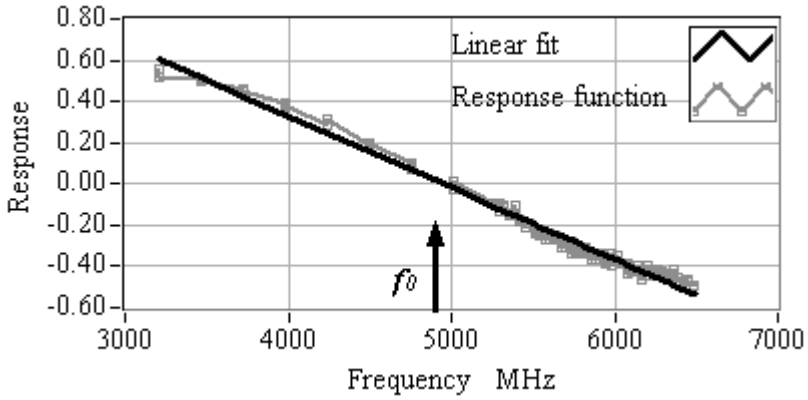

Fig. 5.8 The Rayleigh response values of the atmospheric calibration measurement (grey) and the best linear fit (black) at an altitude of 4 km versus frequency. f_0 is the frequency at the crosspoint of the filter curves (15.11.2005).

The frequency step size changes (at about 5000 MHz) from 231 MHz to 31 MHz. The frequency range of Fig. 5.8 is larger (3.3 GHz) than the wind speed measurement range, because a correlation of measurements and simulations will be seen more clearly for an increased range. The linearity error (Fig. 5.9) for an increased range has a stronger modulation (shape like a sinus).

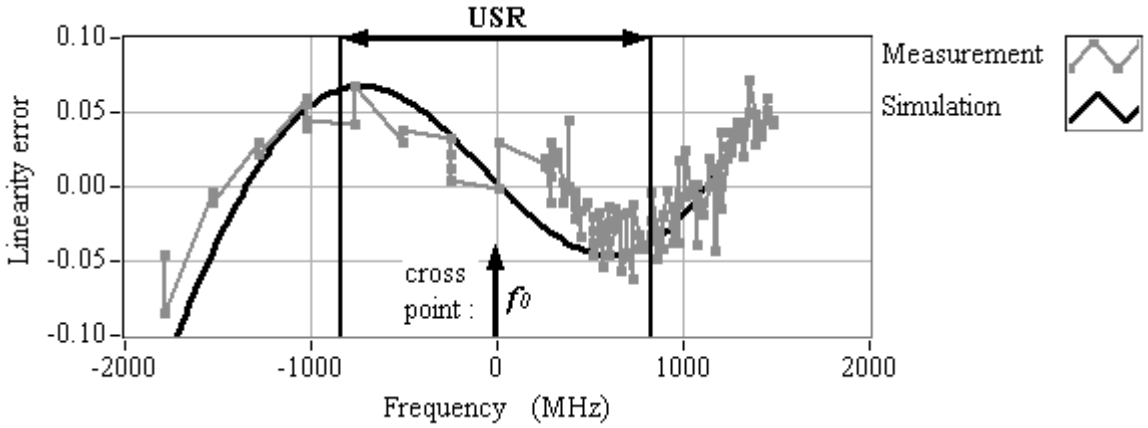

Fig. 5.9 The atmospheric linearity error from measurement (grey, see Fig. 5.8) and a simulation (Rayleigh spectrum at 270 K temperature) at 2 km altitude versus frequency. The USR is located symmetrically to the crosspoint of the filter curves in respect to the frequency range.

The wind measurement range (USR) is indicated in Fig. 5.9. The small fluctuations within the measured curve may arise from the laser properties, photon noise, and the atmosphere. The cross point of simulations (at 270 K temperature) coincide with the cross point of the measurements and the shape and amplitude of the resulting linearity error are in accordance. The maxima is about 0.06 (response) at a frequency of -900 MHz and the minima is -0.04 at a frequency of 900 MHz. The random error (determined by the difference between the measurement and a polynomial fit) is 0.017773 which corresponds to 8 m/s and arises from the fluctuations of the linearity error curve. The measured sensitivities are illustrated in Fig. 5.10a. The sensitivity increases within the first

atmospheric layers because the intensity of the Mie signal decreases. Above 1 km altitude the sensitivity decreases with altitude due to the decreasing signal quality (Fig. 5.10).

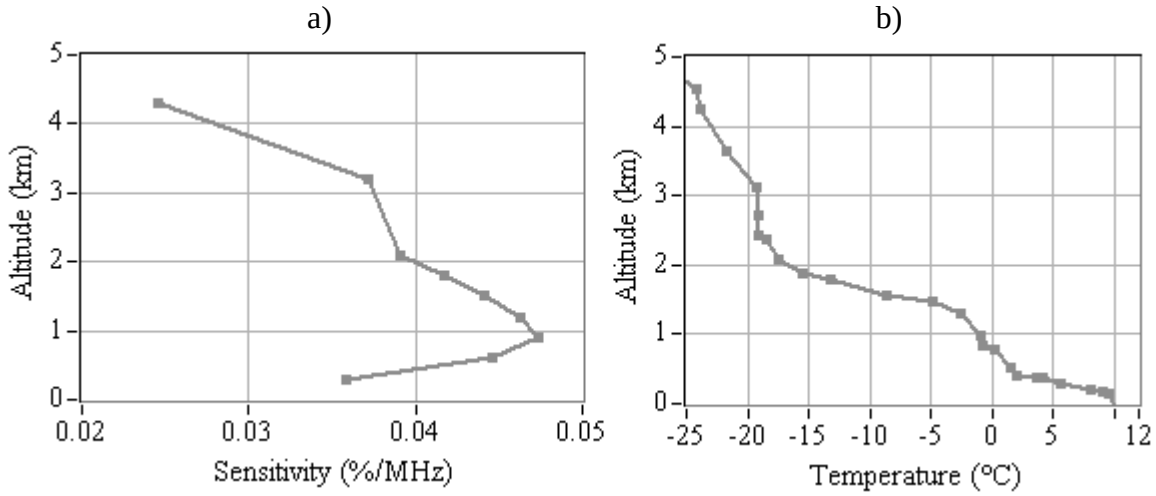

Fig. 5.10 The receiver sensitivity (a) at 15.11.2005 (15:00) and the atmospheric temperature (b) provided by radiosonde data at 15.11.2005 (12:00) above 0.25 km and temperature measurements at DLR below 0.25 km.

The temperature profile (Fig. 5.10b) was obtained from the radiosonde in Oberschleißheim (15.11.2005, 12:00, above 0.25 km altitude) and measurements at DLR (weather station 0-0.25 km altitude). It seems that the sensitivity decrease with an decrease in temperature and this effect was analysed by simulations.

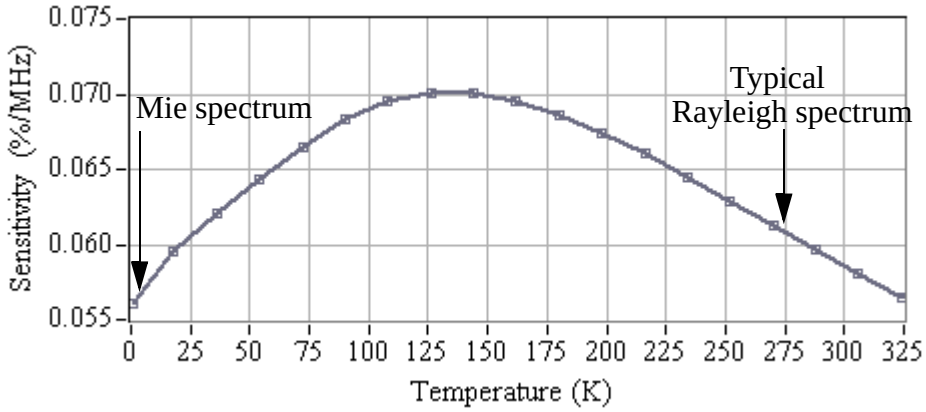

Fig. 5.11 The modelled sensitivity of the Rayleigh response (slope) versus temperature. A typical Rayleigh spectrum is expected at a temperature of 275 K and a Mie spectrum at 0 K.

Fig. 5.11 illustrates the Rayleigh receiver sensitivity dependence on temperature. Around a typical Rayleigh spectrum (275 K), the sensitivity increases with decreasing temperature. For temperatures below 100 K[1], the sensitivity decreases with temperature, which was shown during

1. Simulated spectra at 2 K temperature provide a backscatter signal shape like a Mie spectrum (no longer broadening effects due to temperature).

internal calibration (page 92), consequently the sensitivity increases for a broadened laser (Mie) signal. The sensitivity of the atmospheric measurement decreases with increasing temperature and lower signal quality. This demonstrates that the decrease in the signal-to-noise ratio of the signal is predominant and temperature effects on the sensitivity are small. For the case of Mie backscatter on the Rayleigh signal, the simulated sensitivity decreases to 0.060 %/MHz.

In summary it can be said, that the linearity error of the atmospheric calibration is close to simulation in amplitude and shape but large fluctuations arise due to laser properties, atmosphere, and noise effects. The sensitivity decreases with increasing temperature, increasing Mie backscatter, and lower signal quality (higher altitudes), as expected from simulations.

5.1.2 Mie receiver calibration measurement

During the Mie calibration measurement, the frequency is shifted across the USR with frequency steps of 31 MHz. The internal signal of the measurements referring to different frequencies is shown in Fig. 5.12. At a frequency of 4640 MHz (Fig. 5.12b), the signal maximum is nearly at the centre of the USR.

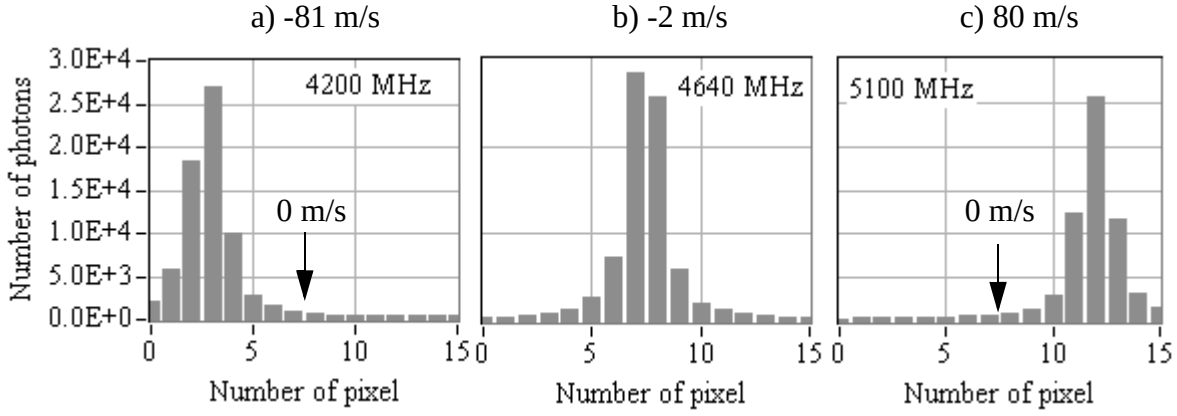

Fig. 5.12 The number of photons versus pixel number of the internal signal at the Mie receiver for different laser frequencies: (a) the signal at the ACCD at a frequency of 4200 MHz (-81 m/s); (b) the signal at a frequency of at 4640 MHz (-2 m/s); (c) the signal at a frequency of 5100 MHz (81 m/s).

The response function (Fig. 5.13) is calculated by applying the Gauss correlation algorithm. As discussed in Section 4.1, the algorithm is sensitive to the FWHM input parameter. The results in the following indicate the FWHM value, which was taken during the signal processing.

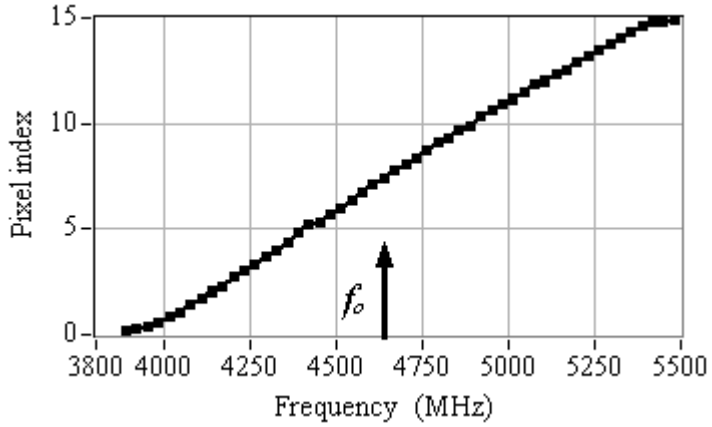

Fig. 5.13 The measured Mie receiver response function depending on frequency and pixel index by applying the Gaussian correlation algorithm (FWHM 0.2 pm). f_0 is the centre frequency of the USR at pixel index 7.5 (22.11.2005).

f_0 is the centre frequency of the USR at pixel index[1] 7.5. The measured Mie receiver sensitivity is 100.13 MHz/pixel compared the sensitivity from simulations being 103.4 MHz/pixel. To compare the results for different FWHM values, the response function was calculated for a FWHM of 0.059 pm and 0.2 pm. The resulting linearity error $\Delta\lambda_{err\_M}$ (EQ. 4.1) is illustrated in Fig. 5.14. f_0 is the centre of the USR corresponding to pixel index 7.5.

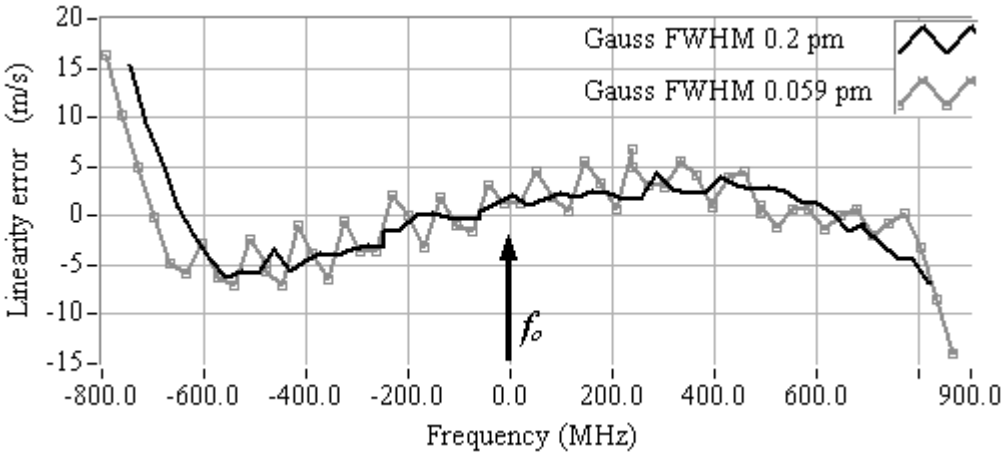

Fig. 5.14 The linearity error from measurements in respect to different FWHM input values of the Gauss correlation algorithm versus frequency. f_0 is the is the centre frequency of the USR at pixel index 7.5 corresponding to a frequency shift of 0 MHz (18.11.2005).

There are oscillations depending on the choice of the FWHM for the Gauss correlation algorithm (Section 4.1.4). The oscillations and the modulation of the algorithm leads to linearity errors smaller than +/-7 m/s (FWHM 0.059 pm), respectively smaller than +/-5 m/s (FWHM 0.2 pm). A

1. Pixel index i = 0.....15.

comparison of the simulated linearity error for measurements and a simulation is demonstrated in Fig. 5.15.

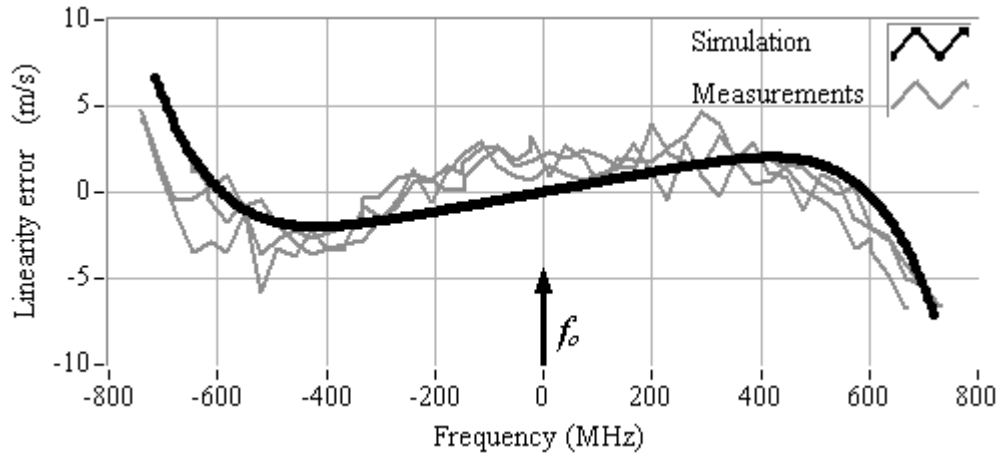

Fig. 5.15 The wind speed linearity error of four different calibration measurements (grey) and from simulation (black, FWHM of 0.2 pm) versus frequency (18.11. and 22.11.2005).

The edge bias and the modulations arise for both the simulation and the measurements (Section 4.1). The fluctuations within the curve may have the same reasons as the fluctuations of the Rayleigh linearity error. The error of the modulation is a bit larger (+/-4 m/s) than during simulations (+/-2 m/s) and not symmetric to f_0. The larger modulation and the asymmetry may arise from an alignment effect within the receiver. A change in the incident angle leads to an asymmetric signal (Section A.2). The mean measured sensitivity of four observations is 99.98 MHz/pixel and the simulated is 103.4 MHz/pixel. The error of the oscillations (fluctuations) of the measured linearity error is 1.1 m/s compared to the simulated error of 0.1 m/s (Table 4.1, error of oscillations). The error of the oscillations (fluctuations) of the linearity error was calculated by the standard deviation resulting from the differences between the measured linearity error an a polynomial curve fit.

Table 5.2 Mie receiver: calibration measurement values

	EADS-Astrium 2004	**Measured**	**Simulator**
Sensitivity (MHz/pixel)	103.48	99.98	103.4
Linearity error	Maximum: 0.72 m/s no modulation Oscillations ~0.5 m/s	Maximum: 4 m/s at 300 MHz; asymmetric; Oscillations 1.1 m/s	Maximum: 2 m/s at 500 MHz; asymmetric; Oscillations 0.1 m/s

5.1.3 Signals measured from atmospheric backscatter

Besides the calibration measurements, first atmospheric measurements from the container were performed. Because of the laser properties, the atmospheric wind speed was not determined but the wind speed measurement accuracy was tested from the return of the surface of a building (Section 5.1.4).

The laser energy was about 20 mJ at the start of the measurements (mid of October) and decreased then to 13 mJ (beginning of November) instead of 70 mJ (requirement). The laser beam profile was not determined, but it was assumed (for simulations) to have a flat top[1] intensity profile instead of a Gaussian profile. The laser divergence was assumed to be significantly larger than the required 70 µrad and even larger than the receiver field of view of 100 µrad. The effects on the backscatter intensities at the receiver due to the laser divergence are presented in Fig. 5.16. There are increased shadowing effects in front of the telescope (Section 3.2.2).

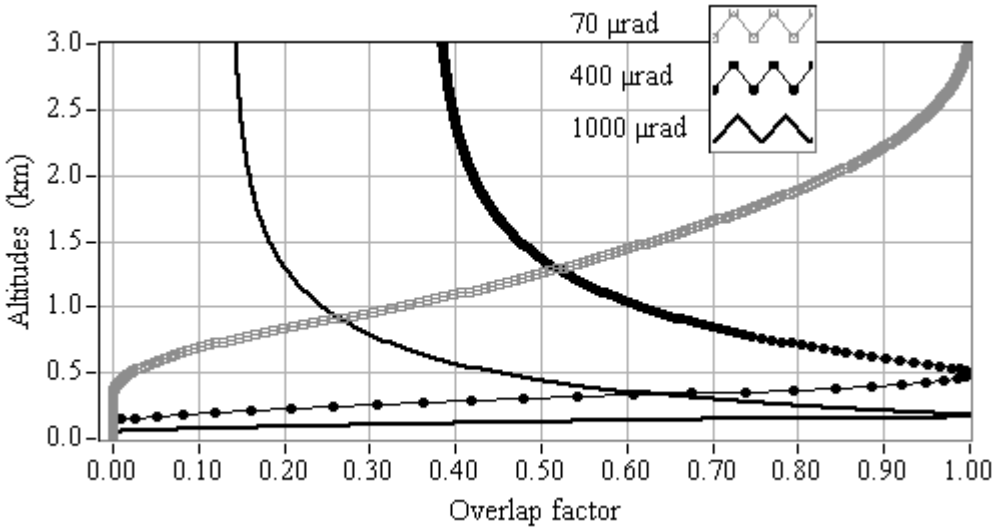

Fig. 5.16 The overlap factor versus altitude for different laser divergence values of 70 µrad (grey dotted line), 400 µrad (black dotted line), and 1000 µrad (black fat line).

Instead of low intensities near the receiver and increased intensities for distances larger than 3 km in respect to a laser divergence of 70 µrad, the intensities increase directly in front of the receiver, whilst intensities further away decrease to 15 % for systems with higher laser divergence (1000 µrad).

Atmospheric measurements were done on November the 17th during day and at night. Fig. 5.17 and Fig. 5.18 show the intensity results of one observation for 700 accumulated laser pulses. The integration times are 2.1 µs for the first six atmospheric layers and above 8.4 µs. This leads to a range bin length of the atmospheric layers of 315 m up to 2.2 km altitude and 1260 m above. The altitude values illustrate the height above ground (Oberpfaffenhofen is at 630 m above sea level, ASL). The background is measured for an integration time of 625 µs. Atmospheric measurements were done in zenith if not denoted otherwise. The results of the Rayleigh receiver for 700 laser

1. A flat top laser intensity profile means a circular uniform illuminated spot.

pulses are shown in Fig. 5.17 (left picture). The figures at the right show the intensity distribution for the different atmospheric layers. *L*0 is the signal in background range bin (index zero), *L*3 is the internal reference signal, and *L*9 is the ninth atmospheric layer referring to 3 km altitude. The signals include the detection chain offset (*dco*) and the background light. The *dco* may be seen in the figures at the right as a constant value at about 2000 electrons (*dco* of 5 measurements). The background light leads to increased illuminated spots of channel *A* and *B*.

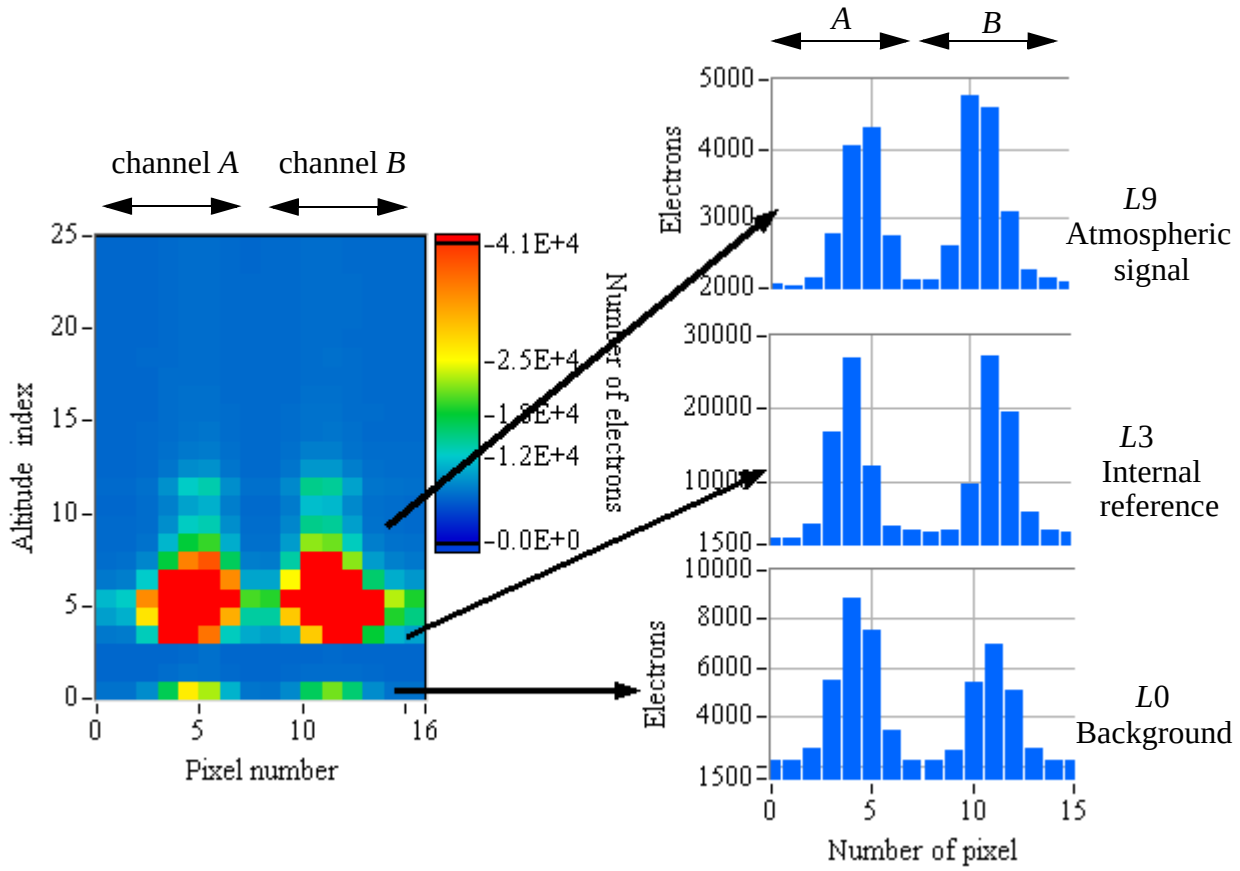

Fig. 5.17 The measured electrons at the Rayleigh ACCD of channel *A* and *B* depending on altitude and pixel index (left), and the corresponding number of electrons at the 16 pixels for different atmospheric layers (right). *L*9 is the atmospheric layer at 3 km distance, *L*3 shows the signal of the internal reference and the background signal is at range bin *L*0 (17.11.2005 10:48:35).

The results of the Mie receiver (10:38:19) for 700 laser pulses are shown in Fig. 5.18 (left figure). The figures on the right demonstrate the intensity distribution for the different atmospheric layers. *L*7 is the range bin at 1.2 km altitude. The signals include the *dco* and the background light. The signal of the atmospheric layer is slightly broadened. The signal at the background range bin (*L*0) was expected to have a uniform distribution and the asymmetric signal points out an inadequately alignment. The fringe is not centred but shifted to the right due to a laser frequency shift.

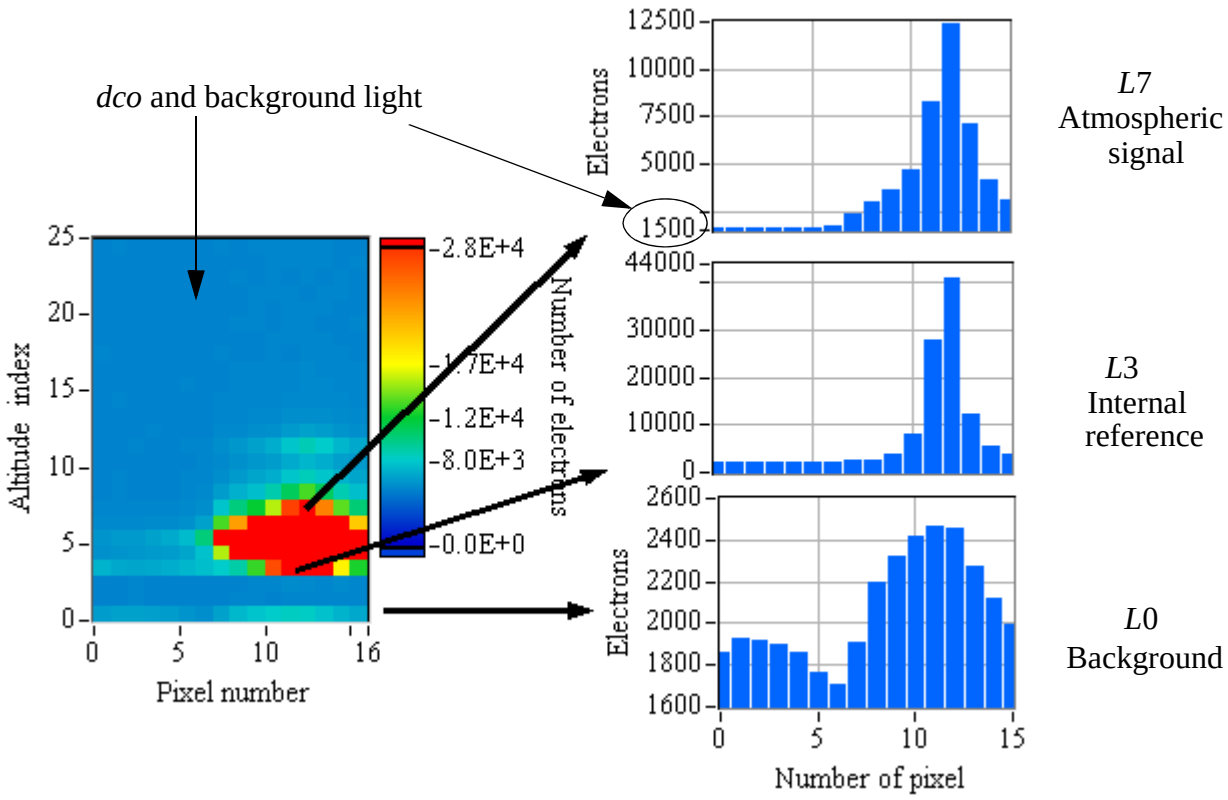

Fig. 5.18 The measured electrons at the Mie ACCD depending on altitude and pixel index (left), and the corresponding number of electrons at the 16 pixels for different atmospheric layers (right). *L*7 is the atmospheric layer at 1.2 km distance, *L*3 shows the signal of the internal reference and the background signal is at range bin *L*0 (17.11.2005 10:48:35).

The Rayleigh and Mie receiver signals after reduction of background light and the *dco* are shown in Fig. 5.19. The output of the detection unit is a numerical value. The number of electrons (*e*-) at the ACCD is calculated by the transfer factor of the analogue-digital converter. The Mie ACCD factor is 0.342/*e*- and the Rayleigh ACCD factor is 0.333/*e*- (EADS-Astrium 2005b). The *dco* for the Rayleigh ACCD is 1204 *e*- (standard deviation 7.5 *e*-) and for the Mie ACCD is 906 *e*- (standard deviation 5.5 *e*-).

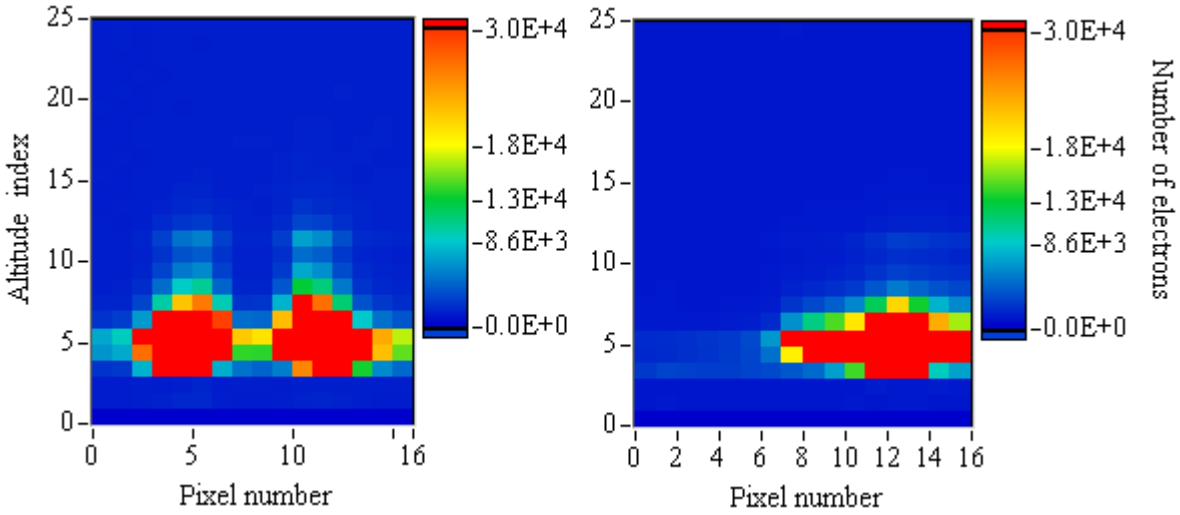

Fig. 5.19 The Rayleigh receiver signals (left) and Mie receiver signals (right) without background light and *dco* (17.11.2005 10:48:35).

The vertical intensity profiles depending on altitude are illustrated in Fig. 5.20 compared to simulations with AProS (assuming a laser energy of 13 mJ, 400 µrad laser divergence, and the median aerosol model). The intensity profiles show the number of electrons added up for all 16 pixel for each altitude layer (without background and *dco*). The left figure (a) demonstrates the electrons at Rayleigh channel *A* and *B* and Fig. 5.20(b) illustrates the number of electrons at the Mie receiver (the electrons of all pixels are summed up).

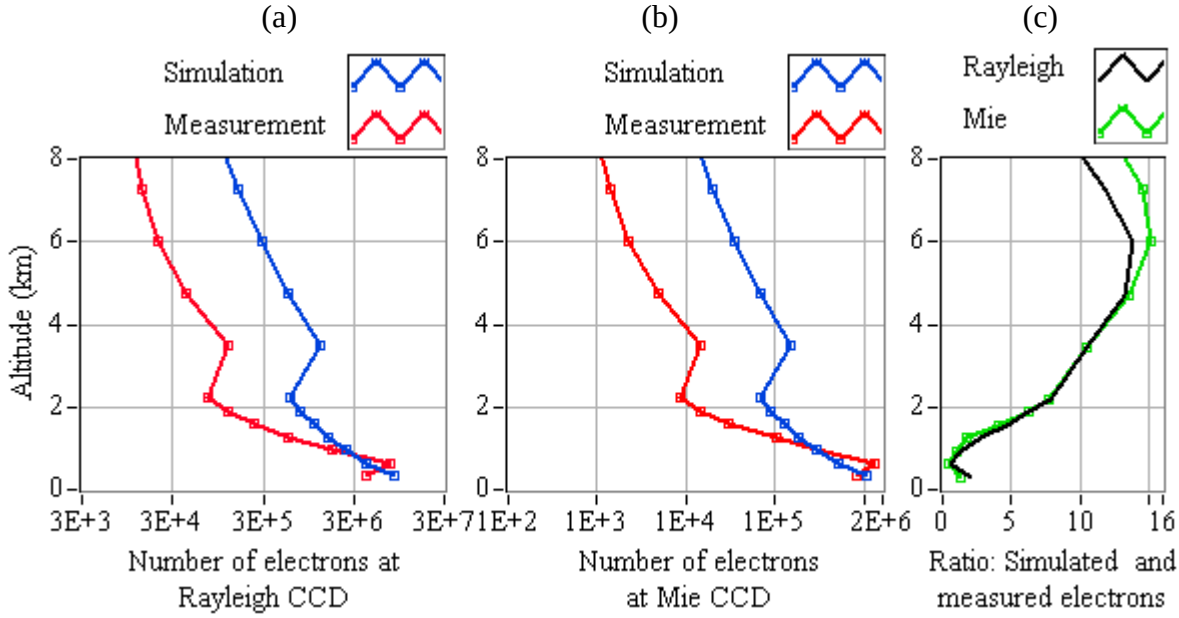

Fig. 5.20 The measured electrons at the ACCD at the Rayleigh receiver (a) and the electrons at the Mie receiver (b) compared to simulation results versus altitude. The ratio of the simulated and measured intensities is shown in the right figure (17.11.2005 10:48:35).

There are backscattered intensities up to 8 km altitude at the Rayleigh receiver in the case of clear air, demonstrating the feasibility how far signals may be measured for the current laser parameters and fine alignment. There is a bend at 3 km caused by an increased integration time of 8.4 µs (instead of 2.1 µs). The ratio of the simulated and measured intensities is illustrated in the right figure. Near the instrument, the intensity values coincide to the simulations, and for an increased distance they differ by a factor smaller than 16, which can be attributed to the alignment of the prototype.

5.1.4 Mie return of a non moving target

A building was used as a non-moving target at 1134 m distance to the container, determined by a laser range finder. The wall of the building generates a high Mie backscatter return, allowing to optimise the alignment of the instrument and to determine the random error at the Mie receiver. The laser beam was reflected to an additional installed mirror at the roof of the container and then directed horizontally to the ground towards the wall (Fig. 5.21). The reflected intensities of the wall were measured in range bin *L*7 containing the range from 975 m to 1290 m. The timing of the laser pulse extraction with respect to the detection integration time is demonstrated in Fig. 5.21. The optical path towards the atmosphere is opened at the time the laser pulse is sending out. To avoid impact of atmospheric backscatter at the internal reference as far as possible, the laser pulse is transmitted close to the end of the third time interval. The signal at the ACCD arises from the internal reference and an atmospheric backscatter corresponding to a range of about 30 m. The atmospheric signal resulting from a 30 m range is quite poor compared to the internal reference at *L*3. The first atmospheric range (*L*4) covers the distances from 30 m to 345 m.

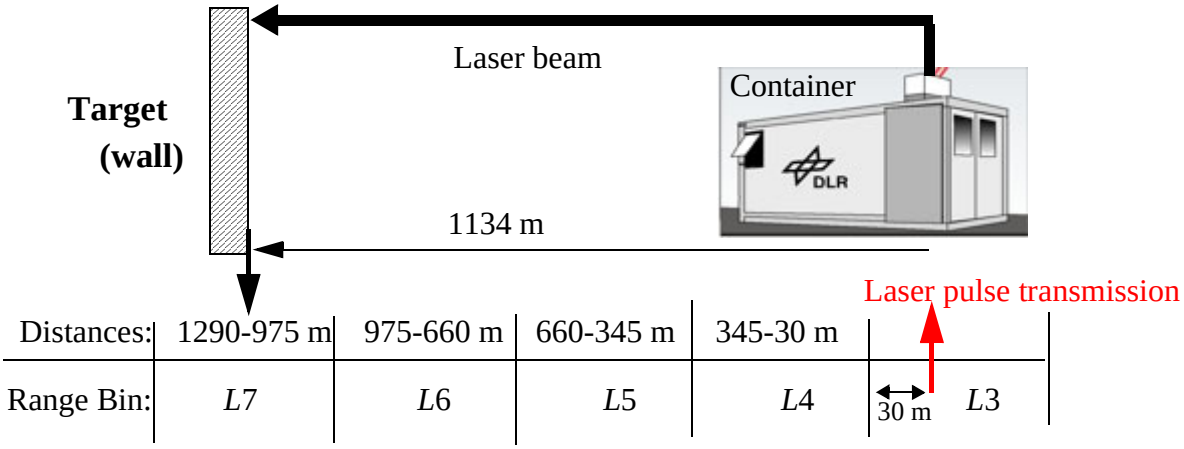

Fig. 5.21 A sketch of the wall, the laser beam path, the container, and the distances in respect to the ACCD integration times (atmospheric layers 3-7). The laser pulse is transmitted during the integration time of the ACCD at range bin *L*3 and the return of the target is obtained in range bin *L*7.

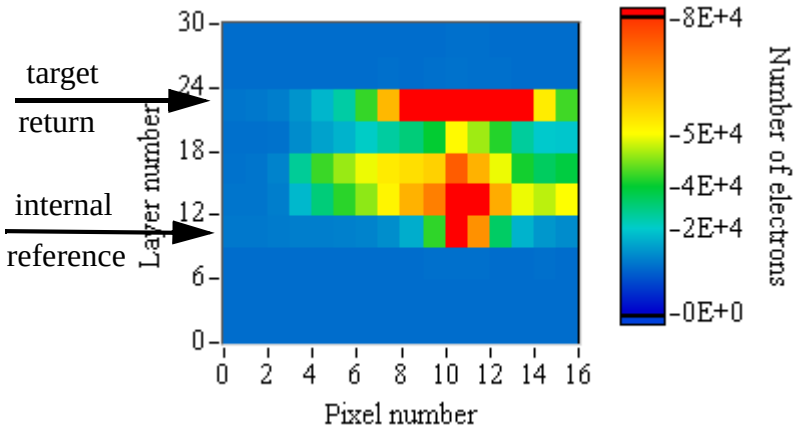

Fig. 5.22 The number of electrons at the Mie ACCD versus pixel index. The internal reference is at range bin 3 and the return of the wall is at range bin 7 (17.11.2005 20:46:08).

There is an increased intensity obtained at *L*7, arising from the hard target. The angle of incidence was 40° (determined from an aerial view). The intensity distribution shows the signal shape from the hard target corresponding to the internal reference (Fig. 5.23).

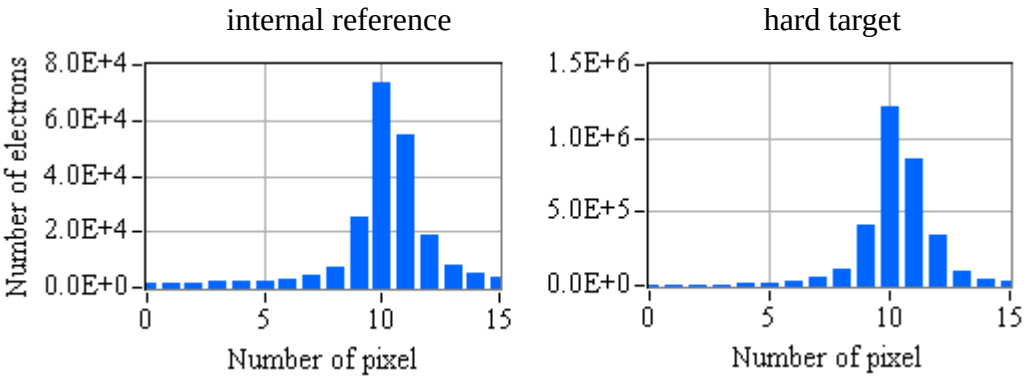

Fig. 5.23 The number of electrons at the ACCD versus pixel index. The signal shape of the internal reference (left) and the hard target (right).

The FWHM of the signal of the internal reference is 1.572 pixel (0.0683 pm) and the backscatter signal from the wall is 1.629 pixel (0.0708 pm), which was calculated from the downhill simplex algorithm (FWHM start value 0.1 pm). This shows a good accordance due to a small discrepancy of 3.5 %. The random error and the bias of the internal reference and the target were calculated and the random error of the difference between both (Table 5.3). The Gauss correlation algorithm was applied for a FWHM of 0.2 pm. The test was used to align the instrument and the number of observations was determined by the time in between the alignments.

Table 5.3 The random error and the bias of the target test

Number of wind estimates	Number of laser pulses per wind estimate	Bias: Δ internal to target (m/s)	Random error internal (m/s)	Random error target (m/s)	Random error Δ internal to target (m/s)	Time
21	700	-3.53	0.80	0.79	0.59	20:31
32	700	-6.31	1.82	1.63	1.04	19:25
25	700	-1.32	1.88	1.67	1.16	19:16
294	50	-3.54	0.89	1.18	1.04	20:31
448	50	-6.28	2.10	1.92	1.54	19:25
350	50	-1.24	2.09	2.03	1.61	19:16

The random error of the internal reference depends on laser frequency fluctuations and varies form 2.1 m/s to 0.8 m/s considering the observations. The difference of the random error between the internal reference and the target depends on the random error of the internal reference signal. The error is small for a low random error of the internal reference and increases for an increased random error of the internal signal. The bias obviously depends on the alignment and is consistent through the observations (for each measurement) between the active alignments of the instrument.

Simulations were performed at 58 mJ laser energy[1], 400 µrad laser divergence, 0.5 km distance to the instrument at ground, with the telescope pointing to zenith, for 700 accumulated laser pulses, and 21 observations, using the median aerosol model. The random errors result in values below 0.1 m/s, smaller than measured (0.79 m/s), because the laser parameter variations (e.g. frequency fluctuations) are not taken into account for the simulations. The signal of the target includes atmospheric backscatter. The calculated signal backscatter from a wall (assuming a backscatter coefficient of 10^{-5} m^{-1} sr^{-1} in an atmospheric layer of 500 m and an albedo of 0.01, like grass) is about 2 times stronger than measured. The atmospheric signal (Doppler-shifted by wind) is mixed with the signal from the wall and may result in a broadened signal at the receiver, with asymmetric signal shape, and a shift of the maximum location.

5.1.5 Clouds

In the case of clouds, increased Mie backscatter is expected. At November 17th, clouds between 800 m and 1000 m altitude were detected by MULIS (MUlti purpose LIdar System, Mattais et al. 2004, Wiegner et al. 2004), which was deployed besides the DLR container of the prototype. Taking the laser transmission time into account, the 6th range bin includes atmospheric backscatter from 660 m to 975 m altitude. The backscatter intensity profiles are shown in Fig. 5.24.

1. The laser energy was determined by the signal strength at the Mie receiver. 58 mJ laser energy during simulations provides the same signal strength at 0.5 km distance as the return of the wall from measurement.

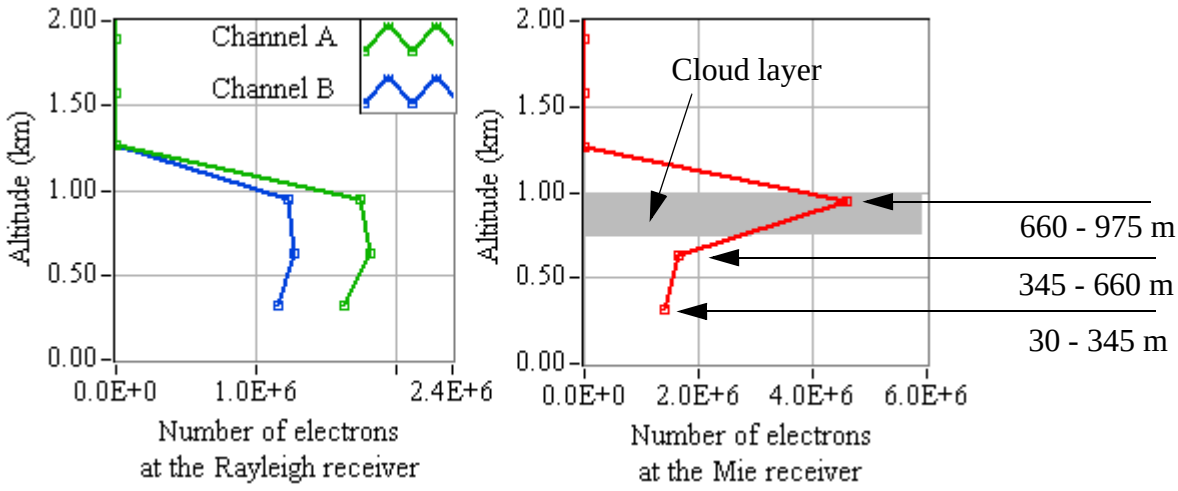

Fig. 5.24 The number of electrons at the Rayleigh receiver channel *A* and *B* (left) and at the Mie receiver (right) versus altitude (17.11.2005 12:03:00). The increased Mie backscatter (red line) of the cloud (grey field) is indicated at the Mie receiver for the distance of 660-975 m.

The intensity distribution of the backscatter signals at the Mie receiver is presented in the following figure. There is a clear fringe at range bin 3 (internal reference). A slightly broadened and asymmetric fringe is detected from the atmospheric layers four and five due to misalignment effects. There is a clear signal at range bin 6 with strongly increased intensities. The intensities at range bin seven are quite low (attenuation above clouds), but a clear fringe is still detected (1 km distance).

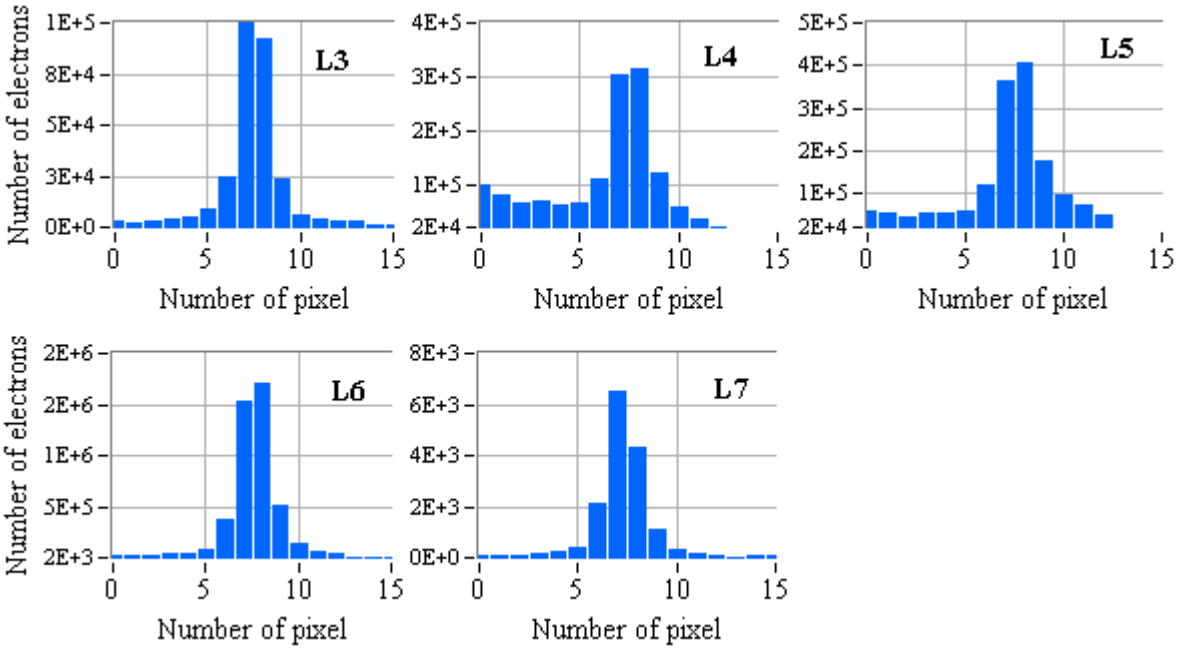

Fig. 5.25 Number of electrons at the Mie ACCD versus pixel index for different range bins. The internal reference at range bin *L*3, atmospheric signal at the range bins *L*4, *L*5, *L*7, and the cloud backscatter at range bin *L*6.

5.2 Airborne measurements

Flights with the prototype instrument were performed on October the 18th and 20th to test the system, concerning vibrations and to ensure the compatibility of the prototype with the aircraft. These were the first airborne direct detection Doppler wind lidar measurements worldwide. The laser was not operating in single frequency mode during flight, because of the vibrations of the aircraft and the signals are only analysed in respect to the intensities. The results presented in the following were provided during the second flight on October 20th. The flight altitude was at 8.2 km (ASL) and the laser beam was sent 20° off nadir into the atmosphere. The measurements start at 13:45 and ended at 17:00. An overview of the backscatter intensities at the Rayleigh and Mie receiver (all pixels summed up per atmospheric layer) along the flight track is shown in Fig. 5.26. Each vertical profile represents the intensities of all pixels for one observation. During these measurements, the internal reference was at range bin 4.

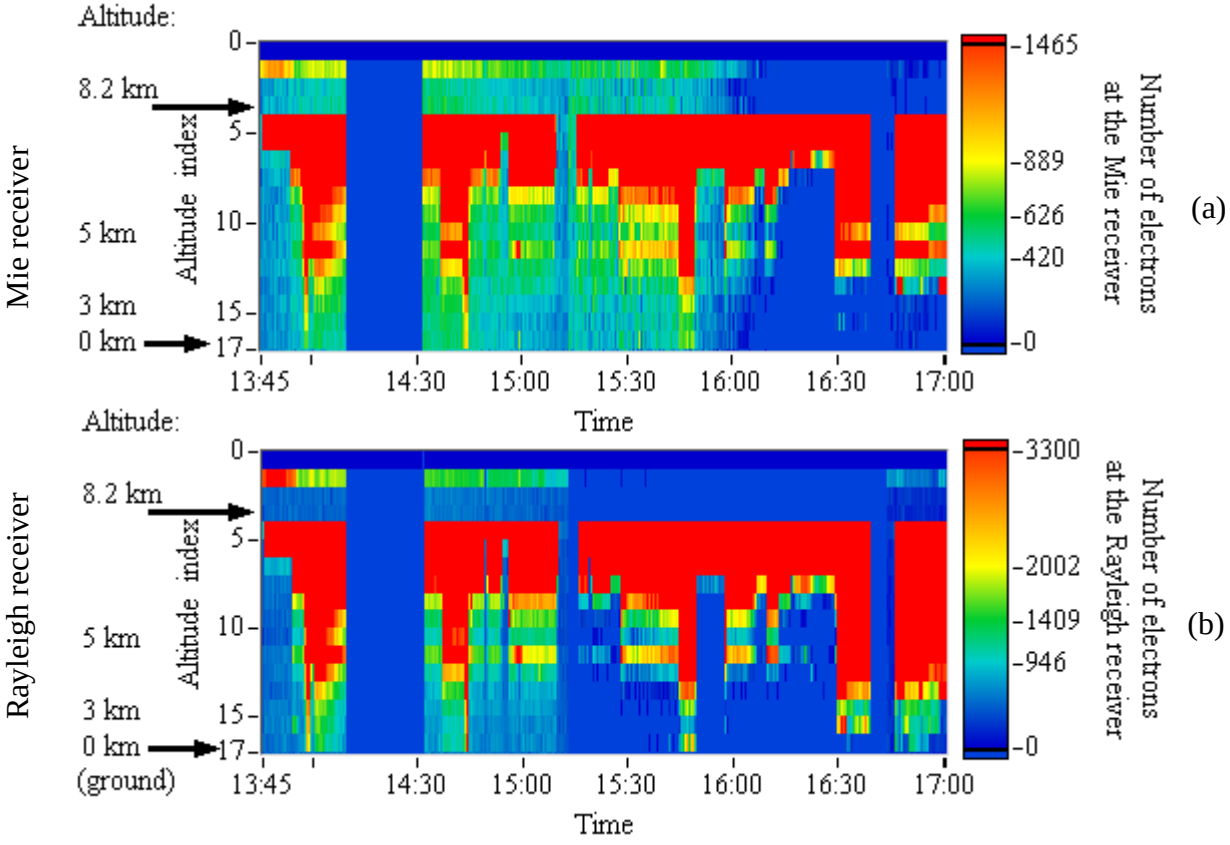

Fig. 5.26 The number of detected electrons at the Mie ACCD (a) and at the Rayleigh ACCD (b) versus the time of the flight. The electrons of each atmospheric layer of one profile is the amount of all electrons at the 16 pixels for both the Mie and Rayleigh receiver (20.10.2005).

At times around 14:20, 15:10, and 16:40 there are no backscatter signals, because the image mode of the ACCD was tested and settings were improved. Depending on the transmitter and the receiver settings and atmospheric conditions, the Rayleigh signal may be detected down to ground (15:45). Strong backscatter from clouds at the Rayleigh and Mie receiver was measured at 3 km distance to the instrument north of Munich (around 13:56:41).

Ground return was detected from the observations depending on ground height. At 15:29:11 the flight passed northern Germany (Frankfurt a. d. Oder, 200 m ASL). The ground was expected at 8 km distance to the aircraft (range bin 16, 7.71 km - 8.9 km range). The results are shown in Fig. 5.27. There are increased intensities at both the Rayleigh and Mie receiver at range bin 16, which results from the Mie backscatter of the ground return.

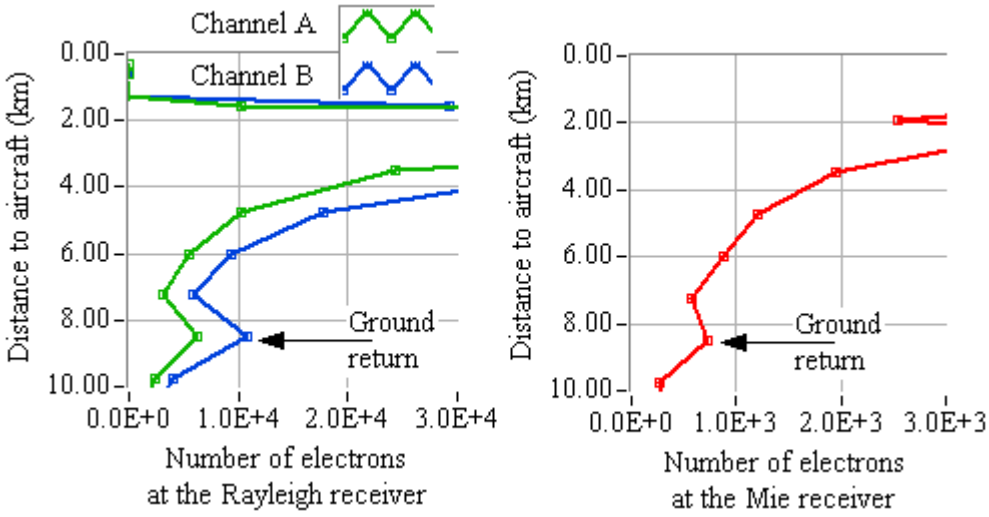

Fig. 5.27 The number of electrons at the Rayleigh receiver of channel *A* and *B* (left) and the number of electrons at the Mie receiver of all 16 pixels (right) versus altitude. The increased number of electrons due to the ground return is detected at the Rayleigh (left) and Mie (right) ACCD (northern Germany, 15:29:11).

Crossing the Bayrischer Wald (1400 m ASL), the ground was at 6.8 km distance to the aircraft (range bin 15). The signal shape of the Mie signal at range bin 15 is more clear than from ground return at range bin 16 (Fig. 5.27) and the results are illustrated in Fig. 5.28.

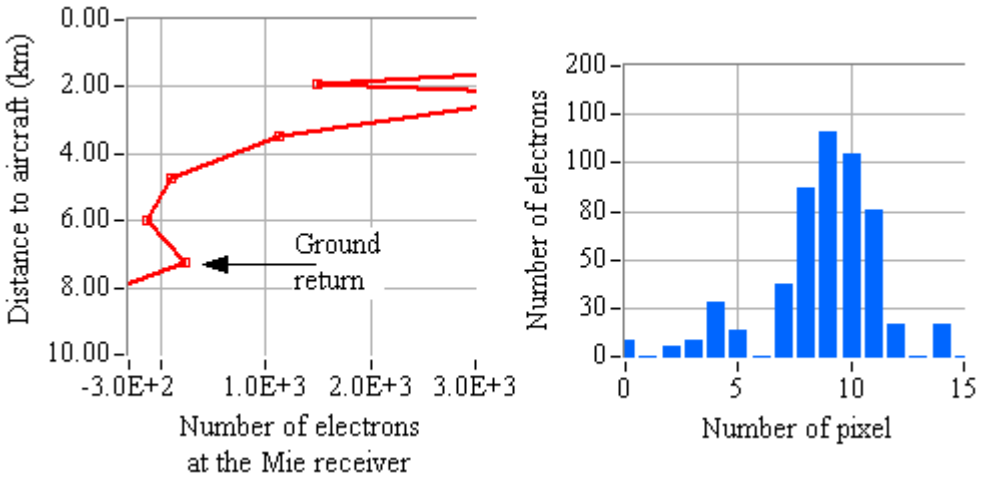

Fig. 5.28 The number of electrons at the Mie receiver for all 16 pixels versus altitude (left) and the number of electrons of the ground return at the Mie receiver versus pixel index (right, Bayrischer Wald, 16:06:22).

During the flight measurements, the Rayleigh backscatter signal was detected down to ground, showing the system capability to provide signals up to 8 km distance. The Mie signal was backscattered near the aircraft and significantly from clouds, and was measured at both the Rayleigh and Mie receiver. The ground return was weak, but was detected, actually the Mie signal shape was observable.

Summary

It was demonstrated, that the atmospheric backscatter intensities for both the Rayleigh and Mie receiver are lower than from simulations by a factor smaller than 16 up to altitudes of 8 km, which can be attributed to the alignment of the prototype. Due to the unknown laser properties, as energy and frequency fluctuations, the wind speed was not determined, but the backscatter signal of the surface of a building demonstrates the wind accuracy of the instrument and leads to a minimum random error of 0.59 m/s. Clouds were detected from ground and from airborne measurements, and the ground return was detected from airborne measurements, which were identified by an increased Mie backscatter signal.

6 Summary and conclusion

In the framework of the ADM programme, an instrumental prototype was designed, consisting of two receivers: one to detect aerosol (Mie) backscatter, and one to detect molecular (Rayleigh) backscatter, and the Doppler shift is determined from these two measurements. The Rayleigh receiver is a radiometric detector, whereby the Doppler shift is determined from a change in intensity, and employs the principle of the double-edge method in a new implementation of the Fabry-Perot interferometer, called the sequential technique. The Mie receiver consists of a Fizeau interferometer, which has never been used for atmospheric wind measurements before, and the Doppler shift is determined from the spatial location of the Mie signal at the detector by employing the fringe imaging technique.

The most important objective of this thesis was the potential to apply advanced signal processing algorithms with regard to the different modelled signals provided by the simulator. Because of the new design of the Mie receiver, and the low wind speed resolution of 18.3 m/s per pixel, various algorithms had to be developed, analysed, and evaluated. The results of a Gauss correlation, a maximum likelihood method, and the downhill simplex algorithm were demonstrated to perform adequately in respect to signals without any noise. The residual LOS wind speed bias was below 0.15 m/s, and the random error was smaller than 0.15 m/s in respect to the algorithms for the case, the signal intensity is about 2 times stronger than the noise. The impact of the number of pixels on the wind speed estimate of the Mie receiver ACCD was analysed and it was shown that increasing the number of pixels at the ACCD from 16 to 20, the error is reduced by a factor of 5.

Mie backscatter leads to a systematic error on the Rayleigh receiver due to differences in the spectral width of the signals, and the impact of Mie backscatter was analysed by simulations. A new method was presented to obtain the wind speed estimate from a new receiver response function, which is modelled by the signal information of the Mie receiver and takes the Mie backscatter into account. The error from Mie contamination at the Rayleigh receiver with a backscatter ratio of 1.56 is reduced by a factor of 10.

In the scope of this work, a simulator was developed to estimate the performance of the prototype for different atmospheric conditions and different instrumental parameters. The simulated LOS wind speed random error of the airborne instrument, at a flight altitude of 10 km and a laser energy larger than 10 mJ, was below 0.5 m/s for both the Mie and Rayleigh receiver. The ground system LOS wind speed random error of the Rayleigh receiver was below 1 m/s (2-10 km altitude) and 0.2 m/s for the Mie receiver (0-2 km altitude).

The first results of measurements from ground and aircraft were presented and analysed by simulations. Both the calibration and the atmospheric measurements were analysed and evaluated. Due to the laser frequency and energy instability, wind was not quantified but the wind speed measurement accuracy was determined by the measured backscatter signal of the surface of a building. This system configuration is the first to be considered worldwide, as well as this being the first time a direct detection Doppler wind lidar has been deployed on aircraft.

The measurements resulting from the Rayleigh internal calibration were in good agreement to the simulated data. The linearity error of the measurements agrees with the simulations in amplitude and shape, but the response function differs in sensitivity, yielding a sensitivity of 0.0398 %/MHz from measurement and 0.057 %/MHz from simulations. It was shown that this discrepancy results

from the simulated filter curves which have a Lorentzian profile, and appear to be steeper for lower transmissions near the cross point, than the filter curves of the measurements. The measurements resulting from the Rayleigh atmospheric calibration demonstrate an evident decrease in sensitivity caused by Mie backscatter and lower signal, which was then confirmed by simulations.

The measurements of the Mie internal calibration correspond well with the simulations. The mean measured sensitivity was 99.98 MHz/pixel, whilst the simulations yielded a sensitivity of 103.4 MHz/pixel. The linearity error of the measurements showed an asymmetric shape compared to the symmetric shape of the simulations, both calculated with the Gauss correlation algorithm.

Atmospheric measurements from the ground were consistent with simulations with respect to the intensities at the detector for near-field measurements assuming a higher laser divergence than specified. For higher altitudes (> 1 km), differences in intensity between simulations and measurements by a factor of 10 arise from lower measured signals from both the Rayleigh and Mie receiver. This can be attributed to higher laser divergence, the alignment of the optical path, and the inadequate knowledge of the atmospheric parameters, hence incorrect simulation input parameters.

A test on ground was performed, where the backscatter signal from the surface of a building was used to align the instrument, to control the integration times, and to assess the random error of the Mie receiver. The building was at a distance of 1134 m, and as expected, the increased Mie backscatter signal of the wall was detected in the corresponding range bin. The random error was determined by a shift of the signal at the Mie receiver with respect to the internal reference. The random error was 1.18 m/s (50 laser pulses accumulation) and 0.79 m/s (700 laser pulses accumulation).

Increased signal intensities at the Rayleigh and Mie receiver were shown in the case of clouds, and the increased attenuation above clouds was demonstrated. It was shown that the Rayleigh signal can be detected from the ground up to altitudes of 10 km in clear air.

The very first airborne measurements were presented and discussed. Signals down to ground, backscatter from clouds, and signals of the Earth’s surface were detected by the instrument at 8.2 km flight altitude.

In conclusion, the end-to-end simulator is a tool for estimating the performance of the prototype, to examine in detail the impact of different instrumental and atmospheric parameters, and to develop and analyse the signal processing algorithms. The extensive development of the algorithms in advance has been shown to provide significant benefits during the first measurements with the prototype. Both the signal processing algorithms and the simulations were crucial to process, analyse, and evaluate the measured signals.

As a next step, the prototype will be tested during a ground campaign at the meteorological observatory of the German Weather Service in Lindenberg. The reference instruments for comparison will be a 2 µm heterodyne Doppler lidar from DLR and a wind-profiler radar from the German Weather Service. The prototype and the 2 µm Doppler lidar will be integrated in the Falcon aircraft for further flight campaigns. The measurement results will be used to validate the signal processing algorithms and to develop quality control schemes necessary for the space-borne lidar data.

A Interferometer

A.1 Fabry-Perot interferometer

Fabry-Perot interferometers are based on thin quartz plates (etalons) coated with high reflectivity layers, and they act as spectral filters. Depending on wavelength the incident light at the etalon surface is transmitted through the filter either with constructive interference, or reduced in magnitude by destructive interference and reflection (Born and Wolf 1972 p. 128, Naumann and Schröder 1992 p. 258). The Fabry-Perot interferometer consists of two parallel etalons, where multiple reflection occur between the plates, which cause the light to interfere. Commonly Fabry-Perot interferometers are used in spectroscopy and for laser resonators. The Fabry-Perot interferometer etalons and the optical path are illustrated in Fig. A.1.

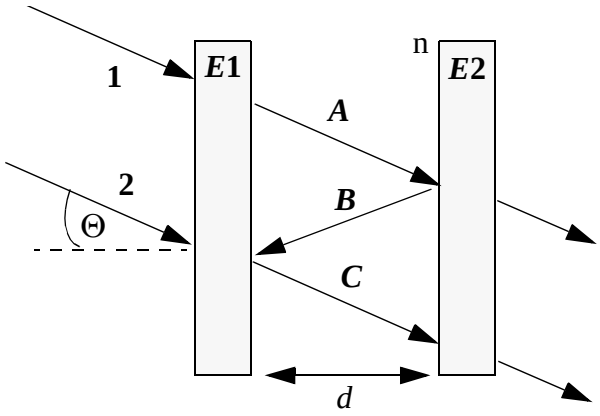

Fig. A.1 A schematic view of the Fabry-Perot interferometer etalons and the optical path.

The incident light (1) travelling from the left to right is transmitted (*A*) by the first etalon (*E*1) and reflected and transmitted by the second etalon (*E*2). Both etalons have a high reflection coating at the inner side. The light is reflected back and forth between both parallel surfaces. The reflected light (*B*) back to *E*1 is superposed with the incident light (2) and is transmitted forward the second etalon (*C*).

The optical path difference caused by the way *B* induces a phase difference ψ to the incident light (2) which is given by:

$$\psi = \frac{2nd}{\lambda} \cdot 2\pi \cdot cos\Theta \tag{A.1}$$

where n is the refractive index of the medium between the etalons, d is the separation of the etalons, λ the wavelength of the incident light, and Θ is the angle of the incident beam. The light interfere by superposition for constructive or destructive interference. The transmitted light of the interferometer has maximum intensity for a phase shift of $2k\pi$, where k is an integer. For the case, the path length difference is a multiple number of the wavelength, the transmission T is maximal:

$$k \cdot \lambda = 2nd \cdot cos\Theta \tag{A.2}$$

Fig. A.2 illustrates the arrangement of a Fabry-Perot interferometer. Light from a monochromatic light source is transmitted through lens one (*L*1) to parallelise the rays of light. The light passing the Fabry-Perot interferometer is reflected and transmitted depending on wavelength. Lens two (*L*2) collimates the light to generate a sharp image at the image plane. The intensity maxima (fringes) at the image plane arise from constructive interference. They (enclosing *P*2) are generated by inclined incident light with an angle Θ. The fringe of the first order (*P*1) is produced by perpendicular incident light. For the incident wavelength λ there is constructive interference at P1 and P2 depending on the angle of incidence.

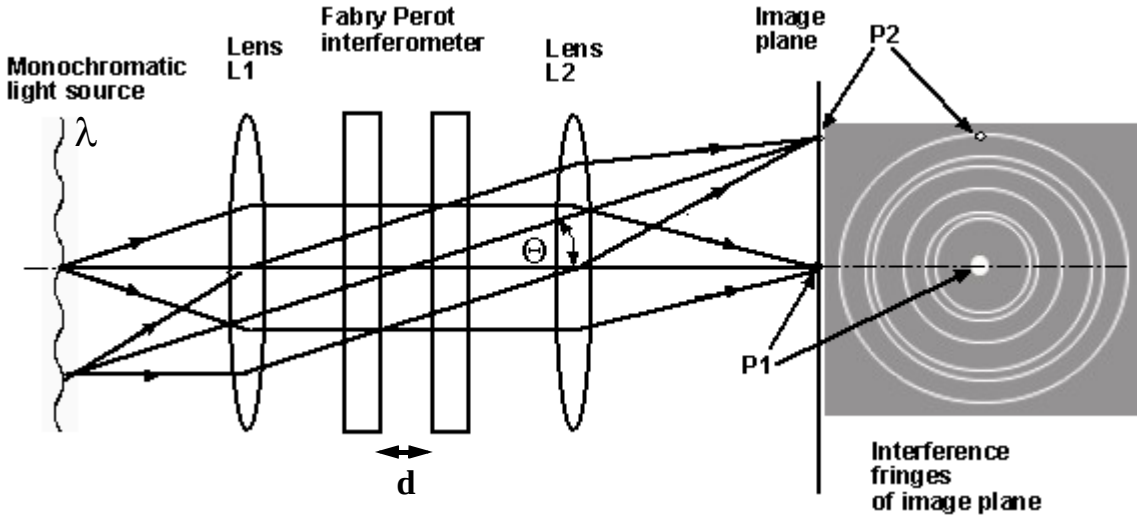

Fig. A.2 An illustration of a basic Fabry-Perot interferometer arrangement. Monochromatic light coming from the left is parallelised by lens *L*1, transmitted through the Fabry-Perot and then collimated by lens *L*2 to image clear and sharp fringes at the detector. The spacing of the plates *d* and the angle of incident light Θ are indicated.

The fringe pattern consists of circular bright rings (Born and Wolf 1972 p. 121), where the intensity distribution of each fringe depends on the phase shift. The transmission depending on ψ (EQ. A.1) can be expressed by the Airy function and may be written as (Koechner 1976 p. 205):

$$T = \left[1 + \frac{4R}{(1-R)^2} \cdot \left(sin\frac{\psi}{2}\right)^2\right]^{-1} \tag{A.3}$$

where *R* is the reflectivity of each the inner coatings of the etalon surfaces. The intensities at the detector are the result of the incident light and the transmission curves of the interferometer as illustrated in Fig. A.3. The transmission curves depend on the reflection of the etalons inner surface coating.

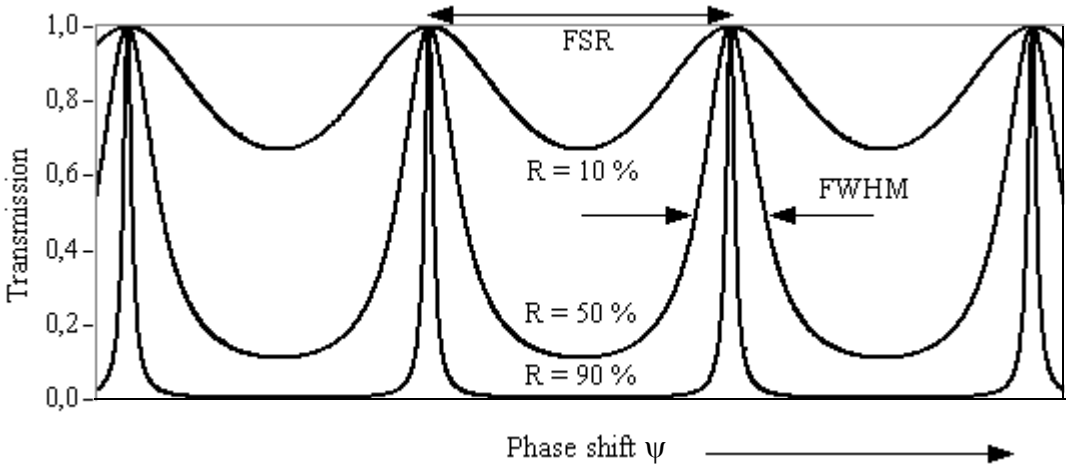

Fig. A.3 The transmission curves of an interferometer depending on phase shift y and referring to different reflection coefficients (10 %, 50 %, and 90 %) of the etalons. The free spectral range FWR and the full-width half-maximum FWHM of the transmission curves are indicated.

Higher reflection (R=90 %) leads to a smaller full-width half-maximum (FWHM) of the transmission curves and results in narrow but intensive fringes at the detector. The spacing of the transmission maxima is called free spectral range (FSR) and depends on the wavelength λ and incidence angle. The wavelength difference between two fringes ($\Delta\lambda_{FSR}$) may be described as (Koechner 1976 p. 206):

$$\Delta\lambda_{FSR} = \frac{\lambda^2}{2nd \cdot cos\Theta} \tag{A.4}$$

Assuming a Lorentzian transmission curve profile, the FWHM ($\Delta\lambda_{FWHM}$) of the Lorentzian shaped fringe and the FSR determine the reflectivity Finesse F_R (Koechner 1976 p. 205):

$$F_R = \frac{\Delta\lambda_{FSR}}{\Delta\lambda_{FWHM}} \tag{A.5}$$

The reflectivity Finesse is a measure of the sharpness of the fringes of a Fabry-Perot interferometer, and may be approximated by:

$$F_R = \frac{\pi \cdot \sqrt{R}}{1 - R} \tag{A.6}$$

leading to the resolvability of a Fabry Perot interferometer (Naumann and Schröder 1992 p.259):

$$\frac{\lambda}{\Delta\lambda_{FWHM}} = \frac{2nd}{\Delta\lambda_{FSR}} \cdot \frac{\pi \cdot \sqrt{R}}{1 - R} \tag{A.7}$$

Common interferometers are characterized by reflection coefficients of about 90 % and provide sharp and intense fringes at the detector.

From EQ. A.2 the factor $cos\,\Theta$ may be expanded with a series resulting in: $cos\,\Theta = 1 - (\Theta^2/2)$ in case of small incident angles. The radius x_k of each fringe of order k is defined by: $\Theta = x_k / f$, where f is the focal length of lens $L2$. Thus x_k may be determined from:

$$x_k = \sqrt{2f^2 \cdot \left(1 - \frac{k\,\lambda}{2nd}\right)} \tag{A.8}$$

A.2 Fizeau interferometer

The difference from a Fizeau to the Fabry-Perot interferometer are the two thin quartz plates where the spacing is not constant (wedge shaped). The Fizeau interferometer produces almost linear narrow interference fringes. The Fizeau transmission curves are shown in Fig. A.4. Each curve is related to a definite spatial location of the incident beam of light at the Fizeau wedge. Accordingly, there is an infinite number of transmission curves in respect to all kinds of possible locations of incoming rays. The Fizeau interferometer is used for the Mie receiver. The wavelength difference between consecutive transmission maxima is defined as the free spectral range (FSR, see EQ. A.4). The useful spectral range (USR) is determined by the wind speed measurement requirement.

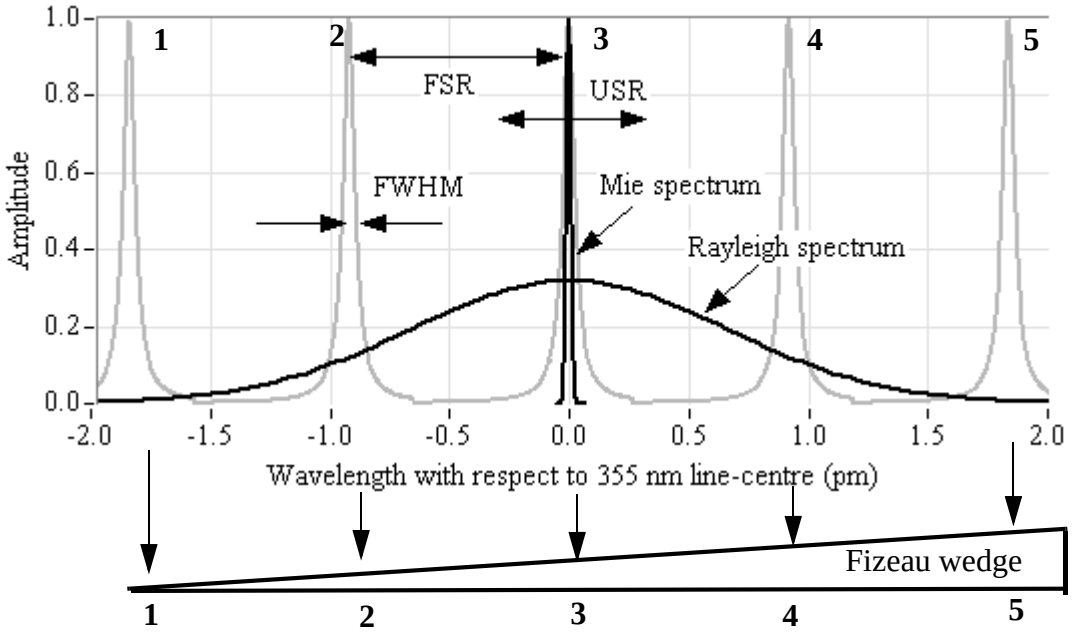

Fig. A.4 Fizeau transmission curves in respect to the spatial locations of the incident light at the Fizeau. The free spectral range FSR, the useful spectral range USR, and the full-width half-maximum FWHM are indicated.

The location of the fringe indicates the wavelength of the incident light. The distance of the fringes at the detector depending on the angle of incidence Θ is determined by:

$$\Delta\lambda_{FSR} = \frac{\lambda}{2\ tan\alpha\ \sqrt{n^2 - (sin\Theta)^2}} \tag{A.9}$$

where α is the wedge angle (angle between both etalons) and n the refractive index of the wedge. The optical gap between the plates and the reflectivity are selected to provide the desired resolution.

Some investigation were done to validate the fringe pattern (Kinosita 1953, Reichlmaier 1985, Meyer 1981) where asymmetric fringes were examined in dependence on the incident angle. An asymmetric fringe is imaged at the detector for increased wedge angles and inclined incidence of light. The symmetry of the Fizeau pattern was examined by Vaughan (2000 p. 462) and a good agreement for the computed and observed pattern was shown. Dolfi-Bouteyre and Garnier (2002) demonstrated fringe patterns for different angles of incidence and demonstrated symmetric fringes for the case of the ALADIN prototype where the angle of incidence may be assumed to be zero (Fig. A.7). The following equation is used to determine the shape of the fringes in respect to the angle of incidence , the reflectivity R, and the wedge angle α (Dolfi-Bouteyre and Garnier 2002):

$$I_0(k, \Theta) = (1 - A - R)^2 \cdot \left| \sum_0^{\infty} R^n \cdot e^{j(\varphi_n - \varphi_0)} \right|^2 \tag{A.10}$$

where n is an integer, A is the absorption, and k and Θ are considered in the phase shift which is determined by:

$$\varphi_n - \varphi_0 = \frac{2\pi k}{tan\alpha} \cdot sinn\alpha \cdot cos(\Theta + n\alpha) \tag{A.11}$$

where n is an integer. The parameter k is determined by $2e/\lambda+\Delta k$, where e is the mean thickness of the air gap between the plates and Δk is the iteration step of the calculation. The impact of the angle of incidence is illustrated in the next figure for a reflectivity of $R = 0.88$, $n \in [0, 50]$, $\Delta k = 0.01$, a mean thickness of $e = 68.5$ mm, and a wedge angle of 5 µrad (EADS-Astrium 2004):

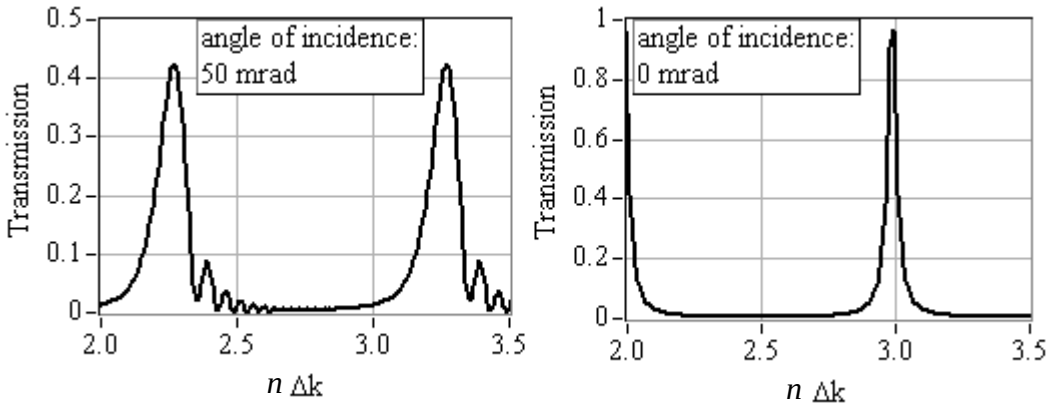

Fig. A.5 Fizeau transfer function for angles of incidence of 50 mrad (left) and 0 mrad (right) in respect to the iteration steps Δk.

For small angles of incidence, the fringe is symmetric (right). For larger angels the fringe is asymmetric, broadened, low in maximum transmission, and oscillations are displayed (left).

Fig. A.6 presents the impact of the reflectivity of the etalon plates for a wedge angle of 5 µrad and perpendicular incident light:

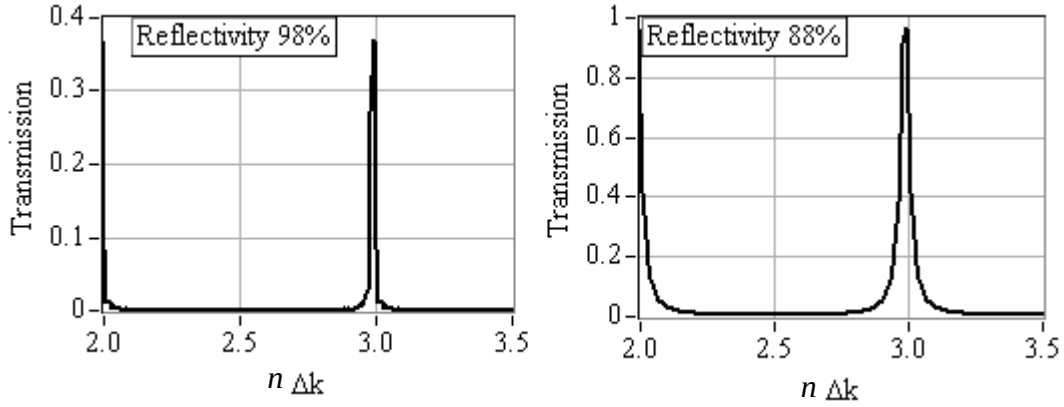

Fig. A.6 Fizeau transfer function due to reflectivity values of 98 % (left) and 88 % (right) of the etalon plates in respect to the iteration steps Δk.

For a smaller reflectivity of 88 % (ALADIN prototype parameter, right figure), the function is broader than for an increased reflectivity of 98 % (left figure).

Fig. A.7 demonstrates the impact of different wedge angles for a reflectivity of 0.88 and perpendicular incident light.

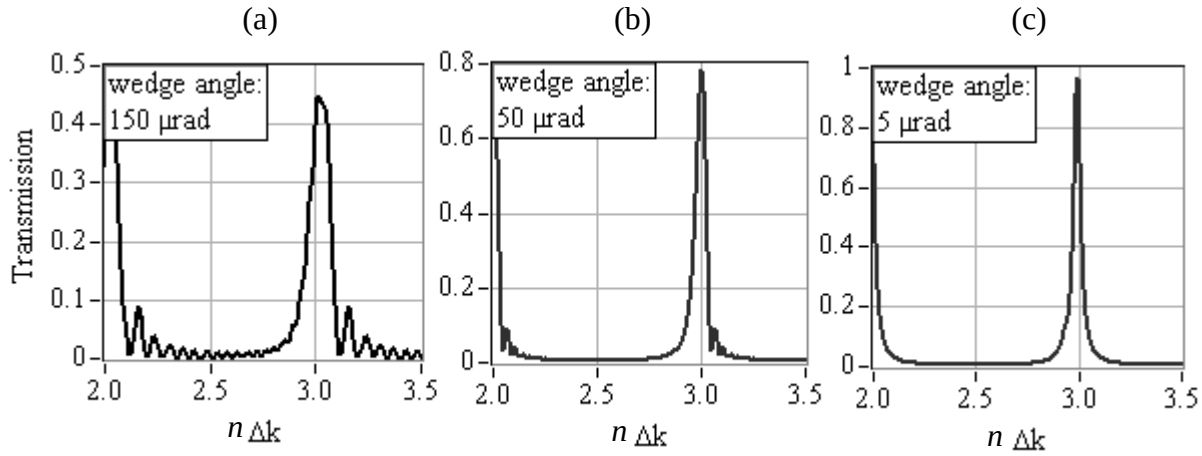

Fig. A.7 Transfer functions of the Fizeau interferometer due to different wedge angles in respect to the iteration steps Δk. The transmission curves in respect to a wedge angel of 150 µrad (a), of 50 µrad (b) and 5 µrad (c).

Fig. A.7(c) shows ALADIN prototype characteristics where the wedge angle is 5 µrad and the function may assumed to be symmetric. The figures left present a broadened function and oscillations for a wedge angel of 50 µrad (b) and 150 µrad (a). For the ALADIN prototype parameters the Fizeau filter function may assumed to be symmetric.

B ADM-Aeolus

The Atmospheric Dynamics Mission ADM-Aeolus by ESA will be the first mission worldwide to provide global observations of wind profiles by applying a Doppler wind lidar on a polar-orbiting satellite. The measurement range altitude is from ground up to 30 km. The wind measurement range for line-of-sight (LOS) wind speed is +/-100 m/s and the duration of the mission will be 3 years. The vertical resolution and accuracy for LOS and HLOS (horizontal LOS) is shown in Table B.1 (ESA 1999).

Table B.1 ADM Aeolus mission requirements: vertical resolution and LOS wind speed accuracy

Altitude	vertical resolution	LOS accuracy	HLOS accuracy
0 - 2 km	0.5 km	0.6 m/s	1 m/s
2 - 16 km	1.0 km	1.2 m/s	2 m/s
16 - 27 km	2.0 km	1.7 m/s	3 m/s

The satellite instrument will be injected into polar orbit at an altitude of 400 km for a satellite ground speed of 7700 m/s. The laser emits pulses at a repetition rate of 100 Hz in the burst mode. During the burst mode the device transmits pulses for 7 seconds followed by a phase of inactivity of 21 seconds. This mode was selected for the satellite system because of low energy demand. There are 700 laser pulses accumulated at the detector during one observation (Fig. B.1).

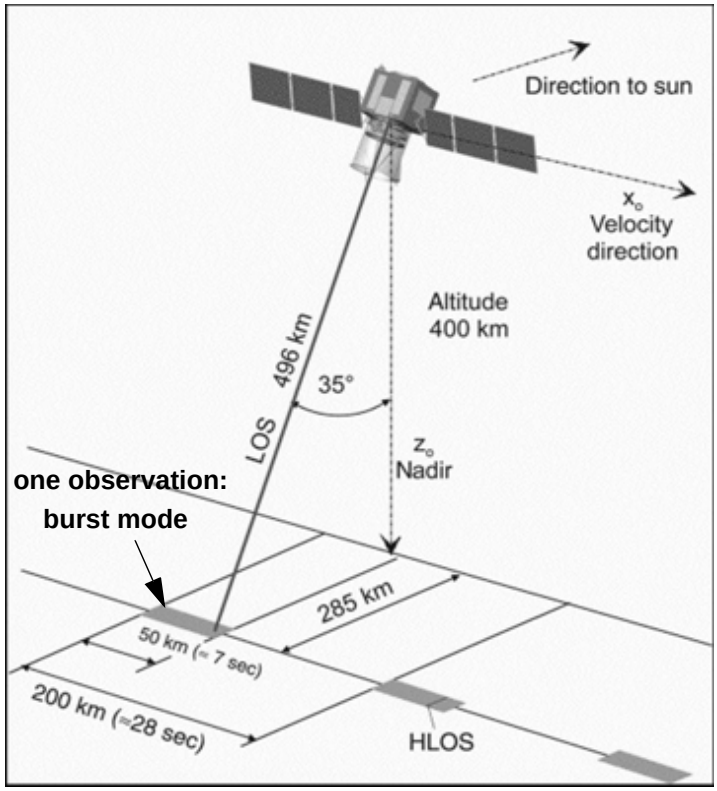

Fig. B.1 ADM-Aeolus satellite: geometry and resolution. The horizontal LOS (HLOS) is measured with 35° off nadir. The burst mode provides one observation over 50 km for every 200 km (Figure: ESA 1999).

The prototype was built to validate the ALADIN measurement concept in realistic atmospheric conditions by providing wind measurements from ground and aircraft during campaigns planned in 2006. For this purpose any differences of the satellite and the prototype have to be considered.

The satellite uses a slant angle 35° off nadir (Section B), which was chosen to optimise the accuracy of the instrument. The aircraft system slant angel (20° off nadir) is constrained by the diameter of the aircraft window, the laser beam extraction, and telescope diameter. The measurements form the ALADIN prototype during ground campaign in Lindenberg will be compared to a wind profiler in Lindenberg, which provides measurements 15° off zenith. To achieve comparable data, the ground system also measures at a slant angle 15° off nadir.

The vertical resolution depends on the slant angle and the integration time of ACCD. The airborne system, with a range resolution of 315 m along the LOS due to the 2.1 µs integration time, and a slant angle of 20°, achieves a vertical resolution of 296 m.

The parameters of the lidar system ALADIN on the satellite platform differs from those used in the prototype in the airborne and the ground system (Table B.2, ESA 1999, Reitebuch 2004).

Table B.2 Satellite and airborne and ground system parameters

	Satellite	**Airborne, ground**
Transmitter type	Diode pumped Nd:YAG	
Emission wavelength	355 nm	
Repetition rate	100 Hz	50 Hz
Pulse energy	150 mJ	70 mJ
Laser linewidth (FWHM)	< 50 MHz	
Operation mode	Pulsed in burst mode	Steady pulsed
Laser frequency stability (standard deviation)	4 MHz over 7 sec.	4 MHz over 7 sec.
Telescope diameter	1.5 m	0.2 m
Slant angle	35°	20° (airborne) 15° (ground)
Measurement range	20 - 30 km	Aircraft flight altitude 10 km Ground: up to 30 km
Instrument altitude	400 km	Aircraft: 10 km Ground: 0 km
Accumulated laser pulses for one observation	700	700
Vertical resolution (minimum)	250 m	296 m
Horizontal resolution	50 km	3 km
Platform speed (typical)	7600 m/s	200 m/s
Laser divergence (µrad)	10 µrad	70 µrad
Receiver field of view	15 µrad	100 µrad

The field of view determines the angle where a backscatter signal is received and is limited by the field stop of the telescope (Born and Wolf 1972 p. 83). The smaller the FOV the less background

light which is collected. This is an important consideration for the satellite, because of the low backscatter signal at 400 km altitude. Consequently the telescope diameter is larger for the satellite system to catch more backscatter light and a higher laser energy is needed to reduce the noise. The horizontal resolution results from the repetition rate and the number of accumulated laser pulses. The concept was designed to produce wind measurements by accumulation of 700 laser pulses. This is equivalent to the time resolution for ground-based measurements of 14 s, which have a pulse repetition rate of 50 Hz, and a horizontal resolution for airborne measurements of about 3 km, assuming an aircraft ground speed of 220 m/s. The measurement range of the ground system is limited by the detectors capability to store data for 25 range bins. The horizontal resolution of the satellite system is one observation over 50 km each 200 km. The major differences between the prototype and the satellite are the vertical and horizontal resolution, the overlap and obscuration of the telescope, and the different backscatter intensities in respect to the laser parameters and the measurement range. Furthermore the footprint of the satellite (24 m) differs to the footprint of the aircraft system (20 m) caused by different divergence angles of the laser. The instrumental settings, such as the filter parameter and the front optics also differ. The front optics of the prototype allows near-field measurements, which is not necessary for the satellite. Both the satellite and the prototype use a coaxial[1] receiving configuration, but they differ in the way of the laser beam transmission. The receiving configuration in the telescope for the satellite is a transceiver system. In the prototype, there is one axis, but separate optics, for transmitted and received light (Fig. B.2a). For cases requiring compactness or scanning ability, a coaxial telescope transceiver configuration is needed (Fig. B.2b). Within a transceiver configuration the telescope is used for the transmitted and received light. In a coaxial system the telescope is only used for collection of the backscatter light and this configuration is applied in the ALADIN prototype. The laser beam of the prototype is directed via a beamsplitter onto the optical axis of the system.

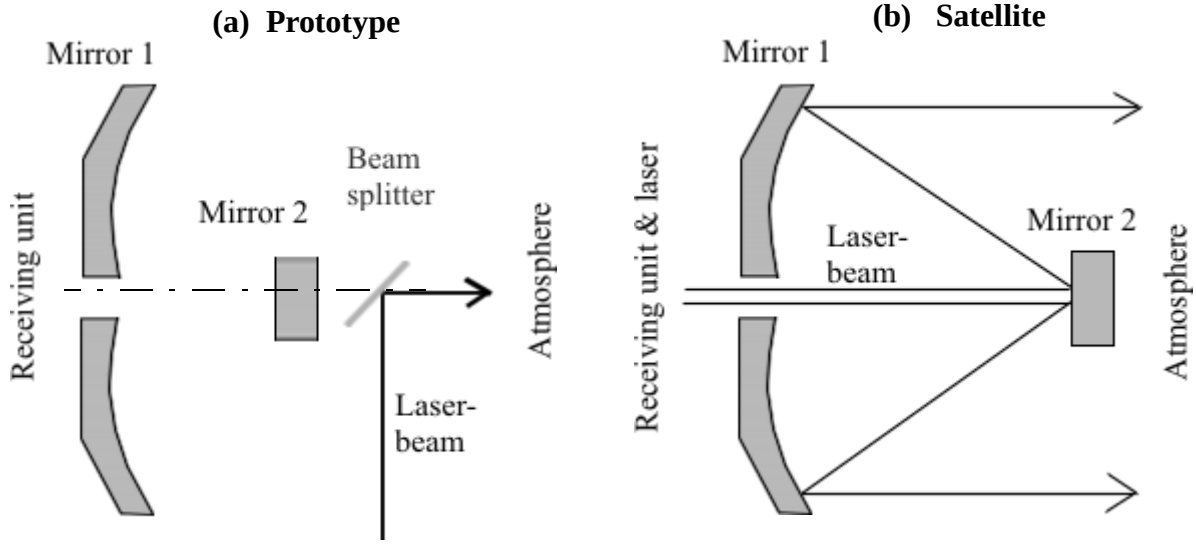

Fig. B.2 The laser beam transmission in the coaxial telescope of the prototype (a) and the transceiver system of the satellite (b).

1. Contrary to coaxial systems where the transmitted and received light use the same optical axis, biaxial systems have different optical axis for the transmitter and receiver.

The number of backscatter photons of the aircraft (flight altitude 10 km), the satellite (flight altitude 400 km), and the ground configuration is shown in Fig. B.3. The results arise from one laser pulse for atmospheric layers of a thickness of 15 m.

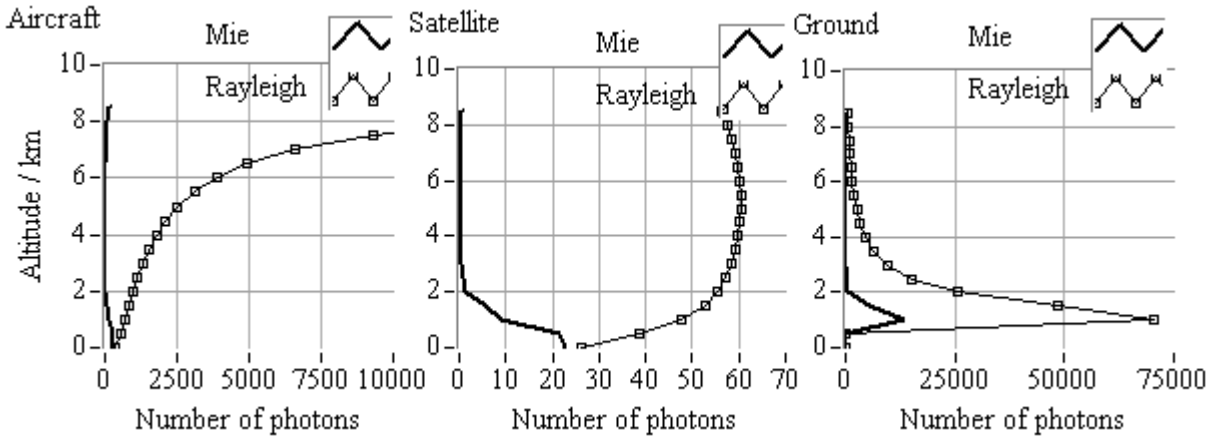

Fig. B.3 The number of backscattered Mie and Rayleigh photons collected by the telescope referring to the aircraft at 10 km flight altitude (left), the satellite at 400 km altitude (middle), and ground system (right), depending on altitude (median aerosol model, 700 shots accumulated, parameters Table B.2 and Table 3.3).

For both the airborne systems and the ground system, the Mie backscatter is mostly affected by the aerosol gradient of the boundary layer which leads to an increased Mie signal near ground. The Rayleigh backscatter signal of the aircraft and the ground system increases towards the instrument and decreases for increasing distance. This arise from the $1/R^2$ dependence of the backscatter photons. In contrast, the Rayleigh backscatter at the satellite is nearly constant for 2-8 km and decreases near ground due to aerosol extinction.

Symbols

Symbol	Name	Units
A	Absorption	
$A(\psi)$	Airy function (phase difference ψ)	
$A'_{R,I}(\lambda)$	Rayleigh intensity measured in channel A	electrons
A_0	Collecting area of the telescope (optical aperture)	m^2
A_0/r^2	Acceptance solid angle	rad
$A_{R,I}(\lambda)$	Rayleigh intensity in channel A, scaled to laser energy	electrons
dco	Detection chain offset per measurement	electrons
E_L	Energy of the laser pulse	mJ
F	Finesse	
F'	Focal point	
f_0	Frequency of the transmitted laser pulse	Hz
i	Pixel index	
I	Intensity	
I'_{bkg}	Measured background light	electrons
I_0	Incident light	
I_A	Intensity on Rayleigh channel A	
I_B	Intensity on Rayleigh channel B	
I_{bkg}	Background light in respect to corresponding integration time	electrons
$I_{M,I}$	Intensities at the Mie receiver from internal signal during measurement	electrons
I_t	Transmitted intensities	electrons
k	Lidar ratio (aerosol extinction-to-backscatter ratio)	sr
$k(\lambda)$	Instrumental constant depending on wavelength λ	
MRR	Mie-to-Rayleigh-ratio	
n	refractive index	
N_{bkg}	Number of background photons	
N_e	Number of electrons	
N_{e_Mie}	Number of electrons at the Mie ACCD	
N_{e_Mie}	Number of electrons at the Mie ACCD	
N_{Fiz}	Number of photons transmitted at the Fizeau	
$N_{Fiz,\ refl}$	Number of photons reflected at the Fizeau	
N_{FP_A}	Number of photons transmitted through the Fabry-Perot interferometer channel A	
N_{FP_B}	Number of photons transmitted through the Fabry-Perot interferometer channel B	

Symbol	Name	Units
N_i	Number of electrons at pixel index *i*	
N_{Mol}	Number of molecules per volume	m^{-3}
N_{noise}	Noise of the ACCD	electrons
N_{ph}	Number of photons	
n_S	Number of all signal electrons at the ACCD	
p	Pressure	Pa
r	Range to target	m
R	Reflection	
$r'_{M,A}$	Mie response value from atmospheric signal during measurement	pixel
$r'_{M,I}$	Mie response value from internal reference signal during measurement	pixel
$r'_{R,A}$	Rayleigh response value from atmospheric signal during measurement	
$r'_{R,A}$	Rayleigh response value from atmospheric signal during measurement	
$r'_{R,I}$	Rayleigh response value from internal reference signal during measurement	
R_β	Backscatter ratio	
$r_{M,A}$	Corrected Mie response value from atmospheric signal during measurement	pixel
$R_{M,C}$	Mie receiver internal response curve during calibration	pixel/pm
$r_{M,I}$	Corrected Mie response value from internal reference signal during measurement	pixel
$r_{R,A}$	Corrected Rayleigh response value from atmospheric signal during measurement	
$R_{R,AC}$	Rayleigh receiver atmospheric response curve during calibration	m^{-1}
$R_{R,C}$	Rayleigh receiver internal response curve during calibration	pm^{-1}
$R_{R,C}$	Rayleigh receiver internal response curve during calibration	m^{-1}
$r_{R,I}$	Corrected Rayleigh response value from internal reference signal during measurement mode	
T	Temperature	K
$T_{A,Mol}$	transmission for aerosols and molecules of the atmosphere	
$T_{Fiz}(\lambda)$	Transmission of Fizeau depending on wavelength	
T_{p_A}	Filter peak transmission of the Fabry-Perot interferometer at channel *A*	
T_{p_B}	Filter peak transmission of the Fabry-Perot interferometer at channel *B*	

Symbol	Name	Units
T_{p_F}	Fizeau interferometer filter peak transmission	
v_{LOS}	line-of-sight wind speed	m/s
Z	altitude of the instrument	m
z	altitude	m
z_t	altitude of the target	m

Greek symbols:

Symbol	Name	Units
μ_{eff}	Detector quantum efficiency	
α	Angle of incident light	rad
α_A, α_{Mol}	Extinction coefficient (aerosol, molecular)	cm^{-1}
$\alpha_{M,A}$	Slope of the Mie receiver atmospheric response during calibration	pixels/pm
$\alpha_{M,C}$	Slope of the Mie receiver internal response during calibration	pixels/pm
β	Backscatter coefficient	$cm^{-1}\ sr^{-1}$
β_A	Aerosol backscatter coefficient	$cm^{-1}\ sr^{-1}$
β_{Mol}	Molecular backscatter coefficient	$cm^{-1}\ sr^{-1}$
$\beta_{R,AC}$	Rayleigh receiver slope of the atmospheric calibration response function	Hz^{-1}
$\beta_{R,C}$	Rayleigh receiver slope of the internal calibration response function	Hz^{-1}
Δf_D	Doppler-shifted frequency	Hz
$\Delta\lambda_{err\_M}$	Linearity error of the Mie receiver internal response during calibration	pm
$\Delta\lambda_{err\_R,AC}$	Linearity error of the Rayleigh receiver atmospheric response during calibration mode	pm
$\Delta\lambda_{err\_R,C}$	Linearity error of the Rayleigh receiver internal response during calibration mode	pm
$\Delta\lambda_{FSR}$	Free spectral range of a filter curve	pm
$\Delta\lambda_{FWHM}$	FWHM of a Gaussian or Lorentzian distribution	pm
$\Delta\lambda_{FWHM\_R}$	FWHM of the Rayleigh spectrum	pm
$\Delta\lambda_{L\_FWHM}$	FWHM of the laser spectrum	pm
$\Delta\lambda_{off}$	Intercept of the Mie receiver internal response during calibration mode	pm
$\Delta\lambda_{off,AC}$	Intercept of the Rayleigh receiver atmospheric response during calibration mode	

Symbol	Name	Units
$\Delta\lambda_{off,C}$	Intercept of the Rayleigh receiver internal response during calibration mode	
$\Delta\lambda_{pix}$	Width of one pixel	pm
$\Delta\lambda_{spac}$	Filter spacing between *A* and *B*	pm
$\Delta\lambda_{spac\_A}$	Filter spacing of filter *A*	pm
$\Delta\lambda_{spac\_B}$	Filter spacing of filter *B*	pm
$\Delta\lambda_{USR}$	Useful spectral range of a filter curve	pm
ΔR	Range of measurement	m
ΔR_{min}	Minimal range of the measurement	pm
ε	Wedge angle	rad
φ	Phase shift	rad
λ_L	Wavelength of the laser	m
σ_M	Standard deviation of Mie spectrum	pm
σ_{Mol}	Rayleigh backscattering cross section	m^2/sr
σ_N	Standard deviation of photon distribution	pm
σ_R	Standard deviation of the Rayleigh spectrum	pm
τ_L	Physical length of the laser pulse	nm
τ_R	Receive optics transmission	
τ_T	Transmit optics transmission	
ψ	Optical separation of the Fabry-Perot interferometer plates	cm

Constants

Avogadro constant	$N_A = 6.023 \times 10^{23}$	mol^{-1}
Boltzmann constant	$k = 1.38 \times 10^{-23}$	J /K
Loschmidt's number (T = 23 ° / p = 1013 atm)	$N_L = 2.479 \times 10^{25}$	m^{-3}
Mean molecular air mass	$m_{air} = 2.9 \times 10^{-2}$	kg/mol
Planck's constant	$h = 6.625 \times 10^{-34}$	J s
Velocity of light	$c = 2.9979 \times 10^{8}$	m/s

Abbrevations

3DWL	Direct Detection DWL
ACCD	Accumulation CCD
ADM	Atmospheric Dynamics Mission
AFG	Air Force Geophysics Laboratory
ALADIN	Atmospheric LAser Doppler lidar INstrument
AProS	ALADIN PROtotype Simulator
Calipso	Cloud-Aerosol Lidar and Infrared Pathfinder Satellite Observation
CCD	Charge Coupled Devices
CLARE'98	Cloud Lidar And Radar Experiment 1998
DWD	Deutscher Wetterdienst
DWL	Doppler Wind Lidar
EARLINET	The European Aerosol Research LIdar NETwork
ECMWF	European Centre for Medium-Range Weather Forecasts
ESA	European Space Agency
FSR	Free spectral range
FWHM	Full-width half-maximum
GLAS	Geoscience Laser Altimeter Satellite
Laser	Light Amplification by Stimulated Emission of Radiation
Lidar	LIght Detection And Ranging
LIPAS	Lidar Performance Analysis Simulator
LITE	Lidar In-space Technology Experiment
LOS	Line-Of-Sight
MOLA	Mars Orbiter Laser Altimeter
Nd:YAG	Neodymium-doped Yttrium Aluminium Garnet
Radar	Radio Detection and Ranging
RMA	Reference Model Atmosphere
Sodar	Sound Detection and Ranging
USR	Useful Spectral Range

References

Abreu V. J. (1979), Wind measurements from an orbital platform using a lidar system with incoherent detection: an analysis, *Appl. Opt*., 18 (17), p. 2992-2997.

Abshire J. B., Sun X., Afzal R. S. (2000), Mars Orbiter Laser Altimeter: receiver model and performance analysis, *Appl. Opt*., 39 (15),p. 2449-2460.

Abshire J. B., Sun X., Riris H., Sirota J. M., McGarry J. F., Palm S., Yi D., Liiva P. (2005), Geoscience Laser Altimeter System (GLAS) on the ICESat Mission: On-orbit measurement performance, *Geophys. Res. Lett*., 32, L21S02.

Astin I., Kiemle C. (2003), Space-borne clear air lidar measurements in the presence of broken cloud, *Annales Geophysicae*, 21, p. 639-647

Astin I., Latter B. G. (1998), A case for exponential cloud fields, *J. App. Meteor.*, 37, p. 1375-1383.

Baker W. E., Emmitt G. D., Robertson F., Atlas R. M., Molinari J. E., Bowdle D. A., Paegle J., Hardesty R. M., Menzies R. T., Krishnamurti T. N., Brown R. A., Post M. J., Anderson J. R., Lorenc A. C., McElroy J. (1995), Lidar-measured winds from space: A key component for weather and climate prediction, *Bull. Am. Meteorol. Soc.*, 76 (6), p. 869-888.

Becker B. D., Roquet H., Stoffelen A. (1996), A simulated future atmospheric observation database including ATOVS, ASCAT, and DWL, *Bull. Am. Meteorol. Soc*., 77, p. 2279-2293.

Benayahu Y., Ben-David A., Fastig S., Cohen A. (1995), Cloud-droplet-size distribution from lidar multiple-scattering measurements, *Appl. Opt.*, 34 (9), p. 1569-1578.

Benedetti-Michelangeli G., Congeduti F., Fiocco G. (1972), Measurement of aerosol motion and wind velocity in the lower troposphere by Doppler optical radar, *J. Atmos. Sci.*, 29, p. 906-910.

Bilbro J. W., DiMarzio C., Fitzjarrald D., Johnson S., Jones W. (1986), Airborne Doppler lidar measurements, *Appl. Opt.*, 25 (21), p. 3952-3960.

Bilbro J. W., Fichtl G., Fitzjarrald D., Krause M., Lee R. (1984), Airborne Doppler lidar wind field measurements, *Bull. Am. Meteorol. Soc*., 65 (4), p. 348-359.

Born M., Wolf E. (1972), *Optik*, Springer Verlag, Berlin, 3rd ed., 591 p.

Bösenberg J., Matthias V. (2003), EARLINET: A european aerosol Research lidar network to establish an aerosol climatology, report 348, Max-Planck-Institut for Meteorology, Hamburg, Germany, 90 p.

Bronstein I. N., Semendjajew K. A. (1987), *Taschenbuch der Mathematik*, 23. ed., Teubner, Leipzig, p. 840.

Champion, K. S. W. (1985), Standard and reference atmospheres, in: *Handbook of geophysics and the space environment*, Unites States Air Force Geophysics Laboratory, p. 14-1.

Chanin M. L., Garnier A., Hauchecorne A., Porteneuve J. (1989), A Doppler lidar for measuring winds in the middle atmosphere, *Geophys. Res. Lett*., 16 (11), p. 1273-1276.

Chen W-N., Chiang Ch-W., Nee J-B. (2002), Lidar ratio and depolarization ratio for cirrus clouds, *Appl. Opt*., 41 (30), p. 6470-6476

Collis R. T. H., Uthe E. E. (1972), Mie scattering techniques for air pollution measurement with lasers, *Opto-Electronics*, 4, p. 87-99.

Cordes J. J. (1995), Economic benefits and costs of developing and deploying a space-based wind lidar, final report, contract No. 43AANW400223, George Washington University, Washington D.C. 20052, 39 p.

Delaval A., Flamant P. H., Aupierre M., Delville P., Loth C. (2000), Intercomparison of wind profiling instruments during the VALID field campaign, *Proc. Int. Laser Radar Conf.*, Vichy, p. 101-103.

Denker C., Tritschler A. (2005), Measuring and maintaining the plate parallelism of Fabry-Perot etalons, submitted to publications of the *Astronomical Society of the Pacific* (available from http://solar.njit.edu/publications.htm).

Dermendjian D. (1964), Scattering and polarization properties of water clouds and hazes in the visible and infrared, *Appl. Opt.*, 3 (2), p. 187-196.

Dho S. W., Park Y. J., Kong H. J. (1997), Experimental determination of a geometric form factor in a lidar equation for an inhomogeneous atmosphere, *Appl. Opt.*, 36 (24), p. 6009-6010.

Di Girolamo P., Summa D., Bauer H., Wulfmeyer V., Behrendt A., Ehret G., Mayer B., Wirth M., Kiemle C. (2004), Simulation of the performance of WALES based on an end-to-end model, *Proc. 22nd Int. Laser Radar Conf.*, Matera, Italy, p. 957.

Doherty S. J., Anderson T. L., Charison R. J. (1999), Measurement of the lidar ration for atmospheric aerosols with a 180° backscatter nephelometer, *Appl. Opt.*, 38 (9), p. 1823-1832.

Dolfi-Bouteyre A., Garnier A. (2002), Fizeau interferometer modelling, final report, ESA, contract No. 14442/00/NL/SF, p. 110-125.

Doms G., Schättler U., Steppeler J. (1999), Kurze Beschreibung des Lokal-Modells und seiner Datenbanken auf dem Datenserver des DWD, Deutscher Wetterdienst, 53 p.

Doppler Ch. (1842), Über das farbige Licht der Doppelsterne und einiger anderer Gestirne des Himmels. Abhandlungen der königlich böhmischen Gesellschaft der Wissenschaften (V Folge, Bd. 2), in: Landespressebüro der Salzburger Landesregierung (Hrsg.): *Christian Doppler - Leben und Werk*. Schriftenreihe Serie Sonderpublikationen 76, 140 p.

Durand Y., Meynart R., Endemann M., Chinal E., Morancais D., Schröder T., Reitebuch O. (2005), Manufacturing of an airborne demonstrator of ALADIN, the direct detection Doppler wind lidar for ADM-Aeolus, *Proc. SPIE*, p. 5984.

Durand Y., Meynart R., Morançais D., Fabre F., Schillinger M. (2004), Results of the pre-development of ALADIN - the direct detection Doppler wind lidar for ADM/AEOLUS mission, poster at the *Int. Laser Radar Conf.*, Matera, p. 247.

EADS-Astrium (2004), ALADIN PDM performance correlation report, EADS-Astrium Toulouse, AE.RP.ASF.AL.00046, 59 p.

EADS-Astrium (2005a), Level 1B master algorithm document, EADS Astrium Toulouse, AE.SW.ASU.GS.023, 80 p.

EADS-Astrium (2005b), ALADIN Airborne demonstrator receiver performance test report, EADS Astrium Toulouse, AE.RP.ASF.AL.00046, 25 p.

Ermakov S. M. (1975), *Die Monte Carlo Methode und verwandte Fragen*, 1st ed., Oldenbourg, München, 291 p.

ESA (1989), European Space Agency, ALADIN, Doppler lidar working group report, SP-1112, 45 p.

ESA (1999), European Space Agency, The four candidate Earth explorer core missions: Atmospheric Dynamics Mission ADM, SP-1233-4, 157 p.

Evans B. T. N. (1988), Sensitivity of the backscatter/extinction ratio to changes in aerosol properties: implications for lidar, *Appl. Opt*., 27 (15), p. 3299-3305.

Fiocco G., Smullin L. D. (1963), Detection of scattering layers in the upper atmosphere by optical radar, *Nature*, 4900, p. 1275-1276.

Flesia C., Korb C. L., Hirt C. (2000), Double edge molecular measurement of lidar wind profiles at 355 nm, *Opt. Lett*., 25 (19), p. 1466-1468.

Flesia C., Korb L. (1999), Theory of the double-edge molecular technique for Doppler lidar wind measurement, *Appl. Opt*., 38 (3), p. 432-440.

Frehlich R. (1999), Performance of maximum likelihood estimators of mean power and Doppler velocity with a priori knowledge of spectral width, *J. Atmos. Oceanic Technol.*, 16, p. 1702-1709.

Frehlich R. G., Yadlowsky M. J. (1994), Performance of mean-frequency estimators for Doppler radar and lidar, *J. Atmos. Oceanic Technol.*, 11, p. 1217-1230.

Gagné J-M., Saint-Dizier J-P., Picard M. (1974), Méthode d'echantillonnage des fonctions déterministes en spectroscopie: application à un spectromètre multicanal par comptage photonique, *Appl. Opt*., Vol. 13, No. 3, p. 581-588.

Garnier A., Chanin M. L. (1992), Description of a Doppler Rayleigh LIDAR for measuring wind in the middle atmosphere, *Appl. Phys. B,* 55, p. 35-40.

Gentry B. M., Chen H., Li S. X. (2000), Wind measurements with a 355 nm molecular Doppler lidar, *Opt. Lett.*, 25 (17), p. 1231-1233.

Gentry, B., M., Korb C. L.(1994), Edge technique for high-accuracy Doppler velocimetry, *Appl. Opt*., 33 (24), p. 5770-5776.

Gittins Ch. M., Lawrence W. G., Marinelli W. J. (1998), A frequency agile bandpass filter for direct detection lidar receivers, *Appl. Opt*., 37 (36), 8327-8335.

Hall F. F., Huffaker R. M., Hardesty R. M., Jackson M. E., Lawrence T. R., Post M. J., Richter R. A., Weber B. F. (1984), Wind measurement accuracy of the NOAA pulsed infrared Doppler lidar, Appl. Opt., 23, (15), p. 2503-2506.

Halldorsson T., Langerholc J. (1978), Geometrical form factors for the lidar function, *Appl. Opt*., 17 (2), p. 240-244.

Hardesty R. M., Brewer W. A., Nardell C. A., Gentry B. W., Yoe J. G., Ryan J. M. (2001), Intercomparison of heterodyne and direct detection Doppler lidars during the 2000 Bartlett, N.H., Measurement Campaign, *Proc. 11th Coherent Laser Radar Conf.*, Malvern, UK, p. 115-118.

Hardesty R. M., Keeler R. J., Post M. J., Richter R. A. (1981), Characteristics of coherent lidar returns from calibration targets and aerosols, *Appl. Opt*., 20 (21), p. 3763-3768.

Hardesty, R. M. (2003), Doppler, in: *Encyclopedia of Atmospheric Sciences*, Holton J. R. ed., Academic Press, London, p. 1194-1202.

Hays P. B.(1991), Image plane detector for Fabry-Perot interferometers: physical model and improvement with anticoincidence detection, *Appl. Opt*., 30 (22), p. 3100-3107.

Hays P. B., Killeen T. L., Kennedy B. C. (1981), The Fabry-Perot interferometer on dynamics explorer, *Space Science Instr.* 5, p. 395-416.

Helstrom C. W. (1968), *Statistical theory of signal detection*, 2nd ed., Pergamon Press, Oxford, 470 p.

Hertzog A., Garnier A. (2002), Validation of virtual instrument simulator, in: Signal processing report, ESTEC, contract No. 14442/00/NL/SF, 338 p.

Huffaker R. M. (1970), Laser Doppler detection systems for gas velocity measurement, *Appl. Opt*., 9 (5), p. 1026-1039.

Hulburt, E. O., (1937), Observations of a searchlight beam to an altitude of 28 kilometers, *J. Opt. Soc. Am*., 27, p. 377-382.

Irgang T. D., Hays P. B., Skinner W. R. (2002), Two-channel direct detection Doppler lidar employing a charge-coupled device as a detector, *Appl. Opt*., 41 (6), p. 1145-1155.

Kajava T. T., Lauranto H. M., Friberg A. T. (1994), Interference pattern of the Fizeau interferometer, *Journal Opt. Soc. Am. A*., 11 (7), p. 2045-2054.

Kaminskii A. A. (1990), *Laser Crystals*, MacAdam D. L. ed., Springer, Heidelberg, 14th ed., 455 p.

Kinosita K., (1953), Numerical evaluation of the intensity curve of a multiple-beam Fizeau fringe, *J. phys. soc. Japan*, 8 (2), p. 219-225.

Kneubühl F. K., Sigrist M. W. (1999), *Laser*, Teubner, Stuttgart, 413 p.

Koechner W. (1976), *Solid-State Laser Engineering*, 1st ed., Springer, New York, 620.

Korb C. L., Gentry B. M. (1990), New Doppler lidar methods for atmospheric wind measurements: the edge technique, *Conf. of Lasers and Electro-Optics*, OSA (Optical Society of America) Technical Digest Series, 7, p. 322-324.

Korb C. L., Gentry B. M., Li S. X. (1997), Edge technique Doppler lidar wind measurements with high vertical resolution, *Appl. Opt*., 36 (24), p. 5976-5983.

Korb C. L., Gentry B. M., Li S. X., Flesia C. (1998), Theory of the double edge technique for Doppler lidar wind measurement, *Appl. Opt*., 37 (15), p. 3097-3104.

Korb C. L., Gentry B. M., Weng C. Y. (1992), Edge technique: theory and application to the lidar measurement of atmospheric wind, *Appl. Opt*., 31 (21), p. 4202-4213.

Leike I. (2000), Direct detection Doppler lidar (D3 Lidar), final report CCN-No 5, ESTEC contract No. 13018/98/NL/GD, 32 p.

Leike I., Streicher J., Werner Ch., Banakh V., Smalikho I., Wergen W., Cress A. (2001), Virtual Doppler lidar instrument, *J. Atmos. Ocean. Technol.*, 18, p. 1447-1456

Leike I., Werner Ch., Streicher J., (2000), Influence of multiple scattering on a Doppler lidar signal, *11th Int. Workshop on Lidar Multiple Scattering Experiments*, Williamsburg, VA, USA.

Liu Z., Sugimoto N., Murayama T. (2002), Extinction-to-backscatter ratio of Asian dust observed with high-spectral-resolution lidar and Raman lidar, *Appl. Opt*., 41 (15), p. 2760-2766.

Marchuk G. I., Mikhailov G. A., Nazareliev M. A., Darbinjan R. A., Kargin B. A., Elepov B. S. (1980), The Monte Carlo methods in atmospheric optics, Springer, Berlin, 208 p.

Marseille G. J., Stoffelen A. (2003), Simulation of wind profiles from a space-borne Doppler wind lidar, *Q. J. Royal Meteorol. Soc*., 129, p. 3079-3098.

Matthais V., Freudenthaler V., Amodeo A., Balin I., Balis D., Bösenberg J., Chaikovsky A., Chourdakis G., Comeron A., Delaval A., De Tomasi F., Eixmann R., Hågård A., Komguem L., Kreipl S., Matthey R., V. Rizi, Rodrigues J. A., Wandinger U., Wang X. (2004), Aerosol Lidar Intercomparison in the Framework of the EARLINET Project. 1. Instruments, *Appl. Opt*. 43 (4), p. 961-976.

McGill M. J., Hart W. D., McKay J. A., Spinhire J. D. (1999), Modeling the performance of direct detection Doppler lidar systems including cloud and solar background variability, *Appl. Opt*., 38 (30), p. 6388-6396.

McGill M. J., Spinhire J.D. (1998), Comparison of two direct detection Doppler lidar Techniques, *Opt. Eng*. 37(10), p. 2675-2686.

McKay J. A. (1998a), Modeling of direct detection Doppler wind lidar. 1) The edge technique, *Appl. Opt*., 37 (27), p. 6480-6486.

McKay J. A. (1998b), Modeling of direct detection Doppler wind lidar. 2) The fringe imaging technique, *Appl. Opt*., 37 (27), p. 6487-6493.

McKay J. A. (1999), Fabry-Perot etalon aperture requirements for direct detection Doppler wind lidar from Earth orbit, *Appl. Opt*., 38 (27), p. 5859-5866.

McKay J. A. 2002, Assessment of a multibeam Fizeau wedge interferometer for Doppler wind lidar, *Appl. Opt*., 41 (9), p. 1760-1767.

McKay J. A., Rees D. (2000), Space-based Doppler wind lidar: Modelling of edge detection and fringe imaging Doppler analyzers, *Adv. Space Res.*, 26 (6), p. 883-891.

Measures, R. M.(1992): *Laser Remote Sensing*, Wiley, Florida, 510 p.

Meister A. (2005), Entwicklung einer UV-Laserlichtquelle sowie Aufbau und Erprobung eines flugzeuggetragenen Ozon-DIAL für Messungen in der unteren Troposphäre, Ph.D. thesis, university of Bayreuth, department of physics, 127 p.

Menzies R. T. (1986), Doppler lidar atmospheric wind sensors: a comparative performance evaluation for global measurement applications from Earth orbit, *Appl. Opt*., 25 (15), p. 2546-2553.

Meyer Y. H. (1981), Fringe shape with an interferential wedge, *Opt. Soc. Am.*, 71 (10), p. 1255-1263.

Naumann H., Schröder G. (1992), *Bauelemente der Optik*, 6th ed., Hansa, München, 638 p.

Nelder J. A., Mead R. (1965), A simplex method for function minimization, *Computer J.*, 7 (4), p. 308-313.

Neumann, G. A., Smith D. E., Zuber M. T. (2002), Two Mars years of clouds observed by the Mars Orbiter Laser Altimeter, *J. Geophys. Res. Planets*, 108 (E4), art. 5023.

Palm S. P., Benedetti A., Spinhire J. (2005), Validation of ECMWF global forecast model parameters using GLAS atmospheric channel measurements, *Geophys. Res. Lett.*, 32, L22S09.

Palm, S.P. and Spinhirne J. D. (1998), The detection of clouds, aerosols and marine atmospheric boundary layer characteristics from simulated GLAS data. *Proc. 19th Int. Laser Radar Conf.*, Annapolis, p. 237-240.

Platt, C. M. R. (2003), Backscatter, in: *Encyclopedia of Atmospheric Sciences*, Holton J. R. ed., Academic Press, London, p. 1176-1183.

Post M. J., Cupp R. E. (1990), Optimizing a pulsed Doppler lidar, *Appl. Opt.*, 29 (28), p. 4145-4157.

Press W. H., Flannery B. P., Teukolsky S. A., Vettering W. T. (1988), *Numerical recipes in C*, 1st ed., Cambridge Press, Cambridge, 735 p.

Rahm S. (1995), Measurement of a wind field with an airborne continuous-wave Doppler lidar, *Opt. Lett.*, 20 (2), p. 216-218.

Rahm S. (2001), Precursor experiment for an active true airspeed sensor, *Opt. Lett.*, 26 (6), p. 319-321.

Rallison R. D., Sorensen D. (2001), Hoe enhanced 355 nm multichannel direct detection Doppler lidar, *Proc. SPIE Int. Soc. Opt. Eng.*, 4291 (33), 10 p.

Rees C., Vyssogorets M., Meredith N. P., Griffin D., Chaxell Y. (1996), The Doppler wind and temperature system of the ALOMAR lidar facility: overview and initial results, *J. Atmos. Terrestrial Phys.*, 58 (16), p. 1827-1842.

Rees D., McDermid I. S. (1990), Doppler lidar atmospheric wind sensor: reevaluation of a 355 nm incoherent Doppler lidar, *Appl. Opt.*, Vol. 29, No. 28, p. 4133-4144.

Reichlmaier S. (1985), Aufbau eines hochauflösenden Fizeau-Interferometers zur Frequenzstabilisierung eines Farbstofflasers, Diploma thesis, University of applied science for Physics, Munich, 57 p.

Reitebuch O. (1999), SODAR-Signalverarbeitung von Einzelpulsen zur Bestimmung hochaufgelöster Windprofile, Ph.D thesis, Fraunhofer institute for atmospheric environmental research, Garmisch-Partenkirchen, Shaker Verlag, Aachen, 175 p.

Reitebuch O., Chinal E., Dabas A., Durand Y., Endemann M., Flamant P. H., Meynart R., Morancais D., Paffrath U., Poberaj G. (2003), Ground and airborne Doppler lidar campaigns for ADM, *Proc. 6th Int. Symp. Tropospheric Profiling*, Leipzig, p. 432-434.

Reitebuch O., Chinal E., Durand Y., Endemann M., Meynart R., Morancais D., Paffrath U. (2004), Development of an airborne demonstrator for ADM-Aeolus and campaign activities, *Proc. Int. Laser Radar Conf.*, Matera, p. 1007-1010.

Reitebuch O., Werner Ch., Leike I., Delville P., Flamant P. H., Cress A., Engelbart D. (2000), Wind profiling by the airborne 10 µm.heterodyne Doppler lidar WIND. A comparison against wind profiler radar - numerical models and simulations, *J. Atmos. Ocean. Technol.*, p. 1331-1334.

Reitebuch O., Werner Ch., Leike I., Delville P., Flamant P. H., Cress A., Engelbart D. (2001), Experimental validation of wind profiling performed by the airborne 10 µm-heterodyne Doppler lidar WIND, *J. Atmos. Ocean. Tech.* 18, p. 1331-1344.

Roedel W. (2000), *Physik unserer Umwelt - Die Atmosphäre*, 3rd ed., Springer, Berlin, 498 p.

Saleh B. E. A., Teich M. C. (1991), *Fundamentals of photonics*, Wiley, Florida, 966 p.

Schillinger M., Morancais D., Fabre F., Culoma A. (2003), ALADIN: the lidar instrument for the Aeolus mission, *Proc. SPIE,* Sensors, Systems, and Next-Generation Satellites VI, 4881, p. 40-51.

Skinner W. R., Hays P. B. (1994), Incoherent Doppler lidar for measurement of atmospheric winds, *Proc. SPIE,* 2266, p. 383-394.

Smalikho I. (2003), Techniques of wind vector estimation from data measured with a scanning coherent Doppler lidar, *J. Atmos. Oceanic Technol.*, 20, p. 276-290.

Souprayen C., Garnier A., Hertzog A. (1999b), Rayleigh-Mie Doppler wind lidar for atmospheric measurements, 2) Mie scattering effect, theory, and calibration, *Appl. Opt*., 38 (12), p. 2410-2421.

Souprayen C., Garnier A., Hertzog A., Hauchecorne A., Porteneuve J. (1999a), Rayleigh-Mie Doppler wind lidar for atmospheric measurements, 1) Instrumental setup, validation, and first climatological results, *Appl. Opt*., 38 (12), p. 2422-2431.

Spinhire J. D., Chudamani S., Cabanaugh J. F., Bufton J. L. (1997), Aerosol and cloud backscatter at 1.06, 1.54, and 0.53 µm by airborne hard-target-calibrated Nd:YAG/methane Raman lidar, *Appl. Opt*., 36 (15), p. 3475-3489.

Spinhirne J. D., Palm S. P., Hart W. D., Hlavka D. L., Welton E. J. (2005), Cloud and aerosol measurements from GLAS: Overview and initial results. *Geophys. Res. Lett.*, 32, L22S03.

Stoffelen A., Flamant P., Hakansson M., Källen E., Marseille G-J, Pailleux J., Schyberg H., Vaughan M. (2002), Measurement error and correlation impact on the Atmospheric Dynamics Mission, Executive summary, ESA contract 15192/01/NL/MM, 30 p.

Streicher J., Leike I., Werner Ch. (1998), ALIENS: Atmospheric lidar end-to-end simulator, *Proc. SPIE*, 3583, p. 380-386.

Tan D. G. H., Andersson E. (2004), Simulation of the yield and accuracy of wind profile measurements from the Atmospheric Dynamics Mission (ADM-Aeolus). Reading, UK, European Centre for Medium-range Weather Forecast (ECMWF), Research Department, Tech. Memo. 431, 29 p.

Van Trees H. L. (1968), Detection, estimation, and modulation theory 1, 1st ed., Wiley & Sons, New York, 349 p.

Vaughan J. M. (2002), *The Fabry-Perot interferometer*, Hilger, Bristol, 583 p.

Vaughan J. M., Geddes N. J., Flamant P. H., Flesia C. (1998), Establishment of a backscatter coefficient and atmospheric database, ESA contract 12510/97/NL/RE, 110 p.

Vaughan, J. M., Brown D. W., Nash C., Alejandro S. B., Koenig G. G. (1995), Atlantic atmospheric aerosol studies 2. Compendium of airborne backscatter measurements at 10.6 μm, *J. Geophys. Res.*, 100 (D1), p. 1043-1065.

Veldman S. M., Knobbout H. A., Stoffelen A., Marseille G. J., Fuchs J. (1999), Lidar performance analysis simulator - LIPAS, study report, ESA contract No. 12718/98/NL/GD, 88 p.

Wandinger U. (2003), Air mass modification process, EARLINET: a european aerosol research lidar network to establish an aerosol climatology, report No. 348, Max-Planck-Institute for meteorology, Hamburg, 90 p.

Wandinger U., Ansmann A. (2002), Experimental determination of the lidar overlap profile with Raman lidar, *Appl. Opt*., 41 (3), p. 511-514.

Weissmann M., Braun F. J., Gantner L., Mayr G. J., Rahm S., Reitebuch O. (2005), The alpine mountain-plain circulation: Airborne Doppler lidar measurements and numerical simulations, *Am. Meteorol. Soc*., 43, p. 3095-3109.

Weissmann M., Cardinali C. (2006), The impact of airborne Doppler lidar observations on ECMWF forecasts, submitted to *Q. J., Royal Meteor. Soc*., 16 p.

Werner C. (2005), Doppler wind lidar, in: *Lidar*, Weitkamp C. ed., Springer, Singapore, 455 p.

Werner C., Streicher J., Leike I., Münkel C. (2005), Visibility and cloud lidar, in: *Lidar*, Weitkamp C. ed., Springer, Singapore, 455 p.

Wiegner M., Freudenthaler V., Heese B., Seefeldner M. (2004), Lidar measurements for aerosol remote sensing, Poster, *Proc. DPG Tagung*, München, p. 188.

Winker, D. M., Couch, R. H., and McCormick, M. P. (1996), An overview of LITE: NASA's Lidar In-space Technology Experiment, *Proc. IEEE*, 84 (2), p. 164-180.

Winzer P. J., Pfennigbauer M., Strasser M. M., Leeb W. R. (2001), Optimum Filter Bandwidths for Optically Preamplified NRZ Receivers, *J. Lightwave Tech*. 19, p. 1263-1273.

Wiscombe W. J. (1980), Improved Mie scattering algorithms, *Appl. Opt.* 19 (9), p. 1505-1509.

Zwally H. J., Schutz B., Abdalati W., Abshire J., Bentley C., Brenner A., Bufton J., Dezio J., Hancock D., Harding D., Herring T., Minster B., Quinn K., Palm S., Spinhirne J., Thomas R. (2002), ICESat's laser measurements of polar ice, atmosphere, ocean, and land, *J. Geodyn*., 34, p. 405–445.

Acknowledgements

I am very grateful to Professor Schumann and Professor Sattelmayer for their guidance and their encouragement, giving me the opportunity to carry out this research work. I would like to express my deepest gratitude to my mentor Oliver Reitebuch for the guidance he provided during the study of this thesis, in particular for his advice which was invaluable for the successful completion of this research work. My special thanks go to Jürgen Streicher for his inspiring discussions, his tireless help, and patience in providing me with the details of the lidar topic. I am deeply grateful to Adrian Stannard for the strenuous job of proof reading parts of the manuscript, doing his best in the short time available, and for his excellent, professional, and extensive advice. I want to express my warmest thanks to Ines Leike, whose research results are essential for this work. She has been of great support. I wish to acknowledge Eric Chinal, Marc Chaloupy, and Michael Beslon from EADS-Astrium Toulouse for their engaged and great work at DLR during the first measurements with the prototype. They provided excellent support to perform the measurement results presented in this thesis. I wish to thank Martin Endemann, Herbert Nett, and Olivier Le Rille from ESA-ESTEC Noordwijk for their constructive comments, their professional advice, and productive insights. I also want to thank Christian Lemmerz, Engelbert Nagel, and Torsten Schröder for invaluable assistance and support to enable measurements on ground and aircraft. Lastly, I thank my colleagues at the Institute of Atmospheric Physics of the atmosphere at DLR for the pleasant working atmosphere and for their assistance.